

# Advanced Shaping of Catalysts via Additive Manufacturing – Direct Ink Writing in the Context of Heterogeneous Catalysis

Paula Friederike Großmann

Vollständiger Abdruck der von der TUM School of Natural Sciences der Technischen  
Universität München zur Erlangung einer

Doktorin der Naturwissenschaften (Dr. rer. nat.)

genehmigten Dissertation.

Vorsitz: Prof. Dr.-Ing. Kai-Olaf Martin Hinrichsen

Prüfer\*innen der Dissertation:

1. Prof. Dr. Dr. h. c. Bernhard Rieger
2. Hon.-Prof. Dr. Richard W. Fischer
3. Prof. Dr. Dr. h. c. Frank Rößner

Die Dissertation wurde am 27.02.2023 bei der Technischen Universität München  
eingereicht und durch die TUM School of Natural Sciences am 11.05.2023  
angenommen.



*“Research is formalized curiosity. It is poking and prying with a purpose. It is a seeking that he who wishes may know the cosmic secrets of the world and they that dwell therein.”*

Zora Neale Hurston

*“Nobody climbs mountains for scientific reasons. Science is used to raise money for the expeditions, but you really climb for the hell of it.”*

Sir Edmund Hillary



## Acknowledgements

Allen voran möchte ich meinem Doktorvater Prof. Dr. Bernhard Rieger für die Möglichkeit danken, dass ich meine Doktorarbeit am WACKER-Lehrstuhl anfertigen durfte. Die mir gewährten Freiräume sowie die wertvollen Diskussionen und die Unterstützung während der gesamten Arbeit habe ich sehr genossen.

Dr. Carsten Troll möchte ich dafür danken, dass er mir bei allen technischen Problemen mit dem 3D-Drucker und allen sonstigen Geräten sowie allen anderen Problemen stets mit Rat und Tat zur Seite stand. Vielen Dank auch an Frau Bauer für ihre Unterstützung bei allen organisatorischen Angelegenheiten sowie Dr. Sergei Vagin für seinen stets hilfreichen Input.

Darüber hinaus möchte ich Prof. Dr. Richard Fischer, Dr. Normen Szesni und Dr. Markus Tonigold von der Clariant Produkte (Deutschland) GmbH für ihre Anregungen, Ideen und Vorschläge während meiner Arbeit danken. Auch Dr. Alexander Seidel danke ich für seine Hilfe bei der Umsetzung der katalytischen Tests sowie für die durchgeführten Messungen.

Besonders bedanken möchte ich mich bei meiner „Projekt-Buddy“ My Bui für die tolle Zusammenarbeit, all die fachlichen und fachfremden Gespräche sowie die vielen lustigen gemeinsamen Stunden vor diversen 3D-Druckern und Geräten. Du warst die beste Projektpartnerin, die ich mir hätte wünschen können.

Dr. Zahid Hussain möchte ich für all die guten Ideen danken, auch wenn ich leider nicht alle umsetzen konnte, sowie für die Einführung in die Welt der MOFs.

Katia Rodewald danke ich für die REM-Messungen und die Bestellungen. Max Koch danke ich für die Durchführung meiner ICP-OES Messungen. Dr. Carsten Peters möchte ich für seine Geduld und stetige Hilfe beim TEM-Messen danken. Dr. Klaus Achterhold danke ich für die  $\mu$ CT-Messungen sowie seine fortwährende Unterstützung und guten Vorschläge hinsichtlich der Datenauswertung.

Meinem Masteranden Sebastian W. möchte ich an dieser Stelle für die gute und konstruktive Zusammenarbeit danken. Ein großer Dank geht natürlich auch an all meine motivierten Studenten Matthias, Silva, Sebastian R., Sebastian W., Larissa, Marlene, Jan, Steffi, Mira und Andreas. Es hat mir Freude gemacht euch zu betreuen.

Selbstverständlich möchte ich auch allen Doktoranden und Masteranden des WACKER-Lehrstuhls danken für die tolle Arbeitsatmosphäre am Lehrstuhl, insbesondere in der Makro Süd (danke an Gitty, Marina, Elli, Steffi und Baohui), aber auch in der Makro Nord (danke an Lucas und Jonas). Auch dem Lehrstuhl für Technische Chemie 1 möchte ich danken, dass ihr mich als Ehrenmitglied aufgenommen habt. Ein besonderer Dank geht zudem an Jonas für seine stete Hilfe beim 3D-Drucker, Matthi für die vielen Stunden vor dem Rheometer, Andi als Tauch- und Schwimmbuddy, Alina für die PubQuizze und Amelie für all die Gespräche und ihren Rat. Ein herzlicher Dank geht auch an Moritz für seine stete Unterstützung und Hilfe über die letzten Jahre.

Abschließend möchte ich mich noch bei meiner Familie, allen voran natürlich meinen Eltern, für ihr Vertrauen in mich und ihre stetige Unterstützung bedanken.



# Table of contents

<b>Acknowledgements</b> .....	<b>V</b>
<b>Table of contents</b> .....	<b>VII</b>
<b>List of abbreviations</b> .....	<b>IX</b>
<b>Publication list</b> .....	<b>XI</b>
<b>Abstract</b> .....	<b>XIII</b>
<b>Zusammenfassung</b> .....	<b>XIV</b>
<b>1 Introduction</b> .....	<b>1</b>
<b>2 Theoretical background</b> .....	<b>3</b>
2.1 Heterogeneous Catalysis.....	3
2.1.1 Macrostructure and shaping of catalysts.....	4
2.1.2 Microstructure of catalysts.....	7
2.2 Selected catalytic systems.....	10
2.2.1 Pt/Al <sub>2</sub> O <sub>3</sub> as catalyst for the dehydrogenation of perhydro-dibenzyltoluene .....	11
2.2.2 NH <sub>2</sub> -MIL-125 (Ti) derived catalyst for photocatalytic water splitting .....	16
2.3 Additive manufacturing as a novel shaping technique .....	20
2.3.1 Direct Ink Writing/Robocasting.....	22
2.3.2 3D printing in catalysis .....	25
<b>3 Aim of this thesis</b> .....	<b>36</b>
<b>4 3D Printed MOF-Derived Composites for Enhanced Photocatalytic Hydrogen Generation</b> .....	<b>38</b>
4.1 Bibliographic data.....	38
4.2 Abstract graphic (TOC) .....	38
4.3 Content.....	39
4.4 Manuscript .....	40
<b>5 Influence of internal and external surface area on impregnation and activity of 3D printed catalyst carriers</b> .....	<b>50</b>
5.1 Bibliographic data.....	50
5.2 Abstract graphic (TOC) .....	50
5.3 Content.....	51
5.4 Manuscript .....	52
<b>6 Comparison of Direct Ink Writing and Binder Jetting for additive manufacturing of Pt/Al<sub>2</sub>O<sub>3</sub> catalysts for the dehydrogenation of perhydro-dibenzyltoluene</b> .....	<b>64</b>
6.1 Bibliographic data.....	64
6.2 Abstract graphic (TOC) .....	64
6.3 Content.....	65

6.4	Manuscript .....	66
<b>7</b>	<b>Summary and Outlook .....</b>	<b>78</b>
<b>8</b>	<b>Appendix.....</b>	<b>81</b>
8.1	Additional information for Chapter 4 “3D Printed MOF-Derived Composites for Enhanced Photocatalytic Hydrogen Generation” .....	81
8.1.1	Reprint permission .....	81
8.1.2	Supporting information.....	82
8.2	Additional information for Chapter 5 “Influence of internal and external surface area on impregnation and activity of 3D printed catalyst carriers” .....	94
8.2.1	Reprint permission .....	94
8.2.2	Supporting information.....	95
8.3	Additional information for Chapter 6 “Comparison of Direct Ink Writing and Binder Jetting for additive manufacturing of Pt/Al <sub>2</sub> O <sub>3</sub> catalysts for the dehydrogenation of perhydro-dibenzyltoluene” .....	107
8.3.1	Reprint permission .....	107
8.3.2	Supporting information.....	108
8.4	Reprint permissions for figures.....	113
<b>9</b>	<b>List of figures.....</b>	<b>117</b>
<b>10</b>	<b>List of tables .....</b>	<b>118</b>
<b>11</b>	<b>References.....</b>	<b>119</b>



## List of abbreviations

0H-DBT.....	dibenzyltoluene
12H-BT.....	perhydro-benzyltoluene
18H-DBT.....	perhydro-dibenzyltoluene
AM.....	additive manufacturing
BDC.....	1,4-benzenedicarboxylic acid
BJ.....	Binder Jetting
CAD.....	computer aided design
CB.....	conduction band
CFD.....	computational fluid dynamics
DIW.....	Direct Ink Writing
DLP.....	Digital Light Processing
FDM.....	Fused Deposition Modeling
HER.....	hydrogen evolution reaction
IR.....	infra red
LOHC.....	liquid organic hydrogen carrier
MOF.....	metal-organic framework
NHE.....	normal hydrogen electrode
OER.....	oxygen evolution reaction
SLA.....	Stereolithography
SLM.....	Selective Laser Melting
SLS.....	Selective Laser Sintering
STL.....	standard tessellation language
VB.....	valence band



## Publication list

- I. Hussain, M. Z.<sup>\*,#</sup>; Großmann, P. F.<sup>#</sup>; Kohler, F.; Kratky, T.; Kronthaler, L.; van der Linden, B.; Rodewald, K.; Rieger, B.; Fischer, R. A.; Xia, Y.\* 3D Printed MOF-Derived Composites for Enhanced Photocatalytic Hydrogen Generation. *Sol. RRL*, 6, 2200552 **2022**. DOI: 10.1002/solr.202200552.
- II. Großmann, P. F.; Tonigold, M.; Szesni, N.; Fischer, R. W.; Seidel, A.; Achterhold, K.; Pfeiffer, F.; Rieger, B.\* Influence of internal and external surface area on impregnation and activity of 3D printed catalyst carriers. *Catal. Commun.* **2023**, 175, 106610. DOI: 10.1016/j.catcom.2023.106610.
- III. Bui, H. M.<sup>#</sup>; Großmann, P. F.<sup>#</sup>; Berger, A.; Seidel, A.; Tonigold, M.; Szesni, N.; Fischer, R.; Rieger, B.; Hinrichsen, O.\* Comparison of Direct Ink Writing and Binder Jetting for additive manufacturing of Pt/Al<sub>2</sub>O<sub>3</sub> catalysts for the dehydrogenation of perhydrodibenzyltoluene. *Chem. Eng. J.* **2023**, 12 (4), 141361. DOI: 10.1016/j.cej.2023.141361.

<sup>#</sup> These authors contributed equally. \* Corresponding author.

Publications beyond the scope of this thesis:

- Bui, H. M.; Großmann, P. F.; Gros, T.; Blum, M.; Berger, A.; Fischer, R.; Szesni, N.; Tonigold, M.; Hinrichsen, O.\* 3D printed co-precipitated Ni-Al CO<sub>2</sub> methanation catalysts by Binder Jetting: Fabrication, characterization and test in a single pellet string reactor. *Appl. Catal. A: Gen.* **2022**, 643, 118760. DOI: 10.1016/j.apcata.2022.118760.
- Kränzlein, M.<sup>#</sup>; Pehl, T. M.<sup>#</sup>; Halama, K.<sup>#</sup>; Großmann, P. F.; Kratky, T.; Mühlbach, A. M.; Rieger, B.\* Azide-Modified Poly(diethyl vinylphosphonate) for Straightforward Graft-to Carbon Nanotube Functionalization. *Macro Materials & Eng.* **2022**, 2200635. DOI: 10.1002/mame.202200635.
- Stieglitz, L.; Geiger, C.; Großmann, P. F.; Kränzlein, M.; Rodewald, K.; Müller-Buschbaum, P.; Rieger, B.\* Fiber Spinning of Ultrahigh Molecular Weight Isotactic Polypropylene: Melt Spinning and Melt Drawing. *ChemPlusChem*: **2023**, e202300045. DOI: 10.1002/cplu.202300045.
- Chen, X.; Stasi, M.; Rodon-Fores, J.; Großmann, P. F.; Bergmann, A. M.; Dai, K.; Tena-Solsona, M.; Rieger, B.; Boekhoven, J.\* A Carbodiimide-Fueled Reaction Cycle That Forms Transient 5(4H)-Oxazolones. *J. Am. Chem. Soc.* **2023**, 145, 12, 6880–6887. DOI: 10.1021/jacs.3c00273.

## Conference contributions:

- Großmann P.; Ludwig, T.; Troll, C.; Fischer, R.; Tonigold, M.; Rieger, B. „*Balancing material and additive properties for the usage of additive manufacturing in heterogeneous catalysis*”, February 18<sup>th</sup> – 19<sup>th</sup> **2019**: Chemie hilft 3D-Druck (Frankfurt am Main, Germany); Poster.
- Großmann, P. F.; Troll, C.; Rieger, B. „*Direct Ink Writing as an additive manufacturing technique for shaping heterogeneous catalysts*”, October 16<sup>th</sup>-19<sup>th</sup> **2019**: 13<sup>th</sup> Conference for Young Scientists in Ceramics (Novi Sad, Serbia); Talk.
- Großmann P. F.; Bui H. M.; Troll, C.; Tonigold, M.; Fischer, R.; Hinrichsen, O.; Rieger, B. „*Tuning the shape of heterogeneous catalysts by Direct Ink Writing of ceramics*”, May 13<sup>th</sup> **2020**, 53. Jahrestreffen Deutscher Katalytiker, virtual Postershow.
- Großmann P. F.; Bui H. M.; Troll, C.; Tonigold, M.; Fischer, R.; Hinrichsen, O.; Rieger, B. „*Advantages and Challenges of Shaping Heterogeneous Catalysts by Direct Ink Writing*”, October 28<sup>th</sup> – 30<sup>th</sup> **2020**: young Ceramists Additive Manufacturing Forum 2020; online conference in gather.town; Poster.
- Großmann P. F.; Bui H. M.; Troll, C.; Tonigold, M.; Fischer, R.; Hinrichsen, O.; Rieger, B. „*Improving catalytic activity by direct ink writing of heterogeneous catalysts*”, December 16<sup>th</sup> – 21<sup>st</sup> 2021: The International Chemical Congress of Pacific Basin Societies 2021 - Pacificchem 2021, online conference; Poster.
- Großmann P. F.; Troll, C.; Tonigold, M.; Fischer, R.; Rieger, B., “*Combining heterogeneous catalysis and direct ink writing: Towards well-defined catalyst shapes for improved catalytic activity*”, March 20<sup>th</sup> – 24<sup>th</sup> 2022: ACS Spring 2022 (San Diego, USA); Poster.
- Großmann P. F.; Bui H. M.; Tonigold, M.; Fischer, R.; Hinrichsen, O.; Rieger, B. “*Binder Jetting and Direct Ink Writing: Advantages and Disadvantages of Two Additive Manufacturing Techniques in Heterogeneous Catalysis*”, June 27<sup>th</sup> – 30<sup>th</sup> 2022: 55. Jahrestreffen Deutscher Katalytiker (Weimar, Germany); Poster.

## Abstract

Heterogeneous catalysis for the synthesis of raw and fine chemicals has become indispensable in the chemical industry. Not only is the composition of the catalyst itself a critical factor for its productivity, but its shape also has a significant impact on critical process parameters. This includes for instance reactor bed pressure drop, as well as heat and mass transfer processes. To overcome the existing limitations of traditional techniques for catalyst shaping, this work investigates Direct Ink Writing (DIW), an extrusion-based additive manufacturing process, as a modern shaping method for heterogeneous catalysts. Two different approaches are used, the direct printing of an active material, or a precursor thereof, and the printing of a support material that is subsequently loaded with the active species. In the first case, a titanium-based metal-organic framework is printed as precursor of the active component, which is then converted thermally to titanium oxide and thus tested as a photocatalyst for hydrogen evolution by water splitting. In this reaction, the 3D printed monolithic structures show an approximately five-fold increase in hydrogen release compared to unformed powder. This increase is attributed to the improved illumination by UV-Vis light for the 3D structures. Additional loading with platinum further improves the activity of the catalyst. Moreover, the recyclability of the 3D printed structure is demonstrated successfully.

Furthermore, the influence of the geometric outer and inner surface on the impregnation behavior of alumina catalyst supports is investigated. The dehydrogenation of perhydro-dibenzyltoluene, a so-called hydrogen storage molecule, serves as a test reaction. Overall, it is shown that increasing the surface-to-volume ratio reduces the penetration depth of platinum as active component. This makes it more accessible to the reactant and increases the productivity of the catalyst. In a batch reactor test setup, it is demonstrated that the catalyst volume can be reduced by almost two-thirds using the monolithic structures compared to a packed bed while maintaining approximately the same productivity, which reduces process costs.

Since different 3D printing techniques offer various advantages and disadvantages, their impact on the application in catalysis is investigated. Therefore, the DIW process is compared in detail with powder bed Binder Jetting as a method for forming catalyst supports. Catalysts printed by Binder Jetting result in significantly higher (macro-)porosities regardless of the sintering temperature. After impregnation with platinum, DIW shows a significantly lower depth of platinum penetration as well as an overall lower loading. However, regardless of the differences in the catalyst supports in terms of platinum penetration depth, particle size or loading, both catalysts are equally productive in the dehydrogenation of perhydro-dibenzyltoluene, independently if they are tested as powders or as shaped monoliths. This shows that both methods are suitable for printing catalyst supports, and thus other characteristics such as scalability or cost of the printing technique should be considered when selecting the appropriate technique. Overall, the potential of DIW as a catalyst shaping method is evaluated and detailed characterizations are added in this work.

## Zusammenfassung

In der chemischen Industrie ist die heterogene Katalyse zur Synthese von Roh- und Feinchemikalien heutzutage nicht mehr wegzudenken. Dabei ist nicht nur die Zusammensetzung des Katalysators selbst ein entscheidender Einflussfaktor auf dessen Produktivität, auch seine Form spielt eine essenzielle Rolle, da diese kritische Prozessparameter wie den Druckverlust der Reaktorschüttung aber auch Wärme- und Stofftransportprozesse beeinflusst. Um die bestehenden Limitierungen der traditionellen Katalysatorformgebungstechniken zu überwinden, wird im Rahmen dieser Arbeit Direct Ink Writing (DIW), ein extrusionsbasierter additiver Fertigungsprozess, als Formgebungsmethode für heterogene Katalysatoren detailliert untersucht. Dabei werden zwei unterschiedliche Vorgehensweisen genutzt: einmal der Direktdruck eines Präkursors der Aktivkomponente sowie das Drucken von Trägermaterial, welches im Anschluss mit der aktiven Spezies beladen wird. Als Vorstufe der Aktivkomponente wird im ersten Fall eine titanbasierte metall-organische Gerüstverbindung verdruckt, welche im Anschluss thermisch zu Titanoxid umgesetzt wird. Dieses wird als Photokatalysator für die Wasserspaltung zu Wasserstoff getestet. Dabei weisen die 3D-gedruckten monolithischen Strukturen verglichen mit ungeformtem Pulver eine etwa fünffach erhöhte Wasserstofffreisetzung auf, welche auf die verbesserte Beleuchtung durch Licht im UV-Vis Bereich zurückgeführt werden kann. Eine zusätzliche Beladung mit Platin verbessert die Aktivität des Katalysators weiter, wobei auch dessen Rezyklierbarkeit gezeigt wird.

Weiterhin wird der Einfluss der geometrischen äußeren, sowie der inneren Oberfläche auf das Imprägnierverhalten von Aluminiumoxid Katalysatorträgern untersucht. Als Testreaktion dient hierbei die Dehydrierung von Perhydrodibenzyltoluol, einem sogenannten Wasserstoffspeichermolekül. Insgesamt zeigt sich, dass bei einem erhöhten Oberflächen-zu-Volumenverhältnis die Eindringtiefe des Platins als aktive Komponente verringert wird. Dieses ist dadurch für die Reaktion leichter zugänglich und die Produktivität des Katalysators steigt. In einem absatzweise betriebenen Rührkessel als Testaufbau kann zudem gezeigt werden, dass bei annähernd gleicher Produktivität das Katalysatorvolumen bei der Nutzung der monolithischen Strukturen verglichen mit einer Zylinderschüttung um knapp zwei Drittel reduziert werden kann, was sich positiv auf die Prozesskosten auswirkt.

Da verschiedene 3D-Drucktechniken unterschiedliche Vor- und Nachteile bieten, werden ihre Auswirkungen auf die Anwendung in der Katalyse untersucht. Dafür wird das DIW-Verfahren detailliert mit dem pulverbettbasiertem Binder Jetting als Formgebungsmethode für Katalysatorträger verglichen. Durch das Binder Jetting wird unabhängig von der Sintertemperatur eine deutlich erhöhte (Makro-) Porosität erreicht. Bei der Beladung mit Platin zeigt sich für das DIW eine deutlich geringere Eindringtiefe des Platins sowie eine insgesamt geringere Beladung. Unabhängig von Unterschieden der Katalysatorträger hinsichtlich Platineindringtiefe, innerer Oberfläche, Partikelgröße oder Beladung sind jedoch beide Katalysatoren bei der Dehydrierung von Perhydrodibenzyltoluol sowohl als Pulver als auch als Formkörper gleich produktiv. Dies zeigt, dass beide Methoden geeignet sind, um Katalysatorträger zu drucken und für die Auswahl der geeigneten Technik weitere Charakteristika wie Skalierbarkeit oder Kosten der Drucktechnik berücksichtigt werden sollten. Insgesamt wird im Rahmen dieser Arbeit das Potential von DIW als Katalysator-Formgebungsmethode evaluiert und um detaillierte Charakterisierungen ergänzt.

# 1 Introduction

For spherical, uniform particles, cubic close-packed (face-centered cubic) and hexagonal close-packed structures have been shown to be the two close-packings with a packing density of around 74 %. On the other hand, the packing densities of randomly packed monodisperse spheres are around 62 %, as determined from experimental and computational data. However, Donev et al. showed 2004 that ellipsoidal particles, such as those found in M&M's candies, surprisingly have packing densities of 68 to 71 %, which are significantly higher than the ones of random packings of equal spheres. Depending on the shape of the ellipsoid, they can even reach 74 % and are thus in the range of the close-packing of equal spheres.<sup>1</sup> The authors attribute this to the higher number of degrees of freedom per particle, which increases from 6 for spheres to about 10 for the studied ellipsoids. Accordingly, the number of particle contacts also increases in order to eliminate the corresponding local and collective degrees of freedom and to ensure jamming which results in such high densities.<sup>1,2</sup> Thus, in areas where high particle densities are to be achieved, ellipsoidal instead of spherical particles could be used to approach densities of the close-packing. A difference between spherical and ellipsoidal particles was also investigated by Yunker et al. in 2011. They showed that the so-called coffee-ring effect, the deposition of suspended particles in a ring-like fashion during drying of a drop of liquid, depends on the shape of the particles. While spherical particles exhibit this effect, it is suppressed in the case of ellipsoidal particles, resulting in uniform particle deposition on the surface.<sup>3,4</sup>

Geometric shape as a characteristic plays a role not only in the field of particle technology, but in almost all areas of life. For example, the shape of the endoplasmic reticulum plays an important role, since morphology defects can be linked to the pathology of several diseases.<sup>5</sup> But also in technical applications, shape and corresponding design are important influencing factors, for example in aeronautics with optimized aircraft geometries in terms of aerodynamics.<sup>6</sup> Since manufactured shapes vary considerably in geometric complexity as well as in size, it is important to know the plethora of available shaping processes also with regard to advantages and limitations. Furthermore, the used molding processes have a non-negligible influence on the properties of the shaped material, such as its stability or homogeneity.<sup>7</sup>

Traditionally, four broadly classified shaping categories can be distinguished, namely casting, manipulative processes, powder techniques, as well as cutting and grinding operations.<sup>7</sup> In casting, a liquid is poured into a prefabricated mold and cured. Manipulative processes include the plastic deformation of the corresponding material, for example through the extrusion of polymers. Powder techniques describe the shaping of powders via compacting, such as tableting. Cutting and grinding are so-called subtractive manufacturing techniques in which the desired object geometry is achieved by removing superfluous material. Meanwhile, additive manufacturing is another shaping category that builds up the desired object in a layer wise fashion. The respective shaping techniques employed depend on the materials to be shaped as well as the desired geometries and properties of the corresponding object. Consequently, shaping is relevant in many industrial processes today, and ranges from the simple shaping of the product or its precursors via corresponding packaging to optimization of product properties by varying the respective shapes.<sup>7,8</sup>

A subject area in science in which shaping does not play an overriding role at first glance is chemistry. However, shaping does play an important role in technical, industrial chemistry. The shaping of catalysts in heterogeneous catalysis is the subject of industrial research and is of essential importance, which is reflected for example in the various patented geometries.<sup>9</sup> Traditionally, tableting, extrusion and granulation are the primary shaping methods employed, although these are limited in terms of possible shape variation. To overcome these limitations, additive manufacturing as a shaping method in heterogeneous catalysis has been increasingly investigated in recent years. Various catalyst and support materials have already been additively manufactured in literature, demonstrating improved catalytic performance in the corresponding test reactions.<sup>10,11</sup> In the context of this work, the shaping of heterogeneous catalysts with the extrusion-based additive manufacturing technique Direct Ink Writing is investigated. Both alumina-based support materials and subsequent impregnation as well as direct printing of active material are investigated regarding the printing thereof. The obtained shapes are characterized subsequently, and the catalysts examined in corresponding catalytic test reactions. Ultimately, the influence of advanced shaping of catalysts for heterogeneous catalysis is to be investigated.



## 2 Theoretical background

### 2.1 Heterogeneous Catalysis

In chemical industry, catalysis and especially heterogeneous catalysis play a crucial role for the fabrication of basis and fine chemicals. It is said that about 80 to 90 % of all industrial processes are heterogeneously catalyzed, even though they often lose regarding selectivity or activity compared to homogeneous catalysis.<sup>12-14</sup> However, one of the main benefits when having catalyst and reactant/products in different phases is the improved separation of the catalysts, thus facilitating its recyclability, a huge factor influencing the process costs.<sup>12-14</sup> Due to its importance for large-scale industrial applications, a lot of research is carried out in the field of heterogeneous catalysis. University research usually focuses on improving the activity of the material itself. For example, optimized porosities or skillful doping are used to improve selectivity and/or turnover.

The example of zeolites shows that the design of catalysts must be adapted over several orders of magnitude. At the atomic level (0.1 nm), the nearest neighbors in the structure play an important role, as they influence acidity, for example. The size of the zeolite pore structure, which is in the nanometer range, is a decisive factor influencing the residence time of reactant and product molecules. In addition, via so-called reactant, product, or reaction selectivity, an influence on the selectivity of the reaction itself is possible through corresponding pore systems.<sup>15,16</sup> Ideally, the catalyst materials produced in this way form larger crystallites of 5 to 5000 nm in size. The shape of the resulting particles and crystallites in turn influence the porosity of the catalyst and, for example, its mechanical stability. The resulting catalytic powder will then be shaped to various geometries of a few millimeters to centimeters. These will then be tested in laboratory-scale test reactors before the catalyst is applied in large-scale industrial plants on a scale of up to a hundred tonnes.<sup>16,17</sup> In general, the characteristics of the different stages should be preserved throughout the whole process and the final industrial reaction. The shaping of catalysts is a key step in the transition from catalyst research to technical production and an important step in up-scaling. In most cases, the transition from the laboratory to technical application is tested using appropriate pilot plants, although this step is usually no longer part of academic catalyst research. The aim in shaping is to adapt the geometries to the corresponding process designs in order to reduce the pressure loss, for example, and thus save operating costs.<sup>12,18</sup>

Considering heterogeneous catalysts and their shape, one must take into account two different regimes, the micro- and the macroscopic structures, which will be briefly discussed in the following sections. Additionally, selected catalytic systems which are prone to influences by catalyst shaping will be presented.

### 2.1.1 Macrostructure and shaping of catalysts

Depending on the shaped materials and the target reactions, different shaping methods are used in heterogeneous catalysis. The most important are extrusion and tableting as well as spray drying and granulation. All techniques differ in terms of the geometries and macroscopic sizes that can be obtained, but also, for example, mechanical stability, uniformity, and porosity are influenced by the shaping method. An overview of some technically applied catalyst geometries is given in **Figure 1**.<sup>12,19,20</sup>

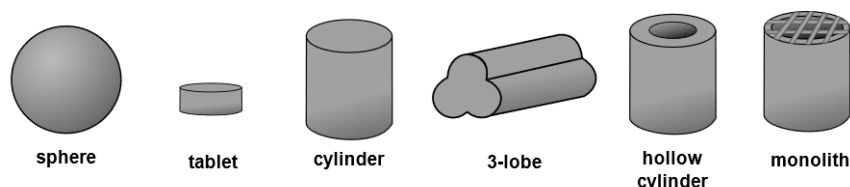


**Figure 1:** Selection of typical catalytic shapes applied in industry, namely cylinders, hollow cylinders, tablets, spheres and multi-lobe structures.<sup>9,13</sup>

Spray drying produces uniform, spherical particles of about 20 to 100  $\mu\text{m}$  in size, which are then used in fluidized bed reactors and slurry reactors. In this application, the uniformity of the particles is important, so simple crushing of larger particles is not suitable as a shaping method in this case. In spray drying, a particle slurry is finely atomized through a nozzle and the aerosol is dried by hot air.<sup>12,19</sup> The decisive factor influencing the particle size is the droplet size, which is influenced by the feed rate, film-forming characteristics, and gas velocity, among other factors. Spherical geometries can also be produced by granulation. The snowball effect is used to spray the small particles with a cohesive slurry, which causes the particles to grow. Uniform particle growth is aimed at by rotating the particles, consequently more or less spherical particles are obtained.<sup>12,19</sup> By means of tableting, respective tablet-shaped catalysts can be produced. Dry powder is densified under pressure ranging from 450 to 2000 MPa in a compression mold, so that the corresponding tablets are obtained.<sup>13</sup> As a rule, tableting is used to produce mechanically very stable molded bodies, whereby, depending on the material used, various lubricants and binders must be added in order to obtain the corresponding properties. In addition, it must be taken into account that the macroporosity in particular is greatly reduced at high tableting pressures.<sup>19,21–23</sup> Geometry variations can be achieved on a limited scale by modifying the compression mold, although these are often associated with high costs.<sup>12</sup> During extrusion, a highly viscous ceramic slurry is forced through a die. The resulting extrudate is then cut according to requirements to obtain geometries with defined lengths. Shape variation is possible during extrusion by modifying the cross-section. In addition to the cylinders obtained in this way, multi-lobe structures or hollow cylinders are available, for example. As a further development of the latter, so-called monolithic catalysts can be seen. In cross-section, these have a large number of channels that run through the molded part along the extrusion direction with thin walls inbetween.<sup>24,25</sup> In general, extrusion is one of the most frequently used shaping techniques in heterogeneous catalysis, whereby additives are often added, similar to those used in tablet pressing, to enable processing and to obtain the corresponding geometries.<sup>12,26</sup>

The variety of shaping methods as well as shapes employed is a good indication that the shape of a catalyst is an important influencing factor in heterogeneous catalysis. The geometry influences various process parameters such as pressure drop and bulk density, but also fluid dynamics and thus has an influence on the conversion and selectivities of the reaction.<sup>14</sup> In a fixed-bed reactor, the bulk density of the catalyst shapes and the resulting bed porosity  $\varepsilon$  play a major role, as they have a decisive influence on the pressure drop  $\Delta p$  in the reactor bed. This pressure difference is caused by frictional forces of the fluid both on the wall and on the inner shaped bodies. The Ergun equation is usually used to estimate the pressure loss in catalyst beds, whereby the relationship between bed porosity and pressure loss becomes clear. Basically, the higher the bed porosity, the lower the pressure drop. Since powders generally have the lowest bed porosity, fixed-bed reactors with powders are not used on an industrial scale, but the catalysts are shaped. When comparing a cylindrical pellet with a ring of similar length and diameter, the ring reduces the pressure drop by 50 % and offers a 20 % increased external surface area than the pellet.<sup>16</sup> Monolithic systems are known to have one of the lowest pressure losses in their application especially with respect to the available surface area.<sup>13,27</sup>

In addition to the pressure drop, transport phenomena within the chemical reactor and the catalyst material are also of great importance. Both mass and heat transport processes are relevant, the latter being linked to the former by convection. In the case of mass transport, the residence time at the active center is particularly relevant. The corresponding catalytic reactions must be feasible, whereby blocking of the active centers should be avoided by means of sufficient diffusion. In addition, if the products are removed too slowly, consecutive reactions forming undesired by-products can take place, which consequently reduces the selectivity of the reaction. Heat transport is important in catalysis for both endothermic and exothermic reactions. In endothermic reactions, it is necessary to ensure the availability of sufficient heat of reaction to allow the reaction to take place, whereas in exothermic reactions, the heat of reaction generated must be removed. The latter is particularly important to avoid the formation of so-called hot spots, local temperature increases. These can have a negative effect on selectivity and thermally deactivate the catalyst. In addition, uncontrolled hot spot formation also affects reactor safety.<sup>28</sup> Accordingly, a homogeneous temperature profile over the entire reactor bed is desired. In general, sufficient radial and axial mixing by turbulent flow is useful here to ensure corresponding mixing and homogeneity. Since the fluid flow and correspondingly convective processes also depend on the bed porosity and the available channels, the catalyst shape is also an influencing factor in this respect.<sup>12,20</sup>

To further facilitate mass transfer to the active centers, the active geometric surface can also be increased. Spheres, cylinders, and simple tablet structures have the worst surface-to-volume ratios, whereas monolithic structures have the highest values. When increasing the active surface area, however, it must be considered that the geometry also always influences the mechanical stability of the catalyst. Particularly the stability during loading and unloading of a catalyst bed, as well as the stability under its own weight in meter-high reactors, should be fulfilled with the corresponding catalyst geometries to avoid abrasion of the catalyst. Not only is active component lost, but the resulting powder also increases the pressure loss in the catalyst bed and must be avoided accordingly. **Figure 2** shows an overview of the most important process parameters factors which are influenced by the catalyst geometry.<sup>18,29</sup>

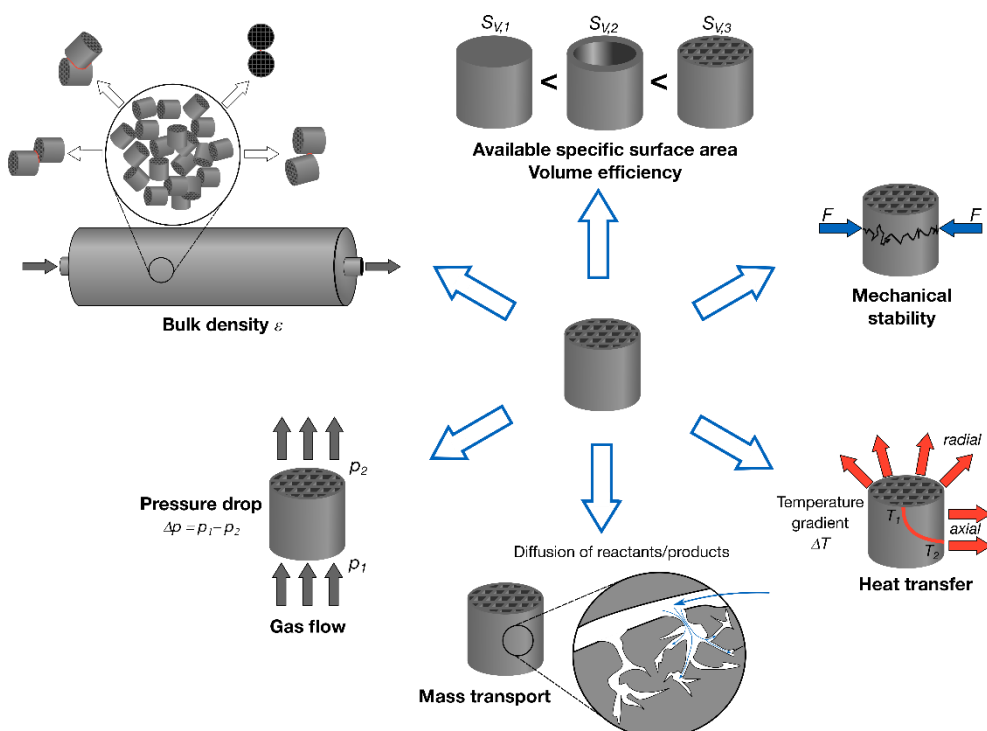


**Figure 2:** Schematic overview of important process characteristics influenced by the shape of the heterogeneous catalyst used.<sup>18,29</sup>

Recently, fluid dynamic simulations and machine learning are increasingly used to optimize catalyst geometries. This saves time-consuming test reactions if the number of geometries to be tested can be limited. However, when using traditional shaping techniques, the corresponding limitations must be taken into account, which may conflict with improved geometries.<sup>30</sup> This was shown, for example, by Jungreuthmayer et al. using computational fluid dynamics (CFD) simulations. They found alternation of wide and narrow channels for monoliths beneficial, which cannot be produced with any of the traditional shaping methods.<sup>31</sup>

As detailed before, however, not only the macroscopic geometry is decisive for the catalytic activity, but also the internal (micro) structure of the catalyst influences the reaction. This will be investigated further in the following. The structure of supported catalysts, which can presumably be assigned to the intermediate area between macroscopic shaping and catalytic microstructure, will also be discussed.

### 2.1.2 Microstructure of catalysts

In order to save usually more cost intensive active components and to achieve higher stability, not only uniform catalysts are used in technical applications, in which the entire body consists homogeneously of the corresponding material, but also supported catalysts are used. In this case, a mechanically stable, inexpensive carrier, usually oxidic materials such as silica or alumina, is shaped according to the requirements and then loaded with the active component e.g. Pt, Cu, Fe, or Ni.<sup>16</sup> This loading is typically carried out by means of coating or impregnation processes.<sup>12</sup> Hereby, the characteristics of both the carrier material and the species to be loaded are relevant, as they influence the subsequent dispersion of the active component. In general, a distinction is made between different approaches. In incipient wetness impregnation, the desired amount of active species is dissolved in a solvent, whose volume equals the pore volume, and distributed on the carrier material. Since the pore volume is taken into account, the carriers are never completely wet. In so-called wet impregnation, an excess of impregnating solution is used. The substrates are immersed in the impregnation solution before it is removed either by evaporation or filtration. The impregnation can take place either without interaction between the carrier and the active component, for example, where the solubility of the materials is the decisive characteristic.<sup>14,16,17,32</sup>

In impregnation processes with interactions, these are mostly of a physical nature. In wet impregnation, and especially in the variant in which the overflowing impregnating solution is filtered off, ion exchange plays an important role. In this process, the charged active components are exchanged with the corresponding surface charges, with thermodynamics being the driving force here. In order to ensure the corresponding surface charges, the isoelectric point of the support material is important and should be precisely adjusted by changing the pH value.<sup>32,33</sup> Ion exchange as an impregnation method is an equilibrium process, which, however, does not lead to uniform results, since the concentration of active components at the edge is usually higher than in the pores, where diffusion processes are limited. In general, however, a catalyst is obtained in which the active component is located only on the outer layer of the geometry and the inner part of the shaped body remains a porous carrier structure.<sup>16,17</sup> Such supported catalysts are generally referred to as egg-shell catalysts. A reduced amount of expensive active component is the reason for considering such a production. A large proportion of noble metal catalysts are manufactured by this technique accordingly. Especially in areas such as automotive exhaust catalysis, where the feed steam traditionally contains unavoidable catalyst poison, it can be advantageous if the catalytically active component is not located on the outside of the catalyst carrier but further inside. This is produced by competitive adsorption, in which more strongly adsorbing components attach themselves to the outside of the catalyst and the active component thus diffuses further inward. Depending on the depth of impregnation, this leads to so-called egg-white or egg-yolk catalysts (**Figure 3**).<sup>34</sup> In wet impregnation, it also plays a role whether the substrate is already moistened before the active material is added or whether the substrate is dry. In the former case, all pores are already filled with solvent, which means that diffusion processes are the only decisive factor for the penetration depth of the catalytically active species. In the impregnation of dry material, in addition to diffusion processes, capillary forces also play a role, drawing the impregnating solution deeper into the pores in the first step. For complete impregnation, however,

it must be considered in both cases that air may still be entrapped in the micropores, which reduces the volume of the catalysts to be impregnated. After successful impregnation, the resulting catalyst is subsequently dried and activated by calcination and reduction.<sup>35</sup>

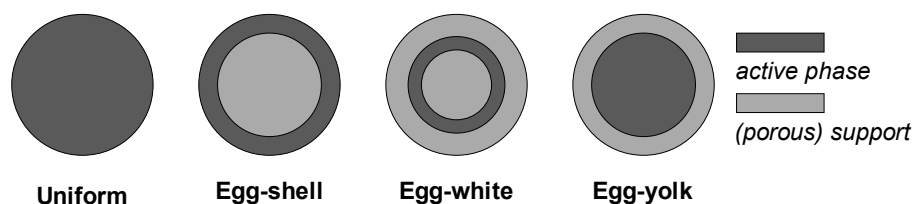


**Figure 3:** Schematic illustration of an uniform and the different egg-type catalyst.<sup>32,34</sup>

The surface charges mentioned are not only dependent on the selected support material but are also influenced, for example, by the sinter temperature with which the support material was treated. In general, a distinction is made between Lewis and Brønsted acid centers with regard to surface acidity. While the latter can donate protons as acid centers of surfaces, the former are non-protic acid centers. They act as electron acceptors at the catalyst surface (**Figure 4**). The calcination temperature has an influence on the acidity of carrier materials. Freshly precipitated alumina, for example, is completely hydroxylated at the surface up to 100 °C and has corresponding Brønsted centers. If the temperature is increased, water is removed and Lewis acid sites are formed, which are present next to the Brønsted acid sites. From temperatures above 900 °C, the carrier is quasi-dehydroxylated, so that only Lewis centers are present.<sup>9,20</sup> The distribution and ratio of the two centers can influence the product distribution and is characterized in heterogeneous catalysis, for example, by IR spectra of adsorbed pore molecules such as pyridine or carbon monoxide.<sup>36–38</sup>

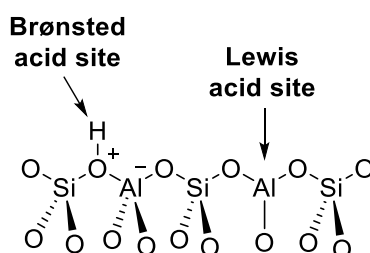


**Figure 4:** Lewis and Brønsted acid sites in zeolite catalysts.<sup>16,20,39</sup>

Furthermore, the pore structure of the catalyst is also important since it influences essential diffusion processes and the inner surface. Depending on their size, protruding pores are divided into micropores (< 2 nm), mesopores (2 – 50 nm) and macropores (> 50 nm). While micropores and mesopores are normally accessible via gas adsorption and corresponding evaluation of the adsorption isotherms, mercury porosimetry is still used for the detection of macropores.<sup>40</sup> The pore structure is a material-specific component and is influenced by thermal sintering processes. For example, from the highly porous  $\gamma$ -Al<sub>2</sub>O<sub>3</sub> with surface areas between 5 – 300 m<sup>2</sup>·g<sup>-1</sup>, the metastable  $\delta$ - and  $\theta$ -Al<sub>2</sub>O<sub>3</sub> phases and finally the  $\alpha$ -Al<sub>2</sub>O<sub>3</sub> (corundum) are formed by thermal treatment between 1000 – 1200 °C, the latter usually having a surface area of only 3 – 5 m<sup>2</sup>·g<sup>-1</sup>.<sup>12</sup>

In this process, the thermal treatment usually sinters the small pores first, with the porosity generally decreasing.<sup>41</sup> Usually, support materials have high porosities, and the pore structure is adapted to the reaction in each case. Especially with large reactants, it can be advantageous if the pores are not too small and cannot be reached by the reactant. Zeolites, crystalline aluminosilicate compounds are well-known catalysts and support materials in this respect, as they have different, highly defined porosities depending on their type. Recurring blocks of formation form a network of channels and voids. The selectivities of the reaction can be influenced and tuned by selecting the appropriate zeolite structures.<sup>15,16</sup>

When describing the course of a catalytic reaction, the following seven different process steps are usually distinguished:<sup>12,42</sup>

1. Diffusion of the reactants through a boundary layer surrounding the catalyst
2. Intraparticle diffusion of the reactants into the catalyst pores to the active sites
3. Adsorption of the reactants on the active sites
4. Surface reactions from reactant to product, possibly including surface diffusion steps
5. Desorption of products from the active sites
6. Intraparticle diffusion of the products through the catalyst pores
7. Diffusion of the products through the boundary layer surrounding the catalyst particle.

The first two steps (1.-2.) and the last two steps (6.-7.) are transport processes, which consequently, among other, depend on the catalyst geometry, the porosity, and the pore structure, whereas the adsorption (3.) and desorption (5.) to the surface as well as the surface reaction (4.) depend on the catalyst material itself (**Figure 5**).

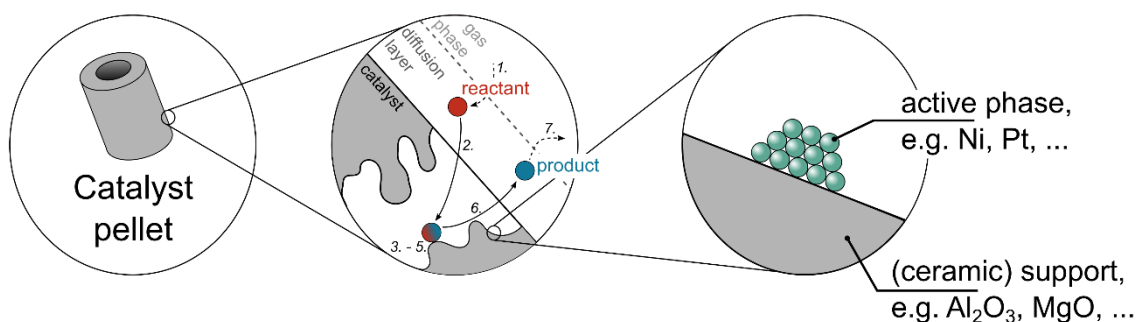


**Figure 5:** Schematic overview of the transport processes taking place in heterogeneous catalysis on catalyst carriers.<sup>12,42</sup>

While the previously discussed macro- and microstructure are generally considered in heterogeneous catalysis on a technical scale, each reaction comes with its own specific requirements with respect to reaction parameters, influencing factors and behavior in terms of technical process development. In the following paragraph, selected catalytic systems that are important for the context of this thesis are discussed.

## 2.2 Selected catalytic systems

Joseph Prisley was one of the first researchers describing heterogeneous catalysis in the decomposition reaction of ethanol to ethylene and water on alumina in 1783. Other such phenomena were reported in the late 18<sup>th</sup> to early 19<sup>th</sup> century. Louis J. Thénard recognized the decomposition of ammonia and hydrogen peroxide on heated metals while Johann W. Döbereiner discovered in 1823 the ignition of hydrogen in the presence of a platinum sponge.<sup>13,43</sup> The latter discovery led to the production of the Döbereiner lighter, which became widely known as 5 years later already 20 000 lighters were in use.<sup>43,44</sup>

Nevertheless, it took until 1835 for the word "catalysis" to be introduced by Jöns J. Berzelius as a terminology for what had hitherto been known as "contact phenomena". The modern definition of catalysis as we know it today was introduced almost 60 years later by Wilhelm Ostwald, who, on the basis of comparative investigations of different reaction rates, concluded in 1894 that "catalysis is the acceleration of a slow process by the presence of a foreign substance".<sup>45</sup> Based on his research in the field of catalysis and the study of chemical equilibria and reaction rates, Ostwald was awarded the Nobel Prize in Chemistry in 1909.<sup>46</sup> In addition to the Deacon process for the synthesis of chlorine gas from hydrochloric acid and oxygen via a mixed oxide of copper and manganese oxide, which was patented in 1868,<sup>47-49</sup> the contact process for the production of sulfuric acid is one of the first large-scale applications of heterogeneous catalysis.<sup>48</sup> In this process, which was first industrially applied at BASF in 1888, sulfur dioxide was oxidized over a Pt on asbestos catalyst whereas nowadays, vanadium pentoxide is used as catalyst.<sup>50,51</sup>

Another important heterogeneous catalytic process is the synthesis of ammonia from hydrogen and nitrogen, which Fritz Haber first achieved in a significant quantity in 1909 using osmium catalysis.<sup>16</sup> The realization of a high-pressure process on an industrial scale was developed by Carl Bosch thereafter and the first plant at BASF produced up to 30 tons ammonia per day in 1913.<sup>52</sup> At about the same time, Alwin Mittasch carried out more than 6500 experiments trying to replace osmium and thus developed the iron-based catalyst promoted with aluminum and potassium oxides, which is used almost unchanged today.<sup>52,53</sup> Both Fritz Haber (1918) and Carl Bosch (1931) were awarded the Nobel Prize in Chemistry for this work.<sup>16</sup> Another related Nobel Prize was awarded in 2007 to Gerhard Ertl for his research on chemical processes on solid surfaces, including the Haber-Bosch catalyst.<sup>54-56</sup> According to current estimates, fertilizers based on the Haber-Bosch catalyst have fed about 27 % of the world's population in the 100 years since its development, which is equivalent to four billion people born since 1908.<sup>57</sup> Today, the Haber-Bosch process still dominates, producing up to 90 % of the ammonia consumed worldwide.<sup>52</sup> However, since the energy for the Haber-Bosch process still comes largely from fossil fuels, about 1 – 2 % of global CO<sub>2</sub> emissions can be attributed to ammonia synthesis.<sup>58</sup> In addition, the origin of the hydrogen is important, as Smith et al. calculated that ammonia production with hydrogen from electrolysis produces 0.38 – 0.53 tons of CO<sub>2</sub> per ton of NH<sub>3</sub>, whereas 1.67 tons of CO<sub>2</sub> per ton of NH<sub>3</sub> are produced when hydrogen is used from methane reforming.<sup>59</sup> On the other hand, there is the consideration to use ammonia in the future for long-term energy storage.<sup>59</sup> Since renewable energies are not always and everywhere available, the energy must be stored and transported in the form of a transportable and commercially usable commodity. One possibility under investigation is the conversion of hydrogen to ammonia and the subsequent decomposition



of ammonia. However, hydrogen purification has to be considered as well as the endothermicity of this reaction.<sup>60</sup> Direct usage of ammonia e.g. in solid oxide fuel cells or in internal combustion engines and gas turbines is also possible.<sup>60,61</sup> Nevertheless, ammonia is a toxic and corrosive chemical whose safety and health hazards should be considered.<sup>62</sup> Another method of chemically storing and transporting hydrogen is the use of liquid organic hydrogen carriers (LOHC), organic components that can also be reversely hydrogenated and dehydrogenated.<sup>63,64</sup>

### 2.2.1 Pt/Al<sub>2</sub>O<sub>3</sub> as catalyst for the dehydrogenation of perhydro-dibenzyltoluene

LOHCs are liquid organic compounds that can be used for the transport and storage of hydrogen. The reversible hydrogenation of such systems was first discussed in Harry G. Oswin's patent letter in 1968 and in the following years researched as a source of hydrogen for powering automobiles.<sup>65</sup> In this context, the Swiss Paul Scherrer Institute built the first prototype of such a truck in the 1980s.<sup>66,67</sup> Starting especially in the end of the 2000s, LOHC systems have been increasingly researched again as a storage medium to compensate for the local and temporal discrepancy between energy generation and energy demand against the background of current environmental problems. Further possible usage could be solely as hydrogen transport media as well as heat storage.<sup>68-71</sup>

The concept of LOHC storage is one possibility to overcome the drawbacks of established hydrogen storage methods such as compressed or liquefied hydrogen. The high pressure storage always requires extremely robust tanks, however still bears the risk associated with an inflammable gas stored under high pressure.<sup>63,72</sup> Cryogenic storage requires temperatures of -253 °C at least, as well as insulated vessels to reduce heat transfer to a minimum. In general, high volume-to-surface ratios reduce heat transfer and thus the boil-off effect associating larger reservoirs.<sup>64,73-75</sup> Further combinations of cryogenic and liquefied storage, so called cryo-compressed hydrogen storage have been examined, where hydrogen is stored as a super critical cryogenic gas - compressed at -233 °C with typically < 300 bar, no liquefaction takes place. It is told to have the potential of good gravimetric and volumetric capacity while reducing the hydrogen dormancy loss. Still, the respective infrastructure for cooling and pressurizing as main requirements are also hurdles to its usage.<sup>72,76</sup> Physical storage of hydrogen in metal-organic frameworks has also become part of research nowadays, however, it often requires either low temperatures or high pressures to store reasonable amounts of hydrogen thus leading to comparable disadvantages as pressurized or cryogenic storage methods.<sup>77-79</sup> On the other hand, chemical hydrogen storage as metal hydrides as well as in small molecules such as ammonia and methanol often correlate with safety issues alongside with drawbacks of high weight or volume or the state of aggregation of the respective storage material.<sup>61,64,80</sup> Further, the targeted application must be considered when examining different storage systems and the decision criteria as well as their weighting have a significant impact on the result.<sup>81</sup> For mobility applications the ideal storage medium should allow high volumetric and gravimetric energy densities as well as quick and easy uptake and release of fuel.<sup>82,83</sup> Further ambient operation conditions and little or no safety issues are required while maintaining a certain cost-effectiveness. Therefore, Rivard et

al. stated hydrogen storage under pressure, even though not perfect, might be the best option.<sup>73</sup> Lee et al. on the other hand compared lithium-ion battery based storage systems and concentrated solar power to the use of LOHC or compressed hydrogen gas in combination with an electrolyzer and fuel cell as energy storage technology. When evaluating the energy stored on investment values, the storage in LOHC was much better for monthly (< 1000 h) and seasonal energy storage than any other energy storage technology due to the low embodied energy cost of LOHC materials proofing the benefit of long-term energy storage using electrolyzer, LOHC and fuel cell.<sup>63</sup> Furthermore, LOHCs offer advantages in handling through their liquid aggregate state. Due to their compatibility with existing infrastructure, they can be transported through pipeline systems already present. The requirements for storage sites are also correspondingly lower than for other hydrogen storage methods.<sup>61,70</sup>

In general, a LOHC medium is recycled between an energy-rich and an energy-poor form by means of hydrogenation and dehydrogenation. In this process, catalytic hydrogenation takes place when there is a hydrogen surplus or when hydrogen can be obtained from renewable sources for example by splitting water. The hydrogen-rich form can then be stored or transported before being catalytically dehydrogenated to release hydrogen. The dehydrogenated species can then be hydrogenated again (**Figure 6**).<sup>70</sup>

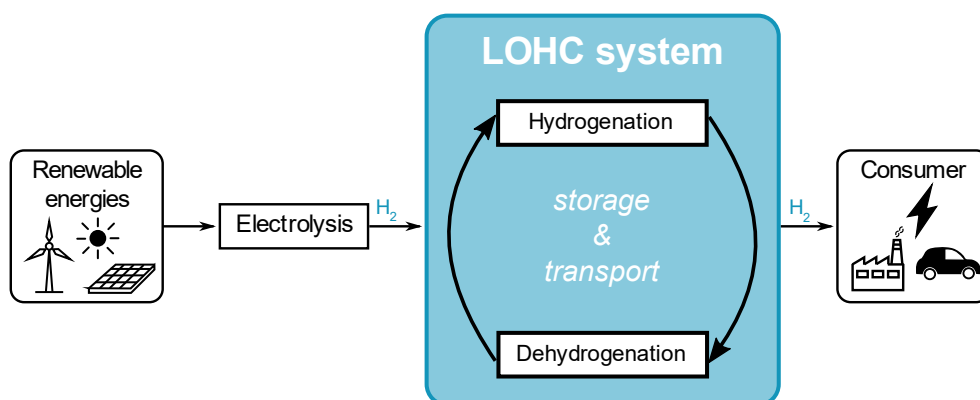


**Figure 6:** Schematic overview of the LOHC concept.<sup>70</sup>

Several different aromatic and heteroaromatic compounds such as benzyl, toluene, naphthalene, *N*-ethylcarbazol or dibenzyltoluene have been discussed in literature as possible LOHC systems.<sup>84-91</sup> In general, to be suited as a hydrogen storage and carrier molecule, the following requirements should be met:<sup>80,90</sup>

- favorable reaction enthalpies for reversible hydrogenation and dehydrogenation,
- both volume and weight based high storage densities,
- liquid state throughout the range of use and low viscosity for good pumpability,
- low vapor pressure to ensure high hydrogen purity,
- high cycling and temperature stability,
- environmental compatibility and low toxicity, and
- low cost and wide availability.

Based on these prerequisites, it can be concluded that the much-studied systems dodecahydro-*N*-ethyl carbazole/*N*-ethyl carbazole and perhydro-dibenzyl toluene/benzyl toluene are the most promising candidates. Although *N*-ethyl carbazole has the more efficient process, dibenzyltoluene is probably one of the best solutions due to its other properties (melting point, low vapor pressure, and availability/cost).<sup>80,90</sup> It is therefore chosen for this work and thus presented here in more detail.

The perhydro-dibenzyl toluene/dibenzyl toluene system was first presented by Brückner et al. in 2014.<sup>92</sup> The advantage is that the low-hydrogen component is already used as a heat transfer oil under the brand names Marlotherm SH and Jarytherm DBT and is therefore cheap and readily available, as well as having suitable properties (**Table 1**).<sup>93,94</sup> Perhydro-dibenzyltoluene is often referred to as 18H-DBT whereas the hydrogen lean component is named 0H-DBT. The system consists of a mixture of six regioisomers and, according to the reaction equation (**Figure 7**), can absorb 9 mol of hydrogen per mole of carrier, which corresponds to a weight-related hydrogen storage of 6.2 wt.%. Furthermore, using the physical data, the hydrogen storage density can be calculated to be 56.4 kg·m<sup>-3</sup> and the energy density is 1.9 kWh·L<sup>-1</sup>. The reaction enthalpy for the hydrogenation is -65.4 kJ·mol<sub>H<sub>2</sub></sub><sup>-1</sup> related to the hydrogen and thus lies between the values for small aromatics and heteroaromatic systems.<sup>80,95</sup>

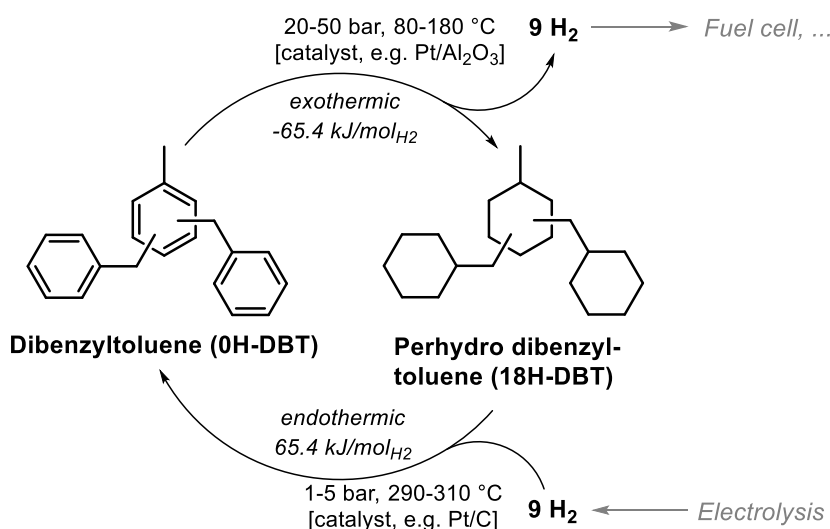


**Figure 7:** Catalytic perhydro-dibenzyl toluene/dibenzyl toluene cycle.<sup>80,95</sup>

The catalytic hydrogenation of 0H-DBT is usually carried out under a hydrogen pressure of 20 to 50 bar at temperatures reaching from 140 to 250 °C. Different catalysts have been used within this process such as Ru/Al<sub>2</sub>O<sub>3</sub><sup>96-98</sup>, Rh/Al<sub>2</sub>O<sub>3</sub><sup>99</sup>, Pt/Al<sub>2</sub>O<sub>3</sub><sup>100</sup>, Pd/Al<sub>2</sub>O<sub>3</sub><sup>99</sup> or Ni<sup>101,102</sup> based ones. The dehydrogenation on the other hand is carried out at low pressure of 1 to 5 bar and due to the endothermicity of the reaction at 200 to 320 °C using platinum catalysts with various support materials such as Al<sub>2</sub>O<sub>3</sub><sup>103-105</sup>, CeO<sub>2</sub><sup>98</sup>, TiO<sub>2</sub><sup>106</sup> and C<sup>92</sup>.

**Table 1:** Physico-chemical properties of dibenzyltoluene und perhydro-dibenzyltoluene.<sup>84,93–95,105,107</sup>

	Dibenzyltoluene	Perhydro-Dibenzyltoluene
Molecular formula	C <sub>23</sub> H <sub>28</sub>	C <sub>23</sub> H <sub>46</sub>
Molar mass / g·mol <sup>-1</sup>	272.40	290.05
Density (20 °C) / kg·L <sup>-1</sup>	1.04	0.91
Dynamic viscosity (20 °C) / mPa·s	49	424
Vapor pressure (100 °C) / Pa	< 10.0	< 3.9
Surface tension (25 °C) / mN·m <sup>-1</sup>	42	35
Melting point / °C	≤ -32	< -50
Boiling point / °C	≈ 390	≈ 354
Flash point / °C	≈ 212	175

To boost the dehydrogenation activity of Pt/Al<sub>2</sub>O<sub>3</sub> catalysts, Auer et al. added sulfur in form of ammonium sulfate to the catalyst. It was revealed that sulfur compounds gradually block the low-coordinated defect sites while weakening the adsorption of the dehydrogenated products on the catalyst through modification of the electronic properties of Pt. Further, catalysts with sulfur modification show reduced formation of heavies as side products. However, high sulfur loadings decrease the dehydrogenation activity, as S then occupies the Pt terraces. Therefore, the ratio of Pt to S has to be adjusted carefully.<sup>103</sup> This is in correspondence with the findings from Jo et al. proofing 0.21 wt.% of sulfur to lead to the best results.<sup>108</sup> The mean Pt particle diameter should be smaller than 1.5 nm to make best use of this selective catalyst poisoning with sulfur.<sup>104</sup>

To monitor the degree of hydrogenation during the catalytic reaction, usually <sup>1</sup>H-NMR and GC-MS or HPLC are used. Dürr et al. also found <sup>13</sup>C-NMR as well as GC-FID measurements suiting to determine the degree of hydrogenation.<sup>109</sup> As GC and NMR are not viable for industrial application, Müller et al. found refractive index measurements the most promising method as its accuracy is high while temperature dependencies and deviations between different isomers are small. Further, Raman as well as UV-Vis spectroscopy are also suited, contrary to viscosity measurements as the latter one is highly temperature dependent as well as influenced by the isomers present.<sup>110</sup>

Do et al. examined the hydrogenation pathway and proved the two side phenyl rings to be hydrogenated prior to the middle ring.<sup>96</sup> During the dehydrogenation, the central ring is dehydrogenated first, as determined via DFT calculations of the 3,5-isomer by Huynh et al. The rate determining step was calculated to be the dehydrogenation from 12H-DBT to 10H-DBT, which is the first dehydrogenation in the side ring. Additionally, calculations of the dehydrogenation enthalpy as well as the hydrogen capacity were performed when the methyl group was replaced by electron-donating and withdrawing groups. It was found that perhydro-lithium 3,5-dibenzyl phenolate had almost the same hydrogen capacity while the reaction enthalpy is slightly smaller (11.5 kcal/mol vs. 12.6 kcal/mol for 18H-DBT) thus suggesting the OLi derivate for experimental research.<sup>111</sup>

To further improve the reaction, Jorschick et al. added 20 wt.% of perhydro-benzyltoluene (12H-BT) to perhydro-dibenzyltoluene. This reduced the mixture's viscosity by 80 % and increased the dehydrogenation productivity by 12 to 16 % compared to pure 18H-DBT at

otherwise identical conditions. This can be attributed to the fact that the partial pressure is reduced because 12H-BT has a higher vapor pressure. Furthermore, 12H-BT can be dehydrogenated more easily due to better diffusion, and hydrogen transfer between the systems occurs.<sup>112</sup> The lower viscosity of such a mixture improves the pumpability of such a system and is particularly advantageous in winter or in cold regions.<sup>107</sup>

In the large-scale application of 18H-DBT as a storage system for LOHC, the purity of the hydrogen obtained is also important, especially for use in proton exchange membrane fuel cells. Bulgarin et al. were able to show that water as well as oxygenate impurities in perhydrodibenzyltoluene promote the formation of CO, CO<sub>2</sub> and methane (from the CO). However, by drying and purifying the reactant, high purity hydrogen (> 99.999 %; CO < 0.2 ppm) can be obtained. The same effects are achieved by recycling the system several times, which reduces the amount of impurities and correspondingly increases the quality of the hydrogen.<sup>113</sup>

Due to the rather large size of the 18H-DBT/0H-DBT and the resulting mass transport limitations, the dehydrogenation reaction is also strongly dependent on the catalyst support.<sup>98</sup> It has been shown that pore diameters between 25 and 43 nm and layer thicknesses of 20 to 100 μm are advantageous for egg-shell catalysts.<sup>104,105</sup> In addition to a small specific surface area, a reduced acidity of the support material leads to reduced by-product formation and must be taken into account when selecting the catalyst support.<sup>104</sup> While LOHC systems show huge potential in terms of hydrogen storage, the production of hydrogen as important resource chemical from (photocatalytic) water splitting is another important example for heterogeneously catalyzed reactions which will be discussed in the following section.

### 2.2.2 NH<sub>2</sub>-MIL-125 (Ti) derived catalyst for photocatalytic water splitting

Metal-organic frameworks (MOFs) are crystalline porous solids, which were first synthesized in the 1990s.<sup>114,115</sup> Generally, MOFs consist of metal ions/clusters and organic linkers connected through coordination bonds thus forming networks. A broad variety of metals and linkers are being explored dictating the reticular structure and hence specific properties of the respective MOF. In general, crystallinity and high surface area alongside of tunable size and shape of micro/mesopores are main characteristics of MOFs.<sup>116,117</sup> Since last 20 years, a huge variety of MOFs and MOF derived materials are being explored in many application fields, such as gas storage/separation<sup>118–120</sup>, (optical/electro)-chemical sensors<sup>121,122</sup>, drug delivery systems<sup>123,124</sup>, wastewater treatment, water harvesting<sup>125–127</sup>, or as battery materials<sup>128,129</sup>. Their use in catalysis is also being under investigation, with applications ranging from polymerization catalysis to fine chemical production and photo-/electrocatalysis.<sup>130–135</sup>

While in electrocatalysis a catalyst participates in an electrochemical reaction and the reaction rate at the electrode surface is changed,<sup>12,136</sup> in photocatalysis a catalyst absorbs light energy and thus accelerates the surface reaction of the reactants. The process generally takes place in three steps. First, photons of light are absorbed by the catalyst. Then, photoexcited electrons migrate from the valence band (VB) to the conduction band crossing the catalyst's band gap thus forming holes in the valence band and are transferred to the catalyst's surface. Third, reduction and oxidation (redox) of the reactants are initiated by the excited electron-hole pair (**Figure 8**).<sup>136,137</sup>

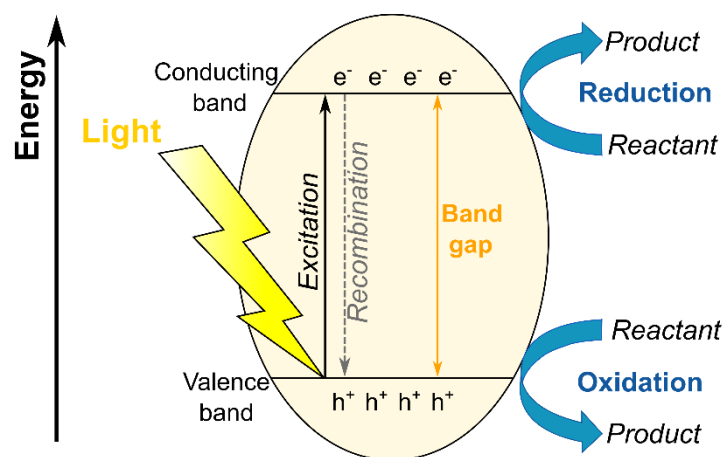


**Figure 8:** Schematic illustration of the band structure of a photocatalyst during reaction.<sup>137,138</sup>

MOFs and/or MOF derived materials are exploited in various photochemical reactions. The most common reactions are CO<sub>2</sub> reduction, photooxidation, pollutant degradation and water splitting.<sup>139–142</sup> In the photocatalytic water splitting into hydrogen (hydrogen evolution reaction (HER)) and oxygen (oxygen evolution reaction (OER)), solar energy is used as a renewable energy source to produce green hydrogen. This reaction is endothermic, requiring a Gibbs energy of  $\Delta G = + 238 \text{ kJ} \cdot \text{mol}^{-1}$  to be overcome. Accordingly, the energy of the incident photons must be higher than 1.23 eV but must not exceed the maximum bandgap 3.26 eV. In general, the valence

band of the catalyst should be more positive than the oxidation potential of  $O_2/H_2O$  (1.23 eV vs. normal hydrogen electrode (NHE)), whereas the conduction band should be more negative than the reduction potential of  $H^+/H_2O$  (0 eV vs. NHE).<sup>115,138,140,142,143</sup>

For MOFs to be suitable as photocatalysts, they must ensure an appropriate charge separation across the bandgap, ideally by means of visible light. As UV light makes up only up to 4 % of the solar energy, usage of visible light, which makes up to 46 % is more desirable.<sup>116,140</sup> At the same time, a good charge migration as well as a sufficiently long lifetime thereof has to be achieved. Due to the variety of metals and linkers, the bandgap or the structure of the respective MOF can be modified and optimized.<sup>116,138,142</sup> Furthermore, the use of co-catalysts has proven useful. Doping with platinum, which serves as a reservoir for electrons and can react with the protons of water, has proven beneficial.<sup>140</sup> Due to the tunable porous structure, such co-catalysts in the form of nanoparticles can also be introduced selectively into the cavities to effect improved interaction.<sup>116,143–147</sup>

In 2009, Dan-Hardi et al. introduced a Ti-based MOF with the formula  $Ti_8O_8(OH)_4-(O_2C-C_6H_4-CO_2)_6$  named MIL-125, where MIL is an abbreviation for Materials from Institute Lavoisier. It is prepared by solvothermal synthesis from terephthalic acid (1,4-benzenedicarboxylic acid, BDC) and titanium tetra-*iso*-propoxide. A suitable choice of solvent and temperature is important to ensure that a highly porous white solid crystallizes.<sup>148–150</sup> Structurally, MIL-125 consists of cyclic octamers ( $Ti_8O_8(OH)_4$ ), which are edge sharing octahedral titanium units. These octamers are connected via BDC linkers to twelve other cyclic octamers. The resulting porous three-dimensional, quasi-cubic tetragonal structure has two types of cages. Both the octahedral (12.5 Å) and tetrahedral (6 Å) cages are accessible through narrow triangular windows of about 6 Å (**Figure 9**).<sup>151</sup> MIL-125 has a bandgap of about 3.6 eV which corresponds to light in the UV region at around 345 nm. By replacing the BDC linker with a monoaminated BDC linker (2-amino benzenedicarboxylic acid  $H_2BDC-NH_2$ ), the absorption band can be shifted into the visible light region to about 2.6 eV or 475 nm.<sup>134,149,152,153</sup> Thus, the MOF  $NH_2$ -MIL-125, which is isostructural to MIL-125, shows a corresponding activity in visible light for photocatalytic HER, for example.<sup>116,154</sup> In general, both MOFs show comparable BET surfaces, but only  $NH_2$ -MIL-125 is stable in aqueous solution.<sup>149,151</sup> Further modification strategies for MIL-125 include metal doping, functional group modification, addition of composite materials, structural regulation or photosensitive modification.<sup>155</sup>

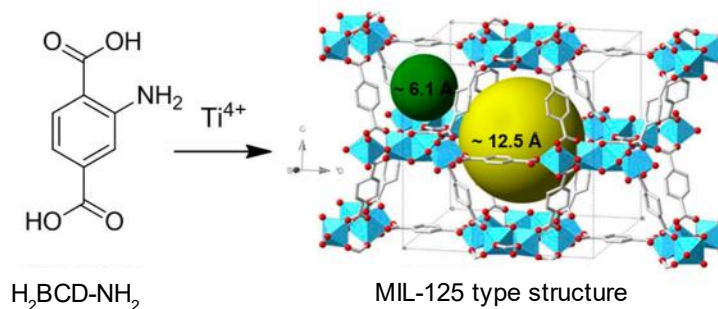


**Figure 9:** Synthesis and structure of  $NH_2$ -MIL-125. Adapted with reprint permission from <sup>151</sup>.

However, when using molecular photocatalysts such as organic molecules or metallic complexes, their inevitable degradation due to their intrinsic properties is a major drawback. MOFs in particular are prone to be degraded during a photocatalytic reaction due to their weak coordination bond as well as oxidative degradation or reactions of linker.<sup>116,138</sup> Metal oxides as inorganic semiconductors on the other hand are durable as well as stable but rather difficult to tune and control their photochemical properties. Since in 1972 Fujishima and Honda showed that TiO<sub>2</sub> is able to generate hydrogen from water, TiO<sub>2</sub> especially in anatase phase has become one of the most widely used photocatalyst.<sup>116,156</sup> While being affordable, non-toxic, highly durable and robust, a high photocatalytic activity is observed upon irradiation under UV light.<sup>140</sup> However, TiO<sub>2</sub> can be solely used in the UV-region as it has a rather larger bandgap. In pure metal oxides, other factors which limit their photocatalytic activity are charge recombination (due to the difference of timescales of charge generation and catalytic reactions) and particle agglomeration (inaccessibility of catalytic active sites).

In addition to the material composition, the morphology and the particle size of the catalyst also influence its photocatalytic activity. Small particle sizes (in the nanometer range) with a correspondingly large surface area for good light absorption improve the transport of photoinduced electrons and holes from the bulk to the surface. Targeted, e.g. one-dimensional structures such as nanotubes, nanowires or nanorods also enhance the charge transport in the vertical direction.<sup>116,142,157,158</sup>

One possibility to fabricate targeted semiconductor structures is based on corresponding MOFs. In general, MOFs can be used in photocatalysis not only as catalysts themselves, but also as photosensitizers, for example in hybrid compounds with TiO<sub>2</sub>.<sup>137,142,143,159–161</sup> As an alternative approach, MOFs can be used as precursor and sacrificial template to produce materials with unique morphologies, and controlled topography and microstructures. Depending on the MOF used and the corresponding pyrolysis, a wide range of metals, metal oxides, metal oxide-carbon hybrid or pure carbon materials can be obtained.<sup>142,143,159,162–164</sup> Especially in hybrid materials of metal oxides in a carbon matrix, the homogeneous distribution of the metal compounds resulting from the precursor is advantageous. It offers a high surface area with tailored porosity and corresponding microstructures. In such MOF derived composites, metal compounds are in situ doped with anions, and the porous carbon matrix (from organic linker) keep them from agglomeration, benefitting the photocatalytic application thus becoming an important research area.<sup>138,155,158,163,165–169</sup>

In the literature, various MOFs are being exploited as sacrificial templates such as Fe-based MIL-101 or MIL-88, Mn-based MIL-100 or Mn-MOF-74, Cr-based MIL-101 and Co-MOFs.<sup>138,143,167,168,170–172</sup> As TiO<sub>2</sub> is in general an efficient photocatalyst, Ti-MOF derived structures have aroused widespread interest as they are a simple and effective way to prepare TiO<sub>2</sub> based porous hybrid materials.<sup>173–175</sup> Hussain et al. investigated the NH<sub>2</sub>-MIL-125 (Ti) pyrolysis in detail at different temperatures in an inert atmosphere and distinguished three decomposition steps. Firstly, up to 300 °C the pure, crystalline, and highly porous NH<sub>2</sub>-MIL-125 is present. Between 350 and 550 °C, an intermediate is present which is amorphous and does not have any accessible porosity as the dissociation of the organic (H<sub>2</sub>BDC-NH<sub>2</sub>) linker and the Ti oxo-cluster takes place. Lastly, above 500 °C, recrystallization of Ti species starts forming anatase



nanoparticle and upon further temperature increase to 650 °C produces the rutile phase. However, the overall 3D tetragonal disk-like morphology of the MOF remains preserved in the derived TiO<sub>2</sub>/C composites.<sup>163</sup> When pyrolyzing a bimetal-organic framework NH<sub>2</sub>-MIL-125(Ti/Cu) in steam at 700 °C, TiO<sub>2</sub> and Cu<sub>x</sub>O are formed in a heteroatom-doped carbon matrix. This leads to a phase junction between nitrogen/carbon co-doped anatase and rutile TiO<sub>2</sub> and the respective Cu<sub>x</sub>O. These multi-heterostructures develop a good efficiency in HER as the charge migration, access to the catalytic active sites and visible light absorption are increased.<sup>165,176</sup> In general, constructing phase junctions either between two phases of the same material (e.g. TiO<sub>2</sub>) or between different metal and/or non-metal compounds enhances separation of photogenerated electrons and holes thus increasing the photocatalytic activity.<sup>165</sup>

Still for multi-heterostructures, pyrolysis is crucial, as shown by Hussain et al. When calcining NH<sub>2</sub>-MIL-125(Ti/Cu) at low temperatures of around 550 °C, only poorly crystalline anatase and Cu<sub>2</sub>O are obtained whereas at temperatures above 800 °C TiO<sub>2</sub> is present in the rutile phase alongside CuO. An appropriate pyrolysis temperature of 700 °C resulted in well-crystalline anatase and rutile TiO<sub>2</sub> phase that can interact with Cu<sub>2</sub>O and CuO. Hereby, as well as through anionic in situ doping with N and C formed from the organic linker decomposition the photocatalytic activity for HER is enhanced.<sup>165</sup> Beside the temperature, the pyrolysis time is also a decisive factor. It determines the crystallinity of the metal oxides, the anatase to rutile ratio and the porous carbon matrix. At short pyrolysis times, the amount of crystallinity is poor, whereas at longer calcination times, the amount of C is reduced due to CO<sub>2</sub> formation.<sup>173,177</sup> Therefore, well-chosen pyrolysis conditions can greatly influence the obtained photocatalytic properties of the resulting MOF-derived catalysts.<sup>155</sup>

## 2.3 Additive manufacturing as a novel shaping technique

Nowadays, the term additive manufacturing (AM) is used virtually synonymously with the word 3D printing. In contrast to subtractive manufacturing techniques such as milling, cutting, or grinding, in which material is removed to obtain the targeted object, AM builds up the object layer by layer. This reduces the material wastage and often allows more complex designs and structures in one step process, as e.g. gluing parts together is not necessary.<sup>178</sup> The first 3D printing technology was developed in the 1970s/1980s.<sup>179</sup> Charles Hull patented his "apparatus for the production of three-dimensional objects by stereolithography" in 1984, in which a photoresponsive polymer is selectively cured by UV light.<sup>180</sup> Through further layers of polymer and their curing steps, the object is built based on a corresponding 3D model.

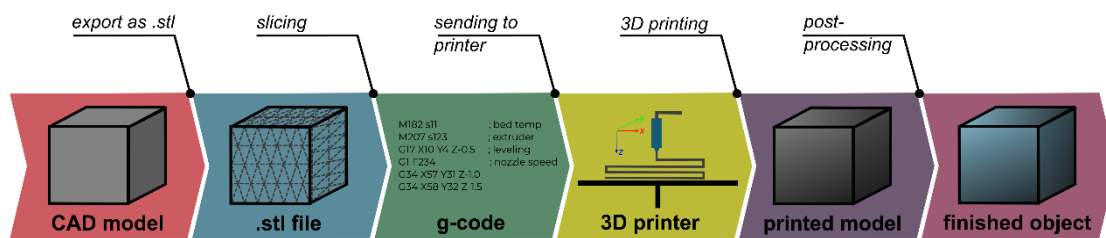


**Figure 10:** Schematic overview of the general process of additive manufacturing.<sup>178,181</sup>

Generally, AM processes always follow the same steps, regardless of the 3D printing method employed (**Figure 10**). It usually starts with a digital model of the corresponding object, which is usually in the form of a so-called computer aided design (CAD). For use in 3D printing, the computer model is then converted into a STL file format (standard tessellation language), in which the object is subdivided into triangles that are defined using their normal vectors. This STL format is then cut into two-dimensional layers (slices) in a process known as slicing, and the commands required for 3D printing are written together in the so-called g-code. The g-code is naturally dependent on the printing technique used, but also on print-specific details such as positions or temperatures are included. The g-code generated in this way then controls the 3D printer in the AM process and the object is built up layer by layer. Depending on the technology used, post-processing steps such as sintering or removal of superfluous material may follow.<sup>178,182</sup>

Although the first 3D printing process was developed so early, it took until the turn of the millennium before AM experienced its current boom. This can be attributed to the cheap availability of computers and computing power, but also to the expiry of key patents and the introduction of Arduino an open access open and easy programmable microcontroller.<sup>183</sup> However, its application changed from rapid tooling/rapid prototyping towards rapid manufacturing with a variety of applications ranging from dental<sup>184,185</sup>, automotive and aerospace<sup>186,187</sup>, construction<sup>188,189</sup>, and food<sup>190,191</sup> to health/medical industry<sup>192</sup> as well as within the private sector.<sup>193</sup> Also the range of possible materials is now wide including ceramics, polymers, metals, electrical and biomaterials. The ISO/ASTM DIS 52900:2018 standard attempts to classify the various 3D printing processes and divides the existing processes into seven process categories based on their printing technology (**Table 2**).<sup>194</sup>

**Table 2:** Overview over commonly known 3D printing techniques based on their process categories according to ISO/ASTM DIS 52900:2018 alongside their technology and materials typically used.<sup>178,182,193-197</sup>

Category	Technology	Techniques	Materials Used
Binder Jetting	Selective deposition of liquid binder on powdery material	Binder Jetting (BJ)	Polymers, ceramics, metals
Directed Energy Deposition	Usage of focused thermal energy to connect materials right after deposition	Laser Metal Deposition, Electron Beam Melting	Metals
Material Extrusion	Selective deposition of extruded material	Direct Ink Writing (DIW), Fused Deposition Modeling (FDM), Fused Filament Fabrication	Polymers, ceramics, biomaterials, metals
Material Jetting	Selective, dropwise deposition of material	Inkjet Printing	Polymer, resins, biomaterials
Powder Bed Fusion	Selective melting of powder in powder bed by means of thermal energy	Selective Laser Sintering (SLS), Selective Laser Melting (SLM)	Metals, ceramics, polymers
Sheet Lamination	Layer wise joining of material	Laminated Object Manufacturing	Paper, polymer, ceramics
Vat Photopolymerization	Layer wise UV induced polymerization of liquid photopolymer	Stereolithography (SLA), Digital Light Processing (DLP), Continuous Liquid Interface Production	UV sensitive polymers (eventually with dispersed ceramics)

Due to their variety, the different AM techniques are not explained in detail here, but reference is made to the corresponding overviews in the literature.<sup>178,182,193,195,196</sup> Based on the different 3D printing techniques, there are different process characteristics such as the materials used, the resolutions of the geometries, and the required printing times. Post-processing is also strongly dependent on the printing technique used. For example, in the case of powder bed-based techniques such as Binder Jetting or selective laser sintering this necessarily involves a depowdering step. The respective advantages and disadvantages of the different printing techniques are crucial decision criteria when it comes to the application.<sup>178</sup> Accordingly, several techniques can be considered for printing ceramics,<sup>198–201</sup> but since this work is mainly concerned with Direct Ink Writing, this will be presented in more detail below.

### 2.3.1 Direct Ink Writing/Robocasting

The Direct Ink Writing technique is classified as material extrusion according to ISO/ASTM DIS 52900:2018.<sup>194</sup> This process was developed and patented in the late 1990s in the USA by Cesarano et al. for printing ceramics.<sup>202,203</sup> The term DIW was subsequently predominantly coined by the research work of Lewis et al. They distinguished between "droplet-based DIW", such as BJ and ink-jet printing, and "filament-based DIW", to which they assigned "robocasting" and FDM, for example.<sup>204–207</sup> In the meantime, the terms robocasting and DIW are used quasi synonymously in the literature, although terms such as direct write fabrication or robot assisted deposition are also sometimes used.<sup>208–210</sup>

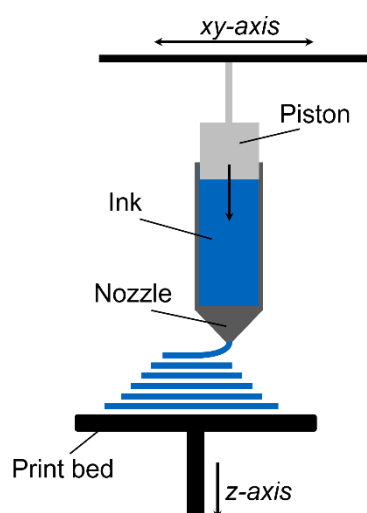


**Figure 11:** Schematic illustration of the Direct Ink Writing process using a syringe-piston system.<sup>183,211</sup>

Generally, in DIW, a so-called paste or ink is extruded through a fine nozzle with typical sizes of 0.15 – 0.5 mm.<sup>207,212,213</sup> In the technical design, the extrusion is realized using the syringe-piston principle, pneumatically or with a screw, whereby combined solutions are also used.<sup>211</sup> The print head moves relative to the print bed, so that the object is built up layer by layer according to the g-code and thus the CAD model (**Figure 11**).<sup>211</sup> Since, unlike FDM, there is no temperature-induced phase transition due to melting in the print head and curing after printing, the rheological properties of the paste are crucial for a good printing result.<sup>206,214,215</sup> The requirements for the paste itself are correspondingly rather high. On the one hand, it must be low viscosity enough to be extruded through the nozzle during printing process, and on the other hand, the paste must be stiff enough to ensure that the printed object is stable and does not flow or deform under its own weight or gravity. It follows that the viscoelastic paste must be shear-thinning to have a low viscosity under increased shear rate during printing, which increases again accordingly after printing and on the print bed under reduced shear rate. Due to the slight drying or evaporation of solvents, the paste also undergoes a transition from pseudoplastic to dilatant, which further helps to maintain the printed shape.<sup>211,216</sup> To ensure uniform printing results, the paste used must also be free of air bubbles or agglomerates, with homogeneity remaining throughout the printing process and subsequent drying.<sup>208,209,211,216</sup> To achieve ceramic pastes with these properties, two main approaches are used, namely colloidal suspensions and gel-embedded suspensions. Depending on the solvent, the latter can be further divided into (aqueous) hydrogel ink and organogel

(**Figure 12**). These are based on the main mechanisms for particle stabilization namely steric, electrostatic and combined electrosteric mechanisms, whereas in gel-embedded suspensions additional polymers stabilize the ink.<sup>208,211,216,217</sup>

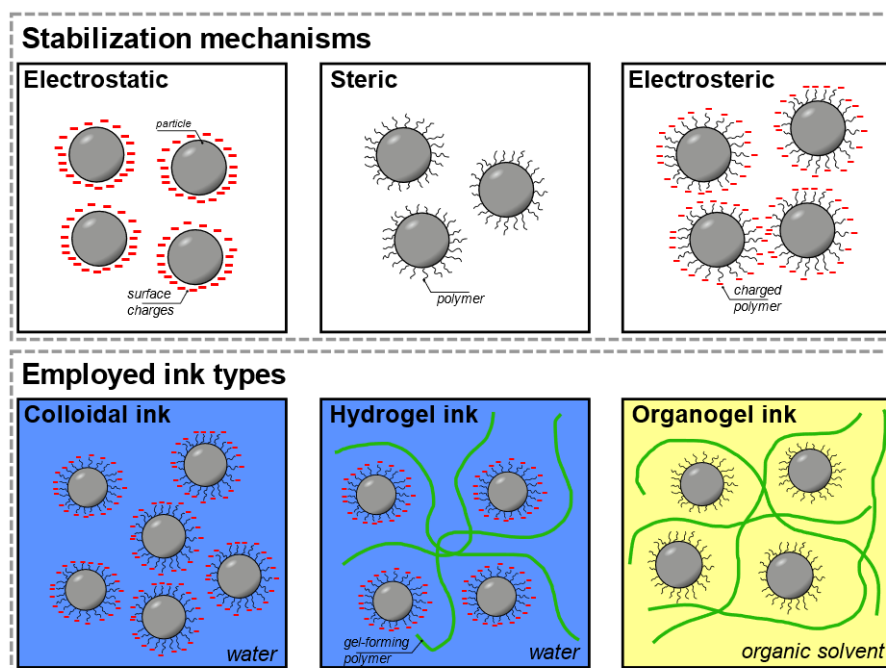


**Figure 12:** Schematic illustration of stabilization mechanisms of ceramic particles (top) and ink types typically employed in Direct Ink Writing.<sup>208,211,217</sup>

In general, most pastes in the literature are water-based, with a high proportion of powdered material and a low proportion of organic or inorganic additives. High solids content enables the robocasting of parts with high green density, low shrinkage and quick drying after printing, so that appropriate dimensional stability is achieved.<sup>211,216</sup> Low organic content facilitates the binder burnout by reducing the risk of cracking during debinding and also enables high densities of the part.<sup>216,217</sup> In this context, typical organic binders in the DIW of ceramics are hydroxypropyl methylcelluloses<sup>218–220</sup>, polyvinyl alcohol<sup>220,221</sup>, polyethyleneimine<sup>222</sup>, polyethylene glycol<sup>223,224</sup> or polyvinylpyrrolidone<sup>209</sup>. Additives such as *iso*-propanol<sup>223</sup> or ethanol<sup>208</sup> are also used to improve the general wettability and optimize the drying behavior. The hydrogel-forming additive most commonly used in robocasting is the commercially available Pluronic®F127. It is an ABA-type triblock copolymer with polyethylene oxide as block A and a polypropylene oxide B block in a rough 2:1 ratio. Below the gelation temperature, the polypropylene oxide block is hydrophilic, and water is a good solvent for Pluronic®F127, at increasing temperature hydrophobicity of the polypropylene oxide increases and thus the solubility decreases. This temperature-dependent hydrophobic association causes the gelation of the hydrogel and thereby enables the stability of the object at the appropriate temperature after printing.<sup>210,225</sup> For example, bentonite<sup>220,221,226–228</sup>, colloidal silica<sup>227</sup> or sodium metasilicate<sup>229</sup> can be used as inorganic additives. Here, it should be considered that the proportion of inorganic additives is still present after sintering and correspondingly reduces the percentage of compressed ceramic. In addition to the rheological properties, which are important for the DIW per se, the drying of the components on the print bed is also important for achieving optimum yields. Uniform, slow drying and good release from the

print bed are important to avoid inhomogeneities and cracks. This is usually achieved by a non-stick surface and an increase in humidity ( $> 65\%$ ) in the build chamber.<sup>216</sup> There are also attempts to print in a (paraffin) oil bath instead of air to further improve drying.<sup>230</sup> However, Feilden et al. were able to show that the pressure in the so-called oil causes oil to be entrapped between the ceramic strands, resulting in voids in the components. These are not present in the case of pressure in air.<sup>216</sup>

Compared with other, non-extrusion-based techniques, DIW usually has poorer layer resolution due to the minimum nozzle diameter. DIW is also limited in terms of printable shapes since strong overhangs or so-called bridges are only possible to a restricted extent. On the other hand, DIW is a comparatively simple 3D printing technique that enables comparably low-cost production. In addition, the process is flexible in terms of the materials that can be printed, and the low organic binder content is advantageous for high-density structures.<sup>209</sup> Furthermore, post-processing is simplified, as e.g. no de-powdering is necessary compared to powder bed-based techniques. Considering the corresponding advantages and disadvantages, DIW is now being investigated in various applications. The main fields thereof include the use of biomaterials such as for bone tissue engineering<sup>213,231–234</sup>, structural components such as refractory products<sup>216,235–237</sup>, electronics including energy storage and piezoelectric components<sup>213,238–240</sup>, and optics<sup>241,242</sup>. Hence, typical materials printed via DIW include titanium<sup>243,244</sup>, hydroxyapatite<sup>245</sup>, graphene<sup>238</sup>, zirconia-toughened alumina<sup>232</sup>, and alumina<sup>212,230,246–248</sup>.

Since the introduction of DIW, there have also been various further developments of the process. For example, to reduce the dependence on rheological properties and ensure that the shape remains maintained, Faes et al. developed pastes containing a photocurable monomer. After printing, the shapes are then cured using UV light to maintain their stability.<sup>217,249</sup> Meanwhile, multi-material printing also plays a role. On the one hand, there are systems with different print heads, each with different materials, and on the other hand, there are print heads with mixing chambers that are fed by different materials. In the latter case, mixing before printing makes it possible to print material gradients, but on the other hand it is not possible to switch between materials without a corresponding mixing fraction. Nevertheless, this makes it possible to print several materials with different properties, such as different harnesses, solubilities or porosities, together to form one multi-functional object.<sup>217,250,251</sup>

### 2.3.2 3D printing in catalysis

Taking advantage of the relative freedom of shape of 3D printing and considering the influence of the macroscopic shape of a catalyst on the reaction, research in this area has increased in recent years to combine additive manufacturing and catalysis. This is also reflected in the number of publications that are published on this topic (**Figure 13**) as well as in the number of patents filed. In general, research in the field of additive manufacturing has been steadily increasing for about two decades, whereas the use of 3D printing in chemistry and especially the application in catalysis are only slowly increasing in recent years.<sup>10,183,252</sup> In the latter, different approaches are being pursued. To produce catalyst shapes, either catalyst supports are printed, like traditional shaping techniques, and subsequently loaded with active component, or active material or the corresponding precursors are printed directly. Techniques for these two approaches range from extrusion-based techniques such as FDM and DIW to powder bed-based BJ, SLM, SLS, and SLA.<sup>10,11,253–255</sup>

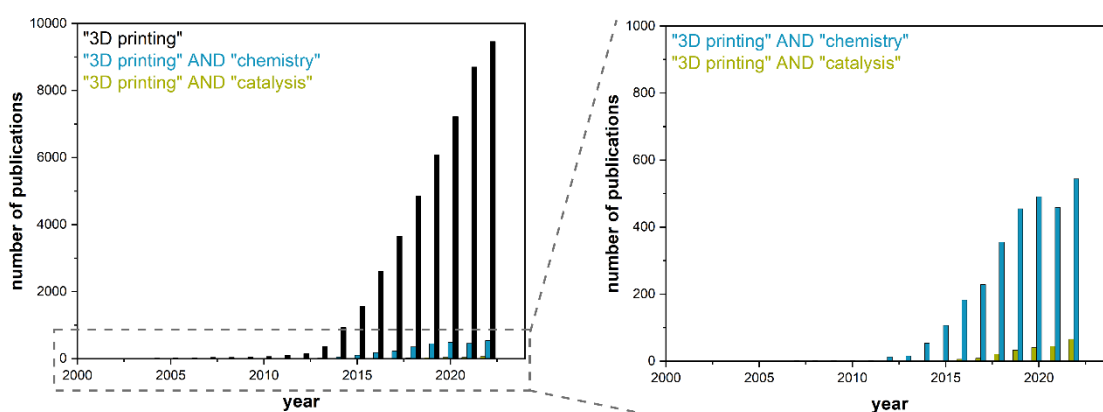


**Figure 13:** Number of publications including the terms “3D printing”, “3D printing and chemistry” and “3D printing and catalysis” per year from 2000 to 2022 based on literature research using Scopus.<sup>183</sup>

For example, Li et al. fabricated two types of monoliths via FDM printing of  $\text{Al}_2\text{O}_3$  polymer filaments, one with only monoaxial channels and the other with radial and axial channels. After coating with Mn-Co nanospheres, the non-thermal plasma catalytic degradation of toluene showed that the monoliths with radial and axial channels have significantly improved energy efficiency compared to the uniaxial monoliths thus demonstrating the significance of radial channels.<sup>256</sup> Sangiorgi et al. immobilized  $\text{TiO}_2$  nanoparticles in a polymer composite. FDM printing was then used to print monoliths that were studied as filter media with respect to methyl orange degradation.<sup>257</sup> Car et al. also fabricated monolithic catalysts via FDM of  $\text{TiO}_2$  composites. Thereby, they showed that with increasing  $\text{TiO}_2$  content, the brittleness of the printed objects also increases. Furthermore, they demonstrated that inert catalyst supports can be fabricated using SLA and subsequent binder burn off, but they exhibit shrinkage of 14 – 20 % and mass loss of about 32 % after thermal post-treatment.<sup>258</sup>

Bui et al. showed that through tailored post-processing including infiltration, both, alumina supports could be printed using BJ that are stable at calcination temperatures as low as 600 °C and, by minor process modification, also Ni-Al based catalysts for the methanation of  $\text{CO}_2$  could be produced by direct printing.<sup>259,260</sup> Via SLM of  $\gamma\text{-Al}_2\text{O}_3$  monolithic structures using epoxy resin as sacrificial binder and pore forming additive, Huo et al. formed carriers with highly complex

and regulated pores that can act as catalyst carriers in future.<sup>261</sup> By means of SLS, Agueniou et al. fabricated monoliths of stainless-steel, which were loaded with Ni/CeO<sub>2</sub>-ZrO<sub>2</sub> via wash coating. In dry reforming of methane, the catalysts produced in this way showed comparable conversions and H<sub>2</sub>/CO ratios to equivalently loaded commercial cordierite monoliths with similar geometric characteristics. Another advantage herein is that the 3D-printed monoliths required no activation time, which the authors attribute to improved heat transport. It should be noted, however, that the stainless steel monoliths also exhibit a certain intrinsic activity based on the nickel content.<sup>262,263</sup> While all techniques offer specific advantages and disadvantages, only Ludwig et al. have attempted to compare the techniques with regard to the manufacture of catalyst supports. In particular, BJ, DIW, fused deposition of ceramics (FDC) and SLA were discussed and the two extrusion-based techniques were investigated in terms of surface area obtained and stability in dependence on calcination temperature.<sup>254</sup>

Furthermore, catalyst shapes can also be produced indirectly via 3D printing, for example when polymer-based sacrificial templates are printed. These are subsequently filled with the corresponding ceramic and then the organic material is removed by thermal post-treatment so that only the catalyst body remains (**Figure 14**). This allows the indirect fabrication of geometries that cannot be produced by direct printing whereas on the other hand, at least one additional step in catalyst shaping is required. In 2016, Michorczyk et al. presented such an approach in which they used digital light processing (DLP) to fabricate monolithic templates with rod sizes of 0.6 mm and 0.3 mm. These were subsequently filled with a ceramic paste of  $\alpha$ -Al<sub>2</sub>O<sub>3</sub> and the template was thermally removed. The resulting  $\alpha$ -Al<sub>2</sub>O<sub>3</sub> monoliths were impregnated with first Na<sub>2</sub>WO<sub>4</sub> and then Mn(NO<sub>3</sub>)<sub>2</sub>, and then investigated for in the oxidative coupling of methane.<sup>264</sup>

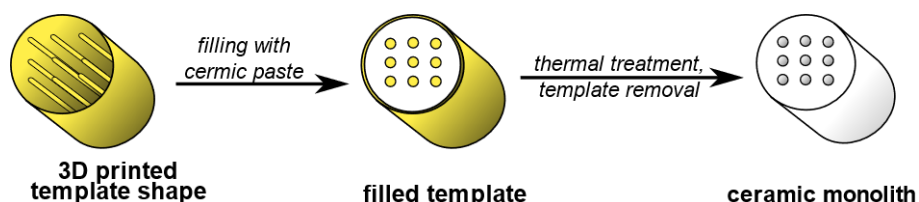


**Figure 14:** Fabrication of monolithic catalysts using polymeric templates.<sup>264</sup>

Alimi et al. used FDM printed polylactic acid as sacrificial template to fabricate  $\gamma$ -Al<sub>2</sub>O<sub>3</sub> monoliths onto which palladium nanoparticles are immobilized via deposition precipitation. The resulting shaped bodies were investigated in Mizoroki-Heck, Suzuki-Miyaura and copper-free Sonogashira-Hagihara cross-coupling reactions and showed better performance than the powdered reference samples. This is since the spatial separation of the Pd nanoparticles within the monolith reduces agglomeration, leaching and catalyst loss. Furthermore, the monoliths show excellent stability and reusability.<sup>265</sup> Similarly fabricated monoliths embedded in a polypropylene-based flow reactor printed via FDM could also catalyze the selective oxidation of styrene.<sup>266</sup> Another example is shown by Rokicińska et al, who generate a corresponding template via DLP, which is used to produce a corundum monolith. It is subsequently covered with an MFI zeolite before the monolith is impregnated with a Co<sub>3</sub>O<sub>4</sub> precursor. In the catalytic combustion of toluene, excellent catalytic activities as well as high turnover frequencies values could be achieved.<sup>267</sup>



Since the template strategy and the simple polymer pressure can be used to change the geometries in a comparable way, this strategy is also used to compare different shapes. Thus, Li et al. print different templates that yield cylinder, tetrahedron and tetrakaidecahedron periodic structures as channels in the final monolith. The resulting phenol-formaldehyde based hierarchical monolith was subsequently covered with  $\text{Al}_2\text{O}_3$  and then impregnated with  $\text{Ni}(\text{NO}_3)_2$ . During CO methanation, the tetrahedron-based monoliths thereby showed the strongest reduction in pressure drop, a low temperature gradient, and the highest catalytic activity of the 3D printed catalytic shapes.<sup>268</sup> For comparison with conventional monoliths, which have a constant cross-section, Davó-Quiñonero et al. fabricated cordierite monoliths in which one has constant symmetrical channels, whereas the second has tapering asymmetrical channels. After loading with  $\text{Cu}/\text{CeO}_2$ , the monoliths were studied in CO oxidation in different atmospheres. The improved geometries showed higher conversions than their symmetric counterparts. This can be attributed to the fact that the asymmetric channels fit better to the equation rates and increase the reaction rate accordingly, and to the fact that they favor turbulent flow.<sup>269</sup> A similar approach to this was chosen by Xu et al., who used DIW to print a hollow cylinder using a  $\text{Al}_2\text{O}_3$  ink that is later filled with a ceramic paste. After thermal treatment, to improve stability and increase porosity by burning off polymeric microspheres present, the ceramic tube is loaded with Pd and tested for the reduction of 4-nitrophenol.<sup>270</sup>

Apart from this, 3D printing also finds application in catalysis in the fabrication of (micro-) flow reactors.<sup>252,271,272</sup> Wei et al. additively fabricated reactors from metal using SLS where the reactors themselves are catalytically active. Depending on the alloy used, this involves, for example, Fischer-Tropsch synthesis and  $\text{CO}_2$  hydrogenation (Fe, Co) or producing syngas by means of  $\text{CO}_2$  reforming of  $\text{CH}_4$  (Ni). Investigations of different reactor geometries further show that this can also influence and optimize the product distribution.<sup>273</sup> In 2016, Kitson et al. present composite catalyst-silicone materials incorporated into 3D-printed reaction ware device. The reaction ware device thus presented, a closed mold built on aligned cubes with two different catalytically active sites and a silica column, enables multistep organic synthesis (**Figure 15**) by tilting and passing the reactant through the reactor step by step.<sup>274</sup>

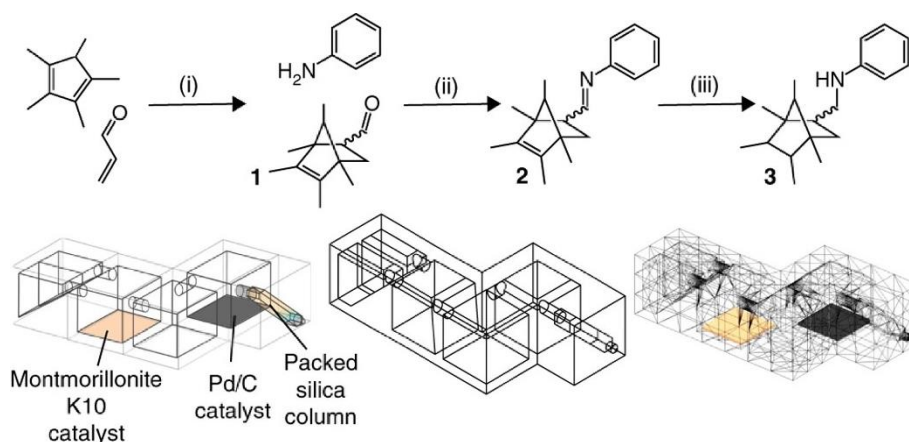


**Figure 15:** Design and function of catalytic active reaction ware presented by Kitson et al.. Adapted with reprint permission from <sup>274</sup>.

To derive improved geometries, especially in combination with experimental data, simulations also become more important. In an experimental and simulative comparison of pressure drop and temperature profile of commercial cordierite monoliths versus woodpile structures fabricated via DLP by Kovacev et al. it was shown that the axial temperature gradient is lower in the printed lattice structure. This is probably due to higher heat transfer based on more tortuous flow and exchange in both axial and radial directions. Pressure drop is also significantly reduced for the 3D printed beam (by 38 – 45 % compared to the commercial monolith), although this is independent of grid size. Still, this also translates to a reduced surface area.<sup>275</sup>

However, since the focus of this work is Direct Ink Writing of catalyst support and catalytically active material directly, the state of the art in this area will be investigated in more detail. To illustrate the same, **Table 3** summarizes additively manufactured catalyst support materials studied in the literature, along with the impregnation technique of the active component and target reaction studied. When looking at the printed shape, it is noticeable that almost always a so-called woodpile or lattice structure is printed, consisting of adjacent strands, each layer rotated. There are various ways of arranging these layers in relation to each other. An overview thereof is given in **Figure 16**. First, the offset angles of the different layers to each other can be changed influencing the geometry of the channels (**Figure 16a**). Furthermore, the offset of the layers to each other can also be changed if the angle remains constant (usually 90 °C). This allows 111, 131 and 135 stackings, which affect the reactant flow along the monolith axis (**Figure 16b**). In addition, the strand thickness of the strands and the distance between them can generally be changed as well (**Figure 16c**).<sup>9</sup>

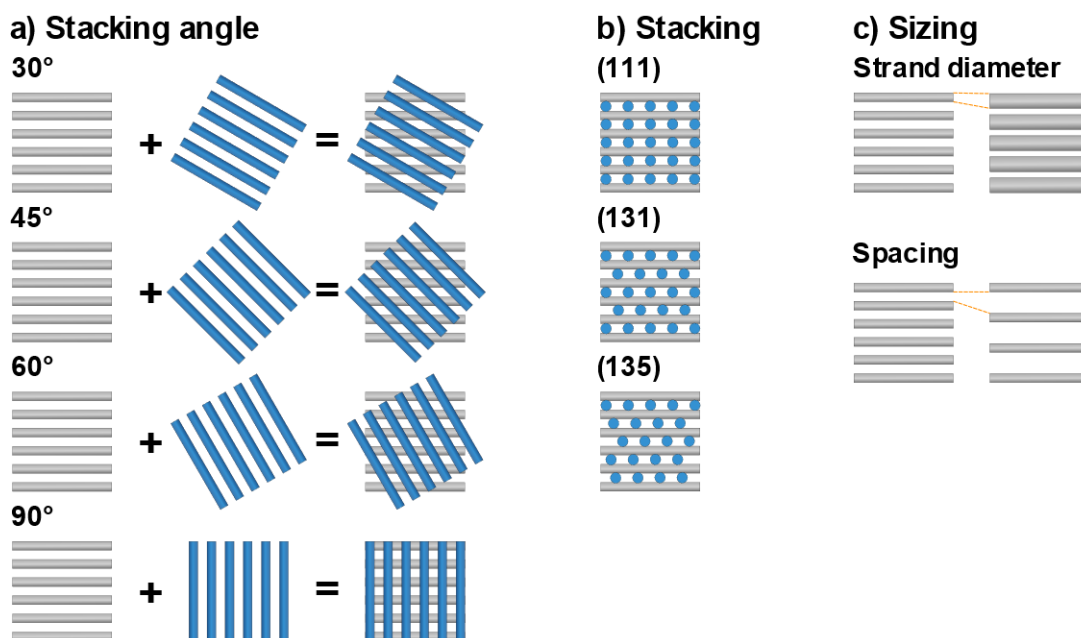


**Figure 16:** Different woodpile patterns accessible by varying a) stacking angle, b) stacking orientation and c) size and spacing of the strands.<sup>10,224,276</sup>

**Table 3:** Overview of DIW printed catalyst support structures, the respective loading of the active component, the shapes investigated and the test reaction in literature.

Printed Carrier	Active Component	Loading Method	Shape Printed	Target Reaction	Ref.
Al <sub>2</sub> O <sub>3</sub>	BaMn <sub>2</sub> Al <sub>10</sub> O <sub>19-α</sub>	Washcoat	Woodpile (131)	Methane combustion	277
α-Al <sub>2</sub> O <sub>3</sub>	γ-Al <sub>2</sub> O <sub>3</sub> , Pt	Washcoat, impregnation	Woodpile (131; 111; 135)	CO oxidation	276
Ti <sub>6</sub> Al <sub>4</sub> V	Fe-MFI Zeolite	Coating, ion exchange	Woodpile (111; 135)	N <sub>2</sub> O decomposition	278
Stainless steel	ZSM-5	Washcoat	Woodpile (131; 111)	Methanol-to-olefin	218
SiO <sub>2</sub>	Cu, Pd	Activated with H <sub>2</sub> O <sub>2</sub> , silanized, wet impregnation	Woodpile	Cycloaddition, Cross-Coupling	223
Cu, Stainless steel	Ni/Al <sub>2</sub> O <sub>3</sub>	Washcoat	Woodpile (131)	CO <sub>2</sub> methanation	279
Cordierite precursor	γ-Al <sub>2</sub> O <sub>3</sub> , TiO <sub>2</sub> , CeO <sub>2</sub> , ZrO <sub>2</sub> , HY Zeolite, Pd, Pt	Washcoat	Woodpile (diff. stacking angles)	Methane oxidation	224
CeO <sub>2</sub>	Ni, Ru	Impregnation	Woodpile	NH <sub>3</sub> decomposition	280

One of the first DIW fabricated catalysts was presented in 2004 by Stuecker et al. Commercially extruded cordierite monoliths (washcoated with Al<sub>2</sub>O<sub>3</sub>) and printed Al<sub>2</sub>O<sub>3</sub> woodpile structures were washcoated with barium manganese hexaaluminate. In addition, a purely BaMn<sub>2</sub>Al<sub>10</sub>O<sub>19-α</sub> based woodpile structure was 3D printed, ensuring that all three shapes had the same outer surface area. During methane combustion as catalytic test reaction, the woodpile structures were shown to perform significantly better than the commercial shaped monoliths, as the 3D printed lattice structures promotes turbulence over the straight channels, which accordingly increases mass transport. This was reflected in an approximately six-fold increase in methane conversion at 600 °C. Higher catalyst quantities, through a higher loading or the direct printing of active components, were able to further increase the conversion.<sup>277</sup> For application in copper alkyne-azide cycloaddition & palladium catalyzed cross-coupling reactions, Díaz et al. fabricated SiO<sub>2</sub> woodpile monoliths. These were subsequently surface activated with hydrogen peroxide, silanized and metalated with Cu and Pd. Test reaction proved efficient and easily reusable monoliths with negligible amounts of metal leaching.<sup>223</sup> The influence of sintering temperature, atmosphere, and technique on Cu woodpile structure (131) were investigated by Danaci et al. A five-hour sintering at 1000 °C under H<sub>2</sub>/N<sub>2</sub> (1:1) in a conventional furnace was identified as the optimal condition. Although pulsed electrical current sintering is significantly faster than conventional furnace sintering, it was not considered useful because of the resulting surface oxidation of the support material. After loading with Ni/Al<sub>2</sub>O<sub>3</sub>, the catalyst moldings were tested in CO<sub>2</sub> methanation. Thereby, the printed shaped bodies were better than corresponding powder measurements and no significant deactivation could be observed within 80 h.<sup>279</sup>

Ferrizz et al. printed various woodpile structures (111 and 131) from  $\alpha$ -Al<sub>2</sub>O<sub>3</sub>. The resulting shapes were then washcoated with  $\gamma$ -Al<sub>2</sub>O<sub>3</sub> and impregnated with H<sub>2</sub>PtCl<sub>6</sub> to obtain Pt/ $\gamma$ -Al<sub>2</sub>O<sub>3</sub> catalysts for the oxidation of CO. All printed shapes performed better than commercial monoliths. The woodpile 131 structure showed good conversions and a three times higher Sherwood number, but the pressure drop is comparable to a packed bed catalyst and thus significantly increased (1000-fold) compared to commercial monoliths. Another woodpile structure with 135 stacking, smaller strands and an increased bulk porosity was able to increase the Sherwood number by a factor of about 1.5 relative to the commercial geometry while only having a quadrupled pressure drop. These results clearly show that with a clever choice of geometry, reaction parameters can be optimized for specific reactions.<sup>276</sup> Working with 111 and 135 woodpile structures and strands of Ti<sub>6</sub>Al<sub>4</sub>V alloy equal size diameter, Noyen et al. showed that after washcoating with MFI-type zeolite and subsequent ion exchange with Fe for N<sub>2</sub>O decomposition, the 135 stacking exhibited the most promising behavior in terms of pressure drop and activity per catalytic site.<sup>278</sup> Lefevre et al. investigated how woodpile 111 and 131 structures of stainless steel with washcoated ZSM-5 affect methanol-to-olefin conversion. Here, 131 structures show the highest yields of light olefins at high weight hourly space velocities due to increased tortuosity and improved heat and mass transport.<sup>218</sup>

For methane oxidation, Hajimirzaee et al. printed cordierite precursors, changing the offset angle of the different layers in the printed woodpile patterns (**Figure 16a**). After washcoating with HY zeolite,  $\gamma$ -Al<sub>2</sub>O<sub>3</sub> various promoters, and after doping with Pd and Pt as active components, it was also shown by simulation that increasing the complexity of the catalytic structures in the support improves the activity of the catalysts. The conversion of methane at e.g. 510 °C was 12.6 % for commercial monoliths, 72.6 % for an offset angle of 90 °, 80.1 % for both 30 ° and 45 °, and with 89.6 % for the 60 ° oriented structures. This is also attributed to the change in the fluid mechanics and the corresponding improvement in the mass transport.<sup>224</sup> Thus, in addition to the offset, the offset angle can also be varied to influence the flow behavior and activity. To investigate the influence of geometry, Lucentini et al. fabricated several CeO<sub>2</sub> based monoliths, which differed in the number of channels, their size and wall thickness. These were loaded with Ni and Ru and studied in catalytic ammonia decomposition for hydrogen production. In addition, the corresponding performances were simulated using a one-dimensional mathematical model, showing good agreement with the experimental data. Based on the results, an optimized monolithic shape was presented, which had 14.5 mm in diameter, 76 channels, a channel width of 0.78 mm, wall thickness of 0.46 mm, and length of 6 mm. The optimized structure exhibited superior catalytic performance, both on a weight and volume basis, and showed good stability.<sup>280</sup>

When comparing the examples of catalyst support DIW described in the literature, it becomes apparent that woodpile structures are usually printed, with the stacking of the different layers to each other being varied in some cases in order to optimize the flow behavior. Also, these examples demonstrate that more turbulent flow, such as that created by the use of 3D printed woodpile structures, improved performance of the catalysts, through appropriate shape variation. However, mostly few different shapes have been compared so far experimentally. With regard to the impregnation method, it is noticeable that washcoating was used almost exclusively. Compared to support printing, direct printing of catalytically active material or its precursors has the

advantage that no further loading step including possible post-processing is necessary. Although the catalytically active component is homogeneously distributed over the entire shape body, almost all the monolithic or lattice structures investigated already have a high surface-to-volume ratio, so that the amount of inactive material in the inside of a catalyst shape is low, compared to e.g. cylinders or pellets. In order to achieve a correspondingly good activity of the catalyst and to avoid, for example, sintering processes, the thermal post-treatment must be adapted to the respective material as a critical step. **Table 4** lists examples of DIW printed catalysts from the literature.

**Table 4:** Overview of DIW printed catalyst material, the shapes investigated and the test reaction in literature.

Catalyst Material	Shape Printed	Target Reaction	Ref.
BaMn <sub>2</sub> Al <sub>10</sub> O <sub>19-α</sub>	Woodpile (131)	Methane combustion	277
Cu/Al <sub>2</sub> O <sub>3</sub> (CuO/CuAl <sub>2</sub> O <sub>4</sub> )	Woodpile	Ullman reactions	219
Al <sub>2</sub> O <sub>3</sub>	Woodpile	Biginelli and Hantzsch reaction	222
NiMoO <sub>2</sub> /C	Woodpile, honeycomb	Syngas conversion to alcohols	281
Fe/SiC	Woodpile	Wet peroxide oxidation processes.	282
ZSM-5 doped with various metals	Woodpile	Methanol to olefins	283
ZSM-5	Woodpile	Methanol to olefin	227
Ni/Al <sub>2</sub> O <sub>3</sub>	Woodpile	Methanation	228
TiO <sub>2</sub>	Solid square-lattice double-diagonal (SLDD) structures	UV degradation of acesulfame	284
ZSM-5	Woodpile	Methanol to hydrocarbon	285
C	Woodpile, different lattice spacing	Benzyl alcohol oxidation to benzaldehyde	286
Fe/SiC	Different pattern for comparison	Phenol hydroxylation	287
MOF-Fe/SiC	Woodpile	Phenol hydroxylation	288
Fe/SiC	Different pattern for comparison and CFD	Phenol hydroxylation	289
ZSM-5 doped with various metals	Woodpile	n-Hexane cracking	290
Mn–Na <sub>2</sub> –WO <sub>4</sub> /SiO <sub>2</sub>	Woodpile	Oxidative coupling of methane	291
Fe/Co/Al <sub>2</sub> O <sub>3</sub> ; Fe/Pd/Al <sub>2</sub> O <sub>3</sub> ; FePd/Graohene	Woodpile (111, 131)	Benzyl alcohol oxidation to benzaldehyde	292
α-Al <sub>2</sub> O <sub>3</sub>	Woodpile, honeycomb; different fill percentage (40 and 50 %)	Ethanol to acetaldehyde	293

By printing acetoxy silicone polymer paste doped with Pd/C, catalytically active reaction ware could be printed. The catalyst was tested in the hybridization of styrene to ethylbenzene using Et<sub>3</sub>SiH as hydrogen source. Quantitative conversions of styrene were observed after 30 minutes

at room temperature. Based on their findings, Symes et al. proposed the printing of active reactors that can control the mixture of reactants, flow behavior and purification methods, thereby forming a low-cost, easily tunable, and highly accessible format.<sup>294</sup>

Similar to the literature on printed support material, Azuaje et al. presented 3D printed Al<sub>2</sub>O<sub>3</sub> woodpile monoliths. However, these were not loaded with active component, but the alumina was directly used as Lewis acid in Biginelli and Hantzsch reactions. The catalysts not only produced good yields of a wide range of reactants with short reaction times, but also showed good performance with up to ten times recycling.<sup>222</sup> Lefevre et al. investigated various factors influencing the 3D printing and activity of ZSM-5 in methanol-to-olefin conversion. It was shown that the selectivity of the reaction depends primarily on the active surface and acidity. This in turn can be attributed primarily to the various inorganic binders used for printing (more precisely bentonite, colloidal silica and aluminophosphates). Regarding the selectivity towards the desired products, aluminophosphate is the most promising binder as it promotes high ethene and propene selectivity alongside a low formation of methane and alkanes than for the other binders. The activity of the catalyst on the other hand, as well as its mechanical stability, was primarily influenced by porosity, strand diameter and layer stacking. Smaller strand diameters improved the activity and stability of the catalyst. In addition, a woodpile structure with a 131 stacking showed increased performance compared to a 111 stacking due to the higher tortuosity of the flow.<sup>227</sup>

In-house synthesized and commercial (Octolyst, Evonik) Ni/Al catalysts were printed by Middelkoop et al. and investigated for methanation. They were evaluated in-situ under typical conditions for CO<sub>2</sub> hydrogenation to methane using X-ray diffraction computed tomography to compare the activity of powder and pellet. The DIW printed commercial catalyst showed the best performance with conversions close to the thermodynamic equilibrium. This was attributed to the more homogeneous Ni distribution compared to the in-house fabricated catalyst. In general, the 3D printed geometries showed the highest activities, followed by the pellet shapes, therefore further confirming the advantage of 3D printing in catalysis.<sup>228</sup>

For wastewater treatment via catalytic wet peroxide oxidation, Quintanilla et al. presented Fe/SiC monoliths that, in addition to good performance in wastewater treatment, also exhibit high long-term stability of over 350 h on stream and are mechanically stable up to 3.5 MPa.<sup>282</sup> 3D printed structures also have advantages in the field of photocatalytic pollutant degradation. In particular, the access to structures with increased surface-to-volume ratios as well as optimized light pathways with a better contact interface and mass transfer for reactions under UV-Vis light should be mentioned. The TiO<sub>2</sub> monoliths printed by Mendez-Arriaga et al. also showed no loss of activity during reuse in the degradation of acesulfam as a model pollutant.<sup>284</sup>

Konarova et al. printed NiMo ions embedded in polyvinyl alcohol and starch in both woodpile and honeycomb monoliths. After thermal treatment, three-dimensional Ni/Mo oxide structures on porous carbon framework were used in the conversion of syngas to alcohols. Especially at high gas hourly velocities, the 3D printed catalysts forced significantly higher CO conversions alongside higher selectivities to alcohols compared to their pellet shape counterparts.<sup>281</sup> Zhou et al. printed a paste consisting of starch/gelatin as carbon source and SiO<sub>2</sub> as hard template. After carbonization, the SiO<sub>2</sub> template was washed out to obtain macroporous monolithic carbon

structures as oxidation catalysts for the conversion of benzyl alcohol to benzaldehyde. It was shown that the increased macroporosity due to the use of templates has a positive effect on the conversion. Similarly, a structure with larger channels (**Figure 16c**) was shown beneficial regarding the benzyl alcohol conversion. Both effects were attributed to enhanced mass transfer within these systems. In addition, for the structures with large channels, the catalyst bed volume is larger for the same catalyst mass, which increases the contact between reactant and catalyst. While the conversions are each dependent on macroporosity and structure of the monoliths, it should be noted, however, that the selectivity to benzaldehyde remains the same.<sup>286</sup>

Apart from the variation within the woodpile stacking, Vega et al. varied the overall cell geometry. They printed Fe/SiC monoliths that exhibited woodpile, troncoconical and triangular cell geometries with parallel channels presenting staggered or faced interconnections. Using Mössbauer spectroscopy, the iron silicides Fe<sub>3</sub>Si and  $\alpha$ -FeSi<sub>2</sub>, the catalytically active species in the phenol hydroxylation reaction to dihydroxy benzenes (such as catechol and hydroquinone), were detected. The products obtained show that with increased cell density and high number of not-facing inter-connected channels and correspondingly altered flux with increased tortuosity, the selectivity to dihydroxy benzenes increases. Accordingly, the inter-connected triangular cell channels with internal staggered pattern show the highest selectivities. Compared with traditional slurry reactors, the 3D printed reactors exhibit significant advantages. Both the weight loss (slurry ~30 wt.%) and the reduction in surface area (slurry 50 % after 3 h) are greatly reduced (2 wt.% loss, no reduction in surface area) by using the monolithic catalysts. Thus, it can be shown that 3D printing provides fundamental advantages in catalysis and that, despite the much-studied woodpile structures with its variations, other shapes can also provide advantages.<sup>287</sup> The same monolithic shapes (square, troncoconical, and triangular) of Fe/SiC were also investigated in combination with CFD simulations. These also show that the triangular cell monoliths with a smaller hydraulic channel diameter and not-facing interconnections lead to a higher internal macrotortuosity. The resulting oscillatory flow of the liquid phase in the channels allows additional transverse flow between the respective channels. This increases the reactant mixing as well as the contact time. Since this is not possible with the other two shapes, the triangular geometry shows the best performance both in terms of reaction rates and product selectivity.<sup>289</sup>

Using DIW printing of a paste of alumina and copper nitrate, followed by sintering at 1400 °C, Tubío et al. prepared a woodpile monolith of Cu/Al<sub>2</sub>O<sub>3</sub>. The catalyst thus prepared showed high efficiency as well as good recyclability in various Ullmann reactions for the synthesis of imidazoles, benzimidazoles, and *N*-aryl-amides. The embedding of Cu in the Al<sub>2</sub>O<sub>3</sub> matrix also prevented the leaching of active component into the reaction medium.<sup>219</sup> The effect of various metal doping of ZSM-5 monoliths by adding the appropriate metal nitrates during the printing process was analyzed by Li et al. In methanol-to-olefins test reactions, Cr, Mg and Y were shown to increase methanol conversion, with Mg and Zn promoting the production of light olefins. While targeted doping can improve selectivities and conversions, an integration of doping into the 3D printing process is a facile and rapid method.<sup>283</sup> Comparably prepared monoliths of ZSM-5 doped by the addition of metal nitrates to the paste were also used in the methanol to hydrocarbon reaction. Experiments in the presence or absence of CO<sub>2</sub> showed that the absence of CO<sub>2</sub> has a

positive effect on the yield of light olefins, especially ethylene. A detailed investigation of the catalysts showed that the changed physicochemical properties due to the incorporation of metal dopants affect the product selectivity by increased acidity or basicity.<sup>285</sup> Regarding the DIW printing of porous material with metal nitrates to obtain the corresponding oxides, the metal loadings are usually limited to below 10 wt.%, otherwise the rheological properties do not allow robocasting. To overcome this limitation, Lawson et al. directly printed a mixed paste consisting of H-ZSM-5 and the corresponding metal oxides such as  $V_2O_5$ ,  $ZrO_2$ ,  $Cr_2O_3$ , and  $Ga_2O_3$ . The resulting bifunctional metal oxide/zeolite catalysts with metal loadings of 15 wt.% were tested in *n*-hexane cracking to light olefins. The 15 wt.% Cr/ZSM-5 monolith showed the best performance with both high conversion and selectivities towards light olefins. Overall, the proof-of-concept was established that it is possible to achieve metal loadings above 10 wt.% by printing mixed pastes of metal oxide and zeolite catalysts.<sup>290</sup>

Karsten et al. printed Mn-Na-W/SiO<sub>2</sub> catalysts for the oxidative coupling of methane. In test reactions, they compared the performance of powders and structured bodies. At laboratory scale, with millimeter reactors, the 3D printed monoliths and their powder measurements show similar performance, beside the powder measurements showing a 40 % increase in conversion. Nonetheless, the decreased pressure drop of the 3D printed monolithic reactors compared to the respective powder measurements is a major advantage that should not be overlooked.<sup>291</sup> FeCo and FePd-supported alumina monoliths have been printed by Jacquot et al.. Tested in the selective oxidation of benzyl alcohol to benzaldehyde, stackings of 111 and 131 were compared with conventional technologies, namely batch and packed bed reactors. The 3D printed monoliths showed higher TOF and conversions than their packed bed counterparts, with the alternating stacking of 131 achieving the best results. Mixed stacking of Fe/Al<sub>2</sub>O<sub>3</sub> and FePd/graphene oxide monoliths also significantly improved the performance compared to the FePd/graphene oxide batch analogous. Furthermore, the authors were able to describe the mixed gas-liquid flow regime in the reactor satisfactorily by a dispersion model. Overall, the study highlights the importance of the reactor concepts, their configuration, and the operation conditions in achieving best performances.<sup>292</sup> Targeting the ethanol conversion to acetaldehyde using an alumina catalyst, Álvarez et al. optimized paste composition and post-processing of the respective monolithic structures. The paste developed with 70 wt.% ceramic content and a sintering temperature of 1550 °C resulted in the best trade-off in terms of rheological properties, stability, microstructure, and shrinkage. In total, woodpile (111) and honeycomb structures, each with an infill of 40 % and 50 %, were printed. In contrast to the woodpile structures, the honeycomb structures have no interconnections between the channels. In gas flow simulations, this leads to shorter residence times for honeycomb monoliths compared to their rectilinear counterparts. In the case of the woodpile structures, the less filled structures (40 %) show better conversions in test reactions, since the residence time is also increased. These results clearly show that optimized geometries with controlled flow behavior, surface-to-volume ratios and catalysts mass for improved catalytic performance can be fast and easy developed combination with CFD simulations, as they reduce the required amount of prototypes to be tested.<sup>293</sup>



By printing of Fe-BTC MOF/SiC mixed pastes, after heat treatment a MOF-Fe fully integrated into the monolithic scaffolds was obtained. These woodpile structures were slightly electrical conductible, highly stable and showed a good catalytic performance for hydroxylation of phenol. Due to a lower number of absorbed species, the printed structures had higher selectivities towards the desired dihydroxy benzene compared to the pure powder, even though the powder's activity was higher.<sup>288</sup> Another application of 3D printed monoliths with active component was presented by Thakkar et al.. Thus, they printed zeolites (13X and 5A)<sup>220</sup>, MOFs (MOF-74(Ni) and UTSA-16(Co)<sup>221</sup>, and presented different approaches to fabricate aminosilica adsorbents<sup>226</sup>. All of these materials were successfully used in CO<sub>2</sub> capture, each achieving performances comparable to or just below those of pure powdered comparable materials.<sup>220,221,226</sup>

In summary, optimized catalyst geometries, which are accessible through 3D printing, can improve both the turnover and the selectivity and yield of the respective catalytic reaction. Improved mass and heat transport, particularly in the radial direction, play a major role here since radial flow is not possible in traditionally extruded monoliths due to unconnected channels. Although various techniques and printing methods are used in the field of 3D printing of catalysts, DIW is one of the most studied techniques, also because it is technically very close to the extrusion already used. Although the possible shapes are more limited than with other techniques, DIW also allows many different geometries (**Figure 16**). However, depending on the targeted reaction, optimized geometries must be found, with reaction simulation becoming a more important tool therefore in the future. Apart from this, further development with regard to the printing process, post-processing and, if necessary, loading with active components are important fields of research in order to be able to use 3D printing in catalysis in future on a larger scale.

### 3 Aim of this thesis

In the course of this work, direct ink writing as an additive manufacturing technique for heterogeneous catalysts is to be further investigated. The aim is to research the direct printing of catalytically active material on the one hand and the printing of catalyst carriers on the other hand. For the printing of catalytically active material, different test reactions are considered. Among others, a Ni/Al based precursor for the methanation reaction is investigated. In addition to intrinsic powder measurements, full particle measurements are to be carried out as well, for example in a single pellet string reactor. As a further catalytic precursor,  $\text{NH}_2\text{-MIL-125(Ti)}$ , an organometallic framework compound, is to be printed. After decomposition to  $\text{TiO}_2$ , test reactions with powder and full particles for photocatalytic water splitting are performed. It should be noted that sufficient illumination in the incident is important for photocatalytic reactions, for which 3D printing can provide complex shapes. In addition to the test reactions themselves, the optimization of the 3D printing process itself is an important consideration with regard to the direct printing of catalytically active material. Among other things, rheological measurements are to be used to enable and improve the printability of the materials themselves by adding suitable additives. These include for example hydroxypropyl methylcelluloses, alcohols and inorganic additives. However, it has to be taken into account that the additives either completely decompose during the sintering process or do not interfere with the respective catalytic reactions. In addition, the calcination step is to be optimized for each material in order to achieve optimum activity and, for example, an ideal pore structure and sufficient mechanical stability.

In addition to the printing of the active component, the printing of the catalyst support material is also investigated. Alumina is selected as support material because of its distinct advantages like high tunability in terms of its properties, is comparably cheap and facilitates good printing results. After loading with platinum as active component, the catalysts are then to be used for the dehydrogenation of perhydro-dibenzyltoluene. This subprocess in chemical hydrogen storage using perhydro-dibenzyltoluene/dibenzyltoluene as a liquid organic hydrogen carrier is chosen for several reasons. On the one hand, the respective test system is three-phased, due to the solid catalyst, the liquid reactant, and the gaseous product. On the other hand, the reaction itself is highly endothermic, which is why good heat transfer as well as mass transport must be ensured. For the fabrication of the corresponding catalysts, the pore structure of the aluminate supports should be characterized first and, potentially improved by appropriate pore-forming additives in order to be suitable for the subsequent application. Sufficient mechanical stability should of course be ensured. The supports should then be impregnated with platinum sulfite acid solution, whereby, for example, the influence of the different geometries with different surface-to-volume ratios on the impregnation process should be investigated. The catalysts produced in this way is tested both semi-batchwise and in continuous operation for dehydrogenation. Among other things, different geometries should be tested to highlight the benefit of combining AM and catalysis. Furthermore, guidelines for deriving optimized geometries should be found and experimentally proven in combination with CFD simulations.

In a last step, a detailed comparison of the AM techniques Binder Jetting and Direct Ink Writing will be carried out. The aim is to compare 3D printing characteristics such as pore structure and mechanical stability alongside any post-processing steps that may be required. The aim is not only to work out the advantages and disadvantages of the respective printing techniques, but also to evaluate them to assess their potential in heterogeneous catalysis. To ensure a good comparison of the test results, same test reactions as for the aim of the investigation in Direct Ink Writing are selected, namely printing catalyst carriers for LOHC dehydrogenation reaction and Ni/Al catalysts for methanation. In the case of printing catalyst carriers, the influence of the print-specific characteristics on the impregnation behavior of the catalyst carriers will also be investigated. In the case of direct printing of active material, investigations are particularly relevant with regard to post-processing and stability since high calcination temperatures cannot be realized. In the catalytic test reactions, comparable geometries of both 3D printing techniques as well as geometries that cannot be realized with the other technique are to be compared with each other. This aims to draw conclusions as to which AM technique is better suited for use in heterogeneous catalysis and which advantages or limitations direct ink writing or Binder Jetting have.

## 4 3D Printed MOF-Derived Composites for Enhanced Photocatalytic Hydrogen Generation

### 4.1 Bibliographic data

Title: “3D Printed MOF-Derived Composites for Enhanced Photocatalytic Hydrogen Generation”

Status: Research Article, Published, July 25, 2022

Journal: *Solar RRL* **2022**, 2200552

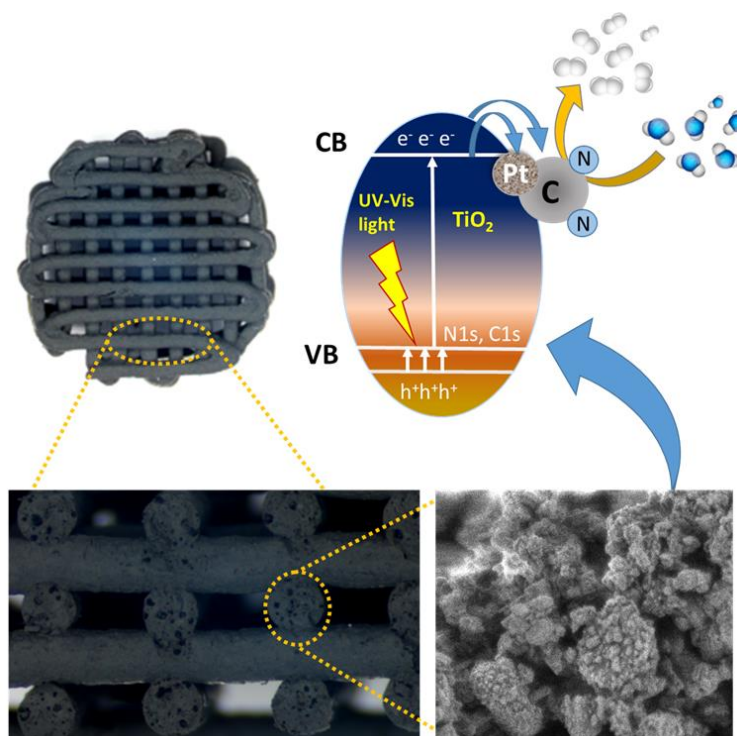
Publisher: Wiley-VCH

DOI: 10.1002/solr.202200552

Authors: Mian Zahid Hussain<sup>#,\*</sup>, Paula F. Großmann<sup>#</sup>, Fabian Kohler, Tim Kratky, Laura Kronthaler, Bart van der Linden, Katia Rodewald, Bernhard Rieger, Roland A. Fischer, Yongde Xia<sup>\*a</sup>

Reference: [295]

### 4.2 Abstract graphic (TOC)



<sup>#</sup> These authors contributed equally. <sup>\*</sup> Corresponding author.

<sup>a</sup> M. Z. Hussain had the initial idea, performed most of the characterization and wrote parts of the manuscript. P. F. Großmann executed the 3D printing part and wrote parts of the manuscript. F. Kohler measured HRTEM. T. Kratky performed the XPS measurements. L. Kronthaler did the ALD of platinum. B. van der Linden executed the photocatalytic water splitting reactions. K. Rodewald performed the SEM and EDX imaging. B. Rieger, R. A. Fischer, Y. Xia contributed with valuable intellectual input and supervised the work.

### 4.3 Content

In the course of this publication, a photocatalyst was 3D printed and its activity in photocatalytic water splitting was tested. To produce this catalyst, the precursor, a NH<sub>2</sub>-MIL-125(Ti) metal-organic framework compound with boehmite dispersal, was printed into monolithic structures via DIW. The monoliths thus produced were subsequently calcined in an argon atmosphere. The resulting catalysts, consisting among others of TiO<sub>2</sub>, Al<sub>2</sub>O<sub>3</sub> support and C and N from the MOF, were subsequently thoroughly characterized and tested in their powder form as well as in their monolithic form for the hydrogen evolution reaction from water. Thereby, the shaped bodies with a value of 71 μmol<sub>H<sub>2</sub></sub>·g<sub>cat</sub><sup>-1</sup>·h<sup>-1</sup> showed a fivefold increased performance compared to the respective powder (14 μmol<sub>H<sub>2</sub></sub>·g<sub>cat</sub><sup>-1</sup>·h<sup>-1</sup>). This could be attributed to the improved interaction between incident light and catalyst, as the maximum amount of catalyst is exposed to the incident UV-Vis light. Due to its co-catalytic properties, the monoliths were also loaded with platinum as active component via atomic layer deposition. The uniformly distributed Pt/PtO<sub>x</sub> species in monoliths increased the activity by about 30 % (100.6 μmol<sub>H<sub>2</sub></sub>·g<sub>cat</sub><sup>-1</sup>·h<sup>-1</sup>) compared to the platinum-free samples. In addition, experiments were carried out on the recyclability and structural stability of the catalyst. The platinum-loaded monolith showed the same photocatalytic activity even when repeated five times. Investigations with XRD, SEM and optical light microscopy showed that neither the phases, nor the disc-like inner morphology, nor the outer shape changed. In contrast to the powdered samples, the monoliths could also be separated more easily from the reaction solution, which improved their handling. In general, the proof-of-concept demonstrated the benefits of 3D printed photocatalysts.

## 4.4 Manuscript

## RESEARCH ARTICLE



www.solar-rrl.com

## 3D-Printed Metal–Organic Framework-Derived Composites for Enhanced Photocatalytic Hydrogen Generation

Mian Zahid Hussain,\* Paula F. Großmann, Fabian Kohler, Tim Kratky, Laura Kronthaler, Bart van der Linden, Katia Rodewald, Bernhard Rieger, Roland A. Fischer, and Yongde Xia\*

Direct ink writing technique is used to 3D print Ti-metal–organic framework (MOF) NH<sub>2</sub>-MIL-125 mixed with boehmite dispersal. Pt is also deposited onto 3D-printed monolith using atomic layer deposition (ALD) to offer additional catalytic sites. The Ti-MOF-derived powder sample and the pyrolyzed 3D-printed monolith samples are evaluated for photocatalytic H<sub>2</sub> evolution under UV–vis light. As a proof of concept, herein, it is demonstrated that 3D-printed MOF-derived monolith photocatalysts show five times higher H<sub>2</sub> evolution performance compared with TiO<sub>2</sub>/C powder sample due to better interaction between 3D-printed photocatalysts and the incident light. The high surface area, the formation of hierarchical macro- to nanopores, and the optimizable shape/size of the 3D-printed catalyst maximize the exposure of catalytic active sites to incident photons and increase their photocatalytic H<sub>2</sub> evolution performance. In addition, the N-functionalized porous carbon from organic linker, and the uniformly distributed Pt/PtO<sub>x</sub> species deposited by ALD, provide cocatalytic active sites for photocatalytic reaction and further enhance photocatalytic activity 30% of 3D-printed monoliths. This work on the 3D-printed MOF-derived free-standing monoliths for photocatalytic application provides a readily available approach to further fabricate a variety of 3D-printed MOF-based and derived materials for different energy and environment applications.

## 1. Introduction

One of the biggest challenges to planet Earth is the unprecedented rising of carbon emissions (estimated 410 ppm in 2020), which is the major contributor to environmental pollution and climate change.<sup>[1–3]</sup> Moreover, the increasing energy demand together with the depleting fossil fuel reserves are ringing alarms to find alternative energy resources. To deal with these global challenges, renewable energy resources are widely recognized as the most plausible options. Among numerous different available renewable energy resources, hydrogen (H<sub>2</sub>) generated from water splitting is considered as the most green, cost-effective, and clean energy carrier and fuel.<sup>[4]</sup> It can be directly used for domestic heating, fuel cells, automobiles, and a variety of applications in industry.<sup>[5–7]</sup> Currently, majority of H<sub>2</sub> is produced via the methane steam reforming process which is environmentally unsustainable and economically expensive.<sup>[8,9]</sup> H<sub>2</sub> production via electrocatalytic water splitting has been extensively interesting and widely explored.<sup>[10–12]</sup> As an alternative, solar

M. Z. Hussain, T. Kratky, L. Kronthaler, R. A. Fischer  
School of Natural Sciences and Catalysis Research Center  
Technical University of Munich  
Lichtenbergstr. 4, 85748 Garching, Germany  
E-mail: ge68muq@tum.de

P. F. Großmann, K. Rodewald, B. Rieger  
WACKER-Chair of Macromolecular Chemistry  
School of Natural Sciences, Department of Chemistry and Catalysis  
Research Center  
Technical University of Munich  
Lichtenbergstr. 4, 85748 Garching, Germany

The ORCID identification number(s) for the author(s) of this article can be found under <https://doi.org/10.1002/solr.202200552>.

© 2022 The Authors. Solar RRL published by Wiley-VCH GmbH. This is an open access article under the terms of the Creative Commons Attribution License, which permits use, distribution and reproduction in any medium, provided the original work is properly cited.

DOI: 10.1002/solr.202200552

F. Kohler  
Laboratory for Biomolecular Nanotechnology  
Physics Department  
Technical University of Munich  
Coulombwall 4a, 85748 Garching, Germany

F. Kohler  
Munich Institute of Biomedical Engineering  
Technical University of Munich  
Boltzmannstr. 11, 85748 Garching, Germany

B. van der Linden  
Catalysis Engineering  
Chemical Engineering Department  
Delft University of Technology  
van der Maasweg, 9, 2629 HZ Delft, Netherlands

Y. Xia  
College of Engineering  
Mathematics and Physical Sciences  
University of Exeter  
Exeter EX4 4QF, United Kingdom  
E-mail: y.xia@exeter.ac.uk

light-driven water splitting in the presence of suitable catalysts is a very promising approach to generate green H<sub>2</sub>. However, the bottleneck is the high cost for the use of noble metal catalysts and the lower efficiencies when non-noble metal photocatalysts are used.<sup>[13]</sup>

Despite the availability of plenty of new materials for photocatalytic water splitting, TiO<sub>2</sub> is still one of the most promising photocatalysts due to its nontoxicity, natural abundance, and low cost.<sup>[14,15]</sup> Nevertheless, the wide-bandgap energy (3.2 eV for anatase TiO<sub>2</sub>), the poor visible light absorption, the low specific surface area, the fast surface charge recombination, and the agglomeration of the particles are the major factors to limit their large-scale utilizations as efficient photocatalysts. However, the bandgap energy of TiO<sub>2</sub> can be readily tuned by controlled doping of cationic or anionic species to expand its light absorption capacities of TiO<sub>2</sub> from ultraviolet light into visible light region of the electromagnetic spectrum.<sup>[14,16,17]</sup> For a high-performing photocatalyst, charge recombination should be minimized and the catalytic active sites should be easily accessible for photocatalytic reactions.<sup>[15,18–20]</sup>

Metal–organic frameworks (MOFs) are a class of coordination polymers in which metal ions/clusters and organic linkers connect through coordination bonds to form reticular structures via a self-assembly method.<sup>[21,22]</sup> Usually they exhibit exceptionally high surface areas, tunable porosities, well-defined morphologies, and highly crystalline structures. Among them, Ti-based MOFs, such as NH<sub>2</sub>-MIL-125(Ti), are chemically stable under ambient conditions and have demonstrated their potential to be functioning as photocatalysts.<sup>[23–26]</sup> Nonetheless, the limited electric charge generation and the poor charge transfer mechanisms make such systems less favorable to be directly employed as photocatalysts.<sup>[27,28]</sup> However, in the past few years, MOFs have been demonstrated to be ideal sacrificial templates and precursors to derive multifunctional and tunable nanocomposites, where self-doped metal or metal compound (oxide, sulfide, carbide, or phosphide, etc.) nanoparticles are embedded in (multi)functionalized porous carbon structures. Ti-MOF-derived TiO<sub>2</sub>/C composites usually offer better catalytic performance compared to conventional TiO<sub>2</sub> due to the self-doped nonmetal species from organic linkers.<sup>[29–33]</sup> Such composite systems inherit high specific surface areas, tunable pores, and easily accessible catalytic active sites.

Despite the great advancement in this field, both conventional metal oxides and MOF-derived metal oxide photocatalysts are usually available in the form of powder.<sup>[5,31,34]</sup> From the application of catalysts in the industrial-scale point of view, practically, it is expensive and difficult to work with powder-based photocatalysts. Moreover, in a photoreactor, not all the powder dispersion is equally exposed to the incident solar light due to the limitations of the reactor design.<sup>[35]</sup> Therefore, the development of novel hybrid materials with optimal photocatalytic properties and practical designs is of utmost importance to obtain easy-to-handle high-performing photocatalysts. Additive manufactured catalysts such as 3D-printed MOFs based and/or derived materials can be an excellent approach to fabricate free-standing and customized catalytic materials for high performance.<sup>[36,37]</sup> Direct ink writing (DIW) technique (also called robocasting) is a readily available process which can be used to 3D print MOF-containing paste.<sup>[38,39]</sup> As a proof of concept, our study on 3D-printed Ti-MOF-derived photocatalysts for H<sub>2</sub> evolution from water splitting is presented in this work. It is demonstrated that under

UV–vis light, H<sub>2</sub> evolution performance of 3D-printed Ti-MOF-derived monolith is five times higher than that of photocatalysts in the form of powder. Moreover, loading of Pt on 3D-printed monoliths via atomic layer deposition provides additional catalytic active sites, which further enhance H<sub>2</sub> evolution performance up to 30%. It is important to note that increasing the MOF content in the 3D-printed monolith precursor can create more catalytic active sites. Furthermore, diffusion limitations (mass transport and/or heat transfer) in H<sub>2</sub> evolution reaction can be minimized by optimizing the shape/size of the printed monoliths. Optimally these parameters can efficiently enhance the interaction between incident light and catalytic active sites to maximize the photocatalytic activity.<sup>[40]</sup> In contrast to powder catalysts, using shaped catalysts allows conveniently switching from (semi-)batch setups to continuous flow reaction processes. In addition, optimal pyrolysis conditions of 3D-printed MOF-derived photocatalysts also play a very crucial role in determining their photocatalytic performance for H<sub>2</sub> production. To the best of our knowledge, this is the first ever study on 3D-printed boehmite/Ti-MOF derived free-standing monoliths for photocatalytic application. This approach can be easily expanded to fabricate a variety of 3D-printed MOF-based or derived materials for energy and environment applications.

## 2. Results and Discussion

The boehmite/MOF monoliths were 3D printed by a DIW method. The grid-like structures of boehmite and boehmite/Ti-MOF with a target diameter of 10 mm and seven layers with each layer height of 0.4 mm were printed by extruding the paste through a thin nozzle (diameter 0.51 mm). The extruded paste is shear thinning, enabling a constant flow through the nozzle when pressure is applied as well as stable structures after the extrusion. As shown in Figure S1a–d, Supporting Information, after drying, the grid-like structures have an overall diameter of 9 mm and a total height of 2.7 mm. The average diameter of the extruded strand is 0.5 mm and the strand length in the printed monolithic structures is ≈61 mm. Compared with the targeted dimensions, only 90% of the overall diameter and 96% of the overall height are present after drying. Upon pyrolysis of these boehmite/Ti-MOF grids at 750 °C for 2 h under Ar atmosphere, a further small but uniform shrinkage in all dimensions was observed (Figure S1e–f, Supporting Information) due to the evaporation of organic species during the pyrolysis process. The precursor material such as boehmite was transformed into γ-Al<sub>2</sub>O<sub>3</sub>, whereas the Ti-MOF NH<sub>2</sub>-MIL-125 was transformed into TiO<sub>2</sub>/C, respectively,<sup>[19,29,31,41,42]</sup> which was confirmed by powder X-ray diffraction (PXRD).

As shown in Figure 1a, the overall diameter of the pyrolyzed monolith (Al<sub>2</sub>O<sub>3</sub>/TiO<sub>2</sub>/Pt/C<sub>3DP</sub>) was measured to be 8.4 mm with a strand diameter of 0.42 mm and the strand length of 55 mm, respectively, which suggest that pyrolyzed Al<sub>2</sub>O<sub>3</sub>/TiO<sub>2</sub>/Pt/C<sub>3DP</sub> monolith retains 93% of original overall diameter, 83% of strand diameter, and 90% of strand length of its 3D-printed boehmite/Ti-MOF monolith precursor. Moreover, the overall height of the pyrolyzed monolith is 2.5 mm, which accounts for 90% overall height of its precursor. In general, compared with the as-printed boehmite/Ti-MOF monoliths,

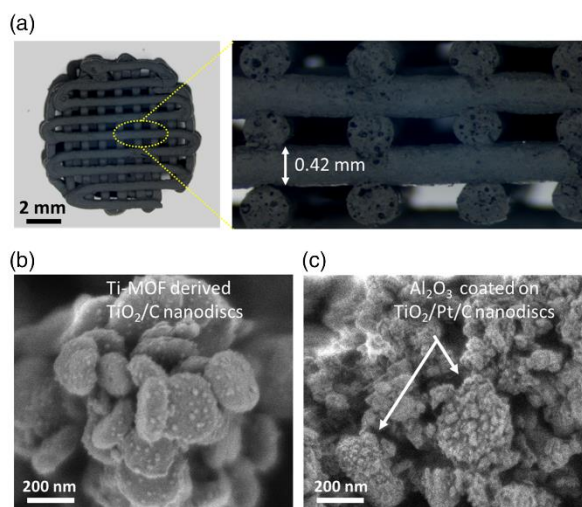


**Figure 1.** a) Optical image of pyrolyzed 3D-printed  $\text{Al}_2\text{O}_3/\text{TiO}_2/\text{Pt}/\text{C}_{3\text{DP}}$  monolith. Right-hand enlarged image is the cross-sectional view of the monolith. SEM images of b) Ti-MOF-derived  $\text{TiO}_2/\text{C}$  and c) Pt-deposited boehmite/Ti-MOF-derived  $\text{Al}_2\text{O}_3/\text{TiO}_2/\text{Pt}/\text{C}_{3\text{DP}}$ .

10% of volume shrinkage was observed in the pyrolyzed  $\text{Al}_2\text{O}_3/\text{TiO}_2/\text{C}_{3\text{DP}}$  monoliths. However, due to the slow and uniform

shrinkage, the geometrical shape remained intact. As shown in Figure 1a (enlarged region), the individual strands in each printed layer of the pyrolyzed samples are stacked uniformly without showing any structural deformation. The formed macropores can be clearly observed in the pyrolyzed monoliths. The formation of hierarchical pores from micropores to macropores was confirmed by  $\text{N}_2$  gas sorption analysis.

Scanning electron microscopy (SEM) images of the precursor boehmite/Ti-MOF paste are shown in Figure S2, Supporting Information.  $\text{NH}_2\text{-MIL-125}(\text{Ti})$  shows disc-like morphologies with an average diameter of 500 nm (Figure S2a, Supporting Information). In boehmite/Ti-MOF paste (Figure S2b, Supporting Information),  $\text{NH}_2\text{-MIL-125}(\text{Ti})$  is coated with small boehmite particles which are uniformly distributed throughout the sample. After pyrolysis at  $750^\circ\text{C}$  for 2 h under Ar atmosphere, the average crystallite size in the derived powder sample  $\text{TiO}_2/\text{C}_\text{P}$  reduces to  $\approx 300$  nm (Figure 1b).<sup>[29]</sup> The SEM images of the pyrolyzed 3D-printed  $\text{Al}_2\text{O}_3/\text{TiO}_2/\text{C}_{3\text{DP}}$  grids show that the MOF-derived  $\text{TiO}_2/\text{C}$  is uniformly covered with  $\text{Al}_2\text{O}_3$  nanoparticles (Figure 1c).

PXRD patterns of boehmite,  $\text{NH}_2\text{-MIL-125}(\text{Ti})$ , and their mixed paste (Figure S3, Supporting Information) confirm that Ti-MOF is chemically stable after 3D printing. The signature peaks of boehmite and  $\text{NH}_2\text{-MIL-125}(\text{Ti})$  remain intact and can be clearly observed in the boehmite/Ti-MOF paste. As shown in Figure 2a, after pyrolysis at  $750^\circ\text{C}$  in Ar atmosphere, Ti-MOF and boehmite/Ti-MOF-derived sample  $\text{TiO}_2/\text{C}_\text{P}$  and

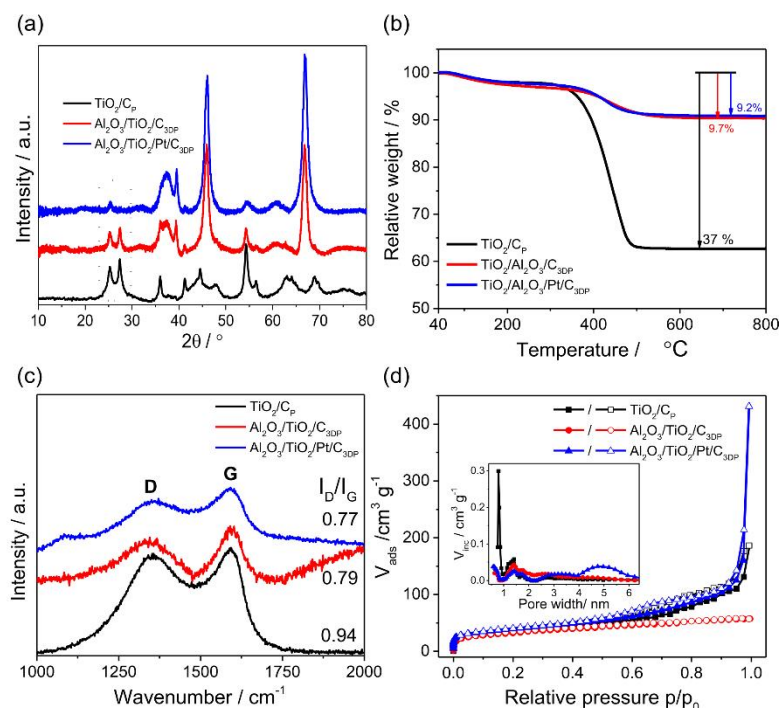


**Figure 2.** a) PXRD patterns, b) TGA curves under synthetic air atmosphere, c) Raman spectra, and d)  $\text{N}_2$  sorption isotherms of Ti-MOF derived  $\text{TiO}_2/\text{C}_\text{P}$  (black) powder and 3D-printed boehmite/Ti-MOF-derived  $\text{Al}_2\text{O}_3/\text{TiO}_2/\text{C}_{3\text{DP}}$  monolith (red) and  $\text{Al}_2\text{O}_3/\text{TiO}_2/\text{Pt}/\text{C}_{3\text{DP}}$  monolith (blue). Inset in d) represents the PSD derived from the adsorption branch of  $\text{N}_2$  sorption isotherms.



$\text{Al}_2\text{O}_3/\text{TiO}_2/\text{C}_{3\text{DP}}$  exhibit the diffraction peak of  $\text{TiO}_2$  at  $2\theta$  of  $25.26^\circ$ , indexed to (101) of anatase, whereas this diffraction peak was shifted to  $25.40^\circ$  in Pt-deposited sample  $\text{Al}_2\text{O}_3/\text{TiO}_2/\text{Pt}/\text{C}_{3\text{DP}}$ . Moreover, the characteristic (110) peak of rutile phase of  $\text{TiO}_2$ , which appeared at around  $2\theta$  of  $27.36^\circ$  in Pt-free samples, almost disappeared in Pt-deposited pyrolyzed sample.<sup>[43,44]</sup> This clearly indicates that the Pt species not only chemically interact with  $\text{TiO}_2$  and  $\text{Al}_2\text{O}_3$  species but also influence their crystalline phases. In sample  $\text{Al}_2\text{O}_3/\text{TiO}_2/\text{C}_{3\text{DP}}$ , the PXRD patterns show signature peaks appearing at  $2\theta$  of  $37.4^\circ$ ,  $39.37^\circ$ ,  $46.0^\circ$ , and  $66.8^\circ$ , which correspond to the (311), (222), (400), and (440) planes of  $\gamma\text{-Al}_2\text{O}_3$  respectively. However, in Pt-deposited samples, two additional peaks were observed at  $2\theta$  of  $36.8^\circ$  and  $39.5^\circ$  which are assigned to (210) of  $\text{PtO}_x$  and (111) of metallic  $\text{Pt}^0$  nanoparticles respectively.<sup>[44–46]</sup> The particle sizes, chemical nature, and oxidation states of the deposited Pt,  $\text{TiO}_2$  and  $\gamma\text{-Al}_2\text{O}_3$  were further confirmed by high resolution transmission electron microscopy (HRTEM), X-ray photoelectron spectroscopy (XPS), and Raman spectroscopy.

When Ti-MOF and boehmite/Ti-MOF precursors are pyrolyzed under Ar atmosphere, it is expected that a significant amount of nitrogen-functionalized porous carbon can be formed due to the decomposition of organic linker  $\text{NH}_2\text{-BDC}$  in the Ti-MOF. Thermogravimetric analysis (TGA) was carried out to quantify the amount of carbon in these pyrolyzed samples. As shown in Figure 2b, Ti-MOF-derived  $\text{TiO}_2/\text{C}_p$  exhibited a relative weight loss of 37 wt% under synthetic air due to the oxidation of carbon and nitrogen species in the form of  $\text{CO}_x$  and  $\text{NO}_x$ , respectively. In samples  $\text{Al}_2\text{O}_3/\text{TiO}_2/\text{C}_{3\text{DP}}$  and  $\text{Al}_2\text{O}_3/\text{TiO}_2/\text{Pt}/\text{C}_{3\text{DP}}$ , the weight loss was observed 9.7 and 9.2 wt% respectively. A small difference of 0.5 wt% in these two (otherwise identical) samples can be due to the presence of Pt in one of the samples. Obviously, the TGA curves of these pyrolyzed samples are

completely different from the TGA curves of their precursor species (as-prepared Ti-MOF, boehmite dispersal, and their mixture) under the same conditions (Figure S4, Supporting Information).

To investigate the nature of Ti-MOF-derived carbon, Raman spectra were recorded. As shown in Figure 2c, D and G bands of graphitic carbon were observed at  $1350$  and  $1590\text{ cm}^{-1}$  respectively in sample  $\text{TiO}_2/\text{C}_p$ . In general, D bands arise from the out-of-plane vibrations therefore correlated to defect or disordered carbon and G bands on the other hand are caused by in-plane vibrations of  $sp^2$ -bonded carbon atoms in hexagonal rings.<sup>[47,48]</sup> The  $I_D/I_G$  ratio in this sample was calculated to be 0.94. However, in 3D-printed boehmite/Ti-MOF-derived sample  $\text{Al}_2\text{O}_3/\text{TiO}_2/\text{C}_{3\text{DP}}$ , the D and G bands were shifted to  $1340$  and  $1593\text{ cm}^{-1}$  respectively with a  $I_D/I_G$  ratio of 0.79. It is interesting to note that in Pt-deposited sample  $\text{Al}_2\text{O}_3/\text{TiO}_2/\text{Pt}/\text{C}_{3\text{DP}}$ , the D and G band values were shifted to  $1357$  and  $1589\text{ cm}^{-1}$  respectively and  $I_D/I_G$  was calculated to be 0.77. The higher  $I_D/I_G$  value indicates the formation of defects in graphitic carbon. A relatively higher  $I_D/I_G$  value in sample  $\text{TiO}_2/\text{C}_p$  is due to the presence of higher N species in porous carbon.<sup>[14,16,18,42,49,50]</sup> However, in 3D-printed boehmite/Ti-MOF-derived  $\text{Al}_2\text{O}_3/\text{TiO}_2/\text{C}_{3\text{DP}}$  and  $\text{Al}_2\text{O}_3/\text{TiO}_2/\text{Pt}/\text{C}_{3\text{DP}}$  samples, the relatively lower  $I_D/I_G$  value can be attributed to the lower amount of N species on carbon. This is likely as less heat can be transferred into the carbon due to the presence of  $\text{Al}_2\text{O}_3$  on the carbon, which results in less surface defects in such carbon.<sup>[29,47,49]</sup>

The Brunauer–Emmett–Teller (BET) surface area and pore size distribution (PSD) of the 3D-printed boehmite/Ti-MOF (precursors) and their derived composites were recorded. As shown in Figure S5, Supporting Information, the specific surface areas (SSAs) of activated Ti-MOF, boehmite, and boehmite/Ti-MOF are  $1460$ ,  $98.4$ , and  $363\text{ m}^2\text{ g}^{-1}$  respectively. It can be clearly seen

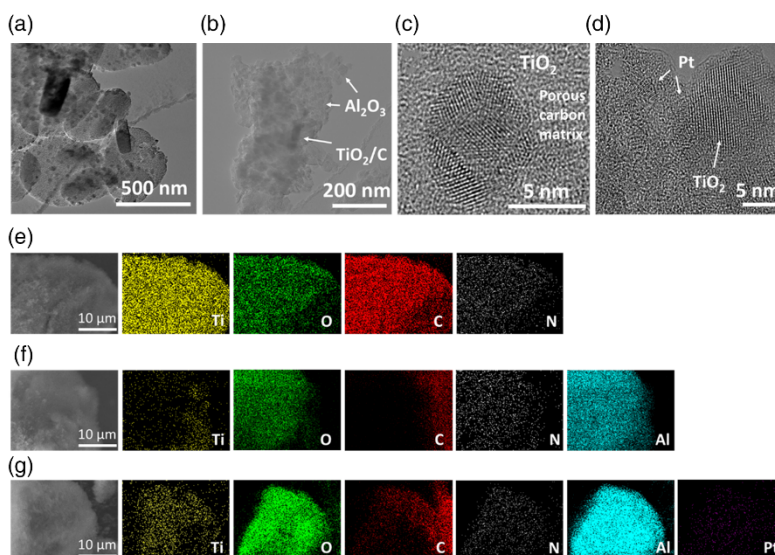


**Figure 3.** TEM images of a)  $\text{TiO}_2/\text{C}_p$  and b)  $\text{Al}_2\text{O}_3/\text{TiO}_2/\text{C}_{3\text{DP}}$ . HRTEM images of c)  $\text{Al}_2\text{O}_3/\text{TiO}_2/\text{C}_{3\text{DP}}$  and d)  $\text{Al}_2\text{O}_3/\text{TiO}_2/\text{Pt}/\text{C}_{3\text{DP}}$ . EDX elemental mappings of e)  $\text{TiO}_2/\text{C}_p$ , f)  $\text{Al}_2\text{O}_3/\text{TiO}_2/\text{C}_{3\text{DP}}$ , and g)  $\text{Al}_2\text{O}_3/\text{TiO}_2/\text{Pt}/\text{C}_{3\text{DP}}$ . Color codes for each element are Ti: yellow; O: green; C: red; N: grey; Al: cyan; and Pt: magenta.

that in boehmite/MOF paste, due to the presence of 30 wt% of Ti-MOF, this printed monolith has higher amount of micropores with pore diameter of 0.7 nm that originates from the pure MOF. Moreover, a small amount of relatively larger pores of 1.4 nm are also presented in both samples. In 3D-printed derived pyrolyzed samples (Figure 2d), the SSAs were recorded to be 180, 115, and 140 m<sup>2</sup> g<sup>-1</sup> for samples TiO<sub>2</sub>/C<sub>p</sub>, Al<sub>2</sub>O<sub>3</sub>/TiO<sub>2</sub>/C<sub>3DP</sub>, and Al<sub>2</sub>O<sub>3</sub>/TiO<sub>2</sub>/Pt/C<sub>3DP</sub> respectively. A relatively higher specific surface area of Pt-deposited sample may be due to the fact that the presence of Pt benefits to create additional mesopores (as shown in the PSD of the inset in Figure 2d), which offers additional surface area and resultingly provides more catalytic active sites.

Figure 3a shows the transmission electron microscopy (TEM) image of NH<sub>2</sub>-MIL-125(Ti)-derived TiO<sub>2</sub>/C<sub>p</sub>. The TiO<sub>2</sub> nanoparticles are distributed in a porous carbon matrix, inheriting a disc-like morphology of the Ti-MOF precursor that can also be seen in the SEM images. When mixed with boehmite paste, NH<sub>2</sub>-MIL-125(Ti) was homogeneously distributed within the paste. After pyrolyzing the 3D-printed monoliths, the derived TiO<sub>2</sub>/C was enveloped by  $\gamma$ -Al<sub>2</sub>O<sub>3</sub> nanoparticles (Figure 3b). High-resolution TEM images confirm that the Ti-oxo clusters are transformed into crystalline TiO<sub>2</sub> nanoparticles. The crystalline phase of TiO<sub>2</sub> is determined by the pyrolysis temperature as well as the surrounding chemical environment.<sup>[19,42]</sup> In Figure 3c, a polyhedral TiO<sub>2</sub> nanoparticle exhibiting different crystalline phases embedded in a porous carbon matrix can be clearly observed. The lattice spacing of the different phases is averaged to be 0.227 and 0.202 nm, attributed to (101) and (200) planes respectively. In sample TiO<sub>2</sub>/Al<sub>2</sub>O<sub>3</sub>/Pt/C<sub>3DP</sub> (Figure 3d), individual Pt nanoparticles with size around 1.5 nm located next to a larger TiO<sub>2</sub> nanoparticle are clearly seen. The lattice spacing between planes of TiO<sub>2</sub> is measured to be 0.328 nm, corresponding to (101) plane of anatase phase. Compared with the major lattice spacing of pure anatase (0.352 nm) and pure rutile (0.243 nm), the differences in lattice spacing of these MOF-derived TiO<sub>2</sub> nanoparticles are caused by the in situ-doped N and C derived from the organic linker (NH<sub>2</sub>-BDC) of precursor NH<sub>2</sub>-MIL-125(Ti).<sup>[29,42]</sup> This was further confirmed by XPS.

Energy dispersive X-ray analysis (EDX) elemental analysis was also carried out to evaluate the distribution of atomic species. As shown in Figure 3e, in Ti-MOF-derived powder sample TiO<sub>2</sub>/C<sub>p</sub>, elements including Ti, O, C, and N are homogeneously distributed throughout the sample. It is interesting to observe that in 3D-printed samples such as Al<sub>2</sub>O<sub>3</sub>/TiO<sub>2</sub>/C<sub>3DP</sub> (Figure 3f), all elements including Al are uniformly distributed with content determined by their relative weight percentages in the sample. In Pt-coated 3D-printed sample Al<sub>2</sub>O<sub>3</sub>/TiO<sub>2</sub>/Pt/C<sub>3DP</sub>, a small amount of Pt can also be observed in Figure 3g.

XPS spectra were recorded to investigate the chemical states of the atomic species in 3D-printed precursors (Figure S6, Supporting Information) and the pyrolyzed monoliths (Figure 4). The XPS peaks of Ti 2*p* confirm that Ti<sup>4+</sup> oxidation state are present in all these samples. It is interesting to note that in the 3D-printed boehmite/MOF paste, after loading Pt, the Ti 2*p* peaks remain unchanged (Figure S6a, Supporting Information), indicating that Ti-MOF is very stable. In pyrolyzed Ti-MOF-derived TiO<sub>2</sub>/C<sub>p</sub> powder, the Ti 2*p* peaks show higher intensities (Figure 4a), whereas in pyrolyzed 3D-printed

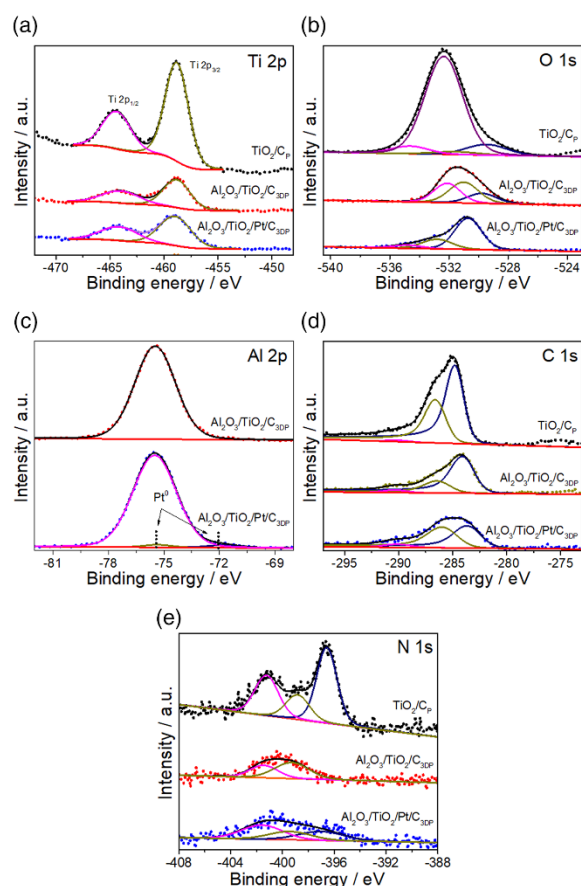


**Figure 4.** XPS spectra of a) Ti 2*p*, b) O 1*s*, c) Al 2*p*, d) C 1*s*, and e) N 1*s* of the pyrolyzed samples TiO<sub>2</sub>/C<sub>p</sub>, Al<sub>2</sub>O<sub>3</sub>/TiO<sub>2</sub>/C<sub>3DP</sub>, and Al<sub>2</sub>O<sub>3</sub>/TiO<sub>2</sub>/Pt/C<sub>3DP</sub>.

Al<sub>2</sub>O<sub>3</sub>/TiO<sub>2</sub>/C<sub>3DP</sub> monoliths, relatively lower intensity of the Ti 2*p* peaks is the reason that TiO<sub>2</sub> nanoparticles are covered with alumina particles.<sup>[29,42]</sup> The deconvoluted O 1*s* peaks in Ti-MOF precursor (Figure S6b, Supporting Information) are observed at 532.6, 530.5, and 534.8 eV, which are attributed to Ti(IV)-O bond in Ti-oxo cluster and -OH/-COOH group respectively.<sup>[23]</sup> However, after deposition of Pt, an obvious shift in binding energies is observed. In this sample, the strongest deconvoluted O 1*s* peak is observed at around 532.5 eV, along with the other peaks at 530.1 and 534.7 eV. The change in relative intensity of the deconvoluted O 1*s* peaks clearly indicates that the deposited Pt chemically interacts with O species, forming either Pt-O-like bonds and/or other surface defects.<sup>[45,46]</sup> In Ti-MOF-derived sample TiO<sub>2</sub>/C<sub>p</sub>, the main O 1*s* peak (Figure 4b) appearing at 532.4 eV is the signature peak of lattice O in TiO<sub>2</sub>. The other two peaks observed at 529.3 and 534.7 eV can be assigned to surface-attached -OH and -COOH functional groups. However, in the presence of alumina in sample Al<sub>2</sub>O<sub>3</sub>/TiO<sub>2</sub>/C<sub>3DP</sub>, the O 1*s* peaks are shifted to the binding energies of 529.7, 531.03, and

532.18 eV respectively.<sup>[17,18,51]</sup> The presence of Disperal-60, Pural-SB, and acetic acid and a small amount of hydroxypropylmethylcellulose in boehmite/MOF paste precursor contribute to the multiple oxygen species, which upon high-temperature pyrolysis may remain as residues in the form of oxygen-based functional groups, exhibiting higher intensity of  $-OH/-COOH$  species compared with the sample  $TiO_2/C_p$ . In Pt-deposited sample  $Al_2O_3/TiO_2/Pt/C_{3DP}$ , the relative intensity of the deconvoluted O 1s peaks is changed and the peak positions are shifted to 530.7, 532.8, and 535.2 eV respectively. It clearly indicates that the deposited Pt particles chemically interact strongly with the O species.<sup>[46,52]</sup>

The oxidation states of the deposited Pt on Ti-MOF precursor were determined by XPS spectra. As shown in Figure S6c, Supporting Information, two main peaks of Pt  $4f_{7/2}$  and Pt  $4f_{5/2}$  appearing at 69.5 and 72.86 eV respectively represent  $Pt^0$  species, deposited on the Ti-MOF.<sup>[45,52]</sup> Two small peaks were also observed at 71.6 and 74.9 eV, which can be assigned to Pt  $4f_{7/2}$  and Pt  $4f_{5/2}$  of  $Pt^{4+}$  species.<sup>[53,54]</sup> However, in 3D-printed MOF-derived composite  $Al_2O_3/TiO_2/C_{3DP}$ , the binding energy of Al and Pt overlaps and lies in the same region as the signature peak of Al  $2p$  is observed at 75.5 eV. In Pt-deposited sample  $Al_2O_3/TiO_2/Pt/C_{3DP}$ , Al  $2p$  peak remains unchanged (Figure 4c). However two additional low intensity peaks can be observed at around 71.9 and 75.5 eV, suggesting the presence of  $Pt^0$  species. It is expected that upon pyrolysis of 3D-printed boehmite/Ti-MOF(Pt) monolith, most of the Pt migrates to  $TiO_2$  at high temperatures and are entrapped only partially in  $Al_2O_3$  but mostly in  $TiO_2$ ,<sup>[55]</sup> which is also confirmed by HRTEM and EDX elemental mappings. The presence of Pt in(to)/around  $TiO_2$  was further confirmed by Raman spectra. As shown in Figure S7, Supporting Information, the main vibrational mode  $E_g(1)$  of  $TiO_2$  (anatase) appeared at  $154\text{ cm}^{-1}$ . A blueshift in  $E_g(1)$  compared with pure  $TiO_2$  ( $144\text{ cm}^{-1}$ ) is due to the localized doping of N and C atoms from organic linkers of MOF into  $TiO_2$ .<sup>[55]</sup> The peak appeared at  $427\text{ cm}^{-1}$  is assigned to the  $E_g$  vibrational mode of rutile  $TiO_2$ . In Pt-deposited sample, a small shoulder peak and two new low intensity peaks at around  $856.6$  and  $1082.3\text{ cm}^{-1}$  were observed, which can be attributed to the vibrational modes of metallic  $Pt^0$  and  $PtO_x$  species.<sup>[44,55]</sup>

As shown in Figure 4d, the XPS binding energy peak of  $sp^2$ -bonded C=C was observed at 284.8 eV in sample  $TiO_2/C_p$ . Two other low-intensity peaks appeared at 286.6 and 290.4 eV that can be assigned to C-O and O-C=O bonds.<sup>[42]</sup> In 3D-printed boehmite/MOF-derived sample  $Al_2O_3/TiO_2/C_{3DP}$ , these peaks show a negligible shift indicating that the presence of  $Al_2O_3$  does not change the nature of MOF-derived carbon. However, in Pt-deposited sample, the  $sp^2$  C=C peak was shifted to 283.7 eV, and the C-O peak at 286.0 eV was more prominent, which clearly suggests that the deposited Pt atoms are chemically bonded, forming Pt-C and Pt-O like bonds and consequently creating additional surface defects.<sup>[47,52,56]</sup>

The deconvoluted N 1s XPS peaks in precursor Ti-MOF and Pt-deposited Ti-MOF are shown in Figure S8, Supporting Information. The main peak that appeared at 399.3 eV is attributed to the Ti-NH<sub>2</sub> bonds. In Pt-deposited sample, this peak is suppressed and a stronger peak is observed at 396.8 eV, clearly indicating that the Pt atoms attract the electrons from the lone

pair of NH<sub>2</sub>, forming Pt-N bonds.<sup>[53]</sup> In sample  $TiO_2/C_p$  derived from Ti-MOF (NH<sub>2</sub>-MIL-125), N 1s spectra (Figure 4e) were deconvoluted into three peaks. The main peak appeared at 396.0 eV can be assigned to Ti-N bonds. The other two low-intensity peaks at 398.9 and 401.3 eV represent pyridinic N and quaternary pyrrolic N atoms in porous carbon matrix derived from organic linker NH<sub>2</sub>-BDC in Ti-MOF.<sup>[29,42]</sup> It is interesting to observe that in 3D-printed boehmite/MOF-derived samples  $Al_2O_3/TiO_2/C_{3DP}$ , no peak at 396.0 eV is observed. This may be due to the fact that the surface of MOF-derived  $TiO_2$  nanoparticles is encapsulated by a large amount of  $Al_2O_3$ , which makes XPS difficult to detect these bonds since XPS is basically a surface technique which normally detects only the surface or near surface of the samples. However, in Pt-deposited 3D-printed sample, this peak appeared at 396.9 eV. The appearance of this peak (in the presence of  $\gamma$ - $Al_2O_3$ ) with a shift to higher binding energy compared with  $TiO_2/C_p$  sample (396.0 eV) confirms that the Pt atoms do form Pt-N bonds with  $-NH_2$  functional groups in Ti-MOF by attracting more electrons due to their high positive charge.<sup>[57-59]</sup>

The optical properties of the as-synthesized 3D-printed monoliths were recorded by UV-vis absorption spectra. The absorption band of Ti-MOF (NH<sub>2</sub>-MIL-125) appeared at 491 nm.<sup>[23,27]</sup> In Pt-deposited NH<sub>2</sub>-MIL-125 sample, the absorption band was redshifted to 517 nm (Figure S9, Supporting Information), which clearly indicates that the absorption of visible light is improved due to the Pt atoms deposited via ALD being chemically coordinated with the  $-NH_2$  functional groups.<sup>[53]</sup> Upon pyrolysis of 3D-printed samples, boehmite/Ti-MOF is transformed into  $Al_2O_3$ ,  $TiO_2$ , and carbon composite. The UV-vis absorption spectra (Figure 5a) and bandgap energy of the pyrolyzed composites from Tauc plots (Figure 5b) are calculated to be 2.6, 3.0, and 2.9 eV for samples  $TiO_2/C_p$ ,  $Al_2O_3/TiO_2/C_{3DP}$ , and  $Al_2O_3/TiO_2/Pt/C_{3DP}$  respectively. The bandgap energy of the pristine  $\gamma$ - $Al_2O_3$  is estimated to be 3.8 eV.

The photocatalytic performance of the Ti-MOF derived and 3D-printed boehmite/Ti-MOF-derived samples for photocatalytic hydrogen (H<sub>2</sub>) evolution by water splitting under UV-vis light was tested. A 285 nm cutoff filter was used, and methanol was added as hole scavenger. As shown in Figure 6a, the photocatalytic H<sub>2</sub> evolution performance of Ti-MOF-derived powder sample  $TiO_2/C_p$  and 3D-printed samples  $Al_2O_3/TiO_2/C_{3DP}$  and  $Al_2O_3/TiO_2/Pt/C_{3DP}$  all increases with reaction time

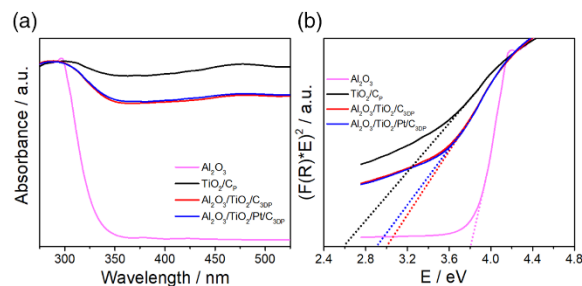


**Figure 5.** a) UV-vis absorption spectra and b) Tauc plots of pristine  $\gamma$ - $Al_2O_3$ , Ti-MOF-derived  $TiO_2/C_p$ , and 3D-printed boehmite/Ti-MOF-derived  $Al_2O_3/TiO_2/C_{3DP}$  and  $Al_2O_3/TiO_2/Pt/C_{3DP}$ .

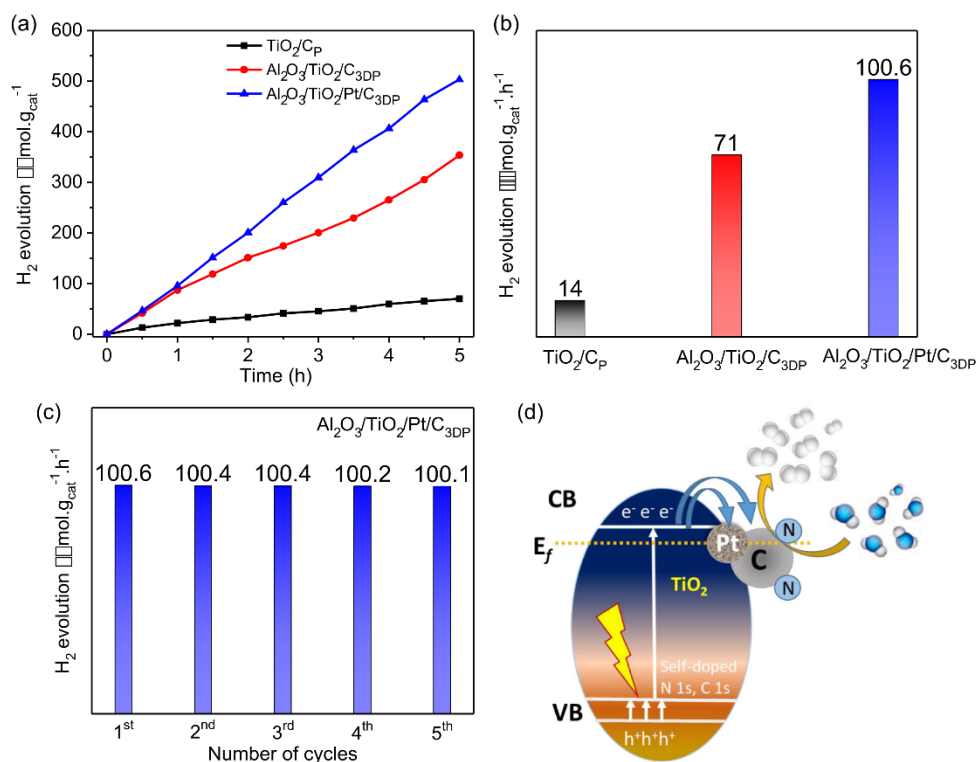


**Figure 6.** a) Photocatalytic H<sub>2</sub> evolution under UV–vis light for 5 h. b) Photocatalytic activity of TiO<sub>2</sub>/C<sub>p</sub> (black), Al<sub>2</sub>O<sub>3</sub>/TiO<sub>2</sub>/C<sub>3DP</sub> (red), and Al<sub>2</sub>O<sub>3</sub>/TiO<sub>2</sub>/Pt/C<sub>3DP</sub> (blue). c) The recyclability of best-performing sample Al<sub>2</sub>O<sub>3</sub>/TiO<sub>2</sub>/Pt/C<sub>3DP</sub>. d) Schematics illustration of the proposed band structure of active photocatalyst in sample Al<sub>2</sub>O<sub>3</sub>/TiO<sub>2</sub>/Pt/C<sub>3DP</sub>. Here, Al<sub>2</sub>O<sub>3</sub> only acts as a support material.

exposure to UV–vis light, and their photocatalytic activities are 70, 354, and 503 μmol.g<sub>cat</sub><sup>-1</sup> respectively after 5 h reaction. In conventional MOF-derived TiO<sub>2</sub>/C<sub>p</sub> sample, the powder catalyst is dispersed throughout the whole reactor, whereas the diameter of the window of incident light is 2.27 cm<sup>2</sup>. Therefore, not all the dispersed catalysts in a traditional reactor configuration are exposed to the photons of the incident light at the same time, which makes it difficult to precisely determine the actual photocatalytic activity of the catalyst.<sup>[35]</sup> A significant increase in the photocatalytic activity of the 3D-printed samples compared with TiO<sub>2</sub>/C<sub>p</sub> powder is due to the fact that the 3D-printed catalyst provides a better and much improved incident light exposure to the photoactive N/C-doped TiO<sub>2</sub> nanoparticles which are uniformly distributed throughout the printed monolith. Actually, all the catalysts in printed monoliths are exposed to the incident light at the same time. As a result, an improved photocatalytic activity is expected. As shown in Figure 6b, samples TiO<sub>2</sub>/C<sub>p</sub> and 3D-printed pyrolyzed monoliths of Al<sub>2</sub>O<sub>3</sub>/TiO<sub>2</sub>/C<sub>3DP</sub> and Al<sub>2</sub>O<sub>3</sub>/TiO<sub>2</sub>/Pt/C<sub>3DP</sub> demonstrated H<sub>2</sub> evolution performance of 14, 71, and 101 μmol.g<sub>cat</sub><sup>-1</sup>.h<sup>-1</sup> respectively. The highest photocatalytic activity of Pt deposited 3D-printed pyrolyzed monoliths can be attributed to various factors including the N/C doped TiO<sub>2</sub>, functionalized porous carbon, and the presence of Pt and PtO<sub>x</sub> nanoparticles which provide additional active sites.<sup>[45,46,56]</sup> In these derived samples, photocatalytically active

species are N/C-doped TiO<sub>2</sub> nanoparticles and Pt/PtO<sub>x</sub> species. A detailed mechanism of photocatalytic H<sub>2</sub> evolution under UV–vis light is discussed in our recently published studies.<sup>[19,42,50]</sup> As mentioned earlier, this study is a proof of the concept that 3D-printed monoliths can provide a novel method to improve the photocatalytic performance of the materials.

Briefly, when UV–vis light is irradiated and hit on the TiO<sub>2</sub>-based catalyst, electrons and holes are generated in anatase and rutile phases of TiO<sub>2</sub> nanoparticles. Since the bandgap energy of γ-Al<sub>2</sub>O<sub>3</sub> is very large, and the derived TiO<sub>2</sub> nanoparticles are embedded inside a porous carbon matrix derived from organic linker, therefore, it is less likely that a heterojunction is formed between TiO<sub>2</sub> and Al<sub>2</sub>O<sub>3</sub>. However, the presence of γ-Al<sub>2</sub>O<sub>3</sub> as a support material may help to suppress the charge recombination which results in improvement of the photocatalytic activity of these composite materials. The self-doping of C and N species from organic linker (NH<sub>2</sub>-BDC) into TiO<sub>2</sub> during pyrolysis at high temperature in our recent studies<sup>[19,42]</sup> as well as Pt as a cocatalyst in this study primarily contributes to the enhanced photocatalytic activity. The photogenerated electrons (e<sup>-</sup>) in anatase and rutile TiO<sub>2</sub> jump to their respective conduction bands, leaving the holes (h<sup>+</sup>) behind in the valence bands. Due to the type-II staggered energy bands (band off-set of 0.4 eV) between anatase and rutile phases of TiO<sub>2</sub>, photogenerated electrons migrate to the conduction band of the anatase

phase while the holes migrate to the valence band of the rutile phase. This accumulation of holes and electrons in different phases reduces the charge recombination, which resultingly enhances the photocatalytic activity compared with pure anatase and/or rutile TiO<sub>2</sub>.<sup>[15,51,60]</sup> As confirmed by PXRD, Raman, and XPS spectra, in Ti-MOF-derived N/C-doped TiO<sub>2</sub>/C<sub>P</sub> and pyrolyzed 3D-printed boehmite/Ti-MOF derived monolith Al<sub>2</sub>O<sub>3</sub>/TiO<sub>2</sub>/C<sub>3DP</sub>, anatase and rutile phases coexist, forming a phase junction.<sup>[42,43]</sup> In these samples, the photogenerated electrons migrate from the conduction band of rutile phase to the conduction band of anatase phase, whereas the photogenerated holes migrate from the valence band of anatase to the rutile phase. Due to the presence of nitrogen-functionalized porous carbon matrix (9.7 wt%) from organic linker (NH<sub>2</sub>-BDC) of Ti-MOF, these photoelectrons also migrate to this carbon, resulting in the minimization of the charge recombination.<sup>[50]</sup> The photocatalytic reduction reaction takes place at the electron-rich conduction band of anatase phase, which acts as an active site for half reaction, reducing the water molecules into H<sub>2</sub>, while the other half reaction of oxidation (in the presence of MeOH) is accommodated by the photogenerated holes in the valence band of rutile phase.<sup>[16,20,51]</sup> However, in Pt-deposited 3D-printed pyrolyzed monolith Al<sub>2</sub>O<sub>3</sub>/TO<sub>2</sub>/Pt/C<sub>3DP</sub>, only anatase phase is observed by PXRD.<sup>[43,45,52,55]</sup> This may be due to the deposition of heavy Pt atoms into Ti-MOF, and the phase transformation from anatase to rutile does not take place at 750 °C.<sup>[43]</sup> Although only anatase phase of TiO<sub>2</sub> is present in 3D-printed pyrolyzed Al<sub>2</sub>O<sub>3</sub>/TiO<sub>2</sub>/Pt/C<sub>3DP</sub>, the uniformly distributed Pt/PtO<sub>x</sub> species (calculated to be 0.55 wt% via TGA) provide additional cocatalytic active sites for photocatalytic H<sub>2</sub> evolution reaction. Synergistically, other parameters including high BET surface area, N-functionalized porous carbon, and the presence of γ-Al<sub>2</sub>O<sub>3</sub> enable the enhanced accessibility to the photocatalytic active sites; consequently, the printed samples Al<sub>2</sub>O<sub>3</sub>/TO<sub>2</sub>/C<sub>3DP</sub> and Al<sub>2</sub>O<sub>3</sub>/TO<sub>2</sub>/Pt/C<sub>3DP</sub> monoliths display much improved photocatalytic performance in H<sub>2</sub> evolution than TiO<sub>2</sub>/C<sub>P</sub> powder.

The recyclability and the structural stability of the best-performing sample Al<sub>2</sub>O<sub>3</sub>/TiO<sub>2</sub>/Pt/C<sub>3DP</sub> was also evaluated. As shown in Figure 6c, the photocatalytic H<sub>2</sub> activity almost remains stable and unchanged after five successive photocatalytic performance cycles, each of 5 h. Throughout the reaction process, the structure and morphology of the catalysts also remain unchanged. XRD patterns of the used catalysts Al<sub>2</sub>O<sub>3</sub>/TiO<sub>2</sub>/C<sub>3DP</sub> and Al<sub>2</sub>O<sub>3</sub>/TiO<sub>2</sub>/Pt/C<sub>3DP</sub> are the same as that of catalysts prior to the reaction (Figure S10, Supporting Information). Moreover, the optical image (Figure S11a, Supporting Information) confirms that the mechanical stability of the photocatalysts is not sacrificed in water/methanol solution and the overall geometry of the monolith is largely stable. The SEM image (Figure S11b, Supporting Information) further confirms that the disc-like morphology of Ti-MOF-derived photocatalyst embedded in Al<sub>2</sub>O<sub>3</sub> is still preserved after the reaction. The benefits of these 3D-printed photocatalysts may offer that the separation of the catalyst from the leftover reaction solution is very easy and no trivial separation processes with excess solvents are needed. Furthermore, by changing from powdery to shaped catalyst, these 3D-printed MOF derivatives offer freedom of customizing the microstructure of the printed monoliths to be fitted to the designed reactor-specific shapes. In addition, the

potential change of the use of 3D-printed catalysts from batch or semi-batch setup to continuous flow processes is another advantage. All these suggest that 3D-printed photocatalysts can offer a practical available solution to improve the catalytic performance as well as scaling up of the use of catalyst. For MOF-derived photocatalysts, the catalytic activity can be further improved by optimizing the synthesis parameters such as better shape and size of the printed monoliths (to overcome diffusion limitations that might negatively influence the reaction), controlling over the pyrolysis temperature and tuning gaseous atmosphere. Moreover, increasing and optimizing the content of MOFs in the boehmite/MOF paste precursor to maximize the amount of active catalyst in 3D-printed monoliths can also significantly improve the photocatalytic performance.

### 3. Conclusion

Ti-MOF NH<sub>2</sub>-MIL-125, mixed with boehmite dispersal, was 3D printed by DIW technique followed by Pt deposition using atomic layer deposition. The 3D-printed monoliths were pyrolyzed at 750 °C under Ar atmosphere and the resulting 3D-printed samples were evaluated for photocatalytic H<sub>2</sub> evolution under UV-vis light. As a proof of concept, this study demonstrates that the 3D-printed photocatalytic monoliths exhibit 5 times higher H<sub>2</sub> evolution performance compared with the powder samples due to the better interaction between incident light and the printed catalyst as a maximum amount of catalyst can be exposed to the incident photons. Moreover, the uniformly distributed Pt/PtO<sub>x</sub> species, deposited by ALD, provide additional cocatalytic active sites to improve 30% of the H<sub>2</sub> evolution activities compared with Pt-free 3D-printed monoliths. Additionally, N-functionalized porous carbon, high BET surface area, and the presence of porous Al<sub>2</sub>O<sub>3</sub> synergistically enhance the accessibility to the photocatalytic active sites. Consequently, the 3D-printed samples Al<sub>2</sub>O<sub>3</sub>/TO<sub>2</sub>/C<sub>3DP</sub> and Al<sub>2</sub>O<sub>3</sub>/TO<sub>2</sub>/Pt/C<sub>3DP</sub> monoliths display much improved photocatalytic performance in H<sub>2</sub> evolution than TiO<sub>2</sub>/C<sub>P</sub> powder.

### 4. Experimental Section

**Synthesis of NH<sub>2</sub>-MIL-125(Ti) Powder.** To scale up the synthesis of Ti-MOF, NH<sub>2</sub>-MIL-125, 6.875 g (38 mmol) of 2-aminoterephthalic acid (NH<sub>2</sub>-BDC) was dissolved in 100 mL of dimethylformamide (DMF) and 25 mL methanol (MeOH) mixed solvent. Then, 9.01 mL (26.5 mmol) Ti(OBu)<sub>4</sub> was slowly added, followed by the addition of 0.5 mL water, and constantly stirred in an oil bath at 120 °C for 42 h. Yellow colored precipitates were collected by centrifugation. To remove the organic ligand species, the precipitate was washed twice with DMF and then several times with MeOH for solvent exchange. The obtained NH<sub>2</sub>-MIL-125(Ti) was dried in air at 70 °C overnight.

**Preparation of Boehmite/Ti-MOF Paste and 3D Printing.** Following a published procedure,<sup>[38]</sup> boehmite paste with Disperal-60 and Pural-SB (Sasol Germany GmbH) in a mass ratio of 2.3:1 were mixed with acetic acid (pH = 3, Sigma-Aldrich) to obtain a paste with the solid content of 65 wt%. For the preparation of a mixed paste containing Ti-MOF, the boehmites Disperal-60 and Pural-SB (in the same mass ratio as mentioned before) were mixed with the dried NH<sub>2</sub>-MIL-125(Ti) powder in an overall mass ratio of 1.6:0.7:1. The liquid share in the paste was 45 wt%, consisting of acetic acid (pH = 3) and 1 wt%

hydroxypropylmethylcellulose solution in water (Methocel 311, Dow Wolff Cellulosis) in a mass ratio of 1:1.2.

For the DIW printing, a self-constructed printer was used, where the paste was filled in a 2 mL syringe and extruded through a nozzle with a diameter of 0.51 mm. The shapes of 3D-printed monoliths had an overall infill of 40% and a targeted layer height of 0.4 mm. The printed structures were dried overnight on the print bed prior to pyrolysis at high temperatures.

**Atomic Layer Deposition (ALD) of Pt:** The deposition of Pt on the as-printed boehmite/Ti-MOF monoliths was realized via a commercially available ALD reactor (Savannah S200, UltraTech). Approximately, 50 mg of the pristine MOF powder or 3D-printed boehmite/Ti-MOF monolith was loaded into a standard powder sample holder and held at 150 °C for 2 h to adapt to the process temperature. Argon (Ar) was used as carrier and process gas to introduce the Pt precursor species (5 sccm) and for purging steps (20 sccm of Ar gas). Trimethyl (methylcyclopentadienyl)platinum (IV) ( $\text{Me}_3\text{PtCpMe}$ ) inside an ALD precursor cylinder was heated to 75 °C prior to the loading experiment. The ALD process was performed at 150 °C with a standard pulse sequence of  $t_1-t_2-t_3$ , where precursor pulse time  $t_1$  was 0.015 s, exposure time  $t_2$  was 300 s, and Ar purge time  $t_3$  was 180 s and repeated 50 times. After Pt deposition into the Ti-MOF powder or 3D-printed monoliths, the deposited samples were further purged for several hours to ensure the removal of excess  $\text{Me}_3\text{PtCpMe}$  or any other side products.

**Pyrolysis of 3D-Printed Monoliths:** The Ti-MOF and the 3D-printed boehmite/Ti-MOF-derived composites were synthesized by one-step direct pyrolysis of respective samples at 750 °C under Ar atmosphere. For that, precursor materials were loaded in an alumina boat and placed in the center of a tube furnace. The heating rate and dwell time of the furnace were set to 5 °C  $\text{min}^{-1}$  and 2 h, respectively. Prior to the pyrolysis, the quartz tube was purged with Ar gas for 60 min to remove oxygen. The pyrolyzed samples were named as  $\text{TiO}_2/\text{C}_P$ ,  $\text{Al}_2\text{O}_3/\text{TiO}_2/\text{C}_{3DP}$ , and  $\text{Al}_2\text{O}_3/\text{TiO}_2/\text{Pt}/\text{C}_{3DP}$ . (Here, P stands for powder sample, while 3DP refers to 3D-printed sample.)

**Material Characterizations:** PXRD patterns of precursor and their derived composites were performed by Rigaku Miniflex. The microscopic images were taken with a MZ8 from Leica that was equipped with a MicroCam II (Bresser). Analysis of the respective images was carried out using ImageJ software. The morphologies of the samples were determined by the images taken by JEOL JSM-7500F field-emission scanning electron microscope coupled with EDX INCA System (software) with 50 mm<sup>2</sup> X-MAX detector from Oxford Instruments. For TEM, samples were applied to glow-discharged C-Flat 1.2/1.3 4C grids (Protochips). Micrographs were acquired at room temperature on a 300 kV Titan Krios electron microscope equipped with a Falcon 3 detector (Thermo Scientific) and a Cs corrector (CEOS). TGA measurements of as-prepared samples, prior to pyrolyzation, were carried out on a TGA Q5000 from TA Instruments under synthetic air with a heating ramp of 10 °C  $\text{min}^{-1}$ . TGA of derived composites was measured using Mettler Toledo TGA/STA 409 PC apparatus under synthetic airflow with a heating ramp of 10 °C  $\text{min}^{-1}$ . Raman spectra were recorded by Renishaw inVia Reflex Raman System RL532C, Class 3B. The surface chemical analysis was obtained by Kratos Axis Ultra DLD spectrometer with a monochromated Al K $\alpha$  X-ray source operating at 168 W (12 mA  $\times$  14 kV). To calculate the bandgap energies of the nanocomposites, UV-vis absorption spectra were recorded by ThermoScientific Evolution 200 spectrophotometer. For the measurement of BET surface area and the pore PSDs from the  $\text{N}_2$  sorption at 77 K, Quantachrome autosorb iQ2 ASIQwin equipped with a micropore port ( $1 \times 10^{-5}$  bar) was employed. Before the  $\text{N}_2$  gas sorption analysis, all the samples were degassed for 6 h at 150 °C under vacuum. The PSD of all the samples was calculated from the adsorption branch using nonlocal density functional theory (NLDFT) method.

Photocatalytic hydrogen ( $\text{H}_2$ ) evolution reactions were performed in a custom-made Pyrex-glass reactor under 500 W Xe/Hg lamp (66 983, Newport). To analyze the evolved gases in headspace, a gas chromatograph (CP 9001, Chrompack), a KSLA gas pump, and the light source were employed. The photocatalytic reactor consisting of a total volume of 42.1 mL (17.1 mL headspace, 2 mL dilution volume) was equipped with a water jacket to precisely control the temperature. In the experiment,

either Ti-MOF-derived powder or 3D-printed monoliths were suspended in the photocatalytic reactor with 7.5 mL  $\text{CH}_3\text{OH}$  and 17.5 mL  $\text{H}_2\text{O}$ . The reactor was purged by Ar gas (30 mL  $\text{min}^{-1}$ ) for 30 min to completely deoxygenate the system prior to the reaction and the reactor temperature was set at 30 °C. After complete deoxygenation of the reactor, the UV-vis light illumination was applied, and the reaction products were analyzed by means of the gas chromatography analysis.

## Supporting Information

Supporting Information is available from the Wiley Online Library or from the author.

## Acknowledgements

M.Z.H. and P.F.G. contributed equally to this work. The authors gratefully acknowledge TUM Innovation Network Artificial Intelligence in Material Science (ARTEMIS), Bayerische Forschungsstiftung (BFS), and Royal Society (IEC\NSFC\201121) for financial support.

## Conflict of Interest

The authors declare no conflict of interest.

## Data Availability Statement

Research data are not shared.

## Keywords

hydrogen generation, metal-organic frameworks, photocatalysis,  $\text{TiO}_2$ , 3D printing

Received: June 20, 2022

Revised: July 17, 2022

Published online:

- [1] W. Gao, S. Liang, R. Wang, Q. Jiang, Y. Zhang, Q. Zheng, B. Xie, C. Y. Toe, X. Zhu, J. Wang, L. Huang, Y. Gao, Z. Wang, C. Jo, Q. Wang, L. Wang, Y. Liu, B. Louis, J. Scott, A.-C. Roger, R. Amal, H. He, S.-E. Park, *Chem. Soc. Rev.* **2020**, *49*, 8584.
- [2] R. N. E. Huaman, T. X. Jun, *Renewable Sustainable Energy Rev.* **2014**, *31*, 368.
- [3] S. Sun, H. Sun, P. T. Williams, C. Wu, *Sustainable Energy Fuels* **2021**, *5*, 4546.
- [4] R. D. Tentu, S. Basu, *Curr. Opin. Electrochem.* **2017**, *5*, 56.
- [5] S. Cao, L. Piao, X. Chen, *Trends Chem.* **2020**, *2*, 57.
- [6] L. Yuan, C. Han, M.-Q. Yang, Y.-J. Xu, *Int. Rev. Phys. Chem.* **2016**, *35*, 1.
- [7] I. P. Jain, *Int. J. Hydrogen Energy* **2009**, *34*, 7368.
- [8] L. Barelli, G. Bidini, F. Gallorini, S. Servili, *Energy* **2008**, *33*, 554.
- [9] M. Kayfeci, A. Keçebaş, M. Bayat, in *Solar Hydrogen Production* (Eds: F. Calise, M. D. D'Accadia, M. Santarelli, A. Lanzini, D. Ferrero), Academic Press, United Kingdom **2019**, p. 45.
- [10] Z. Huang, Z. Yang, Q. Jia, N. Wang, Y. Zhu, Y. Xia, *Nanoscale* **2022**, *14*, 4726.
- [11] X. Zhang, Z. Chen, Y. Luo, X. Han, Q. Jiang, T. Zhou, H. Yang, J. Hu, *J. Hazard. Mater.* **2021**, *405*, 124128.
- [12] Z. Huang, Z. Yang, M. Z. Hussain, B. Chen, Q. Jia, Y. Zhu, Y. Xia, *Electrochim. Acta* **2020**, *330*, 135335.
- [13] J. Low, J. Yu, M. Jaroniec, S. Wageh, A. A. Al-Ghamdi, *Adv. Mater.* **2017**, *29*, 1601694.

- [14] C. Di Valentin, E. Finazzi, G. Pacchioni, A. Selloni, S. Livraghi, M. C. Paganini, E. Giamello, *Chem. Phys.* **2007**, 339, 44.
- [15] N. Rahimi, R. A. Pax, E. M. Gray, *Prog. Solid State Chem.* **2016**, 44, 86.
- [16] X. Chen, C. Burda, *J. Am. Chem. Soc.* **2008**, 130, 5018.
- [17] S. G. Kumar, L. G. Devi, *J. Phys. Chem. A* **2011**, 115, 13211.
- [18] R. Asahi, T. Morikawa, T. Ohwaki, K. Aoki, Y. Taga, *Science* **2001**, 293, 269.
- [19] M. Z. Hussain, B. van der Linden, Z. Yang, Q. Jia, H. Chang, R. A. Fischer, F. Kapteijn, Y. Zhu, Y. Xia, *J. Mater. Chem. A* **2021**, 9, 4103.
- [20] D. O. Scanlon, C. W. Dunnill, J. Buckeridge, S. A. Shevlin, A. J. Logsdail, S. M. Woodley, C. R. A. Catlow, M. J. Powell, R. G. Palgrave, I. P. Parkin, G. W. Watson, T. W. Keal, P. Sherwood, A. Walsh, A. A. Sokol, *Nat. Mater.* **2013**, 12, 798.
- [21] H. Li, M. Eddaoudi, M. O'Keeffe, O. M. Yaghi, *Nature* **1999**, 402, 276.
- [22] H. Zhou, J. R. Long, O. M. Yaghi, *Chem. Rev.* **2012**, 112, 673.
- [23] P. Karthik, A. R. M. Shaheer, A. Vinu, B. Neppolian, *Small* **2020**, 16, 1902990.
- [24] F. Song, W. Li, Y. Sun, *Inorganics* **2017**, 5, 40.
- [25] H. L. Nguyen, *Sol. RRL* **2021**, 5, 2100198.
- [26] K. Meyer, M. Ranocchiari, J. A. van Bokhoven, *Energy Environ. Sci.* **2015**, 8, 1923.
- [27] M. A. Nasalevich, M. van der Veen, F. Kapteijn, J. Gascon, *CrystEngComm* **2014**, 16, 4919.
- [28] H. Luo, Z. Zeng, G. Zeng, C. Zhang, R. Xiao, D. Huang, C. Lai, M. Cheng, W. Wang, W. Xiong, Y. Yang, L. Qin, C. Zhou, H. Wang, Y. Zhou, S. Tian, *Chem. Eng. J.* **2020**, 383, 123196.
- [29] M. Z. Hussain, M. Bahri, W. R. Heinz, Q. Jia, O. Ersen, T. Kratky, R. A. Fischer, Y. Zhu, Y. Xia, *Microporous Mesoporous Mater.* **2021**, 316, 110957.
- [30] S. V. Dummert, H. Saini, M. Z. Hussain, K. Yadava, K. Jayaramulu, A. Casini, R. A. Fischer, *Chem. Soc. Rev.* **2022**, 51, 5175.
- [31] M. Z. Hussain, Z. Yang, Z. Huang, Q. Jia, Y. Zhu, Y. Xia, *Adv. Sci.* **2021**, 8, 2100625.
- [32] W. Xia, A. Mahmood, R. Zou, Q. Xu, *Energy Environ. Sci.* **2015**, 8, 1837.
- [33] L. Oar-Arteta, T. Wezendonk, X. Sun, F. Kapteijn, J. Gascon, *Mater. Chem. Front.* **2017**, 1, 1709.
- [34] Z. Huang, Z. Yang, M. Z. Hussain, Q. Jia, Y. Zhu, Y. Xia, *J. Mater. Sci. Technol.* **2021**, 84, 76.
- [35] N. Serpone, A. V. Emeline, V. K. Ryabchuk, V. N. Kuznetsov, Y. M. Artem'ev, S. Horikoshi, *ACS Energy Lett.* **2016**, 1, 931.
- [36] C.-Y. Lee, A. C. Taylor, A. Nattestad, S. Beirne, G. G. Wallace, *Joule* **2019**, 3, 1835.
- [37] B. Yao, S. Chandrasekaran, J. Zhang, W. Xiao, F. Qian, C. Zhu, E. B. Duoss, C. M. Spadaccini, M. A. Worsley, Y. Li, *Joule* **2019**, 3, 459.
- [38] T. Ludwig, J. von Seckendorff, C. Troll, R. Fischer, M. Tonigold, B. Rieger, O. Hinrichsen, *Chem. Ing. Tech.* **2018**, 90, 703.
- [39] Z. Lyu, G. J. H. Lim, R. Guo, Z. Kou, T. Wang, C. Guan, J. Ding, W. Chen, J. Wang, *Adv. Func. Mater.* **2019**, 29, 1806658.
- [40] B. Kraushaar-Czarnetzki, S. Peter Müller, in *Synthesis of Solid Catalysts* (Eds: K. P. de Jong), Wiley-VCH Verlag, Weinheim, Germany **2009**, p. 173.
- [41] Y. Chen, O. Ola, G. Liu, L. Han, M. Z. Hussain, K. Thummavichai, J. Wen, L. Zhang, N. Wang, Y. Xia, Y. Zhu, *J. Eur. Ceram. Soc.* **2021**, 41, 3970.
- [42] M. Z. Hussain, Z. Yang, B. V. D. Linden, Z. Huang, Q. Jia, E. Cerrato, R. A. Fischer, F. Kapteijn, Y. Zhu, Y. Xia, *J. Energy Chem.* **2021**, 57, 485.
- [43] M. Bouslama, M. C. Amamra, Z. Jia, M. Ben Amar, K. Chhor, O. Brinza, M. Abderrabba, J. L. Vignes, A. Kanaev, *ACS Catal.* **2012**, 2, 1884.
- [44] T. Huizinga, J. Van Grondelle, R. Prins, *Appl. Catal.* **1984**, 10, 199.
- [45] J. Yu, L. Qi, M. Jaroniec, *J. Phys. Chem. C* **2010**, 114, 13118.
- [46] Y. Zhang, H. Hu, X. Huang, Y. Bi, *J. Mater. Chem. A* **2019**, 7, 5938.
- [47] A. C. Ferrari, J. Robertson, *Phys. Rev. B* **2000**, 61, 14095.
- [48] A. Y. Lee, K. Yang, N. D. Anh, C. Park, S. M. Lee, T. G. Lee, M. S. Jeong, *Appl. Surf. Sci.* **2021**, 536, 147990.
- [49] B. N. Bhadra, A. Vinu, C. Serre, S. H. Jung, *Mater. Today* **2019**, 25, 88.
- [50] M. Z. Hussain, Z. Yang, A. M. E. Khalil, S. Hussain, S. U. Awan, Q. Jia, R. A. Fischer, Y. Zhu, Y. Xia, *J. Mater. Sci. Technol.* **2022**, 101, 49.
- [51] J. Schneider, M. Matsuoka, M. Takeuchi, J. Zhang, Y. Horiuchi, M. Anpo, D. W. Bahnemann, *Chem. Rev.* **2014**, 114, 9919.
- [52] P. Wang, S. Zhan, Y. Xia, S. Ma, Q. Zhou, Y. Li, *Appl. Catal., B* **2017**, 207, 335.
- [53] Y. Zhong, R. Wang, X. Wang, Z. Lin, G. Jiang, M. Yang, D. Xu, *Front. Chem.* **2020**, 8, 660.
- [54] J. Wang, A. S. Cherevan, C. Hannecart, S. Naghdi, S. P. Nandan, T. Gupta, D. Eder, *Appl. Catal., B* **2021**, 283, 119626.
- [55] L. Chen, L. Kovarik, J. Szanyi, *ACS Catal.* **2021**, 11, 12058.
- [56] Q. Xiang, J. Yu, M. Jaroniec, *Nanoscale* **2011**, 3, 3670.
- [57] Y. Hu, Y. Qu, Y. Zhou, Z. Wang, H. Wang, B. Yang, Z. Yu, Y. Wu, *Chem. Eng. J.* **2021**, 412, 128749.
- [58] H. Sun, R. Ullah, S. Chong, H. M. Ang, M. O. Tadé, S. Wang, *Appl. Catal., B* **2011**, 108–109, 127.
- [59] Q. Shi, C. Zhu, M. H. Engelhard, D. Du, Y. Lin, *RSC Adv.* **2017**, 7, 6303.
- [60] R. Su, R. Bechstein, L. Sø, R. T. Vang, M. Sillassen, B. Esbjörnsson, A. Palmqvist, F. Besenbacher, *J. Phys. Chem. C* **2011**, 115, 24287.

## 5 Influence of internal and external surface area on impregnation and activity of 3D printed catalyst carriers

### 5.1 Bibliographic data

Title: "Influence of internal and external surface area on impregnation and activity of 3D printed catalyst carriers"

Status: Research Article, Published online: January 13, 2023

Journal: *Catalysis Communications* **2023**, 175, 106610

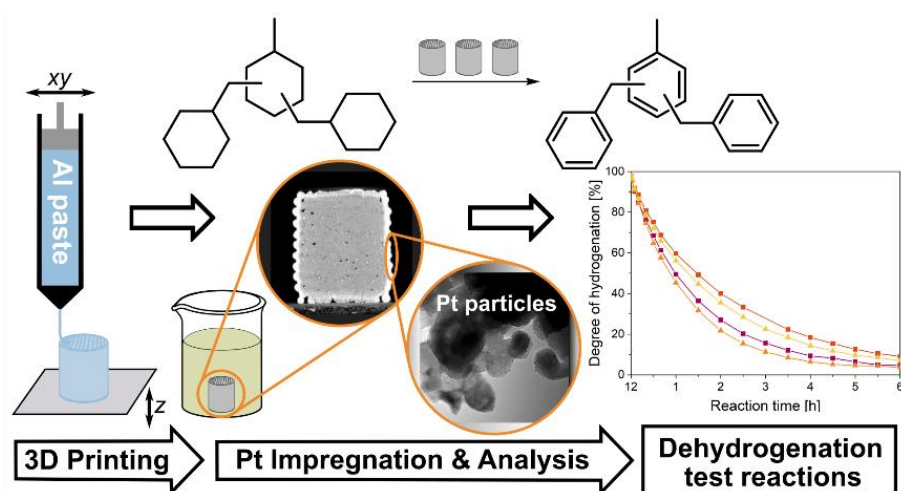
Publisher: Elsevier

DOI: 10.1016/j.catcom.2023.106610

Authors: Paula F. Großmann, Markus Tonigold, Normen Szesni, Richard W. Fischer, Alexander Seidel, Klaus Achterhold, Franz Pfeiffer, Bernhard Rieger<sup>\*.b</sup>

Reference: [296]

### 5.2 Abstract graphic (TOC)



\* Corresponding author.

<sup>b</sup> P. F. Großmann executed the 3D printing, impregnation, analyzation, carried out the test reactions and wrote most parts of the manuscript. M. Tonigold, N. Szesni, R. W. Fischer provided valuable intellectual input and project supervision. A. Seidel gave valuable input regarding the dehydrogenation test reactions and their evaluation. K. Achterhold performed and analyzed all  $\mu$ CT data. F. Pfeiffer and B. Rieger contributed with valuable intellectual input and supervised the work.



### 5.3 Content

When using additive manufacturing as a shaping technique for carriers in heterogeneous catalysis, not only the shaping itself is important, but also the loading of the support material with (metal) active components following 3D printing. In this context, the characteristics of the impregnation such as penetration depth, metal particle dispersion or loading are important factors influencing the subsequent reaction. Since the impregnation of 3D printed support materials has been little studied in previous literature, this work investigated the influence of the outer geometric and inner (BET) surface on the impregnation of catalyst carriers. For this purpose, two different alumina supports, namely cylindrical and monolithic structures with lateral holes, were fabricated using DIW. The monoliths exhibited a surface-to-volume ratio about five times greater than the corresponding cylinders. Two different calcination temperatures were chosen which resulted in substrates with two different microstructures. Calcination at 1000 °C led to a bimodal pore distribution and a surface area of 55 m<sup>2</sup>·g<sup>-1</sup>, while a calcination temperature of 1100 °C resulted in a monomodal pore distribution and reduced surface area of 22 m<sup>2</sup>·g<sup>-1</sup> due to sintering of the smaller pores. After wet impregnation with platinum sulfite acid solution, optical light microscopy showed that at higher loading (0.9 wt.% versus 0.3 wt.%) and reduced surface-to-volume ratio, the Pt penetrates more into the shaped body. This behavior could also be confirmed by  $\mu$ CT scans, where the platinum concentration, corresponding to the mean gray value, decreases with penetration depth. Due to the increased porosity and BET surface area, the samples at 1000 °C also showed a lower penetration depth compared to the higher calcined samples. The catalysts were then studied in the dehydrogenation of perhydro-dibenzyltoluene in a semi-batch reactor at a constant Pt/reactant ratio. To rule out diffusion limitations of the catalysts per se powder measurements were carried out first, followed by full-particle measurements. In the full particle measurements, the monolithic structures always showed higher productivity than the analogously produced cylinders, since the former had a significantly larger outer surface area as well as lower Pt penetration. Conversely, shapes with higher loading exhibited lower activity at constant Pt/reactant ratio, due to lower outer surface area and deeper Pt penetration. With same loading and shape, the carriers calcined at 1100 °C showed higher productivity because perhydro-dibenzyltoluene is relatively large as a reactant molecule and, accordingly, can penetrate poorly into the small pores present at 1000 °C. When highly loaded monoliths were compared with low-loaded cylinders, the latter show comparable productivity based on platinum. However, the monoliths occupied only one-third of the catalyst volume. This clearly showed that the combination of 3D printing and catalysis is advantageous, as expensive active components, reactor volume or reaction time can be saved with comparable productivities. In addition, further insights into the impregnation behavior of the 3D-printed catalyst supports were gained, in particular through the  $\mu$ CT scans, which provide knowledge for further investigations.

## 5.4 Manuscript

Catalysis Communications 175 (2023) 106610



Contents lists available at ScienceDirect

Catalysis Communications

journal homepage: [www.elsevier.com/locate/catcom](http://www.elsevier.com/locate/catcom)

## Influence of internal and external surface area on impregnation and activity of 3D printed catalyst carriers

Paula F. Großmann<sup>a</sup>, Markus Tonigold<sup>b</sup>, Normen Szesni<sup>b</sup>, Richard W. Fischer<sup>b</sup>, Alexander Seidel<sup>c</sup>, Klaus Achterhold<sup>d</sup>, Franz Pfeiffer<sup>d,e</sup>, Bernhard Rieger<sup>a,\*</sup><sup>a</sup> WACKER-Chair of Macromolecular Chemistry, Catalysis Research Center, Department of Chemistry, School of Natural Sciences, Technical University of Munich, Lichtenbergstr. 4, 85748 Garching, Germany<sup>b</sup> Clariant Produkte (Deutschland) GmbH, Waldheimer Str. 13, 83052 Bruckmühl, Germany<sup>c</sup> Hydrogenious Lohc Technologies GmbH, Weidenweg 13, 91058 Erlangen, Germany<sup>d</sup> Chair of Biomedical Physics, Department of Physics, School of Natural Sciences and Munich Institute of Biomedical Engineering, Technical University of Munich, James-Frank-Str. 1, 85748 Garching, Germany<sup>e</sup> Department of Diagnostic and Interventional Radiology, School of Medicine, Klinikum rechts der Isar, Technical University of Munich, Ismaninger Str. 22, 81675 München, Germany

## ARTICLE INFO

## Keywords:

3D printing  
Additive manufacturing  
Direct ink writing  
Impregnation  
Heterogeneous catalysis  
Ceramics  
Liquid organic hydrogen carrier  
Dehydrogenation reaction

## ABSTRACT

Direct ink writing as additive manufacturing technique was used to print two different boehmite based shapes, cylinders and monoliths, serving as catalyst carriers. These were wet impregnated targeting 0.3–0.9 wt% platinum loadings. ICP-OES,  $\mu$ CT and microscopy revealed dependencies from calcination temperature, geometry and platinum loading. Dehydrogenation reactions of perhydro dibenzyltoluene as liquid organic hydrogen carrier were performed examining the catalytic performance. Differences when executing full particle measurements led to the conclusion that direct ink writing as shaping technique for catalyst carriers and the respective impregnation is highly beneficial as more complex shapes can be obtained, resulting in higher activities.

## 1. Introduction

Over the past years, 3D printing or so-called additive manufacturing (AM) gained more and more public interest and inspired researchers to elaborate novel solutions in various application fields such as automotive/aerospace industry, bioprinting, medical/dental application or in arts. [1–5] This wide range of applications is based on the plethora of printable materials ranging from metals and plastics even to ceramics. [1,6] In addition, several AM techniques are conceivable for most processible materials, each of which featuring different advantages and disadvantages. [1] For example, in the field of ceramic 3D printing, the processes binder jetting, fused deposition of ceramics, stereolithography, selective laser sintering, or direct ink writing (DIW, also called robocasting) have proven to be suitable options. [7–11] Amongst others they have also been successfully used for ceramic 3D printing in heterogeneous catalysis, whereat direct ink writing is one of the more

frequently used techniques. [12–16] The printed catalysts were shown to be active in different catalytic processes e.g. Tubío et al. printed monolithic Cu/Al<sub>2</sub>O<sub>3</sub> structures for successful use in Ulman reactions [17], Stuecker et al. compared wash-coated printed alumina monoliths and directly printed material to commercial (wash-coated) monolithic structures for the combustion of methane [18], Middelkoop et al. investigated the activity of directly printed Ni/Al<sub>2</sub>O<sub>3</sub> monolithic structures for the CO<sub>2</sub> methanation reaction [19], and Xu et al. reported printed Al<sub>2</sub>O<sub>3</sub> tubes with Pd immobilized in the porous inner Al<sub>2</sub>O<sub>3</sub> ceramic to be used as continuous flow reactor for the reduction of 4-nitrophenol [20]. Compared to conventional shaping techniques such as tableting, granulation or extrusion, 3D printing offers access to tailor-made geometries as well as more complex shapes including e.g. lateral channels. The geometrical shape of a catalyst it influences important process parameters such as pressure drop as well as heat and mass transport within the catalyst bed and is therefore crucial for technical

*Abbreviations:* AM, additive manufacturing; cyl, cylinder; DIW, direct ink writing; ICP-OES, inductively coupled plasma optical emission spectrometry; monol, monolithic structure; TEM, transmission electron microscopy;  $\mu$ CT, micro computed tomography; 18H-DBT, perhydro dibenzyltoluene.

\* Corresponding author.

E-mail address: [rieger@tum.de](mailto:rieger@tum.de) (B. Rieger).

<https://doi.org/10.1016/j.catcom.2023.106610>

Received 24 November 2022; Received in revised form 23 December 2022; Accepted 12 January 2023

Available online 13 January 2023

1566-7367/© 2023 The Authors. Published by Elsevier B.V. This is an open access article under the CC BY-NC-ND license (<http://creativecommons.org/licenses/by-nc-nd/4.0/>).

realization. [10,21–25]

When combining additive manufacturing and heterogeneous catalysis, a distinction must be made between whether a mold is printed and later burned off, the catalytically active material or one of its precursors is printed itself, or a carrier is printed first which is afterwards loaded with the active component. [7,12,26–29] The latter two main approaches are comparable with the existing technical production methods for heterogeneous catalysts, where extrusion, tablet pressing, and granulation are the common shaping processes and either the active component itself or a carrier is used. [25,30,31] One example of unsupported catalysts is the mixture of iron oxide, potassium oxide and alumina for ammonia synthesis [32], whereas platinum (doped with rhenium) on alumina is an industrially applied supported catalyst for reforming. [30,32] Two main techniques are used to impregnate the carrier with the active component: Dry impregnation (incipient wetness impregnation) describes the method in which a quantity of impregnating solution corresponding to the exact pore volume of the support material is applied. However, if the volume of the impregnating solution exceeds the pore volume by a multiple, it is called wet impregnation. [32–35] The oxidic supports contain surface hydroxyl groups which are positively or negatively charged, depending on the pH value of the impregnation solution relative to the point of zero charge, and interact with the dissociated metal salts. [33,36] As-prepared materials are so-called egg-shell catalysts, in which the active component is in the outer layers of the shape. Competitive adsorption with other anions can be used to influence the penetration depth of the metal precursor into the catalyst leading to egg-yolk or egg-white distributions. Hereby, the respective active component is not directly on the surface but further inside the catalyst particle, which prevents catalyst poisoning. [32,33]

One reaction in which platinum catalysts impregnated on alumina are used is the dehydrogenation reaction of perhydro dibenzyltoluene (18H-DBT). [37–39] This reaction has attracted more and more interest in the last years, as it is an integral part for the use of liquid organic hydrogen carriers (LOHC) since its first introduction by Brückner et al. in 2014. [37,40–42] With the help of aromatic or heteroaromatic compounds such as methylcyclohexane, dodecahydro-*N*-ethyl carbazole or perhydro dibenzyltoluene, it is possible to store hydrogen chemically. [42,43] For this purpose, the corresponding materials are hydrogenated at a hydrogen surplus and dehydrogenated at hydrogen demand. For the system 18H-DBT and its corresponding dehydrogenated form 0H-DBT (dibenzyltoluene) a non-toxic compound, a hydrogen storage capacity of 6.2 wt% is reported and thus proving to be well suited. [42] In literature, perhydro dibenzyltoluene dehydrogenation reactions are carried out using e.g. Pt/AlO<sub>x</sub> catalysts such as the egg shell catalysts EleMax-102D or EleMaxD 101 from Clariant which usually are mortared or ball-milled prior to reaction. [44–46] However, also different metals (Pt, Pd, Ru) and carriers (SiO<sub>2</sub>, CeO<sub>2</sub>, C, TiO<sub>2</sub>) have been investigated as catalysts. [41,47,48] As this reaction is highly endothermic, [49] it is therefore, prone to heat and mass transport limitations when performed with commercial shaped catalysts. These could be overcome by using AM as a novel shaping technique that allows tailor-made catalyst shapes for improved flow behavior within the reactor. To the best of our knowledge, so far, no 3D printed catalyst has been investigated in the dehydrogenation reaction of perhydro dibenzyltoluene.

The aim of this work was to investigate the influence of shapes manufactured by the 3D printing technique direct ink writing on catalyst carriers and their subsequent wet impregnation with a platinum precursor. The effect of tailored geometries and thus surface-to-volume ratios, as well as calcination temperatures and target loadings on the impregnation with platinum was examined in detail using BET analysis, light microscopy, TEM and  $\mu$ CT, providing useful insight into the impregnation process. Using the prepared catalysts, the catalytic activity for the dehydrogenation reaction in a semi-batch set-up was investigated.

## 2. Materials and methods

### 2.1. Printing procedure

To produce a printable paste based on boehmite (AlOOH), 45.5 wt% Disperal 60 (Sasol Germany GmbH), 19.5 wt%. Pural SB (Sasol Germany GmbH) and 35 wt% acetic acid (pH = 3, Sigma Aldrich) were mixed twice by means of a SpeedMixer® (Hauschild GmbH & Co. KG) for 2 min at a maximum speed of 3500 rpm with 3 min cooling time after each mixing cycle. The printing itself was carried out with a self-constructed lab-scale DIW printer. For printing of 4 × 4 mm cylinders the nozzle size was 0.41 mm, whereas for printing the monolithic structures with an overall size of 23 × 4 mm and a 4 mm central hole, 0.51 mm nozzles were used. To simplify the removal of the print bed for the bigger shapes, it was covered with a thin layer of Formentrennöl C (Clariant Produkte Deutschland GmbH). The structures were dried on the print bed for 24 h at room temperature prior to thermal post-treatment.

Calcination was carried out in a WiseTherm®FHP-12 (witeg Labortechnik GmbH) muffle furnace with a heating rate of 1 K/min and an 1 h isothermal step at the target temperatures 1000 °C or 1100 °C respectively.

### 2.2. Platinum loading

Wet impregnation of the calcined carriers was performed by adding the desired amount of platinum sulfite acid (Clariant Produkte Deutschland GmbH) to the pre-wetted shapes in bidistilled water. The cylinders were placed directly in the water whereas the monolithic structures were immersed hanging to minimize contact areas. Impregnation was carried out for 3 h before removing excessive solution. A second calcination step was carried out in a WiseTherm®FHP-12 (witeg Labortechnik GmbH) muffle furnace by heating to 60 °C at 1 K/min for 1 h, followed by further temperature increase to 120 °C at a rate of 2 K/min for 3 h. The final temperature of 400 °C was reached with a rate of 2 K/min and held for another 3 h. Consecutive reduction was carried out at 400 °C for 3 h in a tube furnace R50/250/12 (Nabertherm GmbH) under constant flow of forming gas (H<sub>2</sub>/N<sub>2</sub> = 5 / 95, Westfalen GmbH) at a heating rate of 1 K/min.

### 2.3. Catalyst characterization

Size and mechanical stability of printed and calcined shapes were measured using a MultiTest 50 (Dr. Schleuniger Pharmatron). Uniaxial compression tests vertically to the cylinder axis allowed calculation of the side crushing strength  $\sigma_{\text{crush}}$  from the fracture load  $F$ , the cylinder diameter  $d$  and its height  $h$  by using the equation given by Timoshenko and Goodier [50]:

$$\sigma_{\text{crush}} = \frac{2F}{\pi dh} \quad (1)$$

N<sub>2</sub> physisorption measurements were performed on a NOVAtouch analyzer (Quantachrome Instruments) at 77 K. Prior to measurement the samples were degassed under vacuum at 120 °C for 3 h. The specific surface area  $S_{\text{BET}}$  was calculated according to the method of Brunauer, Emmett, and Teller (BET) between  $p/p_0 = 0.05$  and 0.3. According to the method of Barrett, Joyner, Halenda (BJH), the desorption branch of the isotherm was used to determine the pore size distribution.

Powder X-Ray diffraction (XRD) measurements were performed on a PANalytical Empyrean diffractometer (Malvern) using Cu K $\alpha$  radiation with a voltage of 45 kV and a monochromator. The powders were scanned in the range of 5° to 90° (2 $\theta$ ) with a step size of 0.0065°. Obtained data was processed using HighScore Plus.

For infrared spectroscopy (IR) of adsorbed pyridine, the catalyst carrier was pelleted into a thin wafer and heated to 450 °C with a rate of 10 K/min for 1 h activation under vacuum. After cooling down to 150 °C, the apparatus was filled with pyridine until the sample was fully

saturated and equilibrated for 1 h prior to another evacuation for 1 h. Scans were taken using a Nicolet 5700 FT-IR spectrometer after activation and after outgassing.

Detailed images of the catalysts were taken with a MZ8 microscope (Leica) equipped with a MicroCam II (Bresser). To determine the penetration depth of platinum into the cylinders, they were embedded in epoxy resin (EpoFix and TekMek, Struers) and later polished using a Beta Grinder Polisher (Buehler).

Micro-computed tomography ( $\mu$ CT) measurements (v|tome|x s 240, phoenix/GE) were performed to enable non-destructive analysis of the internal structure of printed cylinders as well as their impregnation behavior. The direct tube xs 240 D was operated at 70 kVp and 60  $\mu$ A. To minimize beam hardening artifacts, a 0.5 mm aluminum filter was used for all measurements. The X-ray detector was a DXR-250RT with 200  $\mu$ m  $\times$  200  $\mu$ m pixel size on a 1000  $\times$  1000 pixel matrix of amorphous silicon directly coupled to a CsI scintillator. The distance of the X-ray focus to the detector was 812.0 mm and the focus to object distance was 18.8 mm for all measurements. This results in a magnification of 43.25 and an effective voxel size of the reconstructed volume of 4.62  $\mu$ m. 1600 projections were taken for 360° rotation of the sample. The reconstruction was done with the software xaid (MITOS, Germany).  $\mu$ CT images were processed using Fiji ImageJ.

Even low local concentrations of platinum in a matrix of Al<sub>2</sub>O<sub>3</sub> can very well be visualized by X-ray computed tomography because of the much stronger photo electric absorption of platinum. Fig. 5 shows XY, XZ and YZ slices through  $\mu$ CT scans of impregnated cylinders at different calcination temperatures and different platinum loadings. The diffusion of platinum into a homogeneous Al<sub>2</sub>O<sub>3</sub> matrix follows Fick's second law. The diffusion constant can be determined by fitting the attenuation constant due to the position dependent platinum concentration depending to its nearest distance to the surface of the sample. Due to the many sintered particles within the Al<sub>2</sub>O<sub>3</sub> matrix, this distance cannot be determined by the length of a straight line between the considered voxel and the surface of the sample. Instead, we used the open source software imageJ/Fiji and its macro capabilities for this task. [51] Our macro was inspired by a similar one written by O. Burri [52] and changed for our needs. The wand tracing tool of imageJ and a suitable threshold value served for tracing the sample boarder of 2D slices of the reconstructed 3D volume of each sample. With the freehand lines tool of imageJ a line was drawn between the middle of a sample and its boarder, carefully avoiding to draw through sintered particles. With the plugin "Exact Signed Euclidean Distance Transform (3D)" the shortest distance of each pixel on the freehand line to the tracing line at the boarder was determined and saved along with the grey value of the reconstructed slice at this pixel position.

These data then were fitted with Fick's second law density distribution for platinum plus a constant mean grey value for the Al<sub>2</sub>O<sub>3</sub> matrix. Fitting was done with the module lmfit 0.9.2 in python 3.6.9. Hereby,  $c(x,t)$  is the concentration of platinum in dependence of the distance  $x$  from the outer surface and the time  $t$ .  $N_0$  is the number of particles in an infinitesimal small area  $A$  at  $x,t = 0$ , and  $D$  the diffusion coefficient. Eq. (2), Fick's second law for a diffusion from a boarder into a semi-infinite space, can be transformed to Eq. (3) leading to the fitting parameters  $a$  and  $b$  for the diffusion and the constant background  $c_0$ . [53,54]

$$c(x,t) = \frac{N_0}{A \cdot \sqrt{\pi D t}} \cdot e^{-\frac{x^2}{4Dt}} + c_0 \quad (2)$$

$$c(x,t) = \frac{a}{\sqrt{\pi b}} \cdot e^{-\frac{x^2}{4t}} + c_0 \quad (3)$$

Archimedes buoyancy method by means of a Jolly balance was used to determine bulk densities  $\rho_{\text{bulk}}$ , apparent solid densities  $\rho_{\text{app}}$  and porosities  $\phi$  for cylinders and monoliths according to the DIN EN623–2 standard. [55] Three different masses of each sample were determined: the mass of the dry sample  $m_{\text{dry}}$ , the mass of the completely impregnated

sample  $m_{\text{damp}}$ , and the mass when suspended in water  $m_{\text{suspended}}$ . With the density of water  $\rho_{\text{water}}$  the following calculations were performed [55,56]:

$$\rho_{\text{bulk}} = \frac{m_{\text{dry}}}{m_{\text{damp}} - m_{\text{suspended}}} \cdot \rho_{\text{water}} \quad (4)$$

$$\rho_{\text{app}} = \frac{m_{\text{dry}}}{m_{\text{dry}} - m_{\text{suspended}}} \cdot \rho_{\text{water}} \quad (5)$$

$$\phi = \frac{m_{\text{damp}} - m_{\text{dry}}}{m_{\text{damp}} - m_{\text{suspended}}} \quad (6)$$

Inductively coupled plasma optical emission spectrometry (ICP-OES) was carried out on an Agilent 700 Series ICP Optical Emission Spectrometer to determine the amount of platinum on the impregnated shapes. Therefore, the respective catalysts were grounded and dissolved in aqua regia (hydrochloric acid: nitric acid (both Sigma Aldrich) = 3:1 vol%/vol%). The samples were diluted with bidistilled water and filtered via 0.45  $\mu$ m PTFE syringe filters (VWR). For preparation of the metal standards, several concentrations ranging from 1 ppm to 50 ppm were prepared using a platinum AAS standard (Sigma Aldrich). For concentration determinations the wavelength 214.42 nm was used.

Metal particle size as well as dispersion were examined by means of transmission electron microscopy (TEM). Grounded samples were suspended in absolute ethanol (Sigma Aldrich), dropped on Holey Multi A grids (Quantifoil Micro Tools GmbH) and dried. The measurements were performed on a JEOL JEM 1400 plus instrument at an acceleration voltage of 120 kV. Using the software Fiji ImageJ, the metal particle diameter  $d_{\text{Pt}}$  was determined manually by measuring at least 300 particles each. Based on  $d_{\text{Pt}}$  the metal dispersion  $D_{\text{Pt}}$  can be calculated as following: [57].

$$D_{\text{Pt}} = K \cdot \frac{V_{\text{Pt}}}{S_{\text{Pt}} \cdot d_{\text{Pt}}} \quad (7)$$

with the constant  $K$  reflecting the particle shape ( $K = 6$  for spherical particles),  $V_{\text{Pt}}$  the volume per metal atom and  $S_{\text{Pt}}$  the average surface area of metal particles per metal atom.

#### 2.4. Catalytic test reactions

Dehydrogenation test reactions were carried out semi-batch-wise in a 100 mL flask equipped with two flow breakers and a thermocouple. The required amount of the reactant perhydro dibenzyltoluene (18H-DBT; Hydrogenious LOHC Technologies GmbH) was stirred and heated up to 325 °C under argon atmosphere using a heating mantle (Winkler AG). After reaching the set temperature the catalyst ( $n_{\text{Pt}}/n_{18\text{H-DBT}} = 0.175 \text{ mmol}_{\text{Pt}}/\text{mol}_{18\text{H-DBT}}$ ) was added to the reactant and the temperature was reduced to the reaction temperature of 310 °C. The higher starting temperature was chosen to counterbalance the strong temperature drop at the start of the reaction caused by the strong endothermicity of the dehydrogenation. The mass of the catalyst with 0.9 wt % loading was only 1/3 of the catalyst's mass with a loading of 0.3 wt%, while the fine tuning of the Pt to reactant ratio was carried out adjusting the reactant amount. For full particle test reactions, the cylinders and monoliths were placed in a wire cage or on a wire (V4A stainless steel) as catalyst holder, respectively. Intrinsic test reactions with catalyst powder were carried out by adding the ground catalyst powder to the reactant. Sieving of the samples was not performed to ensure that the entire sample was used and to avoid sieving out alumina or Pt, which would then affect the concentration of active species in the reaction. The reaction was monitored for 6 h using proton nuclear magnetic resonance spectroscopy (<sup>1</sup>H NMR) in acetone-*d*<sub>6</sub> carried out using a Bruker Ascend spectrometer at 400 MHz (300K). All spectra are referred to the solvent residual signal and chemical shifts are given in  $\delta$ -values (ppm). Based on the <sup>1</sup>H NMR data, the degree of hydrogenation (DH) was calculated according to Do et al. [35] and Preuster [58] with the ratio  $x$  of the

integral of the aromatic protons (7.5–6.6 ppm) to the integral of all protons (7.5–6.6 ppm, 4.8–3.6 ppm, 2.6–2.1 ppm, and 2.0–0.4 ppm):

$$DH = 1.3945x^6 - 4.9037x^5 + 5.6287x^4 - 5.207x^3 + 4.0098x^2 - 2.9217x + 1 \quad (8)$$

For better comparison of the dehydrogenation activity, the productivity  $P$  is defined as the ratio of the mass of hydrogen  $m_{H_2}$  evolved per mass Pt  $m_{Pt}$  and time [59,60]:

$$P = \frac{m_{H_2}}{m_{Pt} \cdot t} = \frac{\Delta DH \cdot m_{18H-DBT} \cdot \frac{M_{H_2}}{M_{18H-DBT}} \cdot \frac{\nu_{H_2}}{\nu_{18H-DBT}}}{\Delta t \cdot m_{cat} \cdot \omega_{Pt}} \quad (9)$$

Herein,  $\Delta DH$  is the difference in degree of hydrogenation during the time  $\Delta t$ .  $m_{cat}$  is the catalyst mass,  $M_i$  and  $\nu_i$  are the molar mass and the stoichiometric coefficient of the respective component  $i$  and  $\omega_{Pt}$  is the platinum loading as determined via ICP-OES. For better comparison,  $P$  should be compared at the same  $\Delta DH$ , therefore it was always examined between a degree of hydrogenation of 90% and 40%. Moreover, the productivity per bulk volume  $V_{bulk}$  of the catalyst is defined as  $P_{V_{bulk}}$ :

$$P_{V_{bulk}} = \frac{m_{H_2}}{V_{bulk} \cdot t} = \frac{\Delta DH \cdot m_{18H-DBT} \cdot \frac{M_{H_2}}{M_{18H-DBT}} \cdot \frac{\nu_{H_2}}{\nu_{18H-DBT}}}{\Delta t \cdot V_{bulk}} \quad (10)$$

The bulk volume  $V_{bulk}$  of the monoliths is calculated as the volume of a cylinder with the respective diameter and height of the monoliths used.  $V_{bulk}$  of the cylinders is determined by multiplying the wire cage base area with the measured filling height of the cylinders.

### 3. Results and discussion

#### 3.1. Analysis of the catalyst carrier

In a first step, two different catalyst shapes were printed using direct ink writing of a paste consisting of boehmites and acetic acid as cheap organic binder. [61] The first ones were cylinders with a height and diameter of 4 mm whereas the second shape was a monolithic shape sized  $23 \times 4$  mm including a 4 mm hole in the center (Fig. 2), herein referred to as monolith. While cylinders can be fabricated by extrusion or tableting, such monoliths including lateral holes are not accessible by commercial shaping techniques. Addition of these lateral holes compared to extrusion-based monoliths improves the flow tortuosity and thus catalytic activity by improving mass and heat flow. [18] Afterwards, thermal post treatment was performed to transform the printed aluminum oxide hydroxide to alumina, which acted as final carrier material. 1000 °C and 1100 °C were chosen as calcination temperatures ( $T_{calc}$ ), as within this temperature range the phase transition from  $\gamma$ - to  $\alpha$ -via  $\theta$ -alumina takes place [25,30,32] causing strong changes in surface area and stability [9]. While for other test reactions like the oxidation of ethanol, formation of the more stable  $\alpha$ -Al<sub>2</sub>O<sub>3</sub> phases is suited, [62] pure  $\alpha$ -Al<sub>2</sub>O<sub>3</sub> is not considered reasonable herein as it has an extremely low surface area. It emerges around 1100 °C, thus higher calcination temperatures are not used. [25,30,32,63] The formation of the desired phases has been confirmed via powder XRD measurements of the printed shapes before and after calcination (Fig. S1).

Mostly due to the drying on the print bed but also to some extent caused by calcination, the final shapes turned out slightly smaller than initially aimed (Table S1). For the cylinders using common formulas, the surface-to-volume ratio ( $S/V$ ) was calculated to 1.64 mm<sup>-1</sup> and 1.72 mm<sup>-1</sup> for  $T_{calc} = 1000$  °C and  $T_{calc} = 1100$  °C, respectively. When calculating the surface-to-volume ratio of the monoliths, the strand diameter is the most important characteristic and leads to  $S/V$  ratios of 9.70 mm<sup>-1</sup> for  $T_{calc} = 1000$  °C or 10.11 mm<sup>-1</sup> for  $T_{calc} = 1100$  °C (Table 1). For the mathematical calculations, perfect geometrical shapes were assumed leading to small inaccuracies of the obtained values. However, these inaccuracies are considered negligible small compared to the differences between cylindrical and monolithic shapes. The distance between two strands in the monoliths has been calculated to be

**Table 1**

Surface-to-volume ratio  $S/V$  and porosity  $\phi$  of cylinders and monoliths depending on the calcination temperature  $T_{calc}$ .

$T_{calc} / ^\circ\text{C}$	$S/V^a / \text{mm}^{-1}$		$\phi^b / \%$	
	Cylinder	Monolith	Cylinder	Monolith
1000	1.64	9.70	65.8 ± 3.1	77.9 ± 0.5
1100	1.72	10.1	58.4 ± 2.0	76.2 ± 0.4

<sup>a</sup> Calculated using common mathematical formulas and for monolithic shapes using the assumption of an infinitely long strand with minimal contact areas between the layers.

<sup>b</sup> Determined by Jolly balance.

0.33 mm for the monoliths calcined at 1000 °C and 0.29 mm for the monoliths calcined at 1100 °C. As the overall shrinkage was increased at higher temperatures for both, monoliths and cylinders, the shapes at lower calcination temperatures had higher surface-to-volume ratios. Additionally, the surface-to-volume ratio for monoliths was about 5.9 times higher compared to the cylinders independent of the corresponding calcination temperature.

Using Archimedes buoyancy method by means of a Jolly balance the overall porosity  $\phi$  of the shapes was examined revealing values ranging from 58.4% (cylinders, 1100 °C) to 77.9% (monoliths, 1000 °C). The higher porosity at lower calcination temperature could be explained by temperature-dependent shrinkage behavior as well as the decrease of small pores. As the weight during phase transition remained constant, higher shrinkage led to a smaller porosity. Differences between cylinders and monoliths could be explained as the porosity  $\phi$  determined via Jolly balance is defined as the fracture of the volume of open pores to the sum of the volume of open and closed pores as well as the solid density itself. [56] The higher surface-to-volume ratio of monolithic structures increased the amount of open pores and subsequently increases the porosity.

Regarding the mechanical stability, the crushing strength increased from 0.7 MPa by a factor of six when changing from 1000 °C to 1100 °C calcination temperature (Table 2). This is in accordance with the results from Ludwig et al. [9] Generally, at both calcination temperatures shapes with sufficient crushing strength for catalytic applications can be obtained. The crushing strength can be calculated from the pressure required for compression using literature formulas based on the geometrical shape. [50] As no such formulas are present for the respective monolithic shapes, no values for them could be determined. By means of N<sub>2</sub> physisorption, the specific surface area  $S_{BET}$  was determined quantifying a decrease from 55 m<sup>2</sup>g<sup>-1</sup> to 22 m<sup>2</sup>g<sup>-1</sup> and hereby showing a similar trend as the total pore volume with increasing the calcination temperature. Surface area and pore volume are herein considered as material characteristics and thus primarily based on the calcination temperature rather than the shape printed. Overall pore size distributions determined via BJH method (Fig. 3) showed only mesopores and a bimodal curve for both calcination temperatures with pore radii of approximately 5 nm and 20 nm. However, sintering at higher temperatures led to a decreased amount of both, smaller and bigger pores with a much more prominent decline of the smaller pores. This finding is in accordance with common literature, showing sintering of smaller pores first. [31,64,65]

$\mu\text{CT}$  measurements provided information about the inside of the

**Table 2**

Crushing strength  $\sigma_{crush}$ , surface area  $S_{BET}$  and total pore volume  $V_p$  of cylinders depending on their calcination temperature.

$T_{calc} / ^\circ\text{C}$	$\sigma_{crush}^a / \text{MPa}$	$S_{BET}^b / \text{m}^2 \cdot \text{g}^{-1}$	$V_p^b / \text{mL} \cdot \text{g}^{-1}$
1000	0.7 ± 0.2	55	0.27
1100	4.2 ± 1.5	22	0.14

<sup>a</sup> Determined via uniaxial compression tests.

<sup>b</sup> Determined by N<sub>2</sub> Physisorption.

printed and calcined cylindrical carriers (Fig. S2). XZ and the YZ slices of the shapes (as depicted in Fig. 1) showed a rough outer surface area caused by the layer-wise manufacturing technique independently if the uncalcined so-called green part or the calcined material were scanned. Further, all samples exhibited small cracks on the flat bottom side of the cylinder that are most likely caused by anisotropic shrinkage due to drying on the print bed at room temperature directly after printing. Some small dark spots from entrapped air could be caused either by printing inaccuracies, especially at the outer layer, or from during drying and sintering. As the white spots, that could be seen for both calcined samples, are not present in the green body, these are caused by the thermal treatment and therefore sintering of the alumina particles. In general, the amount of white sintered particles is slightly higher for the samples calcined at 1100 °C.

### 3.2. Analysis of the impregnated catalyst

In a next step, wet impregnation with platinum sulfite acid solution of cylinders and monoliths, both calcined 1000 °C as well as at 1100 °C, was carried out. With 0.3 wt% and 0.9 wt% there are two target platinum loadings for each of the four different carriers resulting in a set of eight different impregnated catalysts (Table 3).

Again, surface area measurements were performed of the impregnated samples. For cylinders calcined at 1000 °C as well as 1100 °C and both target Pt loadings (0.3 wt% and 0.9 wt%), physisorption measurements were carried out after impregnation and calcination of the platinum sulfites to platinum oxides as well as after the subsequent reduction. Comparison of the specific surface area  $S_{\text{BET}}$  as well as the pore volume  $V_p$  showed that those characteristics are not changed by impregnating and reduction of the carrier (Fig. S3). Only the total pore volume decreased slightly most likely caused by the fact that platinum clusters are now partly filling the pores. When comparing the pore size distributions for carriers calcined at 1000 °C, one can see the bimodality was maintained as pores with a radius of approximately 5 nm as well as the ones with 20 nm radius decrease both, which indicates that the platinum was deposited in all pores.

To determine the exact amount of platinum deposited on the catalyst carrier, ICP-OES measurements were performed. The results showed that the target loading was not achieved for any of the samples as the actual loading is lower (Table 3). The achieved loading for 0.9 wt% target loadings is lower relative to the 0.3 wt% target loadings, as a higher amount of platinum was supposed to impregnate on the same overall surface. Further, the loading for monoliths was decisively higher as about 78% to 97% of the targeted loading could be obtained whereas

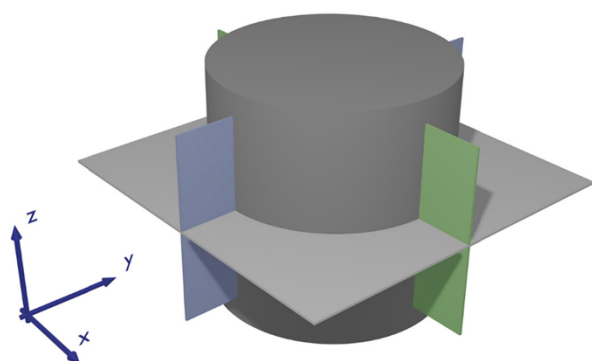


**Fig. 1.** Visualization of the coordinate system of the  $\mu$ CT analysis. XY slices of each layer are depicted by grey cross-sections and are perpendicular to the cylinder axis whereas green (XZ) and blue (YZ) slices are parallel to the cylinder axis and therefore perpendicular to the layer-by-layer manufacturing technique. (For interpretation of the references to colour in this figure legend, the reader is referred to the web version of this article.)

the loading of the cylinders ranged between 37% (1100 °C, 0.9 wt%) and 82% (1000 °C, 0.3 wt%). This can be explained by the fact, that the surface-to-volume ratio of monolithic shapes is about six times greater than for cylinders. When comparing the loading of the shapes at the calcination temperatures, it is remarkably that the relative loading was higher when calcining at 1000 °C, even though the  $S/V$  ratio was higher for shapes calcined at 1100 °C. However, not only the external surface-to-volume ratio must be taken into account but also the specific surface area  $S_{\text{BET}}$  of the carrier itself as determined via  $N_2$  physisorption. Here, the specific surface area of shapes calcined at higher temperatures was lower and therefore explaining why only lower loadings could be achieved. These findings in general correlate with literature. [66]

Transmission electron microscopy (TEM) measurements were carried out to determine the diameter  $d_{\text{Pt}}$  of the platinum clusters on the catalyst (Fig. S4, Fig. S5). In accordance with the previous results from ICP-OES measurements showing that a higher calcination temperature and therefore a lower specific surface area resulted in lower loadings, TEM measurements revealed that the platinum particle diameter was generally higher for higher calcination temperatures. The lower specific surface area as well as a lower amount of surface hydroxyl groups as derived from IR spectra of adsorbed pyridine (Fig. S6) and in accordance to literature [64,67–70] allowed only a limited number of particles to form which consequently get bigger. Despite the fact of the specific surface area, also the  $S/V$  ratio is important for the impregnation as the monoliths show smaller mean values of the platinum cluster size than the cylinders. Interestingly, the platinum cluster diameter decreased with increased loading. One reason for that might be, that if impregnated with higher amounts of platinum, the probability of ion exchange during impregnation is higher leading to more nucleation and thus overall, slightly smaller particles. Longer impregnation times might lead to loadings close to the target loading and similarly to bigger metal particles. This effect was more prominent for the cylinder samples; however, the achieved loading for these is maximum doubled with three-fold targeted loading. However, it has to be noted that the standard deviation is relatively high, so the values have to be treated with caution. As the dispersion  $D_{\text{Pt}}$  is inversely proportional to the metal particle diameter  $d_{\text{Pt}}$ , it showed opposing trends ranging from 74% (cyl. 1100 °C, 0.3 wt%) to 94% (monol. 1000 °C, 0.9 wt%).

When examining enlarged images of the monolithic cross section derived from light microscopy (Fig. 4), it is notable that at a calcination temperature of 1000 °C the overall surface did not seem smooth but shows dark spots that were more prominent for 0.9 wt% but could also be observed at 0.3 wt%. As the metal cluster size determined via TEM was in the same range for all the samples, it can be assumed that these dark spots were caused by the higher porosity of samples calcined at 1000 °C. One possible explanation is the higher number of small pores that were observed which might cause an optical illusion and hereby just appear to be darker. However, the presence of larger Pt particles might also be an explanation thereof. Microscopic analysis of the cylinders (Fig. S7) revealed a similar coloring like the monolithic structures.

Light microscopy was used additionally to examine the impregnation and its depth into the cylinders and monolithic structures. In general, a higher target loading resulted in a deeper platinum penetration for all carriers. Due to the lower specific surface area, platinum penetrated deeper into the shape at calcination temperatures of 1100 °C. Further, the increased surface-to-volume ratio of the monolithic structures led to a decreased penetration depth of the platinum. When comparing cylinder shapes with each other, the penetration depth of cylinders calcined at 1000 °C and a Pt loading of 0.9 wt% was lower than that of those calcined at 1100 °C with 0.3 wt% loading. For monoliths however, shapes calcined at 1100 °C with 0.3 wt% loading showed a smaller penetration depth compared to those calcined at 1000 °C with 0.9 wt%. As previously discussed, two characteristics, namely the surface-to-volume ratio and the specific surface area influence the impregnation with platinum and lead to opposing trends for these sets. Apparently, the high surface-to-volume ratio (compared to the platinum loading) of the

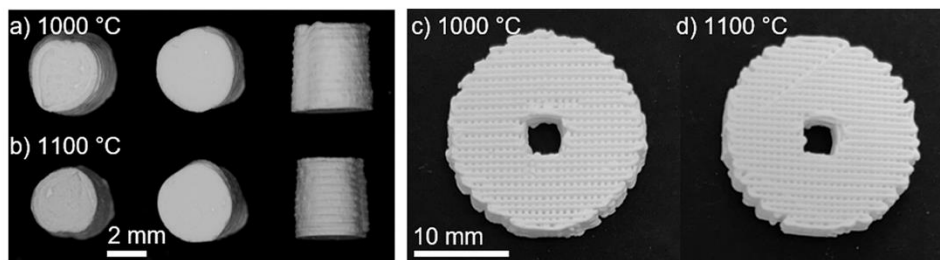


Fig. 2. Printed cylinders (left) and monolithic structures (right) after calcination at 1000 or 1100 °C.

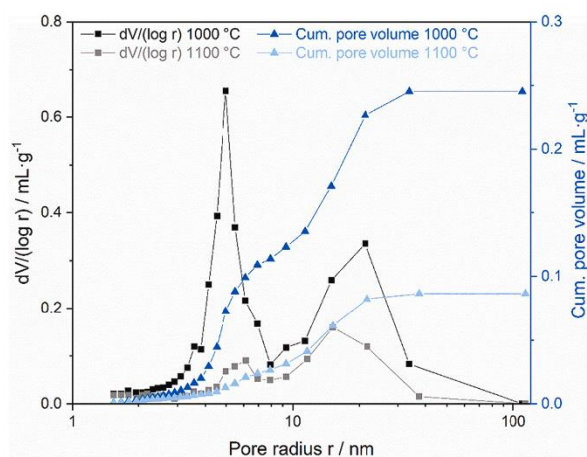


Fig. 3. Pore size distribution of calcined cylinders determined via BJH calculations from  $N_2$  physisorption.

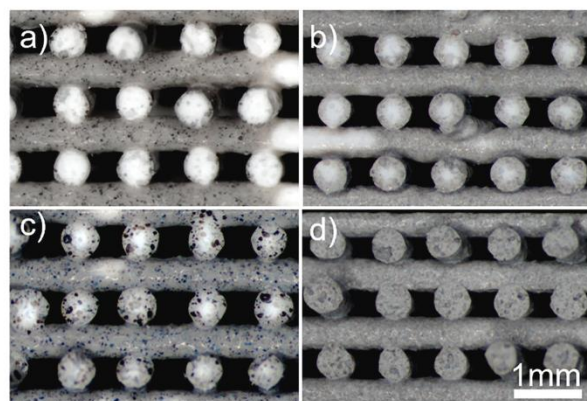


Fig. 4. Light microscopic images of the cross-sectional area of impregnated and reduced monoliths of both calcination temperatures with different platinum loading. a) 0.3 wt%, 1000 °C, b) 0.3 wt%, 1100 °C, c) 0.9 wt%, 1000 °C, d) 0.9 wt%, 1100 °C.

monolithic structures seems to dominate penetration over the specific surface area. For the cylinder on the other hand, the surface-to-volume ratio for both calcination temperatures are so small that the decreased specific surface seems to be predominant at elevated calcination temperatures. According to literature, the layer thickness of the active material in egg-shell catalysts for the dehydrogenation reaction of perhydrodibenzyltoluene should not exceed 90  $\mu\text{m}$  in order to prevent mass

transport limitations. [59] This requirement was only fulfilled for monolithic structures calcined at 1000 °C with a target loading of 0.3 wt% (50  $\mu\text{m}$  penetration depth) and for monolithic structures calcined at 1100 °C with a target loading of 0.3 wt% (90  $\mu\text{m}$  penetration depth) (Table 3, Fig. 4).

To gain a deeper understanding of the platinum penetration depth into the catalyst carrier on a macroscopical scale,  $\mu\text{CT}$  imaging analysis and fitting of the platinum solution diffusion and the concentration decrease into the carrier has been performed (Fig. 5). Due to the considerably higher atomic number of platinum compared to aluminum, the X-ray absorption of Pt is much higher and thus impregnated areas are depicted brighter than unimpregnated centers of the cylinders.  $\mu\text{CT}$  images showed that a higher calcination temperature and a higher loading increased the penetration depth, which is in accordance with the overall trends that were observed via light microscopy. Proving a homogeneous impregnation, one can see that the impregnation occurred on all outer surface areas of the cylinders. Still, the penetration did not only occur lateral but also diagonal, explaining why the rough outer surface area could not be seen as of the boundary layer within the cylinder caused by the platinum impregnation. However, the optical determination of the impregnation depth was in general more difficult for carriers calcined at 1100 °C, due to a reduced overall contrast as the concentration of platinum is more widely spread. Further, no platinum could be observed along the cracks at the bottom side of each cylinder. One explanation for this is that as the catalyst was pre-wetted prior to impregnation, capillary forces do not play an important role but only diffusion processes influence the impregnation. [33] However, it is also possible, that the capillary forces in general were not strong enough to completely fill the cracks with impregnation solution at all. [33]

The penetration behavior itself was further investigated by means of a grey scale analysis of the  $\mu\text{CT}$  scans. Carefully avoiding the white sintered particles, a line was drawn from the center to the edge of the cylinder. The resulting grey value of each pixel as well as its shortest distance to the edge of the cylinder was recorded. These values were then fitted according to the Fick's second law for a semi-infinite cylinder (2) (Fig. S8) and for better comparison only the stacked and fitted grey values are visualized (Fig. 6). Regarding the courses of the grey value, it is obvious that cylinders with equal calcination temperatures show similar trends to each other. In accordance with the microscopic images, one can clearly see that the amount of platinum at the outer surface of the cylinders calcined at 1000 °C is higher but decreases rapidly. On the other hand, for shapes calcined at 1100 °C the overall course is flatter but the penetration deeper. This higher course at lower calcination temperatures can be explained as similar or even higher amounts of platinum are impregnated on a smaller area resulting in higher loadings. As described previously, these differences in penetration depth and loading are caused by the varying amount of surface hydroxyl groups allowing a higher platinum loading. Additionally,  $\mu\text{CT}$  scans show that the penetration depth increases with higher target loadings. In general, the penetration depth obtained via light microscopy approximately corresponds to a platinum density of one tenth of the value at the surface of the cylinder as measured via  $\mu\text{CT}$  (Fig. S9). This shows that  $\mu\text{CT}$

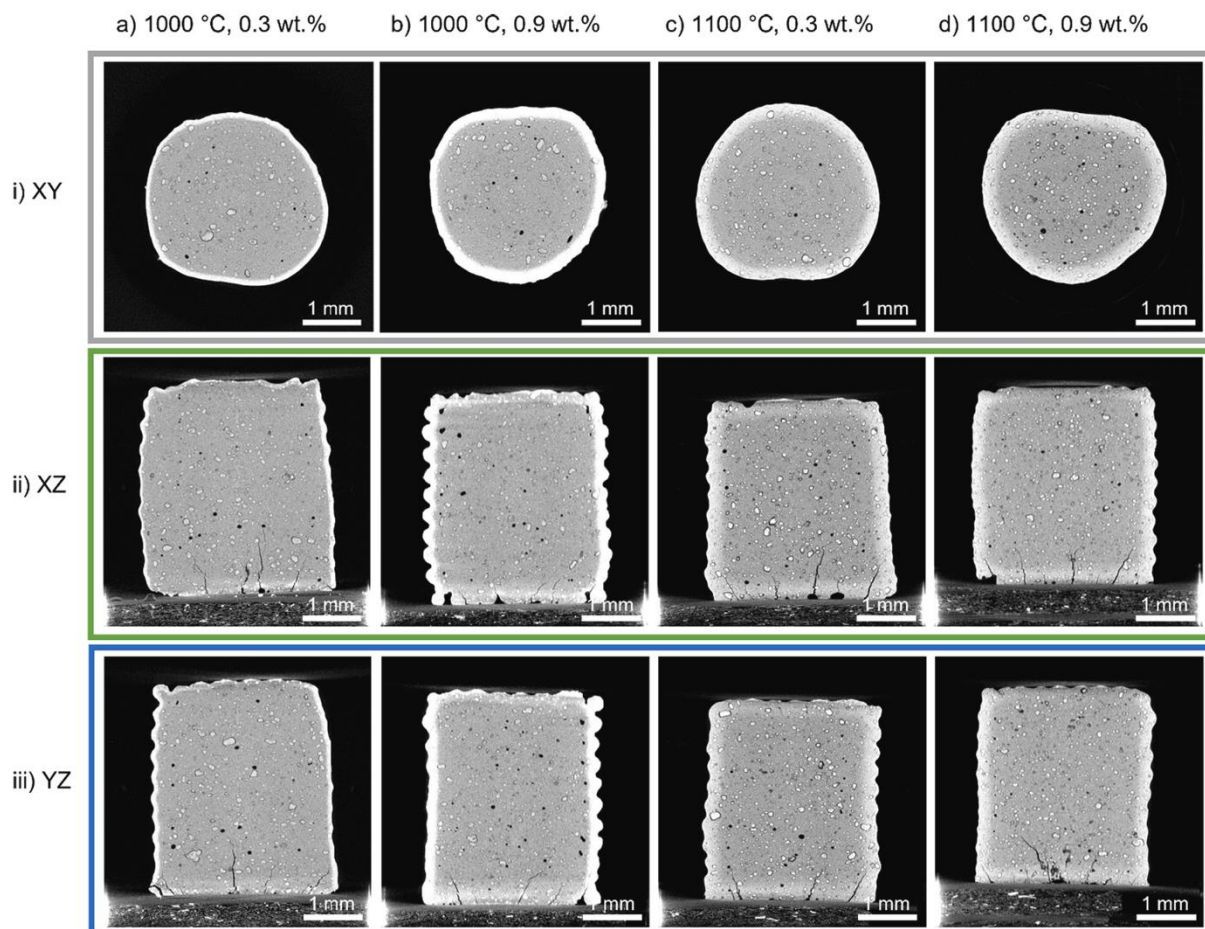


**Fig. 5.**  $\mu$ CT scans of impregnated cylinders at different calcination temperatures showing i) the XY slice (grey), ii) the XZ slice (green) and iii) the YZ slice (blue). a) 1000 °C, 0.3 wt% (left); b) 1000 °C, 0.9 wt% (middle left); c) 1100 °C, 0.3 wt% (middle right) and d) 1100 °C, 0.9 wt% (right). The colors correspond to the cross-sections depicted in Fig. 1.

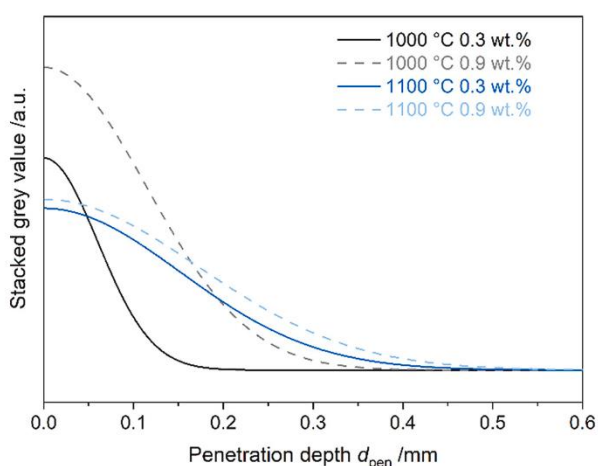


**Fig. 6.** Fit according to Fick's second law for a semi-infinite cylinder (2) of the grey values from  $\mu$ CT analysis of the different impregnated cylinder samples over the penetration depth.

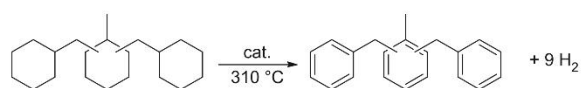


**Fig. 7.** Exemplary catalytic dehydrogenation of perhydro dibenzyltoluene to dibenzyltoluene.

analysis as non-destructive technique is a useful tool to assess impregnation behavior and penetration depth of the catalytically active species, allowing detailed understanding of the impregnation for the preparation of highly active catalysts.

### 3.3. Test reactions

Catalytic test reactions completed the evaluation of the influence of catalyst shape, calcination temperature and Pt impregnation. Therefore, the catalysts were tested for the dehydrogenation of 18H-DBT (Fig. 7). As platinum is the active component, the mass of catalyst was adjusted to the reactant mass, so that a constant Pt to 18H-DBT ratio was maintained throughout all reactions.

To exclude diffusion limitations, intrinsic test reactions were executed with powdered catalysts first (Fig. 8a). These revealed that



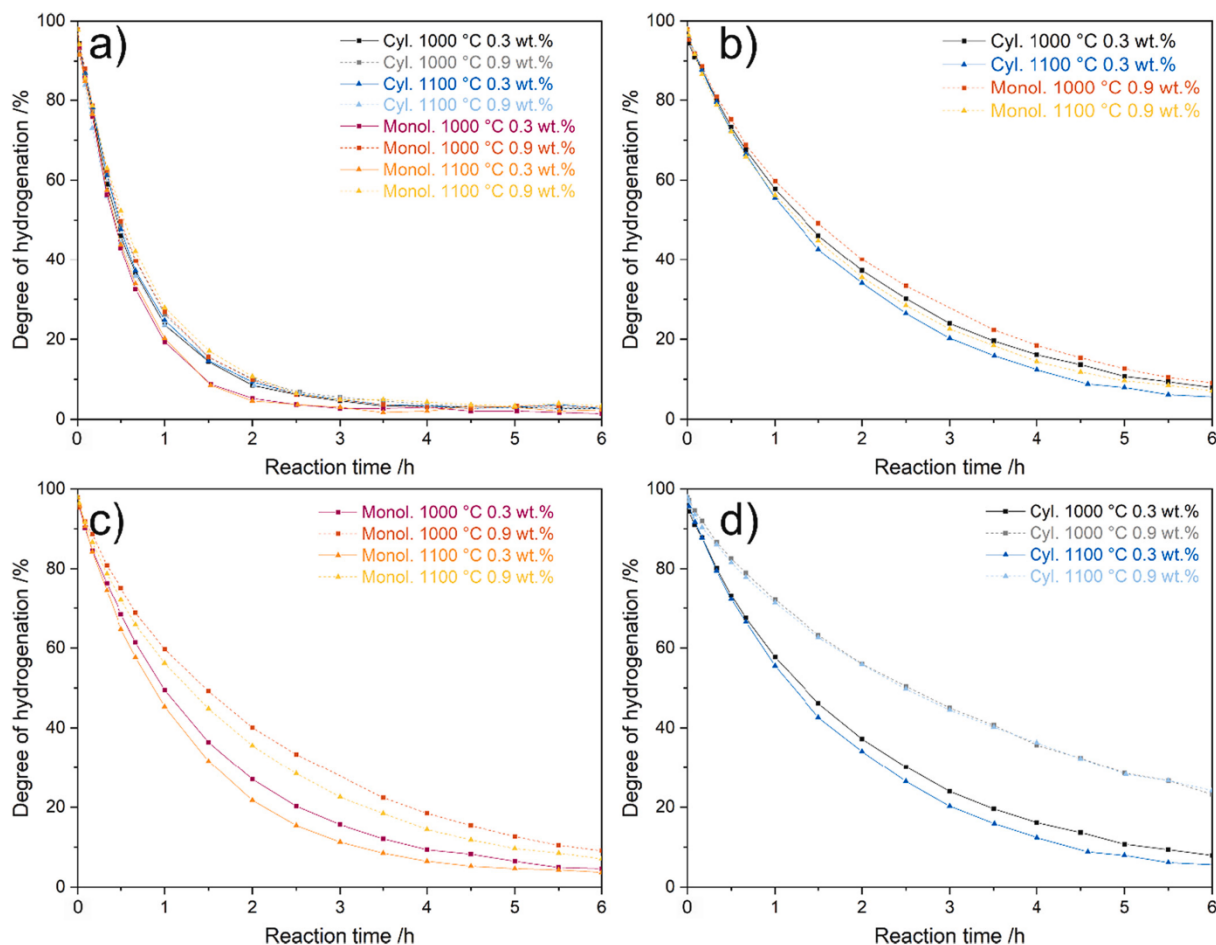


**Fig. 8.** Dehydrogenation test reactions of impregnated catalyst carriers. a) Intrinsic tests; b) Full particle tests of cylinders with a target loading of 0.3 wt% and monoliths with a target loading of 0.9 wt%; c) Full particle test of all monolithic structures; d) Full particle tests of all cylinders. The catalyst mass was adapted to the reactant mass so that a constant Pt to 18H-DBT ratio was maintained throughout all experiments. Reaction conditions:  $T_{\text{react}} = 310 \text{ }^{\circ}\text{C}$ ,  $p = 1 \text{ bar}$ ,  $n_{\text{Pt}}/n_{18\text{H-DBT}} = 0.175 \text{ mmol}_{\text{Pt}}/\text{mol}_{18\text{H-DBT}}$ ,  $t_{\text{react}} = 6 \text{ h}$ , analysis via  $^1\text{H}$  NMR spectroscopy.

**Table 3**

Pt loading  $\omega_{\text{Pt}}$ , metal diameter  $d_{\text{Pt}}$ , dispersion  $D_{\text{Pt}}$  as well as penetration depth  $d_{\text{pen}}$  of reduced shapes.

Shape	$T_{\text{calc}}$ / $^{\circ}\text{C}$	$\omega_{\text{target}}$ / wt%	$\omega_{\text{Pt}}^{\text{a}}$ / wt%	$d_{\text{Pt}}^{\text{b}}$ / nm	$D_{\text{Pt}}^{\text{b}}$ / %	$d_{\text{pen}}^{\text{c}}$ / mm
Cyl.	1000	0.3	0.25	$1.20 \pm 0.27$	84.1	$0.12 \pm 0.01$
		0.9	0.50	$1.13 \pm 0.27$	89.4	$0.21 \pm 0.02$
	1100	0.3	0.23	$1.38 \pm 0.28$	73.5	$0.28 \pm 0.02$
		0.9	0.33	$1.17 \pm 0.27$	86.2	$0.34 \pm 0.02$
Monol.	1000	0.3	0.29	$1.11 \pm 0.21$	91.5	$0.05 \pm 0.01$
		0.9	0.85	$1.08 \pm 0.25$	93.9	$0.13 \pm 0.01$
	1100	0.3	0.28	$1.13 \pm 0.31$	89.4	$0.09 \pm 0.01$
		0.9	0.70	$1.12 \pm 0.25$	90.6	$0.19 \pm 0.01^*$

<sup>a</sup> Determined via ICP-OES. <sup>b</sup> Determined by TEM measurements. <sup>c</sup> Derived from light microscopy images. \* Minimum penetration depth, as strand is completely impregnated.

almost all catalyst samples showed the same dehydrogenation activity independently on catalyst shape, calcination temperature and Pt loading. The productivities of all catalysts are very similar and range from  $6.6 \text{ g}_{\text{H}_2} \cdot \text{g}_{\text{Pt}}^{-1} \cdot \text{min}^{-1}$  to  $8.9 \text{ g}_{\text{H}_2} \cdot \text{g}_{\text{Pt}}^{-1} \cdot \text{min}^{-1}$  (Table 4). Small differences were most likely caused by inaccuracies of the  $^1\text{H}$  NMR

examination. After a reaction time of 1 h the degree of hydrogenation had already decreased from 98% to approximately 25%. A minimum degree of hydrogenation at around 7% seemed to be reached with all samples after 3.5 h. No further decline in the degree of hydrogenation was observed when extending the reaction time. There were only two curves that are not perfectly in line to other reactions, namely the monoliths calcined at 1000  $^{\circ}\text{C}$  and 1100  $^{\circ}\text{C}$  with a target loading of 0.3 wt%. Especially between 0.5 h and 3 h they showed a slightly better dehydrogenation activity. This results in higher productivities with values of  $8.9 \text{ g}_{\text{H}_2} \cdot \text{g}_{\text{Pt}}^{-1} \cdot \text{min}^{-1}$  and  $8.3 \text{ g}_{\text{H}_2} \cdot \text{g}_{\text{Pt}}^{-1} \cdot \text{min}^{-1}$  for 1000  $^{\circ}\text{C}$  and 1100  $^{\circ}\text{C}$ , respectively. One possible explanation is that the overall distribution of platinum on those shapes is the best, as the monolithic structures have the highest S/V ratios and a target loading of 0.3 wt% is rather low.

When executing full particle test reactions, the cylinder catalysts were put in a stainless-steel wire basket whereas the monoliths were placed on a stainless-steel wire. After reaching the set temperature, the catalyst was lowered into the reaction solution and fixated, starting the reaction. The overall courses in Fig. 8 clearly show that the dehydrogenation activity of the powdered catalyst is higher than the respective activity in the full particle reactions. This can be confirmed as the productivities for the full particle test range from  $1.3 \text{ g}_{\text{H}_2} \cdot \text{g}_{\text{Pt}}^{-1} \cdot \text{min}^{-1}$  to 4.0

## 5. Influence of internal and external surface area on impregnation and activity of 3D printed catalyst carriers

**Table 4**

Bulk volume  $V_{\text{bulk}}$ , productivity  $P$  of powdery and full particle test and productivity per bulk volume  $P_{V_{\text{bulk}}}$  of the respective catalytic tests in dependence of shape, calcination temperature  $T_{\text{calc}}$  and target loading  $\omega_{\text{target}}$ .

Shape	$T_{\text{calc}}$ / °C	$\omega_{\text{target}}$ / wt%	$V_{\text{bulk}}$ / cm <sup>3</sup>	$P_{\text{powder}}^{\text{a}}$ / g <sub>H<sub>2</sub></sub> ·g <sub>Pt</sub> <sup>-1</sup> ·min <sup>-1</sup>	$P_{\text{full particle}}^{\text{a}}$ / g <sub>H<sub>2</sub></sub> ·g <sub>Pt</sub> <sup>-1</sup> ·min <sup>-1</sup>	$P_{V_{\text{bulk}}}^{\text{a}}$ / g <sub>H<sub>2</sub></sub> ·min <sup>-1</sup> ·cm <sup>-3</sup>
Cyl.	1000	0.3	3.2	8.0	2.6	0.0050
		0.9	1.9	7.1	1.3	0.0046
	1100	0.3	3.3	7.8	2.9	0.0044
		0.9	1.7	8.2	1.3	0.0029
Monol.	1000	0.3	3.6	8.9	3.5	0.0060
		0.9	1.2	7.3	2.4	0.0139
	1100	0.3	3.1	8.3	4.0	0.0082
		0.9	0.9	6.6	2.7	0.0147

<sup>a</sup> Determined between degrees of hydrogenation of 90% and 40% and the corresponding time interval.

g<sub>H<sub>2</sub></sub>·g<sub>Pt</sub><sup>-1</sup>·min<sup>-1</sup>. The reactions with full particles consequently exhibit only between 16% (cyl. 1100 °C, 0.9 wt%) to 48% (monol. 1100 °C, 0.3 wt%) of the respective powdery productivities (Table 4). A degree of dehydrogenation of 25% required reaction times of approximately 3 to 4 h or even up to 6 h (cyl. 1000 °C and 1100 °C, 0.9 wt%). The enhanced performance of catalyst powder can be attributed to diffusion limitations of full particle catalysts. Throughout the whole reaction all printed shapes remain intact due to their sufficiently high crushing strength enabling easy separation of the catalyst and the reaction mixture afterwards.

Comparing the activities of either the cylinders or the monolithic structures in full particle reactions to each other (Fig. 8c and Fig. 8d) it is remarkable that the performance and productivity of catalysts calcined at 1100 °C is higher than of those calcined at 1000 °C (Table 4). This effect could be observed even though the penetration depth of the platinum is higher at 1100 °C and one would expect that this hinders the diffusion leading to slower reaction speeds. However, another aspect regarding the activity is coming into play here as 18H-DBT is a relatively large molecule and hence a minimum pore diameter of around 26 nm is beneficial for the reaction, making the bigger pores more important. [59,60] As discussed previously, the pore size distributions of the two carriers (Fig. 3) differed as the number of pores with radii of 5 nm was significantly higher when calcining at 1000 °C. As a homogeneous distribution of platinum over all pores is expected, it is likely that there was some platinum present in the smaller pores and thus inaccessible for the reactant. This led to more inaccessible platinum which lowers the overall activity. Yet, when grounding the catalysts for intrinsic reactions this diffusion limitation to smaller pores seemed to be no longer prominent. Nevertheless, the trend that the calcination temperature of 1100 °C with otherwise identical parameters led to a higher activity is not applicable for the cylinders with a loading of 0.9 wt%. These showed a similar but also the lowest activity of all samples examined as well as a productivity of only 1.3 g<sub>H<sub>2</sub></sub>·g<sub>Pt</sub><sup>-1</sup>·min<sup>-1</sup> regardless of the calcination temperature. Even after a reaction time of 6 h the dehydrogenation was lower than for all other systems and the degree of hydrogenation achieved was at around 35%. Compared to the other catalysts, the general uptake of platinum during impregnation was the lowest with values of 56 wt% (cyl. 1000 °C, 0.9 wt%) and even lower 37 wt% (cyl. 1100 °C, 0.9 wt%). This leads to the assumption that even though the platinum particle size is comparable to the other samples, the general accessibility of platinum is hindered due to lower S/V ratios and high target loadings.

For all further examinations, it is important to keep in mind that the bulk volume during the reaction was as identical as possible for cylinders and monoliths when comparing same target loadings. For 0.3 wt%  $V_{\text{bulk}}$  was in average  $3.3 \pm 0.2$  cm<sup>3</sup> whereas for 0.9 wt% it was  $1.4 \pm 0.4$  cm<sup>3</sup>. Due to higher measurement inaccuracies for cylinders with a 0.9 wt% target Pt loading as well as the relatively lower loadings compared to the target loadings, the standard deviation for the latter one is high, and values should be regarded with caution. Solely for monoliths with a target loading of 0.9 wt%,  $V_{\text{bulk}}$  can be calculated to  $1.0 \pm 0.1$  cm<sup>3</sup>. On average, the bulk volume for the monoliths with a loading of 0.9 wt%

was only 32% compared to the respective lower loaded cylinders. In general, at the same calcination temperature and target loadings the monolithic structures showed higher activities and productivities than the cylinders. For this trend several factors came into play. As the S/V ratio of monoliths was about six times as high as for cylinders, the same amount of platinum was spread over a larger surface. In consequence, the overall penetration depth was lower and platinum particle diameters were smaller. These factors are important for the reaction, as they influence the accessibility of the platinum for the reactant molecules. Still, it cannot be distinguished how important which of the effects is because of the overlap of these effects. Beside the differences in platinum distribution, it is also likely that the overall fluid dynamics within the semi-batch reactor must be considered. The monoliths with several small channels most likely enabled better mass and heat flow through the catalyst bed than the cylinder bed and hereby also influenced the catalytic reaction beneficially.

Lastly, the influence of the different loadings at similar shapes and calcination temperatures was examined. For all tested full particle reactions, the catalysts with a target loading of 0.9 wt% showed a reduced activity and lower productivities compared to those with 0.3 wt%. On first sight, this seems counterintuitive, but all reactions were carried out with the same platinum to reactant ratio. Therefore, an increased loading resulted in a decreased mass of catalyst in the reaction and therefore a reduced bulk volume. Another factor to be considered is that higher loadings also resulted in deeper penetration of the platinum and therefore were likely to increase reactant diffusion limitation to the active platinum center leading to lower activities. This effect could not be balanced by the fact that the platinum particle sizes are smaller for higher loadings as discussed previously. In general, the best activity and productivity within the full particle tests were observed for the monolith 1100 °C, 0.3 wt% with a value of 4.0 g<sub>H<sub>2</sub></sub>·g<sub>Pt</sub><sup>-1</sup>·min<sup>-1</sup> followed by the monolith with the same loading at the lower calcination temperature (3.5 g<sub>H<sub>2</sub></sub>·g<sub>Pt</sub><sup>-1</sup>·min<sup>-1</sup>).

Interestingly, the comparison of monolithic structures with a loading of 0.9 wt% to cylinders with a loading of 0.3 wt% (Fig. 8b) at same calcination temperatures revealed similar Pt-based productivities. However, a significant difference within this set of catalysts was the bulk volume since for similar platinum to reactant ratios the catalyst mass was reduced for the approximately three-fold increased loading. Hereby, the monoliths had only about 32% of the bulk volume compared to the respective cylinders. Only slightly better Pt-based productivities of cylinders than the respective monolithic structures were achieved (Table 4). The differences in bulk volume changed heat and mass transport within the semi-batch reactor and led to the minimally decreased activities compared to the respective cylinders, even though the platinum particle size or the penetration depth present at the monolithic samples would lead to the assumption of higher activities.

The productivity in respect to the bulk volume  $P_{V_{\text{bulk}}}$  it is in general higher for monoliths than for cylinders. The values for the cylinders range from 0.0029 g<sub>H<sub>2</sub></sub>·g<sub>Pt</sub><sup>-1</sup>·min<sup>-1</sup>·cm<sup>-3</sup> (cyl. 1100 °C, 0.9 wt%) to 0.0050 g<sub>H<sub>2</sub></sub>·g<sub>Pt</sub><sup>-1</sup>·min<sup>-1</sup>·cm<sup>-3</sup> (cyl. 1000 °C, 0.3 wt%). Due to the overall

low activity of the cylinders with higher loading,  $P_{V_{\text{bulk}}}$  for them is slightly smaller than for the ones with 0.3 wt% loading. However, when comparing the monolithic samples regarding their  $P_{V_{\text{bulk}}}$ , a different trend can be observed. The higher loaded monoliths exhibit an approximately two-fold higher volume-based productivity. These contrary trends can be attributed to the differences in surface-to-volume ratio of the monoliths compared to the cylinders and the resulting differences in wet impregnation. When comparing  $P_{V_{\text{bulk}}}$  for the cylinders 1000 °C and 1100 °C at 0.3 wt% ( $0.0050 \text{ g}_{\text{H}_2} \cdot \text{g}_{\text{Pt}}^{-1} \cdot \text{min}^{-1} \cdot \text{cm}^{-3}$  and  $0.0044 \text{ g}_{\text{H}_2} \cdot \text{g}_{\text{Pt}}^{-1} \cdot \text{min}^{-1} \cdot \text{cm}^{-3}$ ) and the respective monolith values of  $0.0139 \text{ g}_{\text{H}_2} \cdot \text{g}_{\text{Pt}}^{-1} \cdot \text{min}^{-1} \cdot \text{cm}^{-3}$  and  $0.0147 \text{ g}_{\text{H}_2} \cdot \text{g}_{\text{Pt}}^{-1} \cdot \text{min}^{-1} \cdot \text{cm}^{-3}$  which exhibit similar Pt based productivities, the three fold average higher  $P_{V_{\text{bulk}}}$  for the monoliths becomes apparent. This shows that by means of increased surface-to-volume ratios the activity and productivities  $P$  and  $P_{V_{\text{bulk}}}$  of a catalyst can be easily increased just by improving the impregnation behavior. Hereby, AM and especially DIW are suited techniques to obtain these varied and more complex shapes with increased surface-to-volume ratios. Furthermore, advanced shape optimization is likely to increase the flow behavior, leading to even improved catalytic activities.

#### 4. Conclusion

Herein, alumina catalyst carriers were fabricated by direct ink writing, namely cylinders and monolithic structures. These shape variations and respective changes in external surface area as well as two calcination temperatures (1000 °C and 1100 °C) resulting in different specific surface areas influenced the wet impregnation behavior and consequently the activity of full particle catalysts in the dehydrogenation of 18H-DBT. The prepared shapes have in been analyzed in depth using a combination of various techniques, including BET, light microscopy, TEM and  $\mu\text{CT}$ . By evaluating the catalysts, the use of  $\mu\text{CT}$  as an advanced analysis technique offers unique advantages for the preparation of 3D printed, heterogeneous catalysts. Using these techniques, some conclusions can be drawn, which provide useful guidance for the impregnation of catalyst carriers. In general, a higher surface-to-volume ratio of the carrier resulted in a higher loading relative to the target loading as well as in smaller platinum particles and lower penetration depth. Similar trends could be observed at lower calcination temperatures and therefore higher specific surface areas as well. Higher targeted loadings on the other side cause a decrease of the platinum loading as well as the average particle size but increase the penetration depth. These deductions can be used for the preparation of well-defined catalysts by means of impregnation with an active species. Especially when focusing on very complex structures accessible via 3D printing, such findings help understanding the preparation processes, enabling tailor-made impregnation of such advanced structures.

Resulting from the intrinsic and full particle catalytic dehydrogenation test reactions one can conclude that fabrication of catalysts by direct ink writing is beneficial for the catalytic reaction in general. As a higher exposed surface of the catalyst is beneficial for the catalytic performance, variation of the geometries by DIW or even printing e.g. a continuous flow reactor itself might influence our catalytic activity even further. [20,62] Overall, higher calcination temperatures were beneficial for the reaction as the pore size distribution of the carrier is enhanced hereby. This seemed to be more important than a higher penetration depth or larger platinum particle sizes. When impregnating monoliths and cylinders with the same target loading and working with similar reactor volumes, the monolithic structures showed significantly higher activities for dehydrogenation of perhydro dibenzyltoluene. Further, when aiming for similar activities with monolithic structures one can either reduce the platinum loading keeping the reactor volume constant or keep the same Pt amount but reduce the reactor volume. Both is beneficial, as it either requires a reduced amount of the very expensive noble metal platinum or decreased reactor sizes and therefore decreased operating costs. This reveals the potential that additive

manufacturing and especially direct ink writing show when fabricating catalyst carriers.

#### CRedit author declaration statement

Based on the requirements of your journal, we want to hereby list a detailed breakdown of all authors contributions:

Paula F. Großmann: conceptualization, writing - original draft, data curation, formal analysis, investigation, visualization, writing - review & editing.

Markus Tonigold: conceptualization, formal analysis, writing - review & editing, resources.

Norman Szesni: formal analysis, visualization, writing - review & editing.

Richard W. Fischer: conceptualization, formal analysis, writing - review & editing, project administration.

Alexander Seidel: formal analysis, visualization, writing - review & editing, resources.

Klaus Achterhold: formal analysis, visualization, data curation, writing - review & editing.

Franz Pfeiffer: supervision, writing - review & editing, project administration.

Bernhard Rieger: supervision, project administration, funding acquisition, resourcing, writing - review & editing.

#### Funding sources

The financial support of the Bayerische Forschungsstiftung (BFS) is gratefully acknowledged. K. Achterhold and F. Pfeiffer acknowledge financial support through the DFG Cluster of Excellence Munich-Centre for Advanced Photonics (MAP, DFG EXC-158), the DFG Gottfried Wilhelm Leibniz Program and the Center for Advanced Laser Applications (CALA).

#### Declaration of Competing Interest

The authors declare that they have no known competing financial interests or personal relationships that could have appeared to influence the work reported in this paper.

#### Data availability

Data will be made available on request.

#### Acknowledgments

P. F. Großmann would like to thank Max Koch for carrying out the ICP-OES measurements and Dr. Carsten Peters and Roland Weindl for their help when carrying out TEM measurements. Furthermore, P. F. Großmann would like to thank Larissa Sommer, Marlene Viertler, Jan Meyer, Stefanie Pongratz and Mira Eggel for their help during printing and in carrying out various measurements and Moritz Kränzlein for his scientific input. Special thanks to the *MuniCat* team and especially Hanh My Bui for the fruitful discussions.

#### Appendix A. Supplementary data

Detailed dimensions and densities for printed shapes, physisorption results of the impregnated cylinders, metal particle distributions as examined via TEM analysis, microscopic images of impregnated cylinders. Supplementary data to this article can be found online at <https://doi.org/10.1016/j.catcom.2023.106610>.

## References

- [1] N. Guo, M.C. Leu, Additive manufacturing: technology, applications and research needs, *Front. Mech. Eng.* 8 (2013) 215–243, <https://doi.org/10.1007/s11465-013-0248-8>.
- [2] D.I. Wimpenny, P.M. Pandey, L.J. Kumar, *Advances in 3D Printing & Additive Manufacturing Technologies*, Springer Singapore, Singapore, 2017.
- [3] A. Gebhardt, *3D-Drucken: Grundlagen und Anwendungen des Additive Manufacturing (AM)*, Hanser, München, 2014.
- [4] Q. Wei, H. Li, G. Liu, Y. He, Y. Wang, Y.E. Tan, D. Wang, X. Peng, G. Yang, N. Tsubaki, Metal 3D printing technology for functional integration of catalytic system, *Nat. Commun.* 11 (2020) 4098, <https://doi.org/10.1038/s41467-020-17941-8>.
- [5] A. Shahzad, I. Lazoglu, Direct ink writing (DIW) of structural and functional ceramics: recent achievements and future challenges, *Compos. B. Eng.* 225 (2021), 109249, <https://doi.org/10.1016/j.compositesb.2021.109249>.
- [6] P. Fastermann, *3D-Drucken*, Springer, Berlin Heidelberg, Berlin, Heidelberg, 2014.
- [7] H.M. Bui, R. Fischer, N. Szesni, M. Tonigold, K. Achterhold, F. Pfeiffer, O. Hinrichsen, Development of a manufacturing process for binder jet 3D printed porous Al<sub>2</sub>O<sub>3</sub> supports used in heterogeneous catalysis, *Addit. Manuf.* 50 (2022), 102498, <https://doi.org/10.1016/j.addma.2021.102498>.
- [8] T. Moritz, S. Maleksaeedi, Additive manufacturing of ceramic components, *Addit. Manuf.* (2018) 105–161.
- [9] T. Ludwig, J. Seckendorff, C. Troll, R. Fischer, M. Tonigold, B. Rieger, O. Hinrichsen, Additive manufacturing of Al<sub>2</sub>O<sub>3</sub>-based carriers for heterogeneous catalysis, *Chem. Ing. Tech.* 90 (2018) 703–707, <https://doi.org/10.1002/cite.201700151>.
- [10] H.M. Bui, P.F. Großmann, T. Gros, M. Blum, A. Berger, R. Fischer, N. Szesni, M. Tonigold, O. Hinrichsen, 3D printed CO-precipitated Ni-Al CO<sub>2</sub> methanation catalysts by binder jetting: fabrication, characterization and test in a single pellet string reactor, *Appl. Catal. A Gen.* 643 (2022), 118760, <https://doi.org/10.1016/j.apcata.2022.118760>.
- [11] J. Azuaje, C.R. Tubío, L. Escalante, M. Gómez, F. Guitián, A. Coelho, O. Caamaño, A. Gil, E. Sotelo, An efficient and recyclable 3D printed  $\alpha$ -Al<sub>2</sub>O<sub>3</sub> catalyst for the multicomponent assembly of bioactive heterocycles, *Appl. Catal. A Gen.* 530 (2017) 203–210, <https://doi.org/10.1016/j.apcata.2016.11.031>.
- [12] E. Bogdan, P. Michorczyk, 3D Printing in heterogeneous catalysis—the state of the art, *Materials* (Basel, Switzerland) vol. 13 (2020), <https://doi.org/10.3390/ma13204534>.
- [13] O.H. Laguna, P.F. Lietor, F.I. Godino, F.A. Corpas-Iglesias, A review on additive manufacturing and materials for catalytic applications: milestones, key concepts, advances and perspectives, *Mater. Des.* 208 (2021), 109927, <https://doi.org/10.1016/j.matdes.2021.109927>.
- [14] C. Parra-Cabrera, C. Achille, S. Kuhn, R. Ameloot, 3D printing in chemical engineering and catalytic technology: structured catalysts, mixers and reactors, *Chem. Soc. Rev.* 47 (2018) 209–230, <https://doi.org/10.1039/c7cs00631d>.
- [15] C. Hurt, M. Brandt, S.S. Priya, T. Bhatelia, J. Patel, P. Selvakannan, S. Bhargava, Combining additive manufacturing and catalysis: a review, *Catal. Sci. Technol.* 7 (2017) 3421–3439, <https://doi.org/10.1039/C7CY00615B>.
- [16] M.Z. Hussain, P.F. Großmann, F. Kohler, T. Kratky, L. Kronthaler, B. van der Linden, K. Rodewald, B. Rieger, R.A. Fischer, Y. Xia, 3D printed MOF-derived composites for enhanced photocatalytic hydrogen generation, *Sol. RRL* (2022) 2200552, <https://doi.org/10.1002/solr.202200552>.
- [17] C.R. Tubío, J. Azuaje, L. Escalante, A. Coelho, F. Guitián, E. Sotelo, A. Gil, 3D printing of a heterogeneous copper-based catalyst, *J. Catal.* 334 (2016) 110–115, <https://doi.org/10.1016/j.jcat.2015.11.019>.
- [18] J.N. Stuecker, J.E. Miller, R.E. Ferrizz, J.E. Mudd, J. Cesarano, Advanced support structures for enhanced catalytic activity, *Ind. Eng. Chem. Res.* 43 (2004) 51–55, <https://doi.org/10.1021/ie030291v>.
- [19] V. Middelkoop, A. Vamvakeros, D. de Wit, S.D.M. Jacques, S. Danaci, C. Jacquot, Y. de Vos, D. Matras, S.W.T. Price, A.M. Beale, 3D printed Ni/Al<sub>2</sub>O<sub>3</sub> based catalysts for CO<sub>2</sub> methanation - a comparative and operando XRD-CT study, *J. CO<sub>2</sub> Util.* 33 (2019) 478–487, <https://doi.org/10.1016/j.jcou.2019.07.013>.
- [20] X. Xu, M. Zhang, P. Jiang, D. Liu, Y. Wang, X. Xu, Z. Ji, X. Jia, H. Wang, X. Wang, Direct ink writing of Pd-decorated Al<sub>2</sub>O<sub>3</sub> ceramic based catalytic reduction continuous flow reactor, *Ceram. Int.* 48 (2022) 10843–10851, <https://doi.org/10.1016/j.ceramint.2021.12.301>.
- [21] C. Huo, X. Tian, Y. Nan, Z. Qiu, Q. Zhong, X. Huang, S. Yu, D. Li, Regulation mechanism of the specific surface area of alumina ceramic carriers with hierarchical porosity fabricated by powder bed fusion, *Ceram. Int.* 47 (2021) 30954–30962, <https://doi.org/10.1016/j.ceramint.2021.08.198>.
- [22] T. Li, J. Gonzalez-Gutierrez, I. Raguz, C. Holzer, M. Li, P. Cheng, M. Kitzmantel, L. Shi, L. Huang, Material extrusion additively manufactured alumina monolithic structures to improve the efficiency of plasma-catalytic oxidation of toluene, *Addit. Manuf.* 37 (2021), 101700, <https://doi.org/10.1016/j.addma.2020.101700>.
- [23] Y. Li, S. Chen, X. Cai, J. Hong, X. Wu, Y. Xu, J. Zou, B.H. Chen, Rational design and preparation of hierarchical monoliths through 3D printing for syngas methanation, *J. Mater. Chem. A* 6 (2018) 5695–5702, <https://doi.org/10.1039/C8TA01597J>.
- [24] K.P. de Jong, *Synthesis of Solid Catalysts*, 1st ed., John Wiley & Sons Incorporated, Weinheim, 2009.
- [25] G. Ertl, H. Knozinger, F. Schuth, J. Weitkamp (Eds.), *Handbook of Heterogeneous Catalysis*, 2nd ed., WILEY-VCH, Weinheim, 2008.
- [26] O.A. Alimi, C.A. Akinawo, R. Meijboom, Monolith catalyst design via 3D printing: a reusable support for modern palladium-catalyzed cross-coupling reactions, *New J. Chem.* 44 (2020) 18867–18878, <https://doi.org/10.1039/D0NJ03651J>.
- [27] P. Michorczyk, E. Hędrzak, A. Węgrzyniak, Preparation of monolithic catalysts using 3D printed templates for oxidative coupling of methane, *J. Mater. Chem. A* 4 (2016) 18753–18756, <https://doi.org/10.1039/C6TA08629B>.
- [28] F. Agueniou, H. Vidal, J. de Dios López, J.C. Hernández-Garrido, M.A. Cauqui, F. J. Botana, J.J. Calvino, V.V. Galvita, J.M. Gatica, 3D-printing of metallic honeycomb monoliths as a doorway to a new generation of catalytic devices: the Ni-based catalysts in methane dry reforming showcase, *Catal. Commun.* 148 (2021), 106181, <https://doi.org/10.1016/j.catcom.2020.106181>.
- [29] X. Zhou, C.-J. Liu, Three-dimensional printing for catalytic applications: current status and perspectives, *Adv. Funct. Mater.* 27 (2017) 1701134, <https://doi.org/10.1002/adfm.201701134>.
- [30] W. Reschetilowski, *Einführung in die Heterogene Katalyse*, Springer, Berlin Heidelberg, Berlin, Heidelberg, 2015.
- [31] F. Schüth (Ed.), *Handbook of Porous Solids*, WILEY-VCH, Weinheim, 2002.
- [32] I. Chorkendorff, J.W. Niemantsverdriet, *Concepts of Modern Catalysis and Kinetics*, WILEY-VCH, Weinheim, 2003.
- [33] P. Munnik, P.E. de Jongh, K.P. de Jong, Recent developments in the synthesis of supported catalysts, *Chem. Rev.* 115 (2015) 6687–6718, <https://doi.org/10.1021/cr500486u>.
- [34] P. Chu, E.E. Petersen, C.J. Radke, Modeling wet impregnation of nickel on  $\gamma$ -alumina, *J. Catal.* 117 (1989) 52–70.
- [35] G. Do, P. Preuster, R. Aslam, A. Bösmann, K. Müller, W. Arlt, P. Wasserscheid, Hydrogenation of the liquid organic hydrogen carrier compound dibenzyltoluene – reaction pathway determination by 1 H NMR spectroscopy, *React. Chem. Eng.* 1 (2016) 313–320, <https://doi.org/10.1039/C5RE00080G>.
- [36] L. Villegas, F. Masset, N. Guilhaume, Wet impregnation of alumina-washcoated monoliths: effect of the drying procedure on Ni distribution and on autothermal reforming activity, *Appl. Catal. A Gen.* 320 (2007) 43–55, <https://doi.org/10.1016/j.apcata.2006.12.011>.
- [37] Y. Sekine, T. Higo, Recent trends on the dehydrogenation catalysis of liquid organic hydrogen carrier (LOHC): a review, *Top. Catal.* 64 (2021) 470–480, <https://doi.org/10.1007/s11244-021-01452-x>.
- [38] Y. Jo, T. Wan Kim, J. Oh, D. Kim, Y.-W. Suh, Mesoporous sulfur-decorated Pt–Al<sub>2</sub>O<sub>3</sub> for dehydrogenation of perhydro benzyltoluene: activity-favorable adsorption of reaction species onto electron-deficient Pt atoms, *J. Catal.* 413 (2022) 127–137, <https://doi.org/10.1016/j.jcat.2022.06.025>.
- [39] F. Auer, D. Blaumeiser, T. Bauer, A. Bösmann, N. Szesni, J. Lübuda, P. Wasserscheid, Boosting the activity of hydrogen release from liquid organic hydrogen carrier systems by sulfur-additives to Pt on alumina catalysts, *Catal. Sci. Technol.* 9 (2019) 3537–3547, <https://doi.org/10.1039/c9cy00817a>.
- [40] H. Jorschick, M. Geißelbrecht, M. Ebl, P. Preuster, A. Bösmann, P. Wasserscheid, Benzyltoluene/dibenzyltoluene-based mixtures as suitable liquid organic hydrogen carrier systems for low temperature applications, *Int. J. Hydrog. Energy* 45 (2020) 14897–14906, <https://doi.org/10.1016/j.ijhydene.2020.03.210>.
- [41] N. Brückner, K. Obesser, A. Bösmann, D. Teichmann, W. Arlt, J. Dungs, P. Wasserscheid, Evaluation of industrially applied heat-transfer fluids as liquid organic hydrogen carrier systems, *ChemSusChem* 7 (2014) 229–235, <https://doi.org/10.1002/cssc.201300426>.
- [42] A. Ali, A.K. Rohini, Y.S. Noh, D.J. Moon, H.J. Lee, Hydrogenation of dibenzyltoluene and the catalytic performance of Pt/Al<sub>2</sub>O<sub>3</sub> with various Pt loadings for hydrogen production from perhydro-dibenzyltoluene, *Int. J. Energy Res.* 39 (2021) 2, <https://doi.org/10.1002/er.7604>.
- [43] P.C. Rao, M. Yoon, Potential liquid-organic hydrogen carrier (LOHC) systems: a review on recent Progress, *Energies* 13 (2020) 6040, <https://doi.org/10.3390/en13226040>.
- [44] Clariant-International-Ltd, EleMax Series - Catalysts for Storage of Hydrogen from Renewable Sources Cia Liquid Organic Hydrogen Carriers (LOHC). <https://www.clariant.com/en/Solutions/Products/2019/05/21/15/19/EleMax-Series> accessed November 11th, 2022.
- [45] S. Dürr, S. Zilm, M. Geißelbrecht, K. Müller, P. Preuster, A. Bösmann, P. Wasserscheid, Experimental determination of the hydrogenation/dehydrogenation - equilibrium of the LOHC system H0/H18-dibenzyltoluene, *Int. J. Hydrog. Energy* 46 (2021) 32583–32594, <https://doi.org/10.1016/j.ijhydene.2021.07.119>.
- [46] H. Jorschick, A. Bulgarin, L. Alletsee, P. Preuster, A. Bösmann, P. Wasserscheid, Charging a liquid organic hydrogen carrier with wet hydrogen from electrolysis, *ACS Sustain. Chem. Eng.* 7 (2019) 4186–4194, <https://doi.org/10.1021/acsschemeng.8b05778>.
- [47] S. Lee, J. Lee, T. Kim, G. Han, J. Lee, K. Lee, J. Bae, Pt/CeO<sub>2</sub> catalyst synthesized by combustion method for dehydrogenation of perhydro-dibenzyltoluene as liquid organic hydrogen carrier: effect of pore size and metal dispersion, *Int. J. Hydrog. Energy* 46 (2021) 5520–5529, <https://doi.org/10.1016/j.ijhydene.2020.11.038>.
- [48] P.T. Aakko-Saksa, M. Vehkamäki, M. Kemell, L. Keskiäli, P. Simell, M. Reinikainen, U. Tapper, T. Repo, Hydrogen release from liquid organic hydrogen carriers catalysed by platinum on rutile-anatase structured titania, *ChemComm* 56 (2020) 1657–1660, <https://doi.org/10.1039/c9cc09715e>.
- [49] H. Jorschick, P. Preuster, S. Dürr, A. Seidel, K. Müller, R. Müller, A. Bösmann, P. Wasserscheid, Hydrogen storage using a hot pressure swing reactor, *Energy Environ. Sci.* 10 (2017) 1652–1659, <https://doi.org/10.1039/c7EE00476A>.
- [50] S.P. Timoshenko, J.N. Goodier, *Theory of Elasticity*, 3rd ed., McGraw-Hill, Auckland, 2004.
- [51] J. Schindelin, I. Arganda-Carreras, E. Frise, V. Kaynig, M. Longair, T. Pietzsch, S. Preibisch, C. Rueden, S. Saalfeld, B. Schmid, J.-Y. Tinevez, D.J. White, V. Hartenstein, K. Eliceiri, P. Tomancak, A. Cardona, Fiji: an open-source platform for biological-image analysis, *Nat. Methods* 9 (2012) 676–682, <https://doi.org/10.1038/nmeth.2019>.

## 5. Influence of internal and external surface area on impregnation and activity of 3D printed catalyst carriers

- [52] <https://gist.github.com/lacan/74f550a21ea97f46c74f1a110583586d>. May 27th 2022, accessed May 27th 2022.
- [53] R.M.A. Roque-Malherbe, Adsorption and Diffusion in Nanoporous Materials, 2nd ed., Taylor & Francis Group, Milton, 2018.
- [54] J. Crank, The Mathematics of Diffusion, 2nd ed., Oxford Univ. Press, Oxford, 1975.
- [55] Deutsches Institut für Normung e.V., Monolithische Keramik Allgemeine und strukturelle Eigenschaften: Teil 2: Bestimmung von Dichte und Porosität, Beuth Verlag GmbH, Berlin, 1993.
- [56] E. Macherauch, H.-W. Zoch, Praktikum in Werkstoffkunde: 100 ausführliche Versuche aus wichtigen Gebieten der Werkstofftechnik, 13th ed., Springer Vieweg, Wiesbaden, 2019.
- [57] A. Borodziński, M. Bonarowska, Relation between crystallite size and dispersion on supported metal catalysts, *Langmuir* (1997) 5613–5620.
- [58] P. Preuster, Entwicklung eines Reaktors zur Dehydrierung chemischer Wasserstoffträger als Bestandteil eines dezentralen, stationären Energiespeichers, Dissertation., Erlangen-Nürnberg, 2017.
- [59] F. Auer, Katalysatorentwicklung für die Dehydrierung von Perhydro-Dibenzyltoluol, Dissertation., Erlangen-Nürnberg, 2020.
- [60] A.M. Seidel, Entwicklung eines technischen Platin-Trägerkatalysators zur Dehydrierung von Perhydro-Dibenzyltoluol, Erlangen-Nürnberg, 2019.
- [61] M. Kotobuki, Properties of Al<sub>2</sub>O<sub>3</sub> pastes using inorganic Na<sub>2</sub>SiO<sub>3</sub> binder and organic binder for direct ink writing, *Phys. Status Solidi B* 259 (2022) 2100520, <https://doi.org/10.1002/pssb.202100520>.
- [62] F. Álvarez, A. Cifuentes, I. Serrano, L. Franco, G. Fargas, F. Fenollosa, R. Uceda, L. Llanes, C. Tardivat, J. Llorca, J.J. Roa, Optimization of the sintering thermal treatment and the ceramic ink used in direct ink writing of  $\alpha$ -Al<sub>2</sub>O<sub>3</sub>: characterization and catalytic application, *J. Eur. Ceram. Soc.* 42 (2022) 2921–2930, <https://doi.org/10.1016/j.jeurceramsoc.2022.01.032>.
- [63] K. Wefers, C. Misra, Oxides and Hydroxides of Aluminum: Alcoa Technical Paper No. 19, Revised, Aluminum Company of America, 1987.
- [64] D.L. Trimm, A. Stanislaus, The control of pore size in alumina catalyst supports: a review, *Appl. Catal.* 21 (1986) 215–238.
- [65] H. Scharper, E. Doesburg, P. Dekorte, L. van Reijen, Thermal stabilization of high surface area alumina, *Solid State Ionics* 16 (1985) 261–265, [https://doi.org/10.1016/0167-2738\(85\)90050-5](https://doi.org/10.1016/0167-2738(85)90050-5).
- [66] W.A. Spieker, Regalbuto JR, a fundamental model of platinum impregnation onto alumina, *Chem. Eng. Sci.* 56 (2001) 3491–3504.
- [67] F. Granados-Correa, J. Jiménez-Becerril, The effect of the calcination temperature of boehmite on its co (II) adsorption properties, *J. Ceram. Process. Res.* 13 (2012) 142–148.
- [68] J.N. Kondo, R. Nishitani, E. Yoda, T. Yokoi, T. Tatsumi, K. Domen, A comparative IR characterization of acidic sites on HY zeolite by pyridine and CO probes with silica-alumina and  $\gamma$ -alumina references, *Phys. Chem. Chem. Phys.* 12 (2010) 11576–11586, <https://doi.org/10.1039/c0cp00203h>.
- [69] M. Tamura, K.-I. Shimizu, A. Satsuma, Comprehensive IR study on acid/base properties of metal oxides, *Appl. Catal. A Gen.* 433–434 (2012) 135–145, <https://doi.org/10.1016/j.apcata.2012.05.008>.
- [70] Y.F. Shen, S.L. Suib, M. Deeba, G.S. Koermer, Luminescence and IR characterization of acid sites on alumina, *J. Catal.* 146 (1994) 483–490, <https://doi.org/10.1006/jcat.1994.1086>.

## 6 Comparison of Direct Ink Writing and Binder Jetting for additive manufacturing of Pt/Al<sub>2</sub>O<sub>3</sub> catalysts for the dehydrogenation of perhydro-dibenzyltoluene

### 6.1 Bibliographic data

Title: “Comparison of Direct Ink Writing and Binder Jetting for additive manufacturing of Pt/Al<sub>2</sub>O<sub>3</sub> catalysts for the dehydrogenation of perhydro-dibenzyltoluene”

Status: Research Article, Published: January 14, 2023

Journal: *Chemical Engineering Journal* **2023**, 141361

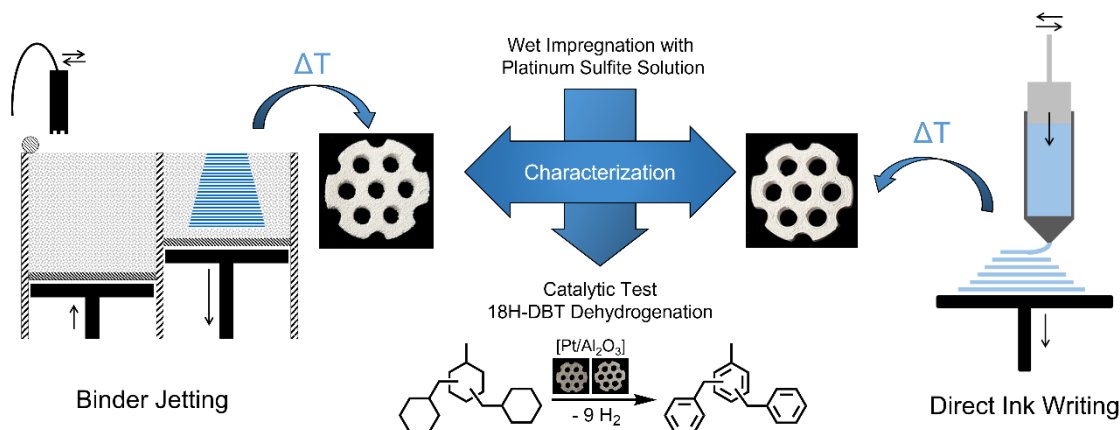
Publisher: Elsevier

DOI: 10.1016/j.cej.2023.141361

Authors: Hanh My Bui<sup>#</sup>, Paula F. Großmann<sup>#</sup>, Anne Berger, Alexander Seidel, Markus Tonigold, Normen Szesni, Richard Fischer, Bernhard Rieger, Olaf Hinrichsen<sup>\*c</sup>

Reference: [297]

### 6.2 Abstract graphic (TOC)



<sup>#</sup> These authors contributed equally. <sup>\*</sup> Corresponding author.

<sup>c</sup> H. M. Bui performed the Binder Jetting experiments while P. F. Großmann executed the Direct Ink Writing. Both carried out further impregnation experiments, the test reactions, analysis of the samples and wrote most parts of the manuscript. A. Berger performed mercury porosimetry measurements. A. Seidel gave valuable input regarding the dehydrogenation test reactions and their evaluation. M. Tonigold, N. Szesni, R. W. Fischer provided valuable intellectual input and project supervision. B. Rieger and O. Hinrichsen contributed with valuable intellectual input and supervised the work.

### 6.3 Content

Although various 3D printing methods have been used in heterogeneous catalysis to date, the question naturally arises as to how the different printing techniques affect catalytic activity for subsequent application. To address this question, extrusion-based Direct Ink Writing was compared with powder bed-based Binder Jetting for the production of alumina catalyst supports. First, cylinders with the same dimensions were printed and the influence of the printing method and calcination temperature on porosity, shrinkage and lateral compressive strength was investigated. It was shown that BJ shapes exhibit a significantly increased (macro-) porosity and correspondingly increased BET surface area, even though the latter effect decreases with increasing calcination temperature. The bimodal pore distribution decreases with increasing calcination temperature, until from 1100 °C, a monomodal, mesoporous support is present. Irrespective of the 3D printing technique, the calcined substrates exhibit a strong, abrupt shrinkage from 1100 °C onwards, with the DIW shapes generally being somewhat smaller. This increase as a function of the calcination temperature can also be observed in the compressive strength. Here, however, it should be emphasized that the DIW parts are, by almost a factor of 5, more stable than the BJ parts. Taking into account the literature prerequisites regarding the test reaction, 1100 °C was set as the calcination temperature for the further tests and the CAD templates of the monoliths were adapted so that, after the shrinkage, DIW and BJ shapes had the same dimensions. These shapes were then wet impregnated with platinum sulfite acid solution. With increasing impregnation time, the platinum loading and the platinum particle size increased. In general, the BJ parts exhibited significantly higher loadings and lower penetration compared to the DIW parts. Finally, catalytic test reactions were carried out for the dehydrogenation of perhydro-dibenzyltoluene. Here, the shapes were loaded to have the same amount of platinum per monolith. Overall, the DIW and BJ shapes each showed equal productivities, although the penetration depth is greater for the BJ parts. However, presumably the greater macroporosity also provides easier diffusion of the reactant. In summary, in the production of the catalyst supports the 3D printing techniques employed, namely BJ and DIW, show differences in terms of physicochemical properties, but in the dehydrogenation of perhydro-dibenzyltoluene they are equally productive. Other differences, such as scalability, costs or shape variations, can also be taken into account when deciding which printing technique is more appropriate for an application.

## 6.4 Manuscript

Chemical Engineering Journal 458 (2023) 141361



Contents lists available at ScienceDirect

Chemical Engineering Journal

journal homepage: [www.elsevier.com/locate/cej](http://www.elsevier.com/locate/cej)



# Comparison of Direct Ink Writing and Binder Jetting for additive manufacturing of Pt/Al<sub>2</sub>O<sub>3</sub> catalysts for the dehydrogenation of perhydro-dibenzyltoluene

Hanh My Bui<sup>a,b,1</sup>, Paula F. Großmann<sup>a,b,c,1</sup>, Anne Berger<sup>a,b,d</sup>, Alexander Seidel<sup>e</sup>, Markus Tonigold<sup>f</sup>, Normen Szesni<sup>f</sup>, Richard Fischer<sup>a,f</sup>, Bernhard Rieger<sup>a,b,c</sup>, Olaf Hinrichsen<sup>a,b,\*</sup>

<sup>a</sup> Department of Chemistry, Technical University of Munich, Lichtenbergstraße 4, 85748, Garching, Germany

<sup>b</sup> Catalysis Research Center, Technical University of Munich, Ernst-Otto-Fischer-Straße 1, 85748, Garching, Germany

<sup>c</sup> WACKER-Chair of Macromolecular Chemistry, Technical University of Munich, Lichtenbergstraße 4, 85748, Garching, Germany

<sup>d</sup> Chair of Technical Electrochemistry, Technical University of Munich, Lichtenbergstraße 4, 85748, Garching, Germany

<sup>e</sup> Hydrogenious LOHC Technologies GmbH, Weidenweg 13, 91058, Erlangen, Germany

<sup>f</sup> Clariant Produkte (Deutschland) GmbH, Waldheimer Straße 13, 83052, Bruckmühl, Germany

## ARTICLE INFO

### Keywords:

Binder Jetting  
Direct Ink Writing  
Heterogeneous catalysis  
Liquid organic hydrogen carrier  
Dehydrogenation  
Characterization  
Impregnation

## ABSTRACT

Two additive manufacturing (AM) techniques, namely extrusion-based Direct Ink Writing (DIW) and powder-based Binder Jetting (BJ), were thoroughly compared to assess their respective advantages and drawbacks for catalyst shaping. The 3D printed monolithic Al<sub>2</sub>O<sub>3</sub> supports were wet impregnated with H<sub>3</sub>Pt(SO<sub>3</sub>)<sub>2</sub>(OH) and tested for the dehydrogenation of perhydro-dibenzyltoluene (18H-DBT), a liquid organic hydrogen carrier (LOHC). The supports were analyzed regarding their specific surface area, compression strength, shrinkage behavior and pore size distribution with calcination temperatures ranging from 600 - 1200 °C as well as 3D print specific characteristics. Benefiting the liquid phase reaction, pore diameters below 26 nm were diminished above  $T_{\text{calc}} = 1050$  °C, revealing a BET surface area of 26 m<sup>2</sup>/g for BJ and 11 m<sup>2</sup>/g for DIW printed supports. Furthermore, increasing the impregnation duration from 0.5 h to 12 h showed increased Pt loading, larger metal particles, and a deeper penetration into the support. Most notably, for BJ the Pt loading is generally higher due to higher meso- and macroporosity of the support. Catalytic 18H-DBT dehydrogenation with powder and monolithic catalysts showed equal dehydrogenation rates with both 3D printing methods, respectively. The achieved Pt productivity was about 4.3 g<sub>H<sub>2</sub></sub> g<sub>Pt</sub><sup>-1</sup> min<sup>-1</sup> for powder tests and 2.7 g<sub>H<sub>2</sub></sub> g<sub>Pt</sub><sup>-1</sup> min<sup>-1</sup> for monolithic pellets.

## 1. Introduction

Since the first additive manufacturing (AM) concept was patented 1986 by Charles W. Hull [1], numerous AM technologies have been introduced using a wide range of materials [2,3] for different applications ranging from the (bio)medical [4], dental [5], to automotive [6,7] and aerospace [8,9] industry. The chemical industry, including heterogeneous catalysis, has been hesitant due to its relatively low agility and adaptability of its oftentimes large scale productions [10,11]. However, AM increasingly finds its way into the chemical engineering sciences to facilitate process intensification, e.g. for gas adsorption [12–15].

From an advanced manufacturing viewpoint, 3D printing of structured catalysts becomes relevant since it facilitates the design of com-

plex tailor-made shapes, optimizing pressure drop, heat and mass transfer properties, fluid and particle flow, as well as reaction thermodynamics. Therefore, the catalyst performance and overall reactor design and efficiency can be rapidly manipulated and customized to the need of each chemical reactor system by AM [10,16].

Several review and research articles have already outlined the current state of the art of AM for catalytic applications [11,17–19]. Not all AM methods are suitable for catalyst manufacturing since processing of ceramic material poses certain challenges due to the material's inherent brittleness and low toughness [20,21]. Direct Ink writing (DIW) is the most commonly used printing method to generate catalysts such as Fe/γ-Al<sub>2</sub>O<sub>3</sub> monoliths for the hydroxylation of phenol [22], doped HZSM-5 zeolite for *n*-hexane cracking [23] or Ni/Al<sub>2</sub>O<sub>3</sub> for CO<sub>2</sub> methanation [24] as examples of studied catalytic systems. Furthermore,

\* Corresponding author at: Department of Chemistry, Technical University of Munich, Lichtenbergstraße 4, 85748, Garching, Germany.

E-mail address: [olaf.hinrichsen@ch.tum.de](mailto:olaf.hinrichsen@ch.tum.de) (O. Hinrichsen).

<sup>1</sup> These authors equally contributed to this work.

<https://doi.org/10.1016/j.cej.2023.141361>

Received 8 November 2022; Received in revised form 31 December 2022; Accepted 5 January 2023

Available online 14 January 2023

1385-8947/© 2023 Elsevier B.V. All rights reserved.



## 6. Comparison of Direct Ink Writing and Binder Jetting for additive manufacturing of Pt/Al<sub>2</sub>O<sub>3</sub> catalysts for the dehydrogenation of perhydro-dibenzyltoluene

H.M. Bui et al.

Chemical Engineering Journal 458 (2023) 141361

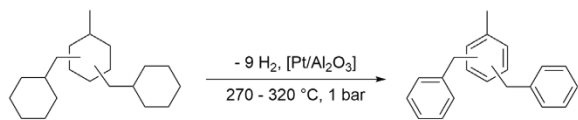


Fig. 1. Schematic representation of the 18H-DBT dehydrogenation.

Stuecker et al. compared robocasted woodpile-structured monoliths to conventional honeycomb ceramic structures and discovered enhanced catalytic methane combustion activity of 3D printed structures [25]. Binder Jetting (BJ) has only been used by Bui et al. for fabrication of precipitated NiAl catalysts for CO<sub>2</sub> methanation in a single pellet string reactor [26], necessitating further studies on the use of BJ in catalysis. Ludwig et al. [27] investigated the suitability of different 3D printing methods for the generation of pure Al<sub>2</sub>O<sub>3</sub> parts for catalytic purposes. Among the evaluated printing techniques, BJ and DIW were chosen as suitable methods.

Direct Ink Writing, or so-called robocasting, is categorized as Material Extrusion by ISO [28] and can further be distinguished in discontinuous (droplet based) and continuous extrusion [29,30]. The latter operating mode is used in this work. Hereby, high-viscosity slurries are used as printing material and extruded through a thin nozzle [30–32]. The process occurs at ambient temperature and no chemical reactions take place. Therefore, solely the rheological, shear thinning properties of the ink determine the solidification process after printing [31,33,34]. After successful printing, post-processing in form of binder removal or calcination can be necessary to obtain required material properties [35, 36].

Binder Jetting is a powder-based 3D printing technology, which uses a roller to distribute and spread a thin powder layer over a print platform. An inkjet print head selectively jets a printing liquid over each powder layer in order to glue the powder particles together to form a three-dimensional part. After printing, the so-called green part is still embedded in unbound powder, which has to be removed. BJ creates inherently porous parts, making post-processing steps such as infiltration crucial for sufficient mechanical stability [37]. Moreover, BJ offers a relatively high build rate and easier scalability as the duration of a print is mainly determined by the height of the print job and the number of printable object is limited by the print bed area. Nevertheless, the powder-ink interaction regarding powder wetting [38], adequate powder flowability [39], and rheological properties of the ink needs to be considered when developing new material combinations [40,41]. Different powdery materials such as metal, polymers, ceramics and biomaterials can be processed with BJ [42], making it a versatile alternative to conventional manufacturing methods.

The additively manufactured Pt/Al<sub>2</sub>O<sub>3</sub> catalysts in this study were tested for the dehydrogenation of perhydro-dibenzyltoluene, the hydrogen-rich form of the liquid organic hydrogen carrier pair perhydro-dibenzyltoluene/ dibenzyltoluene (OH-DBT). In contrast to the conventional hydrogen storage technologies, LOHC poses an attractive method for the decentralized storage of renewable excess energy. LOHCs can be handled, transported and stored using the existing fuel infrastructure [43–45]. OH-DBT, which has been commercially used as a heat transfer oil, is hydrogenated to 18H-DBT at about 140 °C. Subsequent dehydrogenation takes place at 270 - 320 °C, mostly catalyzed by Pt/Al<sub>2</sub>O<sub>3</sub> egg-shell catalysts [46,47], see Fig. 1. The reaction is endothermic with a reaction enthalpy for 18H-DBT of 65.4 kJ/mol<sub>H<sub>2</sub></sub> [43,48] and is the key step for the release of hydrogen in this LOHC system.

This paper aims to directly compare the two 3D printing techniques BJ and DIW regarding the fabrication of a monolithic alumina support for Pt/Al<sub>2</sub>O<sub>3</sub> catalysts for the dehydrogenation of 18H-DBT. To the best of our knowledge, this study is the first to comprehensively compare two AM methods with profoundly different functional principles in order to assess their potential for a specific catalytic application regarding

e.g. shrinkage, and stability alongside physicochemical properties such as BET surface area and pore size. With respect to these properties, impregnation experiments were carried out which point out differences based on the printing method used. The more commonly used technique DIW is compared to BJ which lacks insights regarding catalytic application. Consequently, the findings from this study help to further the utilization of AM in catalysis and provide manufacturing guidelines for preparation of catalysts involving 3D printing. Generating more insights into the dehydrogenation step of a liquid organic hydrogen carrier (LOHC) additionally contributes to the application of 3D printing to improve the performance of chemical hydrogen storage and release and helps to face the future demand thereof.

## 2. Experimental

Fig. 2 gives an overview of the general experimental outline of this work. Two different shaped alumina supports were additively manufactured by BJ as well as DIW.

First, alumina cylinders with a target height and diameter of 6 mm were fabricated with both printing methods and calcined at different temperatures  $T_{\text{calc}}$ . Cylinders were used for characterization regarding their specific surface area  $S_{\text{BET}}$ , pore size distribution (poreSD), part shrinkage and compression strength  $\sigma_{\text{comp}}$ . Based on the findings of the characterization experiments, the optimum  $T_{\text{calc}}$  of 1100 °C was chosen for further support preparation.

Subsequently, monolithic structures were printed by BJ and DIW and calcined at 1100 °C. Monolithic structures were used for impregnation experiments and the catalytic tests. The monolith design is displayed in Fig. 3 and is a cylindrical base body with seven holes located in the corners of an equilateral triangle. This shape was chosen based on the fact that it is equally printable with DIW as well as BJ, neglecting the advantages of each printing technique. Based on the previously determined shrinkage of the calcined 3D printed parts, the CAD model of the monolithic structure was adjusted so that the resulting parts after printing and calcination at 1100 °C had a diameter of 18 mm and a hole diameter of 3 mm. The distance between two holes was 2 mm. The surface-to-volume ratio of the supports after thermal treatment was  $S/V = 1.27 \text{ mm}^{-1}$ .

The effect of impregnation time on the Pt loading, particle size and penetration depth was investigated using the alumina monoliths. Ultimately, catalytic tests were performed on monolithic Pt/Al<sub>2</sub>O<sub>3</sub> catalysts calcined at 1100 °C and wet impregnated for 3 h.

### 2.1. Catalyst preparation

DIW and BJ vary significantly in feedstock preparation and post-processing steps. The studied alumina supports were calcined under identical thermal conditions. Moreover, the final outer part dimensions of the monolithic shapes were identical taking as different shrinkage behaviors of both printing methods were taken into account.

#### 2.1.1. Alumina support fabrication by BJ

The additive manufacturing process for the Binder Jet printed alumina supports generally followed the procedure reported by Bui et al. [49] and only differed in the second thermal treatment step where different calcination temperatures were applied in this study. The powder feedstock consisted of 73 wt.% bayerite Pural BT (Sasol Chemicals, USA), 7 wt.% Actilox S40 (Nabaltec AG, Germany), and 20 wt.% of the solid binder polyvinyl pyrrolidone (PVP) Sokalan K17P (BASF SE, Germany). All powder components were homogeneously mixed in a SpeedMixer (Hauschild GmbH & Co KG, Germany). The powder bed was selectively wetted with an aqueous particle-loaded printing liquid consisting of 7 wt.% finely dispersed pseudo-boehmite Dispal 14N4-80 (Sasol Chemicals, USA), 10 wt.% isopropyl alcohol and 10 wt.% 1,4-butanediol (Merck KGaA, Germany). A general scheme of a Binder Jetting printer setup is depicted in Fig. 4(a).

## 6. Comparison of Direct Ink Writing and Binder Jetting for additive manufacturing of Pt/Al<sub>2</sub>O<sub>3</sub> catalysts for the dehydrogenation of perhydro-dibenzyltoluene

H.M. Bui et al.

Chemical Engineering Journal 458 (2023) 141361

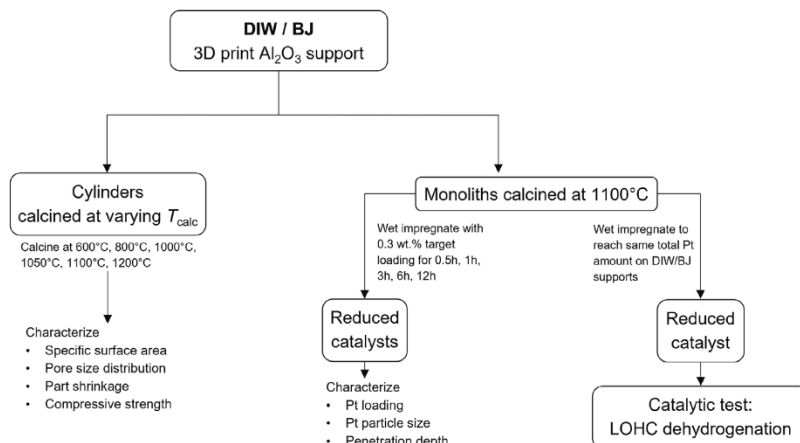


Fig. 2. Overview of the experimental outline.

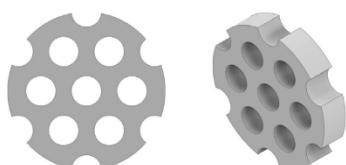


Fig. 3. Front (left) and isometric view (right) of the monolith CAD file.

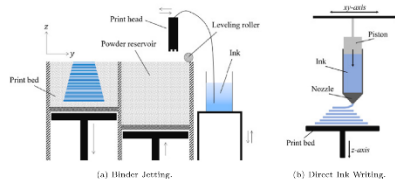


Fig. 4. General schemes of the printing techniques used in this study.

The green parts were cured at 75 °C for at least 2 h after printing and debinded at 600 °C for 3 h in a muffle furnace (witeg Labortechnik GmbH, Germany) until PVP decomposed completely. The debinded parts were infiltrated with a boehmite slurry (see Ref. [49]) and calcined at varying temperatures (600, 800, 1000, 1050, 1100 and 1200 °C). The first step of the temperature program included heating to 120 °C with a ramp of 2 K/min held for 2 h followed by heating to the desired calcination temperature with a ramp of 3 K/min held for 3 h.

### 2.1.2. Alumina support fabrication by DIW

The paste composition for the alumina support obtained via DIW has already been published elsewhere [27]. 45.5 wt.% Disperal 60 and 19.5 wt.% Pural SB (both Sasol Germany GmbH) were mixed two times with 35 wt.% acetic acid (pH 3, Sigma Aldrich, Germany) by means of a SpeedMixer at a maximum of 3500 rpm for 2 min with 3 min cooldown time in between. The paste was then filled into a syringe and installed in a self-constructed DIW printer that was equipped with a 0.41 mm nozzle. A general setup of a DIW printer is shown in Fig. 4(b). To improve removal of the printed monolithic structures from the printbed, it was covered with a thin layer of Formentrennöl C (Clariant Produkte Deutschland GmbH). The printed parts were dried on the printbed for 24 h prior to calcination at different temperatures. Similar to the BJ procedure, a two step calcination in a muffle furnace (witeg

Labortechnik GmbH, Germany) was performed with an isothermal step at 120 °C and final temperatures of 600, 800, 1000, 1050, 1100 and 1200 °C. The first step was held for 2 h, the second one for 3 h with heating rates of 2 K/min and 3 K/min, respectively.

### 2.1.3. Wet impregnation with H<sub>3</sub>Pt(SO<sub>3</sub>)<sub>2</sub>(OH)

Monoliths used for impregnation time variation experiments were impregnated with a target Pt loading of 0.3 wt.% for both 3D printing methods. The monoliths were immersed while hanging in a constant volume of bidistilled water. Subsequently, H<sub>3</sub>Pt(SO<sub>3</sub>)<sub>2</sub>(OH) solution was weighed and added. The platinum sulfite acid solution was stirred at 500 rpm for 0.5, 1, 3, 6 and 12 h.

Monoliths used for the LOHC dehydrogenation test were wet impregnated ensuring that BJ and DIW printed monoliths contained the same total Pt loading per shape, as the weight per calcined shapes varied significantly between BJ and DIW. Thus, BJ printed monoliths were impregnated for 3 h with a target loading of 0.4 wt.% Pt and DIW printed parts with a target loading of 0.2 wt.%.

After wet impregnation, the monoliths were calcined in a muffle furnace (witeg Labortechnik GmbH, Germany). The temperature program comprised heating to 60 °C with a rate of 1 K/min held for 1 h, then a second drying step at 120 °C heated with a rate of 1 K/min and an isothermal phase of 3 h, followed by heating with 2 K/min to 400 °C which was held for 3 h.

The calcined monoliths were then reduced in a tube furnace (Nabertherm GmbH, Germany) under a constant flow of 10% H<sub>2</sub>/N<sub>2</sub> (Westfalen GmbH, Germany) at 400 °C for 3 h using a heating rate of 1 K/min.

## 2.2. Catalyst characterization

### 2.2.1. Variation of calcination temperature

Height and diameter of the printed test cylinder before and after calcination were obtained using a tablet hardness testing system with an integrated option for length measurement (MultiTest 50, Dr. Schleuniger Pharmatron, Switzerland). The part to be measured was placed in the measuring area between two stainless steel brackets, one moving towards the other with a constant moving speed of 2 mm/s. Once a certain resistance from the inserted test body is recognized, the diameter or height, depending on the testing orientation, is recorded.

The compression strength was measured with the MultiTest 50, which was also used for above described size measurement. Uniaxial compression on the lateral surface of the samples between two opposite metal plates was performed, characterizing the cylinder's response to loading perpendicular to its length, until fracturing occurs. One of the

## 6. Comparison of Direct Ink Writing and Binder Jetting for additive manufacturing of Pt/Al<sub>2</sub>O<sub>3</sub> catalysts for the dehydrogenation of perhydro-dibenzyltoluene

H.M. Bui et al.

Chemical Engineering Journal 458 (2023) 141361

plates moved towards the other with a constant velocity of 2 mm/s. The fracture load  $F$  was automatically collected and used in the following equation given by Timoshenko and Goodier [50], yielding the compression strength  $\sigma_{\text{comp}}$ :

$$\sigma_{\text{comp}} = \frac{2F}{\pi dh} \quad (1)$$

where  $F$  is the load at failure,  $d$  and  $h$  are the diameter and height of the cylinder.

The poreSD of the test cylinders calcined at 1100 °C was determined by mercury intrusion porosimetry (MIP) (AutoPore 9600, Micromeritics Instrument Corporation). Per measurement, two cylinders were added to the penetrometer comprised of a 5 mL bulb volume and 0.392 mL stem volume. To reduce the influence of the hydrostatic pressure of mercury in the low pressure region, the pressure range of 0.5 - 45 psi was measured in a horizontal penetrometer position, while the pressure range from 45 - 61 000 psi was obtained in vertical penetrometer position. The pressure steps were chosen to achieve an even spacing on the logarithmic scale with 25 points per decade in a pressure range between 0.5 and 4000 psi and with 40 points per decade in a pressure range between 4000 and 61 000 psi. The latter pressure range with higher resolution correlates to pore diameters of 3.5 - 53.3 nm, respectively. The pressure at each pressure step was held constant until the intrusion rate was below 0.01  $\mu\text{L}/(\text{gs})$ . To convert the pressure  $p$  to a pore diameter  $d_{\text{pore}}$ , Washburn's equation was applied:

$$d_{\text{pore}} = -\frac{4 \cdot \gamma_{\text{Hg}} \cdot \cos \theta}{p} \quad (2)$$

with the surface tension of mercury  $\gamma_{\text{Hg}} = 0.480 \text{ N/m}$  and the contact angle  $\theta = 140^\circ$ .

N<sub>2</sub> physisorption at 77 K (Nova 4200e, Quantachrome Instruments) was used to determine the specific surface area  $S_{\text{BET}}$ . Sample pretreatment comprised degassing under vacuum at 120 °C for 3 h.  $S_{\text{BET}}$  was determined according to the method of Brunauer, Emmett, and Teller (BET) and calculated between  $0.05 \leq p/p_0 \leq 0.3$ . Moreover, the Barrett, Joyner, Halenda (BJH) method was applied to analyze the poreSD using the desorption branch of the isotherm. Data points were collected from  $p/p_0 = 0.01 - 0.999$ .

Phase determination of the alumina supports was obtained via XRD analysis (Empyrean, Malvern Panalytical, UK). Cu-K $\alpha$  radiation ( $\lambda = 1.54056 \text{ \AA}$ ) and a monochromator were employed to scan the samples applying a step size of  $0.007^\circ$  and 70 steps/min from  $2\theta = 5 - 90^\circ$ .

### 2.2.2. Variation of impregnation time

Inductively coupled plasma optical emission spectrometry (ICP-OES) measurements were performed on an Agilent 700 Series ICP Optical Emission Spectrometer to investigate the amount of platinum loaded on the different carriers. Ground catalyst powder of the respective catalysts was dissolved in aqua regia overnight consisting of hydrochloric acid and nitric acid (both Sigma Aldrich, Germany) at a ratio of 3:1 vol.%. The sample was then diluted with bidistilled water and filtered with a  $0.45 \mu\text{m}$  syringe filter (VWR, Germany). A platinum standard (AAS grade, Sigma Aldrich, Germany) was used for calibration. Furthermore, the wavelength of 214.42 nm was used to calculate the platinum loading.

Transmission electron microscopy (TEM) was carried out on a JEOL JEM 1400 plus instrument at an acceleration voltage of 120 kV to determine the metal particle diameter  $d_M$  and the resulting metal dispersion  $D_M$ . The samples were finely ground, suspended in absolute ethanol (Sigma-Aldrich) and finely dispersed by ultrasound. After sedimentation of larger particles, two drops of the suspension were deposited onto a Holey Multi A copper grid (Quantifoil Micro Tools GmbH) and left to dry. The metal particle diameter  $d_M$  was determined using the image processing software imageJ. For each sample, a minimum of 460 particles was counted on several micrographs taken on different zones of the TEM grid.  $D_M$  is indirectly proportional to  $d_M$  and is determined

according to Eq. (3) with the volume of the bulk metal atom  $V_{\text{B,M}}$  and the area occupied by one surface atom  $A_{\text{S,M}}$  [51].

$$D_M = K \cdot \frac{V_{\text{B,M}}}{d_M \cdot A_{\text{S,M}}} = K \cdot \frac{M_M}{d_M \cdot A_{\text{S,M}} \cdot N_A \cdot \rho_M} \quad (3)$$

$V_{\text{B,M}}$  is calculated with the molar mass of the metal  $M_M$ , the Avogadro constant  $N_A$  and the bulk metal density  $\rho_M$ . For spherical particles, the shape factor  $K$  is 6.

The penetration depth of the Pt layer after wet impregnation for varying durations was measured with a light microscope MZ8 (Leica, Germany) equipped with a MicroCam II (Bresser, Germany). The monoliths were fragmented at different locations with a scalpel and microscopically examined. The penetration depth was manually determined with the corresponding software at at least 35 locations and averaged arithmetically.

### 2.3. LOHC dehydrogenation

The catalytic performance of the BJ and DIW printed Pt/Al<sub>2</sub>O<sub>3</sub> catalysts was investigated using the dehydrogenation of perhydro-dibenzyltoluene. The experimental setup was a semi-batch reactor, consisting of a heated three-neck round-bottom flask with flow breakers connected to a reflux condenser, an overpressure valve and a Type K thermocouple for temperature regulation of the endothermic reaction.

The reaction was carried out under an inert Ar atmosphere at ambient pressure. 18H-DBT (Hydrogenious LOHC Technologies GmbH, Germany) was preheated to 325 °C before the catalyst was added to the liquid and stirred at a constant speed of 500 rpm. After complete insertion of the catalyst into the 18H-DBT, the temperature was immediately regulated down to the reaction temperature of 310 °C.

Catalytic tests with monoliths were performed using two monoliths for each measurement. The 3D printed catalysts were stacked on top of each other on a mesh made of stainless steel and immersed into the liquid reactant. For catalyst powder tests, two monoliths were ground and added to the 18H-DBT once the start temperature was reached. The catalyst powder was not pressed and sieved to ensure the usage of the complete egg-shell catalyst during reaction without sorting out Pt-rich or Pt-lean parts of the monolith. The average particle size of  $89 \mu\text{m}$  was determined via laser diffraction (see Supporting Information, Fig. S2). The weight ratio of Pt/18H-DBT = 0.08  $\text{mg}_{\text{Pt}}/\text{g}_{18\text{H-DBT}}$  was kept constant. Consequentially, the amount of used 18H-DBT was adjusted for each reaction.

To determine the degree of dehydrogenation (DoD) during the reaction, 24 samples were withdrawn with a syringe at certain time points during the total reaction time of 9 h. The aliquots were analyzed using proton nuclear magnetic resonance spectroscopy (<sup>1</sup>H-NMR) on a Bruker Ascend spectrometer at 400 MHz. All spectra were referred to the residual proton signal of the solvent acetone-d<sub>6</sub>. The DoD was calculated using the ratio  $x$  of the integral of the aromatic to the integral of all protons based on the <sup>1</sup>H-NMR data according to Do et al. [44] and Preuster [52]:

$$\text{DoD} = 1.3945 \cdot x^6 - 4.9037 \cdot x^5 + 5.6287 \cdot x^4 - 5.207 \cdot x^3 + 4.00985 \cdot x^2 - 2.9217 \cdot x + 1 \quad (4)$$

The Pt productivity  $P$  is introduced for better comparison between measured dehydrogenation activities.  $P$  describes the ratio between the released amount of hydrogen per amount of Pt and time [53,54]:

$$P = \frac{m_{\text{H}_2}}{m_{\text{Pt}} \cdot t} = \frac{\Delta \text{DoD} \cdot m_{18\text{H-DBT}} \cdot \frac{M_{\text{H}_2}}{M_{18\text{H-DBT}}} \cdot \frac{v_{\text{H}_2}}{v_{18\text{H-DBT}}}}{m_{\text{cat}} \cdot w_{\text{Pt}} \cdot \Delta t} \quad (5)$$

$m_{\text{H}_2}$ ,  $m_{18\text{H-DBT}}$  and  $m_{\text{cat}}$  represent the mass of evolved H<sub>2</sub>, mass of 18H-DBT and catalyst mass, respectively.  $M_{\text{H}_2}$  and  $M_{18\text{H-DBT}}$  are the respective molar masses of hydrogen and Pt while  $v_{\text{H}_2}$  and  $v_{18\text{H-DBT}}$  are the stoichiometric coefficients.  $w_{\text{Pt}}$  is the platinum loading.  $P$  was determined in the range  $\Delta \text{DoD} = 10 - 60 \%$  while using the corresponding time difference  $\Delta t$ .

## 6. Comparison of Direct Ink Writing and Binder Jetting for additive manufacturing of Pt/Al<sub>2</sub>O<sub>3</sub> catalysts for the dehydrogenation of perhydro-dibenzyltoluene

H.M. Bui et al.

Chemical Engineering Journal 458 (2023) 141361

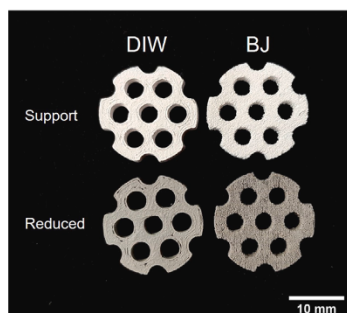


Fig. 5. Photos of monolithic alumina supports (first row) and reduced Pt/Al<sub>2</sub>O<sub>3</sub> catalysts (second row) fabricated by DIW (first column) and BJ (second column).

### 3. Results and discussion

#### 3.1. 3D printed catalysts

Fig. 5 displays the printed alumina supports as well as the reduced Pt/Al<sub>2</sub>O<sub>3</sub> catalysts for BJ and DIW next to each other. For both parts, different surface structure characteristics can be observed that are closely related to the respective printing techniques. DIW creates smoother surfaces with a partially visible printing pathway due to the extrusion-based layering technique. The BJ printed parts are substantially more porous as can be seen by the rough surface texture. Furthermore, the printing and print head moving direction can be detected for the BJ printed based on the parallel line pattern caused by the print head moving back and forth in one direction during printing.

#### 3.2. Calcination temperature variation

##### 3.2.1. Shrinkage

Due to differing printing methods, feedstock properties and post-processing procedures, shapes produced via Binder Jetting and Direct Ink Writing differ in the dimensions of the final part. Figs. 6(a) and 6(b) compare the shrinkage behavior of the two printing methods with increasing calcination temperature  $T_{\text{calc}}$ . Hereby, Fig. 6(a) displays the absolute height and diameter of the printed test cylinders of the green bodies as well as after calcination.

Apart from the green part, both BJ and DIW show the same trend towards decreasing dimensions. For BJ, the green part dimensions exceed the target value of 6 mm for the height and diameter. This is caused by hardware related printing inaccuracies or bleeding, which is macroscopic flow of binder caused by slight oversaturation of the powder bed due to high ink saturation levels [42,55]. Because DIW printed parts are left to dry at room temperature on the print bed immediately after the print job has finished, the green parts are smaller than the target dimensions due to shrinking (see Fig. 6(a)). Fig. 6(b) depicts the shrinkage of both printing methods relative to the green part dimension. While shrinkage for DIW amounts to about 3% until 1100 °C, BJ printed parts exhibit larger relative shrinkage of up to 9% due to a more porous particle framework and the generation from a loose powder bed. Within the ink used for DIW and due to the drying the solid components are more tightly packed, therefore generally inhibiting extensive shrinkage of the printed structure compared to BJ. Furthermore, it has to be taken into account that both green parts, on which the shrinkage is based, vary in height and diameter. Significant shrinkage occurs for BJ and DIW after 1100 °C, visible by a steep decline in cylinder height and diameter (Fig. 6(a)) and a relatively sharp increase in relative shrinkage (Fig. 6(b)). The transition to the thermodynamically most stable phase  $\alpha$ -Al<sub>2</sub>O<sub>3</sub> starts at this temperature

Table 1

Specific surface area  $S_{\text{BET}}$  of 3D printed alumina supports calcined at varying calcination temperatures.

$T_{\text{calc}}$ (°C)	$S_{\text{BET}}$ (m <sup>2</sup> /g)	
	BJ	DIW
600	166	102
800	92	69
1000	65	57
1050	70	36
1100	26	11
1200	9	9

range and induces pronounced sintering and particle shrinkage [56] followed by part densification and mechanical stabilization. Between 1100 °C and 1200 °C part dimensions do not change considerably as further heating does not alter the alumina morphology any more. These differences regarding the shrinkage behavior should be taken into account for accurately sized final parts.

##### 3.2.2. Compression strength

The effect of  $T_{\text{calc}}$  on the compression strength  $\sigma_{\text{comp}}$  is reflected in the uniaxial compression strength test results summarized in Fig. 7. The threshold of 1100 °C is also visible here, where especially DIW printed cylinders gained significant stability compared to shapes calcined below 1100 °C. While cylinders calcined at 1050 °C show a compression strength of 1.4 MPa,  $\sigma_{\text{comp}}$  increases less than four times to 5.2 MPa at 1100 °C and reaches 6.0 MPa at 1200 °C.

Except for the green part, BJ printed test cylinders show a similar robustness as DIW printed parts until 1000 °C. Green parts produced by DIW are more stable by default because of the already consolidated structure after drying at ambient conditions, whereas the particles of the green parts generated by BJ are relatively weakly connected.

The distinct stability increase at 1100 °C is observable for BJ as well, but the absolute  $\sigma_{\text{comp}}$  reaches slightly lower values. Calcined at 1050 °C,  $\sigma_{\text{comp}}$  is located at 0.5 MPa and stagnates at 1.2 MPa above 1100 °C. In accordance with constant part dimensions at high calcination temperatures in Figs. 6(a) and 6(b), further increase of  $T_{\text{calc}}$  does not improve the part stability due to no more densification by sintering.

At 1100 °C, the compression strength of DIW exceeds the stability of BJ printed parts by a factor of 4.3 and even a factor of 5 at 1200 °C. Again, this effect originates from print technique related part properties, which were previously discussed for the shrinkage behavior and specific surface area. The similar compression strength values of BJ and DIW until 1000 °C stem from minor sintering activity in this temperature range so that densification by thermal processing is equally low for both AM techniques. However, above 1100 °C the more densely packed alumina particles in the pasty printing feedstock come into effect by providing a larger number of contacting points, resulting in more effective densification by sintering leading to improved sintering and compression strength.

##### 3.2.3. Specific surface area

The above discussed part shrinkage and increase in compression strength with increasing  $T_{\text{calc}}$  correlates directly with a decline in specific surface area  $S_{\text{BET}}$  (see Table 1). Calcined at 600 °C, BJ and DIW printed alumina cylinders have a specific surface area of 166 m<sup>2</sup>/g and 102 m<sup>2</sup>/g, respectively. In accordance with the observations in Figs. 6(a) and 6(b)  $S_{\text{BET}}$  decreases sharply above 1100 °C due to sintering processes, diminishing micro- and mesoporous structures.

At low calcination temperatures below 1200 °C, BJ printed parts generally possess a larger  $S_{\text{BET}}$  than DIW. Again, the printing principle inherently causes BJ to generate more porous shapes which manifests itself in higher surface areas. Still with the declining trend, the values of  $S_{\text{BET}}$  converge more and more and above 1200 °C the final sintering state is reached where the majority of pores detectable by N<sub>2</sub> physisorption were eliminated, resulting in the same low final specific surface area of 9 m<sup>2</sup>/g for both printing methods.

## 6. Comparison of Direct Ink Writing and Binder Jetting for additive manufacturing of Pt/Al<sub>2</sub>O<sub>3</sub> catalysts for the dehydrogenation of perhydro-dibenzyltoluene

H.M. Bui et al.

Chemical Engineering Journal 458 (2023) 141361

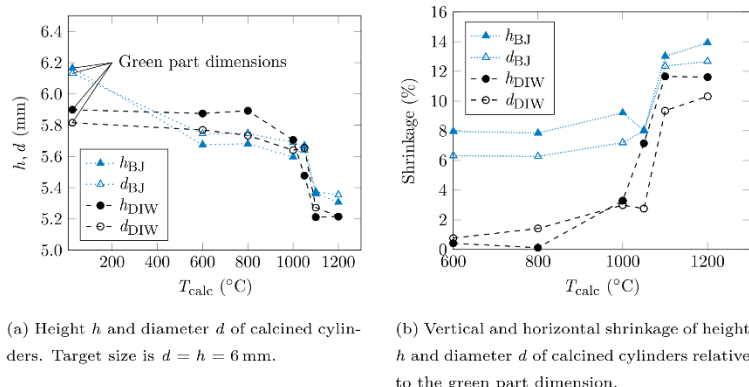


Fig. 6. Size change of BJ and DIW printed alumina test cylinders in dependence of calcination temperature.

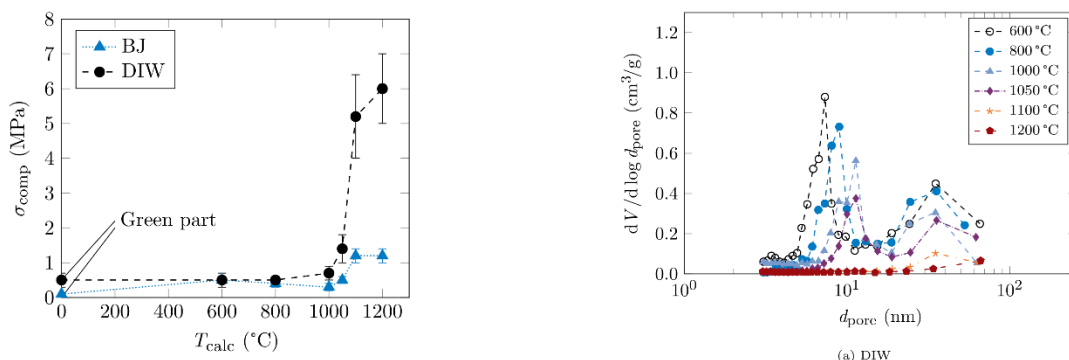


Fig. 7. Comparison of DIW and BJ compression strengths of printed alumina supports calcined with varying calcination temperatures.

### 3.2.4. Pore size distribution

In order to assess the optimal calcination temperature for catalysts for application in the dehydrogenation of perhydro-dibenzyltoluene, the poreSD was analyzed via N<sub>2</sub> gas adsorption. Studies regarding diffusional phenomena during LOHC dehydrogenation on Pt/Al<sub>2</sub>O<sub>3</sub> by Seidel [53] and Auer [54] revealed that a minimum mean pore diameter of 26 nm is necessary in order to avoid reduced activity due to restricted diffusion of the reactant during the dehydrogenation of 18H-DBT. The poreSD of DIW and BJ printed test cylinders are summarized in Fig. 8 and agree with each other such that below  $T_{\text{calc}} = 1100$  °C a bimodal poreSD is present in both cases. According to general consensus [57], pores enlarge and eventually disappear during the heating process. Moreover, the correlation between specific surface area and pore size is inversely proportional, noticeable in Fig. 8.

Below 1100 °C, DIW printed parts show two major pore sizes (Fig. 8(a)). The larger pores were located at about 33 nm, while the smaller pore sizes shift from 7 nm at 600 °C to larger pore sizes of about 11 nm at 1050 °C. Within this temperature range, BJ printed parts display a similar trend (Fig. 8(b)). Larger pores are found between 15 - 20 nm, while the smaller pores also shift to larger sizes ranging between 4 - 10 nm as the calcination temperature rises. Gas adsorption measurements revealed that upon exceeding  $T_{\text{calc}} = 1100$  °C 3D printed parts made by both printing techniques show almost no inherent porosity, visible by the flat curves for the poreSD for  $T_{\text{calc}} = 1100$  °C and 1200 °C. This finding is consistent with the previous observation of declining specific surface area (Table 1) and increasing compression strength with increasing calcination temperature (Fig. 7).

Based on the pore size analysis by nitrogen gas adsorption it was determined that the calcination temperature of 1100 °C was most suitable

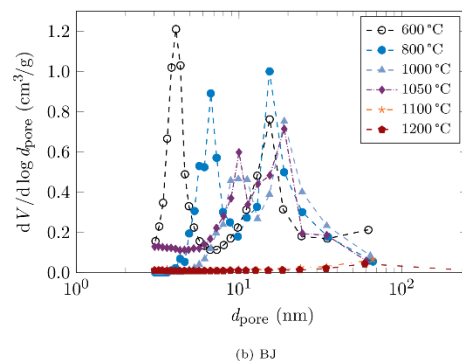


Fig. 8. Pore size distribution of the 3D printed alumina supports from (a) DIW and (b) BJ calcined at varying calcination temperatures, determined by N<sub>2</sub> physisorption.

for the preparation of 18H-DBT dehydrogenation catalyst supports in this study. This way, mean pore diameters below 26 nm could be diminished so that diffusional restrictions during the reaction were avoided.  $T_{\text{calc}} < 1100$  °C were therefore excluded for further investigations. Furthermore, the mechanical stability already increased tremendously at 1100 °C (see Fig. 7) which also favors this choice.  $T_{\text{calc}} > 1100$  °C would lead to slightly higher  $\sigma_{\text{comp}}$  values, but also correlates with a reduced specific surface area and consequently, reduced activity, making higher  $T_{\text{calc}}$  unideal.

Additionally, the poreSD was measured by mercury intrusion porosimetry for the printed samples. Fig. 9 compares BJ and DIW alumina supports calcined at 1100 °C regarding their poreSD. In contrast to N<sub>2</sub> physisorption, larger interparticle pores, hereafter referred

## 6. Comparison of Direct Ink Writing and Binder Jetting for additive manufacturing of Pt/Al<sub>2</sub>O<sub>3</sub> catalysts for the dehydrogenation of perhydro-dibenzyltoluene

H.M. Bui et al.

Chemical Engineering Journal 458 (2023) 141361

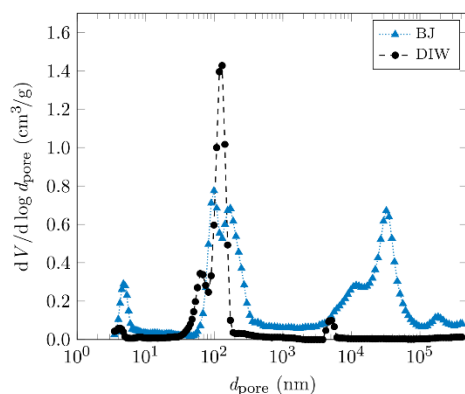


Fig. 9. Pore size distribution of 3D printed alumina supports calcined at 1100 °C, determined by MIP.

to as “voids”, are detected by MIP due to its large measurement range spanning from 3 - 500 000 nm in comparison to gas adsorption, which can theoretically detect pores between 0.3 - 300 nm. However, in this case, pores greater than 100 nm could not be recorded with gas adsorption. N<sub>2</sub> physisorption does not reveal any pores in the micro and mesopore region in Fig. 8, whereas MIP does show a small percentage of pores at 4 - 5 nm (less than 0.3 cm<sup>3</sup>/g), see Fig. 9. This difference might be caused by the different measuring methods. Voids originate from the random powder particle arrangement of specific size and shape and their agglomeration within the paste (DIW) or powder bed (BJ) and the resulting particle framework after thermal treatment. The most prominent difference between BJ and DIW depicted in Fig. 9 is the percentage of very large voidages at about 30 000 nm for BJ alumina supports. These voids do not exist in DIW printed parts.

In general, the data highlights structural differences due to the additive manufacturing method and underlines the coarser pore size structure generated from a powder-based printing method, also indicated by a porosity of 77% for BJ and 56% for DIW, determined directly by MIP.

### 3.3. Impregnation time variation

#### 3.3.1. Metal loading

The fabricated monoliths calcined at 1100 °C were impregnated with a target Pt loading of 0.3 wt.%. The duration of immersion in the impregnation solution was varied to investigate the reached loading, impregnation depth and Pt particle size. As expected, the platinum loading rises with increased impregnation time. However, Fig. 10(a) suggests that neither BJ nor DIW monoliths reach the calculated  $w_{Pt}$  but achieve a maximum Pt loading of 0.21 wt.% and 0.15 wt.%, respectively after 12 h.

The reason for incomplete impregnation of monoliths printed with both methods could be given by the comparably small external surface area due to the geometric design. Choosing another monolith shape with an extended outer surface area would facilitate a higher metal loading. Furthermore, the internal surface area  $S_{BET}$  (see Table 1), controllable by certain parameters including the calcination temperature, plays a role for the impregnation efficiency. At a calcination temperature of 1100 °C,  $S_{BET}$  of BJ and DIW alumina supports drops to 26 m<sup>2</sup>/g and 11 m<sup>2</sup>/g, respectively. Reducing  $T_{calc}$  would lead to a larger specific surface area available for Pt impregnation but in this case would interfere with the minimum requirement for the mean pore diameter of 26 nm.

The difference in obtainable Pt loading between the two printing methods is caused by the pore size and surface area characteristics

of each technique. As already discussed in the previous sections, BJ printed objects are significantly more porous (Fig. 9) and possess a larger specific surface area (Table 1). Therefore, a higher amount of Pt can adsorb on the surface in comparison to a DIW printed support with an identical external surface area.

After an impregnation time of 12 h,  $w_{Pt}$  does not increase substantially, so that the achieved loading after 12 h approximates the highest possible Pt loading. Fig. 10(a) corroborates this by asymptotically approaching a  $w_{Pt}$  maximum.

#### 3.3.2. Metal particle size and dispersion

TEM was used to determine the particle size distribution and the resulting metal dispersion of the Pt particles on the alumina support (Table 2). The detailed particle size distributions are displayed in the Supporting Information (see Fig. S3 and S4). The data shows that prolonged impregnation time leads to increasing metal particle size  $d_p$ . Moreover,  $d_p$  is similar for BJ and DIW, taken into account the relatively high standard deviation, which is in the same range for both printing methods. After 0.5 h, BJ catalysts have a particle size of  $1.10 \pm 0.27$  nm which grows to  $1.50 \pm 0.32$  nm after 12 h. Similarly, the Pt particle size increases from  $1.05 \pm 0.23$  nm to  $1.48 \pm 0.33$  nm for DIW printed catalysts. However, with diameters ranging from 1.05 - 1.50 nm overall, the metal particle size is very small in general for all prepared catalysts, resulting in relatively high Pt dispersion (see Table 2).

As the dispersion is inverse proportional to the platinum particle diameter  $d_p$ , DIW and BJ catalysts show a similar dispersion for the same impregnation duration, suggesting that the crystalline structure of the alumina supports is comparable. Previous studies suggest that metal particle size and dispersion of Pt/Al<sub>2</sub>O<sub>3</sub> catalysts are more strongly affected by the crystalline phase of the support than the BET surface area [58,59]. The available data corroborates this statement, as the specific surface area of BJ printed alumina supports is more than double the DIW printed ones (Table 1) but the dispersion of BJ supports is not superior to DIW. The DIW feedstock consists of boehmite  $\gamma$ -AlOOH, whereas the BJ powder feedstock is mainly bayerite  $\alpha$ -Al(OH)<sub>3</sub>. At 1100 °C, both bayerite and boehmite undergo a similar transformation to late transition alumina phases, which could be either  $\theta$ -Al<sub>2</sub>O<sub>3</sub> or possibly already  $\alpha$ -Al<sub>2</sub>O<sub>3</sub> [60,61]. Nevertheless, the transition pattern is similar for boehmite and bayerite at this temperature range, so that the similar surface morphology of the printed alumina support explains the comparable Pt particle sizes and dispersion.

Increasing impregnation times decrease the metal dispersion, as after 12 h,  $D_{Pt}$  is below 70% in comparison to over 90% after 0.5 h of impregnation. Numerous studies confirm that at lower loadings ( $\leq 1$  wt.%) the amount of Pt per anchoring site on the alumina support is lower so that a high dispersion, even atomic dispersion, is possible [58,62–64]. Increasing the amount of Pt in the dispersed phase favors the formation of Pt clusters as the Pt loading tends to exceed the number of anchoring sites. However, TEM images of the wet impregnated alumina monoliths (Fig. 12) still give evidence for highly dispersed Pt species on the support surface as no severe agglomerates are visible.  $d_p$  increases with increasing impregnation time. Still, the overall particle size is very small, so that the wet impregnation technique is suitable to immobilize Pt species finely dispersed on the printed alumina supports.

#### 3.3.3. Platinum penetration depth

Table 2 indicates that the penetration depth of Pt varies with impregnation time. Penetration depth for DIW printed samples with a target Pt loading of 0.3 wt.% increases from 107  $\mu$ m to 293  $\mu$ m when left in the impregnation solution for 0.5 h and 12 h, respectively. Analogous, the smallest penetration depth of 165  $\mu$ m for BJ catalysts was achieved after 0.5 h whereas the layer thickness grew to 274  $\mu$ m after 12 h.

## 6. Comparison of Direct Ink Writing and Binder Jetting for additive manufacturing of Pt/Al<sub>2</sub>O<sub>3</sub> catalysts for the dehydrogenation of perhydro-dibenzyltoluene

H.M. Bui et al.

Chemical Engineering Journal 458 (2023) 141361

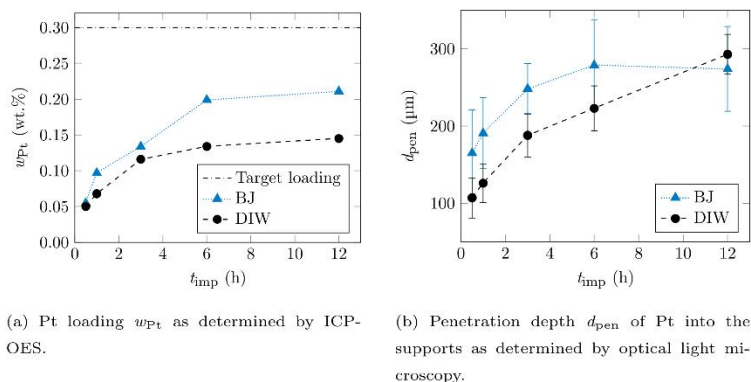


Fig. 10. Pt loading and penetration depth in dependence of the wet impregnation duration  $t_{imp}$ . Supports were calcined at 1100 °C and impregnated with a target Pt loading of 0.30 wt. %.

Table 2

Overview of characterization data for monoliths calcined at 1100 °C: Pt loading  $w_{Pt}$ , average particle size  $d_{Pt}$ , resulting Pt dispersion  $D_{Pt}$  and Pt penetration depth  $d_{pen}$  of BJ and DIW printed samples depending on the impregnation time  $t_{imp}$ .

$t_{imp}$ (h)	$w_{Pt}$ <sup>a</sup> (wt.%)		$d_{Pt}$ <sup>b</sup> (nm)		$D_{Pt}$ (%)		$d_{pen}$ <sup>c</sup> (µm)	
	BJ	DIW	BJ	DIW	BJ	DIW	BJ	DIW
0.5	0.06	0.05	1.10 ± 0.27	1.05 ± 0.23	91.9	96.0	165 ± 56	107 ± 26
1.0	0.10	0.07	1.19 ± 0.30	1.10 ± 0.24	84.7	91.6	191 ± 46	126 ± 25
3.0	0.13	0.12	1.21 ± 0.28	1.32 ± 0.28	83.5	76.4	248 ± 33	188 ± 28
6.0	0.20	0.13	1.28 ± 0.33	1.39 ± 0.29	78.9	72.7	279 ± 59	223 ± 29
12.0	0.21	0.15	1.50 ± 0.32	1.48 ± 0.33	67.4	68.3	274 ± 55	293 ± 26

<sup>a</sup>Determined by ICP-OES. Target loading:  $w_{Pt} = 0.3$  wt. %.

<sup>b</sup>Determined by TEM.

<sup>c</sup>Measured with incident light microscope.

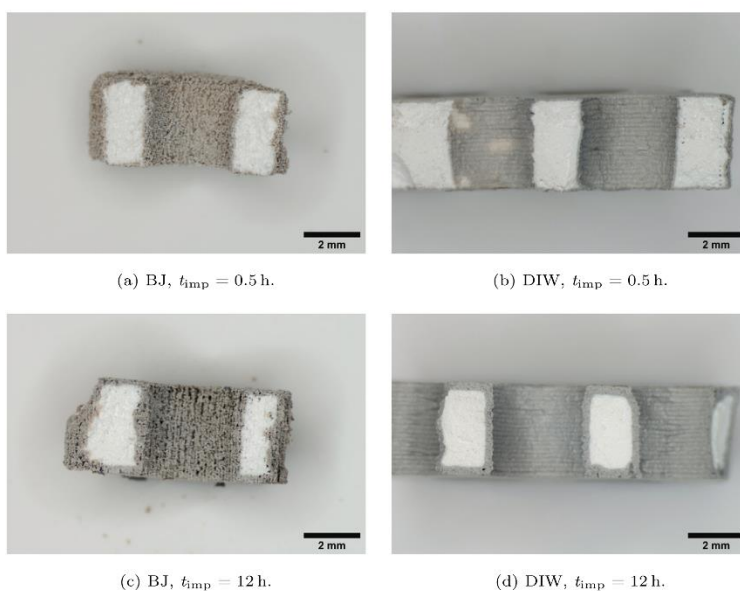


Fig. 11. Light microscopic images of printed Pt/Al<sub>2</sub>O<sub>3</sub> catalysts used for Pt penetration depth analysis in dependence of the wet impregnation times  $t_{imp}$  for BJ and DIW printed supports calcined at 1100 °C. Target Pt loading  $w_{Pt,target} = 0.3$  wt. %.

## 6. Comparison of Direct Ink Writing and Binder Jetting for additive manufacturing of Pt/Al<sub>2</sub>O<sub>3</sub> catalysts for the dehydrogenation of perhydro-dibenzyltoluene

H.M. Bui et al.

Chemical Engineering Journal 458 (2023) 141361

By applying the wet impregnation method, the printed supports were prewetted with bidistilled water before the platinum sulfite salt solution was added, so that the only driving force moving the impregnation front inwards is diffusion [65,66]. Fig. 11 shows light microscopic images of the impregnated catalysts where an egg-shell structure is discernible for all samples, meaning adsorption was faster than diffusion in general and/or relatively strong during wet impregnation.

Fig. 11 shows the resulting sharp border visible in the prepared catalysts in this study. The impregnation front moves further inward with increasing impregnation duration (Table 2) because a longer equilibration time for diffusion of the solvated metal species towards the center is provided [67]. Thus, theoretically there is the possibility that the metal eventually approaches a uniform distribution. However, the large pellet size presumably prevents complete penetration into the center in this case.

The trends in Fig. 10(b) suggest that the impregnation front still has the potential to move further inward for DIW, implied by the continuously rising trend until 12 h in Fig. 10(b). Contrary to this,  $d_{pen}$  for BJ reaches its maximum after 6 h at a thickness of about 280 nm. Factors leading to dissimilar penetration depths between BJ and DIW despite an identical impregnation routine are the surface morphology of the support and the porous structure of the printed supports.

DIW shows a higher penetration depth at 12 h due to a lower BET surface area available for Pt deposition. Thus, Pt diffuses deeper into the catalyst center. Additionally, the catalyst loading is calculated mass based. As the DIW supports are double the mass of BJ parts, the amount of Pt per monolith is higher for DIW which is another reason for the deeper penetration at 12 h. These effects are ruled out at lower impregnation times, as the considerably higher macroporosity of BJ parts enables faster penetration.

The impregnation front is much sharper for DIW catalysts, see Figs. 11(b) and 11(d) than for BJ. The higher voidage generated by BJ (Fig. 9) offers a less obstructed diffusion pathway for the dissolved Pt species, therefore resulting in a deeper impregnation with a frayed impregnation front (Figs. 11(a), 11(c)). This effect is also visible in the higher standard deviations for  $d_{pen}$  of BJ samples, see Table 2.

### 3.4. Characterization of catalysts used for testing

Pt/Al<sub>2</sub>O<sub>3</sub> catalysts which were eventually used for the catalytic tests were prepared by impregnation of printed monolithic supports which were calcined at 1100 °C. Phase determination of the alumina supports via XRD (see Supporting Information, Fig. S1) reveals that BJ printed supports consist of  $\alpha$ -Al<sub>2</sub>O<sub>3</sub> only, and DIW printed supports also contain mainly  $\alpha$ -Al<sub>2</sub>O<sub>3</sub> but include weak reflexes assigned to  $\theta$ -Al<sub>2</sub>O<sub>3</sub>. Due to slightly differing feedstock compositions, namely bayerite for BJ and boehmite for DIW, the final alumina phase composition after calcination at 1100 °C can slightly vary but is assessed to be very similar. Furthermore, the observed alumina phases correspond to reported transition temperatures found in literature [68]. Moreover, the alumina lattice structure is unaffected by 3D printing as no shifts in diffraction angle are visible.

For all dehydrogenation reactions, the total amount of platinum per monolith was held constant, independent of the printing technique. One calcined monolith fabricated via DIW has an average weight of 0.81 g whereas calcined BJ monoliths weigh 0.41 g. Based on the previous results regarding the specific surface area and weight, a target Pt loading of 0.2 wt.% for DIW and 0.4 wt.% for BJ was chosen. The Pt impregnation time of 3 h was selected such that the difference between the characterization data (see Table 3) was minimized or a compromise was found. Ultimately, a Pt dispersion  $D_{Pt} > 90\%$  and small metal particle sizes of about 1.1 nm were targeted for both catalysts.

Similar to previous Pt loading determination by ICP-OES (see Section 3.3.1), the target values were again not met. Instead of 0.4 wt.% for BJ and 0.2 wt.% for DIW, only 0.21 wt.% and 0.11 wt.% were reached, respectively. However, for both printing methods, the loading is lower

than intended by almost the same factor, so that the prerequisite of same total Pt amount of approximately 0.88 mg<sub>Pt</sub>/monolith was ensured.

The metal particles were equally well distributed on supports produced by both AM methods. The particle size is approximately 1.1 nm ( $d_{Pt,BJ} = 1.12$  nm and  $d_{Pt,DIW} = 1.06$  nm), with a similar standard deviation of 0.26 nm (see Figs. 12(a) and 12(b)), indicating similar and fine Pt particle sizes achieved by wet impregnation. TEM image analysis resulted in a dispersion of 90% and 95% for BJ and DIW, respectively.

### 3.5. Catalytic test

Catalytic tests with Pt impregnated monoliths as well as ground monoliths were carried out for BJ and DIW. Fig. 13 compares the degree of dehydrogenation for each reaction while the productivity  $P$  for each catalyst between DoD = 10 - 60% is displayed in Table 4.

#### 3.5.1. Test with powder catalysts

For the activity test with catalyst powder, the impregnated and reduced monoliths fabricated with both printing methods were ground. Powder tests were carried out as a reference to investigate the catalytic activity under exclusion of mass transfer limitations. Fig. 13 reveals that powder samples fabricated with both techniques show the same DoD trend and overall similar values for the DoD, suggesting that the powder catalysts perform equally well regardless of the 3D printing method used for support fabrication. Until about 2 h, a steep initial dehydrogenation rate is visible. At this point, a DoD of about 66% is reached. After 2 h the DoD curve flattens and reaches a plateau at an apparent maximum DoD of 92% after a reaction time of 9 h.

The almost congruent dehydrogenation rates are confirmed by the results tabulated in Table 4 which show similar productivity values for both powder catalysts. The ground catalyst fabricated by BJ shows a productivity  $P_{powder}$  of 4.4 g<sub>H<sub>2</sub></sub> g<sub>Pt</sub><sup>-1</sup> min<sup>-1</sup> and the DIW printed sample 4.2 g<sub>H<sub>2</sub></sub> g<sub>Pt</sub><sup>-1</sup> min<sup>-1</sup>. Due to differences regarding the reactor setup (batch/continuous), catalyst particle size and molar ratio of Pt/18H-DBT, direct comparison of the precious metal productivity from this study with previously conducted dehydrogenation experiments involving Pt/Al<sub>2</sub>O<sub>3</sub> catalysts [53,69–71] is hardly possible. Nevertheless, the hereby determined Pt productivity showcases the similar dehydrogenation activities of the catalyst powders stemming from differing AM processes.

#### 3.5.2. Test with monolithic catalysts

Besides catalytic tests with powder, activity tests with monoliths were conducted (Fig. 13). After a reaction time of 2 h, DoD reaches 53%, in contrast to 66% which are achieved by the powder catalyst. However, after 9 h, powder and monolith samples reach a similar DoD of about 90%. Nevertheless, the overall lower catalytic activity of the monolith samples is attributed to the mass transfer limitations affecting larger catalyst particles more significantly due to longer diffusion pathways within the catalyst particle. This explains the expected lower activity of the monolithic samples. The platinum productivity data in Table 4 corroborates this observation as the average productivity of the monolith samples  $P_{monolith} = 2.7$  g<sub>H<sub>2</sub></sub> g<sub>Pt</sub><sup>-1</sup> min<sup>-1</sup> reaches 63% of  $P_{powder}$ . Analogous to the powder tests, BJ and DIW printed monoliths show the same catalytic activity for 18H-DBT dehydrogenation. Consequently, differences resulting from the usage of two 3D printing methods such as varying penetration depths and specific surface areas (Table 3) do not affect the dehydrogenation rate significantly in this case.

The active layer thickness  $d_{pen} = 361$  μm for BJ is larger than for DIW printed parts where the depth is 200 μm. Auer [54] examined the influence of active layer thickness on the reactivity for H18-DBT dehydrogenation where the Pt containing layer was washed onto an  $\alpha$ -Al<sub>2</sub>O<sub>3</sub> core. Decreasing layer thicknesses from over 200 μm to 92 μm increased the Pt productivity, while layer thicknesses below 92 μm lead to a productivity plateau due to the absence of mass



## 6. Comparison of Direct Ink Writing and Binder Jetting for additive manufacturing of Pt/Al<sub>2</sub>O<sub>3</sub> catalysts for the dehydrogenation of perhydro-dibenzyltoluene

H.M. Bui et al.

Chemical Engineering Journal 458 (2023) 141361

**Table 3**

Characterization data for Pt catalysts fabricated with DIW and BJ which were used for the catalytic tests. Impregnation time  $t_{\text{imp}} = 3$  h.

AM method	$w_{\text{Pt}}$ (wt.%)	$d_{\text{Pt}}$ (nm)	$D_{\text{Pt}}$ (%)	$d_{\text{pen}}$ ( $\mu\text{m}$ )	$S_{\text{BET}}$ ( $\text{m}^2/\text{g}$ )	$\epsilon^{\text{a}}$ (%)
BJ	0.21 <sup>b</sup>	$1.12 \pm 0.26$	90.4	$361 \pm 36$	26	77
DIW	0.11 <sup>c</sup>	$1.06 \pm 0.26$	95.0	$200 \pm 22$	11	56

<sup>a</sup>Porosity determined by MIP.

<sup>b</sup>Target loading  $w_{\text{Pt,BJ}} = 0.4$  wt. %.

<sup>c</sup>Target loading  $w_{\text{Pt,DIW}} = 0.2$  wt. %.

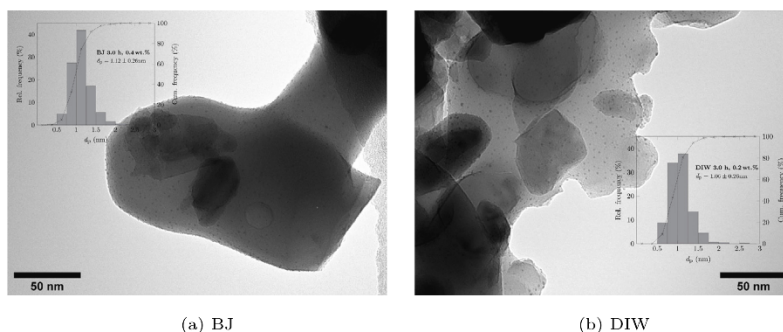


**Fig. 12.** TEM images of the ground Pt/Al<sub>2</sub>O<sub>3</sub> monoliths used for catalytic testing, calcined at 1100 °C and wet impregnated for 3 h, including respective metal particle size distribution.

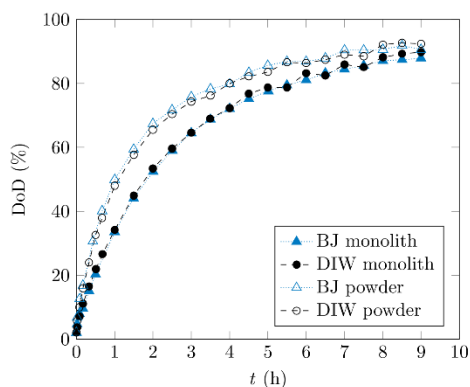


**Fig. 13.** 18H-DBT dehydrogenation over BJ and DIW printed Pt/Al<sub>2</sub>O<sub>3</sub> catalysts in a semi-batch reactor setup, tested with monolithic and powder catalysts, respectively. For each reaction, two monoliths were used.

**Table 4**

Platinum productivities of powder ( $P_{\text{powder}}$ ) and monolithic catalysts ( $P_{\text{monolith}}$ ), determined for the dehydrogenation reaction between DoD = 10 - 60 %.

Catalyst		$P$ ( $\text{g}_{\text{H}_2}, \text{g}_{\text{Pt}}^{-1} \text{min}^{-1}$ )
Powder	BJ	4.4
	DIW	4.2
Monolith	BJ	2.7
	DIW	2.7

transport limitations for very thin layers. 90  $\mu\text{m}$  was chosen to be the optimal layer depth, making a compromise between high activity and mechanical stability of the coating. Peters et al. [69] reported how different active layer thicknesses between 24 and 88  $\mu\text{m}$  affect pore diffusion on washcoated Pt/Al<sub>2</sub>O<sub>3</sub> catalysts. The kinetic regime of the dehydrogenation of perhydro-*N*-ethylcarbazole was limited even at very thin catalyst layers of 24  $\mu\text{m}$  so that it was concluded that pore diffusion affects the dehydrogenation in nearly all commercial catalyst pellets. Transferring those findings to the penetration depths measured in this study, the relatively deep advancement of the impregnation

front for the 3D printed catalysts, especially the BJ printed parts (see Table 3), could negatively affect the catalytic activity of the monolith tests due to mass transfer limitations as the reactant has to travel far into the pore system or does not reach certain regions of the pellet at all. Since the catalytic performance of monolithic DIW and BJ catalysts are congruent, the deeper Pt penetration for BJ does not seem to be an influencing factor. The drawbacks caused by a larger  $d_{\text{pen}}$  are possibly compensated by a greater void fraction and macroporosity in comparison to DIW printed supports ( $\epsilon_{\text{BJ}} = 77\%$  vs.  $\epsilon_{\text{DIW}} = 56\%$ , see Fig. 9 and Table 3), leading to improved pore diffusion of the reactant. Nevertheless,  $d_{\text{pen}}$  was relatively deep for both 3D printed catalysts so that adjustment of the support properties regarding the poreSD, specific surface area as well as the impregnation duration and Pt loading could alleviate mass transfer limitations and therefore further increase catalytic activity.

## 4. Conclusions

Alumina supports were successfully fabricated with the extrusion-based AM technique DIW and the powder-based method BJ. Subsequently, the 3D printed supports were impregnated to obtain Pt/Al<sub>2</sub>O<sub>3</sub> catalysts, which were tested for the dehydrogenation of the liquid organic hydrogen carrier 18H-DBT in a semi-batch reactor setup.

Until a calcination temperature of 1100 °C, the mechanical stability is similar for both printing methods. However, DIW parts are almost six times more robust than BJ parts when calcined at  $T_{\text{calc}} > 1100$  °C which is attributed to the paste extrusion principle and the feedstock preparation from a ceramic paste, whereas BJ inherently generates larger intraparticle voids. Further catalyst characterization revealed finely dispersed Pt particles in all cases. Increasing impregnation duration led to deeper penetration of Pt into the monolith of up to 293  $\mu\text{m}$  for DIW based carriers after 12 h. Despite the differences, catalytic tests revealed that both catalysts perform equally well, regardless of the chosen printing method and the resulting structural variations as the Pt productivities of  $2.7 \text{ g}_{\text{H}_2} \text{ g}_{\text{Pt}}^{-1} \text{ min}^{-1}$  were almost equal for BJ and DIW.

This study demonstrates the importance of catalyst shape and showcases how the advantages of two different additive manufacturing techniques can be exploited to generate tailor-made monolith or pellet geometries, benefiting individual process requirements. Insights from lab-scale catalytic tests using 3D printed catalyst packings can be used

## 6. Comparison of Direct Ink Writing and Binder Jetting for additive manufacturing of Pt/Al<sub>2</sub>O<sub>3</sub> catalysts for the dehydrogenation of perhydro-dibenzyltoluene

H.M. Bui et al.

Chemical Engineering Journal 458 (2023) 141361

to derive improvements for larger industrial-scale chemical reactors. As an outlook, the potential of AM for catalysis can be further exploited by combining it with CFD tools to investigate the influence of differing pellet geometries which can be rapidly realized by 3D printing, enabling quick process adaptations.

DIW generally facilitates lattice- or woodpile-like structures with a high surface-to-volume-ratio for enhanced metal deposition, whereas BJ is more suitable to generate complex channel geometries for improved fluid flow. Since AM of catalysts is still in its early stages, the characterization results provide practical comparative AM guidelines for alumina-based catalysts in terms of surface area, porosity, stability, and impregnation behavior. Moreover, findings in this study generate additional insights into adequate additive processing steps and conditions to achieve active catalysts, which paves the way for smart chemical process development and reactor design by rapid prototyping.

### Declaration of competing interest

The authors declare that they have no known competing financial interests or personal relationships that could have appeared to influence the work reported in this paper.

### Data availability

Data will be made available on request.

### Acknowledgments

The financial support of the Bayerische Forschungsstiftung (BFS), Germany towards this research is gratefully acknowledged. Furthermore, H. M. Bui and P. F. Großmann acknowledge the support of the TUM Graduate School. The authors gratefully acknowledge the fruitful environment within the framework of MuniCat.

### Appendix A. Supplementary data

Supplementary material related to this article can be found online at <https://doi.org/10.1016/j.cej.2023.141361>.

### References

- [1] C.W. Hull, Apparatus for Production of Three-Dimensional Objects by Stereolithography, US4575330A, 1986.
- [2] A. Ertas, A. Stroud, Additive manufacturing research and applications, *Metals* 12 (4) (2022) 634.
- [3] A. Alanmar, J.C. Kois, M. Revilla-León, W. Att, Additive manufacturing technologies: Current status and future perspectives, *J. Prosthodont. : Off. J. Am. Coll. Prosthodont.* 31 (S1) (2022) 4–12.
- [4] R. Kumar, M. Kumar, J.S. Chohan, The role of additive manufacturing for biomedical applications: A critical review, *J. Manuf. Process.* 64 (2021) 828–850.
- [5] S. Nayar, S. Bhumathan, W.M. Bhat, Rapid prototyping and stereolithography in dentistry, *J. Pharm. Bioallied Sci.* 7 (Suppl 1) (2015) S216–9.
- [6] S. Salifu, D. Desai, O. Ogunbiyi, K. Mwale, Recent development in the additive manufacturing of polymer-based composites for automotive structures—a review, *Int. J. Adv. Manuf. Technol.* 119 (11–12) (2022) 6877–6891.
- [7] J.C. Vasco, Additive manufacturing for the automotive industry, in: J. Pou (Ed.), *Additive Manufacturing*, in: *Handbooks in Advanced Manufacturing*, Elsevier, San Diego, 2021, pp. 505–530, <http://dx.doi.org/10.1016/B978-0-12-818411-0.00010-0>.
- [8] B. Blakey-Milner, P. Gradl, G. Snedden, M. Brooks, J. Pitot, E. Lopez, M. Leary, F. Berto, A. Du Plessis, Metal additive manufacturing in aerospace: A review, *Mater. Des.* 209 (2021) 110008.
- [9] M. Khorasani, A. Ghasemi, B. Rolfe, I. Gibson, Additive manufacturing a powerful tool for the aerospace industry, *Rapid Prototyp. J.* 28 (1) (2022) 87–100.
- [10] S. Mehla, R.D. Gudi, D. Mandaliya, T. Hisatomi, K. Domen, S.K. Bhargava, Additive Manufacturing as the Future of Green Chemical Engineering, in: *Additive Manufacturing for Chemical Sciences and Engineering*, Springer, 2022, pp. 239–307.
- [11] C. Hurt, M. Brandt, S.S. Priya, T. Bhatelia, J. Patel, P. Selvakannan, S. Bhargava, Combining additive manufacturing and catalysis: a review, *Catal. Sci. Technol.* 7 (16) (2017) 3421–3439.
- [12] H. Thakkar, S. Eastman, Q. Al-Naddaf, A.A. Rownaghi, F. Rezaei, 3D-printed metal-organic framework monoliths for gas adsorption processes, *ACS Appl. Mater. Interfaces* 9 (41) (2017) 35908–35916.
- [13] L.R. Rosseau, V. Middelkoop, H.A. Willemssen, I. Roghair, M. van Sint Annaland, Review on additive manufacturing of catalysts and sorbents and the potential for process intensification, *Front. Chem. Eng.* 4 (2022).
- [14] G. Vega, A. Quintanilla, N. Menendez, M. Belmonte, J.A. Casas, 3D honeycomb monoliths with interconnected channels for the sustainable production of dihydroxybenzenes: towards the intensification of selective oxidation processes, *Chem. Eng. Process. - Proc. Intensif.* 165 (2021) 108437.
- [15] M. Braconi, Intensification of catalytic reactors: a synergic effort of Multi-scale Modeling, Machine Learning and Additive Manufacturing, *Chem. Eng. Process.-Proc. Intensif.* (2022) 109148.
- [16] Y. Li, S. Chen, X. Cai, J. Hong, X. Wu, Y. Xu, J. Zou, B.H. Chen, Rational design and preparation of hierarchical monoliths through 3D printing for syngas methanation, *J. Mater. Chem. A* 6 (14) (2018) 5695–5702.
- [17] E. Bogdan, P. Michorczyk, 3D printing in heterogeneous catalysis—the state of the art, *Mater. (Basel, Switzerland)* 13 (20) (2020).
- [18] O.H. Laguna, P.F. Lietor, F.I. Godino, F.A. Corpas-Iglesias, A review on additive manufacturing and materials for catalytic applications: Milestones, key concepts, advances and perspectives, *Mater. Des.* 208 (2021) 109927.
- [19] J. Zhu, P. Wu, Y. Chao, J. Yu, W. Zhu, Z. Liu, C. Xu, Recent advances in 3D printing for catalytic applications, *Chem. Eng. J.* 433 (2022) 134341.
- [20] S.M. Sajadi, L. Vászárhelyi, R. Mousavi, A.H. Rahmati, Z. Kónya, Á. Kukovecz, T. Arif, T. Filleter, R. Vajtai, P. Boul, Z. Pang, T. Li, C.S. Tiwary, M.M. Rahman, P.M. Ajayan, Damage-tolerant 3D-printed ceramics via conformal coating, *Sci. Adv.* 7 (28) (2021).
- [21] M.A.S.R. Saadi, A. Maguire, N.T. Pottackal, M.S.H. Thakur, M.M. Ikram, A.J. Hart, P.M. Ajayan, M.M. Rahman, Direct ink writing: A 3D printing technology for diverse materials, *Adv. Mater. (Deerfield Beach, Fla.)* (2022) e2108855.
- [22] A.D. Salazar-Aguilar, A. Quintanilla, P. López, C. Martínez, S.M. Vega-Díaz, J.A. Casas, P. Miranzo, M.I. Osendi, M. Belmonte, 3D-printed Fe/γ-Al<sub>2</sub>O<sub>3</sub> monoliths from MOF-based boehmite inks for the catalytic hydroxylation of phenol, *ACS Appl. Mater. Interfaces* 14 (1) (2022) 920–932.
- [23] S. Lawson, A. Farsad, F. Rezaei, D. Ludlow, A.A. Rownaghi, Direct Ink Writing of Metal Oxide/H-ZSM-5 catalysts for *n*-Hexane Cracking: A New Method of Additive Manufacturing with High Metal Oxide Loading, *ACS Appl. Mater. Interfaces* 13 (1) (2021) 781–794.
- [24] V. Middelkoop, A. Vamvakeros, D. De Wit, S.D. Jacques, S. Danaci, C. Jacquot, Y. De Vos, D. Matras, S.W. Price, A.M. Beale, 3D printed Ni/Al<sub>2</sub>O<sub>3</sub> based catalysts for CO<sub>2</sub> methanation - a comparative and operando XRD-CT study, *J. CO<sub>2</sub> Util.* 33 (2019) 478–487.
- [25] J.N. Stuecker, J.E. Miller, R.E. Ferrizz, J.E. Mudd, J. Cesarano, Advanced support structures for enhanced catalytic activity, *Ind. Eng. Chem. Res.* 43 (1) (2004) 51–55.
- [26] H.M. Bui, P.F. Großmann, T. Gros, M. Blum, A. Berger, R. Fischer, N. Szesni, M. Tonigold, O. Hinrichsen, 3D printed co-precipitated Ni-Al CO<sub>2</sub> methanation catalysts by binder jetting: Fabrication, characterization and test in a single pellet string reactor, *Appl. Catal. A: Gen.* (2022) 118760.
- [27] T. Ludwig, J. Seckendorff, C. Troll, R. Fischer, M. Tonigold, B. Rieger, O. Hinrichsen, Additive manufacturing of Al<sub>2</sub>O<sub>3</sub>-based carriers for heterogeneous catalysis, *Chem. Ing. Tech.* 90 (5) (2018) 703–707.
- [28] ISO/ASTM 52900, Additive manufacturing - general principles - terminology, 2015.
- [29] J.A. Lewis, Direct-write assembly of ceramics from colloidal inks, *Curr. Opin. Solid State Mater. Sci.* 6 (3) (2002) 245–250.
- [30] J.A. Lewis, Direct ink writing of 3D functional materials, *Adv. Funct. Mater.* 16 (17) (2006) 2193–2204.
- [31] A. Shahzad, I. Lazoglu, Direct ink writing (DIW) of structural and functional ceramics: Recent achievements and future challenges, *Composites B* 225 (2021) 109249.
- [32] J. Cesarano, A review of robocasting technology, *MRS Proc.* 542 (1998).
- [33] L. del Mazo-Barbara, M.-P. Ginebra, Rheological characterisation of ceramic inks for 3D direct ink writing: A review, *J. Eur. Ceram. Soc.* 41 (16) (2021) 18–33.
- [34] E. Feilden, E.G.-T. Blanca, F. Giuliani, E. Saiz, L. Vandepierre, Robocasting of structural ceramic parts with hydrogel inks, *J. Eur. Ceram. Soc.* 36 (10) (2016) 2525–2533.
- [35] P. Jiang, Z. Ji, X. Zhang, Z. Liu, X. Wang, Recent advances in direct ink writing of electronic components and functional devices, *Prog. Addit. Manuf.* 3 (1–2) (2018) 65–86.
- [36] J.A. Lewis, J.E. Smay, J. Stuecker, J. Cesarano, Direct ink writing of three-dimensional ceramic structures, *J. Am. Ceram. Soc.* 89 (12) (2006) 3599–3609.
- [37] L.A. Chavez, P. Ibañez, B. Wilburn, D. Alexander, C. Stewart, R. Wicker, Y. Lin, The influence of printing parameters, post-processing, and testing conditions on the properties of binder jetting additive manufactured functional ceramics, *Ceramics* 3 (1) (2020) 65–77.
- [38] M. Li, W. Du, A. Elwany, Z. Pei, C. Ma, Metal binder jetting additive manufacturing: A literature review, *J. Manuf. Sci. Eng.* 142 (9) (2020).

## 6. Comparison of Direct Ink Writing and Binder Jetting for additive manufacturing of Pt/Al<sub>2</sub>O<sub>3</sub> catalysts for the dehydrogenation of perhydro-dibenzyltoluene

H.M. Bui et al.

Chemical Engineering Journal 458 (2023) 141361

- [39] W. Du, G. Miao, L. Liu, Z. Pei, C. Ma, Binder jetting additive manufacturing of ceramics: Comparison of flowability and sinterability between raw and granulated powders, in: Proceedings of the ASME 14th International Manufacturing Science and Engineering Conference - 2019, The American Society of Mechanical Engineers, New York, N.Y., 2019, <http://dx.doi.org/10.1115/MSEC2019-2983>.
- [40] Y. Bai, C. Wall, H. Pham, A. Esker, C.B. Williams, Characterizing binder-powder interaction in binder jetting additive manufacturing via sessile drop goniometry, *J. Manuf. Sci. Eng.* 141 (1) (2019).
- [41] S. Barui, H. Ding, Z. Wang, H. Zhao, S. Marathe, W. Mirihanage, B. Basu, B. Derby, Probing ink-powder interactions during 3D binder jet printing using time-resolved X-ray imaging, *ACS Appl. Mater. Interfaces* 12 (30) (2020) 34254–34264.
- [42] M. Ziaee, N.B. Crane, Binder jetting: A review of process, materials, and methods, *Addit. Manuf.* 28 (2019) 781–801.
- [43] P.M. Modisha, C.N.M. Ouma, R. Garidzirai, P. Wasserscheid, D. Bessarabov, The prospect of hydrogen storage using liquid organic hydrogen carriers, *Energy Fuels* 33 (4) (2019) 2778–2796.
- [44] G. Do, P. Preuster, R. Aslam, A. Bösmann, K. Müller, W. Arlt, P. Wasserscheid, Hydrogenation of the liquid organic hydrogen carrier compound dibenzyltoluene – reaction pathway determination by <sup>1</sup>H NMR spectroscopy, *React. Chem. Eng.* 1 (3) (2016) 313–320.
- [45] P. Preuster, C. Papp, P. Wasserscheid, Liquid organic hydrogen carriers (LOHCs): Toward a hydrogen-free hydrogen economy, *Acc. Chem. Res.* 50 (1) (2017) 74–85.
- [46] Y. Sekine, T. Higo, Recent trends on the dehydrogenation catalysis of liquid organic hydrogen carrier (LOHC): A review, *Top. Catal.* 64 (7–8) (2021) 470–480.
- [47] F. Auer, D. Blaumeiser, T. Bauer, A. Bösmann, N. Szesni, J. Libuda, P. Wasserscheid, Boosting the activity of hydrogen release from liquid organic hydrogen carrier systems by sulfur-additives to Pt on alumina catalysts, *Catal. Sci. Technol.* 9 (13) (2019) 3537–3547.
- [48] N. Brückner, K. Obesser, A. Bösmann, D. Teichmann, W. Arlt, J. Dungs, P. Wasserscheid, Evaluation of industrially applied heat-transfer fluids as liquid organic hydrogen carrier systems, *ChemSusChem* 7 (1) (2014) 229–235.
- [49] H.M. Bui, R. Fischer, N. Szesni, M. Tonigold, K. Achterhold, F. Pfeiffer, O. Hinrichsen, Development of a manufacturing process for Binder Jet 3D printed porous Al<sub>2</sub>O<sub>3</sub> supports used in heterogeneous catalysis, *Add. Manuf.* 50 (2022) 102498.
- [50] S. Timoshenko, J.N. Goodier, *Theory of Elasticity*, second ed., McGraw-Hill, 1951.
- [51] A. Borodziński, M. Bonarowska, Relation between crystallite size and dispersion on supported metal catalysts, *Langmuir* 13 (21) (1997) 5613–5620.
- [52] P. Preuster, *Entwicklung eines Reaktors zur Dehydrierung Chemischer Wasserstoffträger als Bestandteil eines Dezentralen, Stationären Energiespeichers*, 2017, URL: <https://opus4.kobv.de/opus4-fau/files/8289/patrickpreusterdissertation.pdf>.
- [53] A.M. Seidel, *Entwicklung eines technischen Platin-Trägerkatalysators zur Dehydrierung von Perhydro-Dibenzyltoluol* (Dissertation), Friedrich-Alexander-Universität, Erlangen-Nürnberg, 2019.
- [54] F. Auer, *Katalysatorentwicklung für die Dehydrierung von Perhydro-Dibenzyltoluol* (Dissertation), Friedrich-Alexander-Universität Erlangen-Nürnberg, 2020, URL: <https://opus4.kobv.de/opus4-fau/files/14054/dissertationfranziskaauer.pdf>.
- [55] D.A. Snelling, C.B. Williams, C.T.A. Suchicital, A.P. Druschitz, Binder jetting advanced ceramics for metal-ceramic composite structures, *Int. J. Adv. Manuf. Technol.* 92 (1–4) (2017) 531–545.
- [56] C.-L. Huang, J.-J. Wang, C.-Y. Huang, Sintering behavior and microwave dielectric properties of nano  $\alpha$ -alumina, *Mater. Lett.* 59 (28) (2005) 3746–3749.
- [57] D.L. Trimm, A. Stanislaus, The control of pore size in alumina catalyst supports: A review, *Appl. Catal.* 21 (2) (1986) 215–238.
- [58] J. Lee, E.J. Jang, J.H. Kwak, Effect of number and properties of specific sites on alumina surfaces for Pt-Al<sub>2</sub>O<sub>3</sub> catalysts, *Appl. Catal. A: Gen.* 569 (2019) 8–19.
- [59] J.E. Park, B.B. Kim, E.D. Park, Propane combustion over Pt/Al<sub>2</sub>O<sub>3</sub> catalysts with different crystalline structures of alumina, *Korean J. Chem. Eng.* 32 (11) (2015) 2212–2219.
- [60] C.V. Chandran, C.E.A. Kirschhock, S. Radhakrishnan, F. Taulelle, J.A. Martens, E. Breyneart, Alumina: discriminative analysis using 3D correlation of solid-state NMR parameters, *Chem. Soc. Rev.* 48 (1) (2019) 134–156.
- [61] I. Levin, D. Brandon, Metastable alumina polymorphs: Crystal structures and transition sequences, *J. Am. Ceram. Soc.* 81 (8) (1998) 1995–2012.
- [62] J. Lee, E.J. Jang, D.G. Oh, J. Szanyi, J.H. Kwak, Morphology and size of Pt on Al<sub>2</sub>O<sub>3</sub>: The role of specific metal-support interactions between Pt and Al<sub>2</sub>O<sub>3</sub>, *J. Catal.* 385 (2020) 204–212.
- [63] J.H. Kwak, J. Hu, D. Mei, C.-W. Yi, D.H. Kim, C.H.F. Peden, L.F. Allard, J. Szanyi, Coordinatively unsaturated Al<sup>3+</sup> centers as binding sites for active catalyst phases of platinum on  $\gamma$ -Al<sub>2</sub>O<sub>3</sub>, *Science (New York, N.Y.)* 325 (5948) (2009) 1670–1673.
- [64] H. Yao, M. Sieg, H.K. Plummer Jr., Surface interactions in the Pt/ $\gamma$ -Al<sub>2</sub>O<sub>3</sub> system, *J. Catal.* 59 (3) (1979) 365–374.
- [65] P.P. Robinson, V. Arun, K.K.A. Rashid, C.U. Aniz, K.K.M. Yusuff, The active phase (Ni<sup>2+</sup>) distribution in Ni/ $\gamma$ -Al<sub>2</sub>O<sub>3</sub> catalysts prepared by impregnation of Bis(ethylenediamine)nickel(II) complexes, *Chem. Eng. Commun.* 199 (3) (2012) 321–334.
- [66] X. Liu, J.G. Khinast, B.J. Glasser, A parametric investigation of impregnation and drying of supported catalysts, *Chem. Eng. Sci.* 63 (18) (2008) 4517–4530.
- [67] P. Munnik, P.E. de Jongh, K.P. de Jong, Recent developments in the synthesis of supported catalysts, *Chem. Rev.* 115 (14) (2015) 6687–6718.
- [68] C.V. Chandran, C.E. Kirschhock, S. Radhakrishnan, F. Taulelle, J.A. Martens, E. Breyneart, Alumina: discriminative analysis using 3D correlation of solid-state NMR parameters, *Chem. Soc. Rev.* 48 (1) (2019) 134–156.
- [69] W. Peters, A. Seidel, S. Herzog, A. Bösmann, W. Schwioger, P. Wasserscheid, Macrokinetic effects in perhydro-*N*-ethylcarbazole dehydrogenation and H<sub>2</sub> productivity optimization by using egg-shell catalysts, *Energy Environ. Sci.* 8 (10) (2015) 3013–3021.
- [70] F. Auer, A. Hupfer, A. Bösmann, N. Szesni, P. Wasserscheid, Influence of the nanoparticle size on hydrogen release and side product formation in liquid organic hydrogen carrier systems with supported platinum catalysts, *Catal. Sci. Technol.* 10 (19) (2020) 6669–6678.
- [71] L. Shi, Y. Zhou, S. Qi, K.J. Smith, X. Tan, J. Yan, C. Yi, Pt catalysts supported on H<sub>2</sub> and O<sub>2</sub> plasma-treated Al<sub>2</sub>O<sub>3</sub> for hydrogenation and dehydrogenation of the liquid organic hydrogen carrier pair dibenzyltoluene and perhydrodibenzyltoluene, *ACS Catal.* 10 (18) (2020) 10661–10671.

## 7 Summary and Outlook

Throughout this thesis, Direct Ink Writing was employed as an AM technique for heterogeneous catalysts. With respect to direct printing of catalytically active material, the MOF NH<sub>2</sub>-MIL-125(Ti) was successfully printed. The MOF paste was rheologically optimized with alumina as an inorganic binder, which also provides stability after thermal treatment, and hydroxypropyl methylcellulose as an organic additive and successfully printed into monolithic structures. The decomposition to TiO<sub>2</sub> as the active component with C and N from the organic linker as synergistic effects was also successfully carried out. The catalyst presented in this way was subsequently used in photocatalytic water splitting to hydrogen and, as a monolith, showed almost five times the hydrogen evolution compared with corresponding powder measurements. This could be attributed to the improved illumination with incident UV-Vis light. Additional coating with platinum via atomic layer deposition increased the activity by a further 30 %. In addition, the recyclability of the catalyst and its stability in terms of both the internal structure and the 3D printed form were demonstrated. For the direct printing of a methanation catalyst, rheological optimization was also carried out and corresponding monolithic geometries were printed. Due to technical difficulties, test reactions are still to be carried out.

The targeted alumina support materials for the dehydrogenation of perhydro-dibenzyl toluene were successfully printed and characterized during the course of the work. The loading via wet impregnation with platinum sulfite acid solution and the analysis of the catalysts, for example by means of  $\mu$ CT and TEM measurements, were also successfully carried out and provided new insights into the impregnation behavior of additively manufactured catalyst supports. The catalysts obtained in this way were subsequently tested in a semi-batch setup for their dehydrogenation activity. It was shown that monolithic geometries with a significantly increased surface-to-volume ratio exhibit comparable productivity to a packed cylinder bed, even though the required catalyst volume was only about 1/3 for the monoliths. It can be concluded that by means of the advanced geometries accessible via AM, either reactor volume, reaction time or active component can be saved for the same productivity, each of the factors being considered advantageous. Unfortunately, no detailed shape optimization could be carried out for a continuous reactor. Alongside this, the above results, the comparison of a cylinder bed and monolithic geometries, were derived from semi-batch setup measurements.

A comparison of the two AM techniques Binder Jetting and Direct Ink Writing showed that the substrate structures obtained do exhibit 3D printing-specific differences. For example, the substrates produced by BJ are significantly more macroporous, whereas DIW printed carriers feature superior lateral compressive strength, especially at calcination temperatures above 1100 °C. The latter is also due to a higher density of the DIW printed moldings. With regard to the impregnation behavior, both substrates behave similarly, although the penetration depth of the platinum is significantly increased in the case of BJ, which can be attributed to the corresponding macroporosity. In the catalytic test with the same geometries and comparable platinum per monolith loadings and a constant platinum to reactant ratio, both shapes showed the same productivity in powder tests and as full particle test reactions. This shows that in principle both techniques are equally suitable for the production of carriers for LOHC dehydrogenation.

3D printing of active components using both techniques was possible, but due to technical problems no comparative catalytic test reactions could be carried out.

In general, however, it must be pointed out that the shapes examined in the comparison are very simple geometries that can be formed well with both techniques. Accordingly, the outlook should also be used to compare shaped bodies that go to the respective limits of the techniques. In the case of DIW, for example, these are woodpile structures with very small channels, whereas in the case of BJ there is significantly greater freedom of shape variation especially regarding the printability of lateral or oblique channels. CFD simulations and the guidelines derived from them with regard to optimized shapes could also be advantageous. Particularly in comparison with traditional manufacturing techniques such as extrusion and pelletizing, the focus should be on lateral holes and geometries that are only accessible via AM. These should then be optimized in terms of flow profile, mixing and pressure loss in the catalyst bed. Subsequently, catalytic tests could verify the simulated results. However, the corresponding test reaction and its specific requirements/characteristics should be taken into account. In general, it would make sense to carry out various other test reactions (including methanation) both in the comparison of the two 3D printing techniques and in Direct Ink Writing per se, since, for example, other systems and viscosities place significantly different requirements on the AM of the catalyst and its geometries. For the reactions already tested, it would make sense in a next step to print different geometries to obtain further insights into the reactions and correspondingly optimized geometries. Specifically, this could be 3D printing of aluminate carriers for the dehydrogenation of LOHC carriers with the same outer surfaces and surface-to-volume ratios but different channels. In addition, further test reactions should also be carried out in this respect in a continuous setup, as is used industrially, since here the flow profiles once again exhibit significant differences.

Experiments with multi-material printing using DIW could also be interesting. This involves printing either with several print heads next to each other, each with a different material, or with a print head with a mixing chamber that is fed with different materials. In this way, for example, a stable carrier can be printed directly next to a thin layer of the corresponding active component without sacrificing stability or activity. Combined printing then allows a loading step with active components to be omitted, saving time and costs. This provides a multitude of possibilities to further develop DIW printing, especially since multi-material printing is not so easy to realize with all AM techniques.

Furthermore, for a technical application, it should be considered that current margins and production speeds are very slow, and up-scaling is urgently needed for industrial applications. For example, parallel print heads with interchangeable print beds in an ideally automated laboratory are conceivable. In addition, further rheological adjustments are conceivable for the corresponding automation in order to run the process error-free and repeatable. In general, 3D printing as a shaping method for catalysts should rather be used for small scale and special reactions, where transport processes can be improved via the AM. Especially considering that both Binder Jetting and Direct Ink Writing show equally good catalytic activity for fabricated alumina supports, a combination of the two 3D printing techniques could also be conceivable for an industrial application. DIW could be used primarily for testing different geometries, since 3D printing via DIW is simpler and closer to the previously known inductive knowledge, while up-




scaling is carried out using BJ, since this process requires more development, but has some advantages in terms of up-scaling. However, this is under the assumption that optimized geometries of the two printing techniques also show equally good activities in other test reactions. In summary, and also in view of the active research in this area, it can be said that there is a high potential for innovation here, with a great deal of potential also based on the rapid progress in the area of 3D printing in general.

## 8 Appendix

### 8.1 Additional information for Chapter 4 “3D Printed MOF-Derived Composites for Enhanced Photocatalytic Hydrogen Generation”

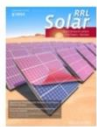
#### 8.1.1 Reprint permission

The contents for Chapter 4 and the corresponding supporting information in Chapter 8.1.2 for the manuscript titled “3D Printed MOF-Derived Composites for Enhanced Photocatalytic Hydrogen Generation” have been published in Solar RRL (Wiley-VCH Verlag GmbH & Co. KGaA) under the terms and conditions of the Creative Commons Attribution CC BY license. The authors possess the copyright of the reprinted material. Manuscript and supporting information have been reprinted from ref. [295].



Help ▾ Live Chat

---



**3D-Printed Metal–Organic Framework-Derived Composites for Enhanced Photocatalytic Hydrogen Generation**

**Author:** Mian Zahid Hussain, Paula F. Großmann, Fabian Kohler, et al  
**Publication:** Solar RRL  
**Publisher:** John Wiley and Sons  
**Date:** Aug 7, 2022

© 2022 The Authors. Solar RRL published by Wiley-VCH GmbH

**Open Access Article**

This is an open access article distributed under the terms of the [Creative Commons CC BY](#) license, which permits unrestricted use, distribution, and reproduction in any medium, provided the original work is properly cited.

You are not required to obtain permission to reuse this article.

For an understanding of what is meant by the terms of the Creative Commons License, please refer to [Wiley's Open Access Terms and Conditions](#).

Permission is not required for this type of reuse.

Wiley offers a professional reprint service for high quality reproduction of articles from over 1400 scientific and medical journals. Wiley's reprint service offers:

- Peer reviewed research or reviews
- Tailored collections of articles
- A professional high quality finish
- Glossy journal style color covers
- Company or brand customisation
- Language translations
- Prompt turnaround times and delivery directly to your office, warehouse or congress.

Please contact our Reprints department for a quotation. Email [corporatesaleseurope@wiley.com](mailto:corporatesaleseurope@wiley.com) or [corporatesalesusa@wiley.com](mailto:corporatesalesusa@wiley.com) or [corporatesalesDE@wiley.com](mailto:corporatesalesDE@wiley.com).

## 8.1.2 Supporting information

### *Supporting Information*

#### **3D Printed MOF-Derived Composites for Enhanced Photocatalytic Hydrogen Generation**

*Mian Zahid Hussain,<sup>†\*</sup> Paula F. Großmann,<sup>†</sup> Fabian Kohler, Tim Kratky, Laura Kronthaler, Bart van der Linden, Katia Rodewald, Bernhard Rieger, Roland A. Fischer, and Yongde Xia\**

Dr. Mian Zahid Hussain, Tim Kratky, Laura Kronthaler, Prof. Dr. Roland A. Fischer  
Department of Chemistry and Catalysis Research Center  
Technical University of Munich  
Lichtenbergstr. 4, 85748 Garching, Germany  
Email: [ge68muq@tum.de](mailto:ge68muq@tum.de)

Paula Großmann, Katia Rodewald, Prof. Dr. Bernhard Rieger  
WACKER-Chair of Macromolecular Chemistry  
Department of Chemistry & Catalysis Research Center  
Technical University of Munich  
Lichtenbergstr. 4, 85748 Garching, Germany

Dr. Fabian Kohler  
Department of Physics  
Technical University of Munich  
Coulombwall 4a, Garching, 85748, Germany

Bart van der Linden  
Catalysis Engineering, Chemical Engineering Department  
Delft University of Technology  
van der Maasweg, 9, 2629 HZ Delft, Netherlands

Dr. Yongde Xia  
College of Engineering, Mathematics and Physical Sciences  
University of Exeter  
Exeter EX4 4QF, United Kingdom  
Email: [Y.Xia@exeter.ac.uk](mailto:Y.Xia@exeter.ac.uk)



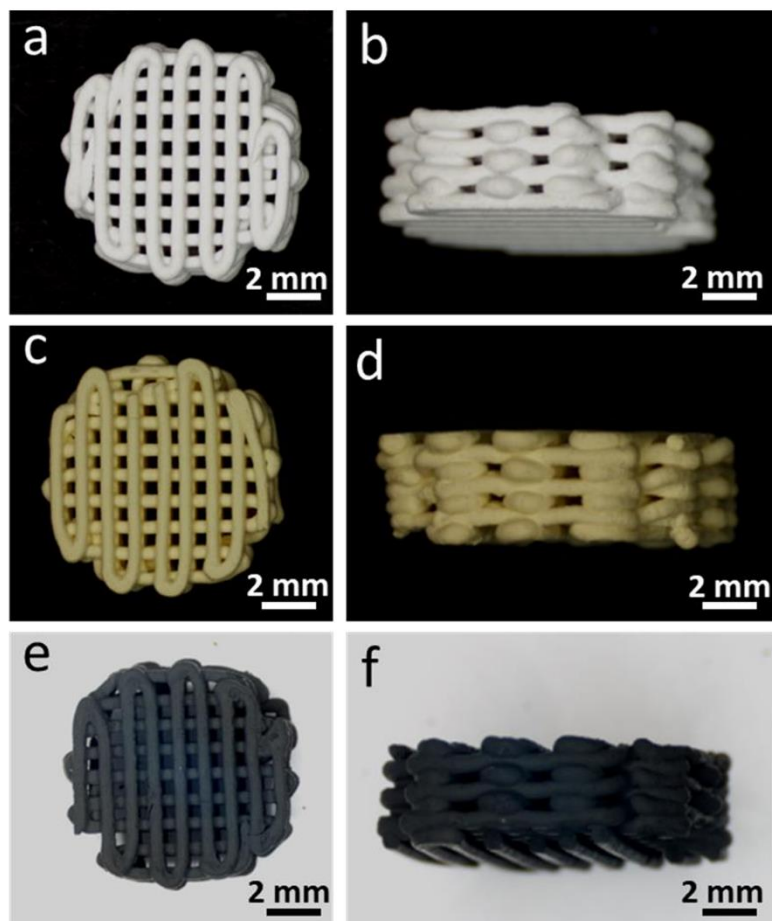


**Figure S1.** Optical images of 3D printed monoliths of (a, b) boehmite (c-d) boehmite/Ti-MOF and (e-f) pyrolyzed monolith  $\text{Al}_2\text{O}_3/\text{TiO}_2/\text{Pt}/\text{C}_{3\text{DP}}$ .

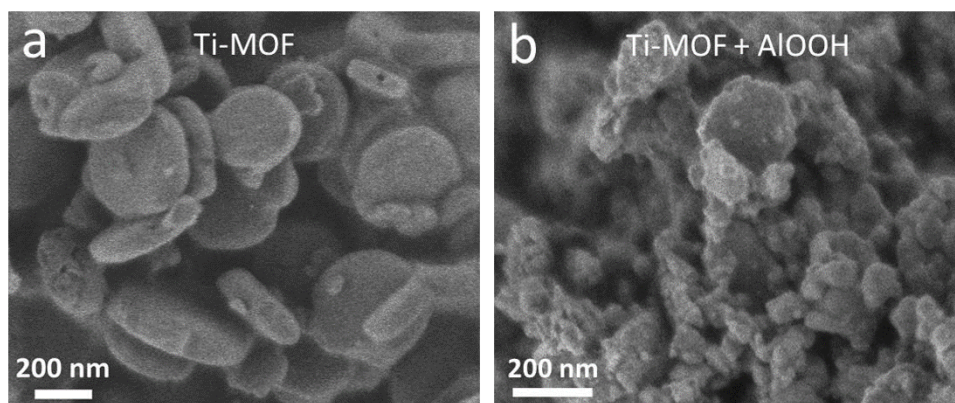


**Figure S2.** SEM images of the (a) as-synthesized Ti-MOF and (b) boehmite/Ti-MOF.

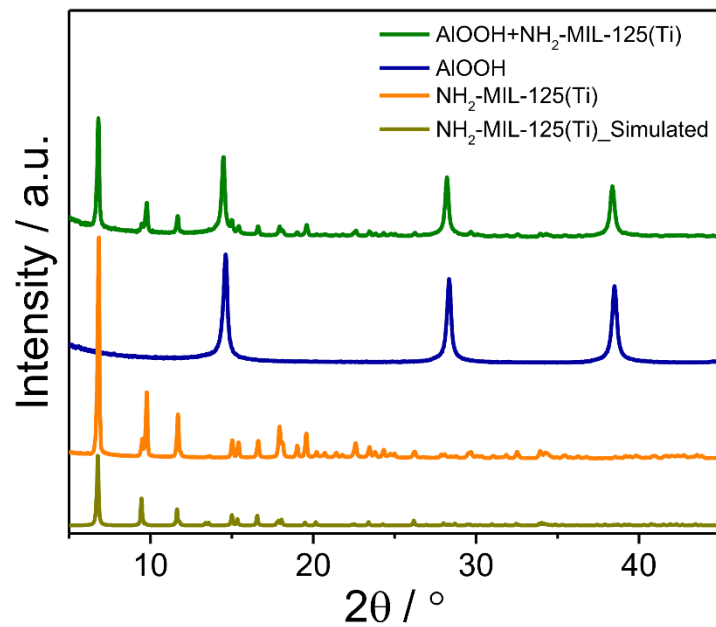


**Figure S3.** PXRD patterns of simulated and as-synthesized Ti-MOF, boehmite dispersal, and their mixed paste boehmite/Ti-MOF, as used in 3D printing.

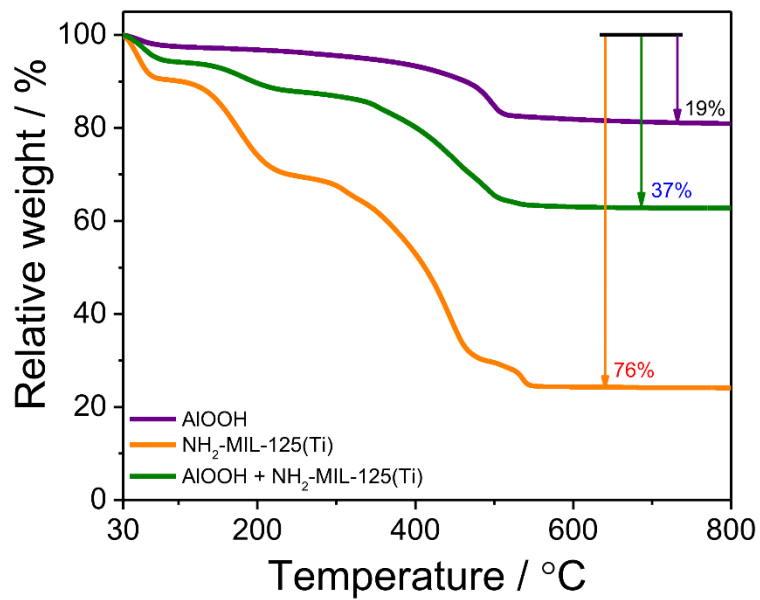


**Figure S4.** TGA patterns of boehmite dispersal, Ti-MOF and their mixed paste used for 3D printing. The curves are recorded under synthetic air atmosphere.

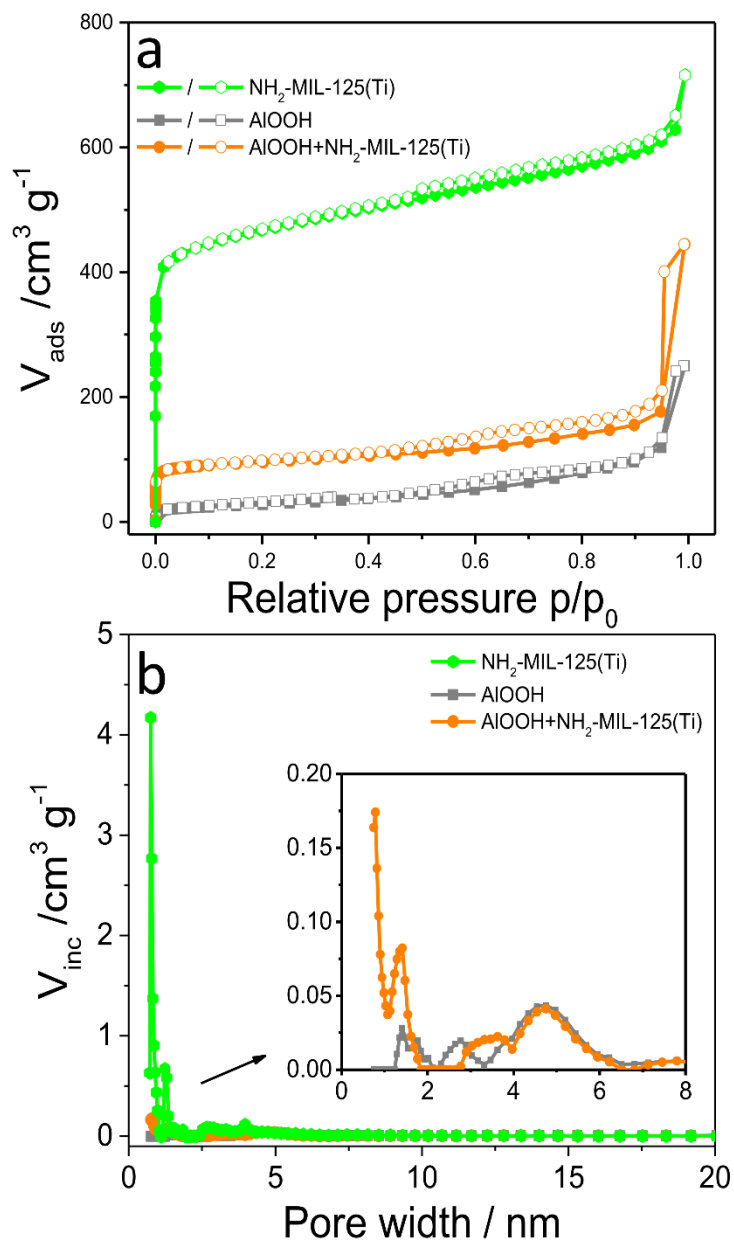


**Figure S5.** (a)  $\text{N}_2$  sorption isotherms of Ti-MOF (green), boehmite (grey), and boehmite/Ti-MOF (orange). The solid and empty symbols represent the adsorption and desorption branches of  $\text{N}_2$  isotherms respectively; (b) Pore size distribution of Ti-MOF, boehmite and boehmite/Ti-MOF.

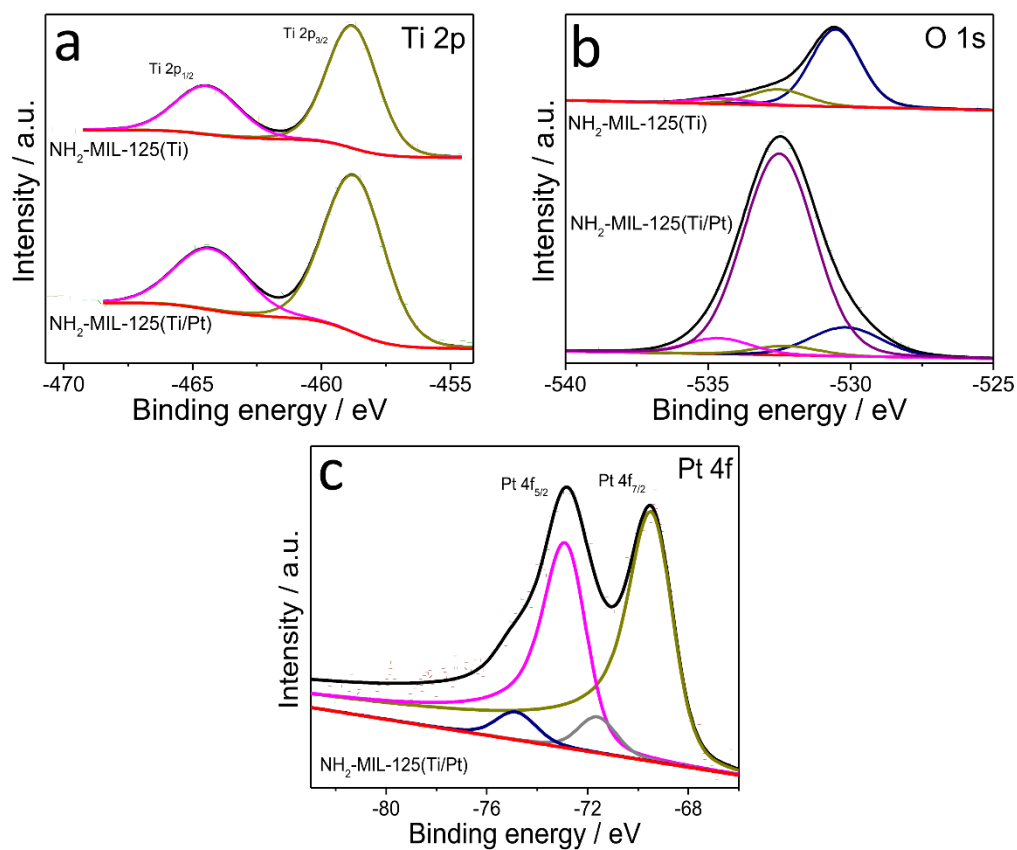


**Figure S6.** XPS spectra of (a) Ti 2p, (b) O 1s, (c) Pt 4f for sample NH<sub>2</sub>-MIL-125(Ti) and Pt deposited NH<sub>2</sub>-MIL-125(Ti/Pt) via atomic layer deposition.

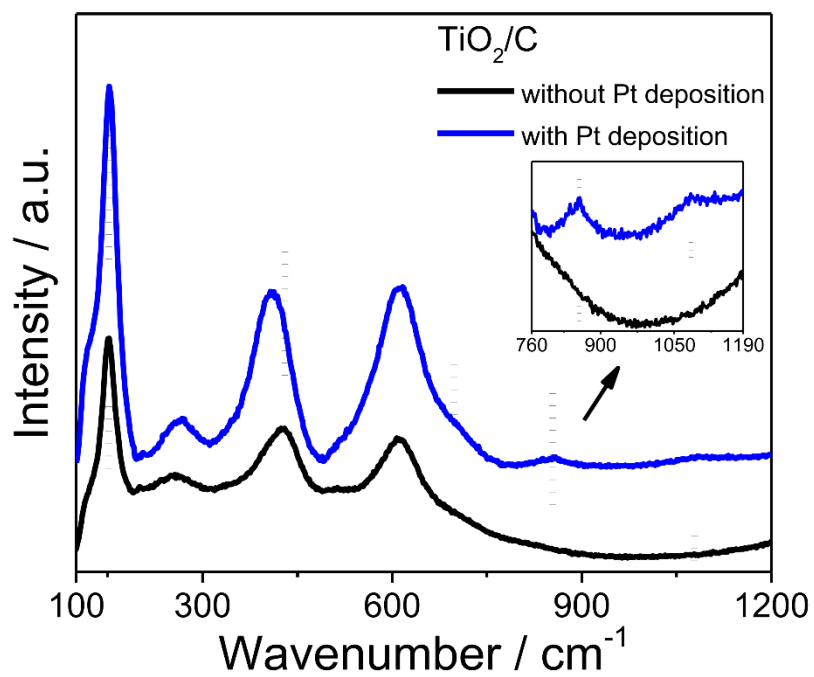


**Figure S7.** Raman spectra of Ti-MOF derived TiO<sub>2</sub>/C in the absence (black) and presence of Pt (blue).

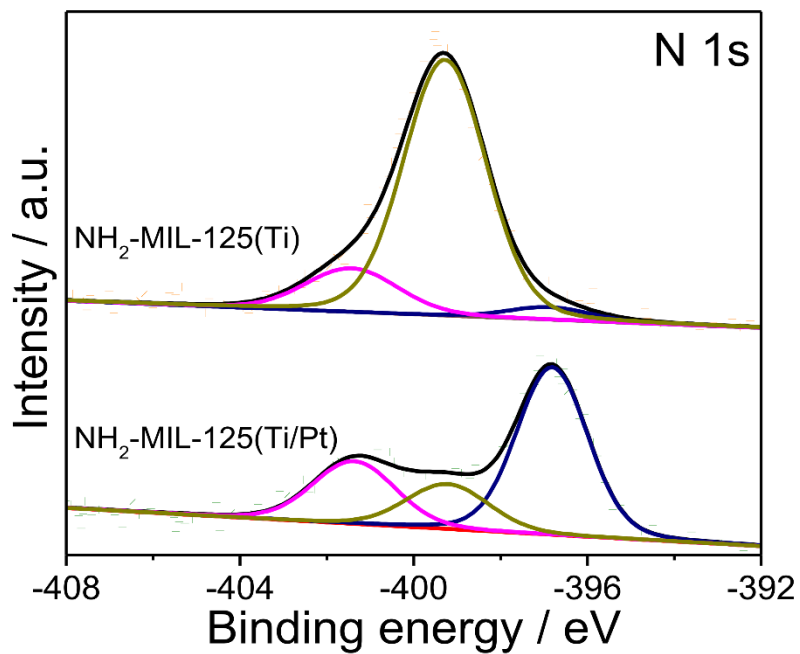


**Figure S8.** N 1s XPS spectra of as-synthesized samples Ti-MOF and Pt deposited Ti-MOF via atomic layer deposition.



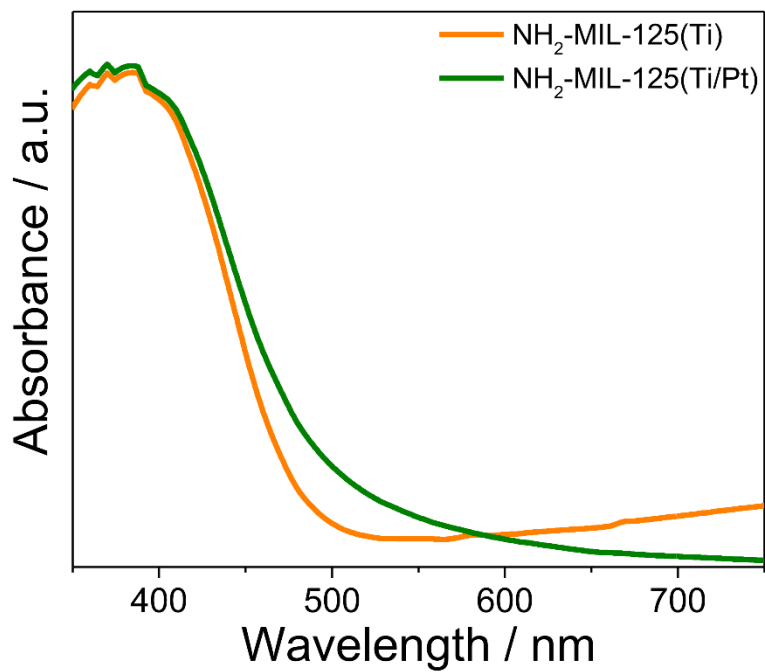


**Figure S9.** UV-Vis absorption spectra of as-synthesized samples Ti-MOF and Pt deposited Ti-MOF via atomic layer deposition.

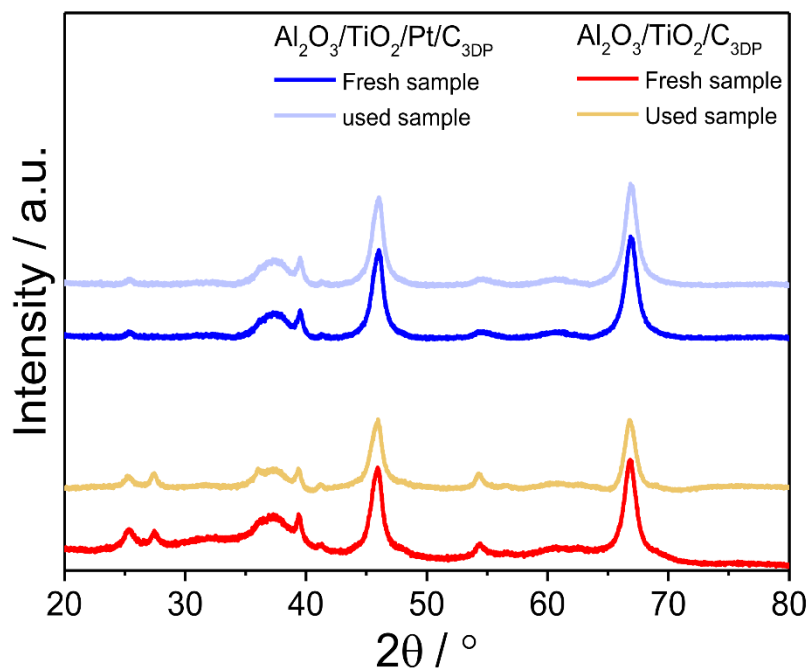


**Figure S10.** PXRD patterns of the used Al<sub>2</sub>O<sub>3</sub>/TiO<sub>2</sub>/Pt/C<sub>3</sub>DP after the reaction.

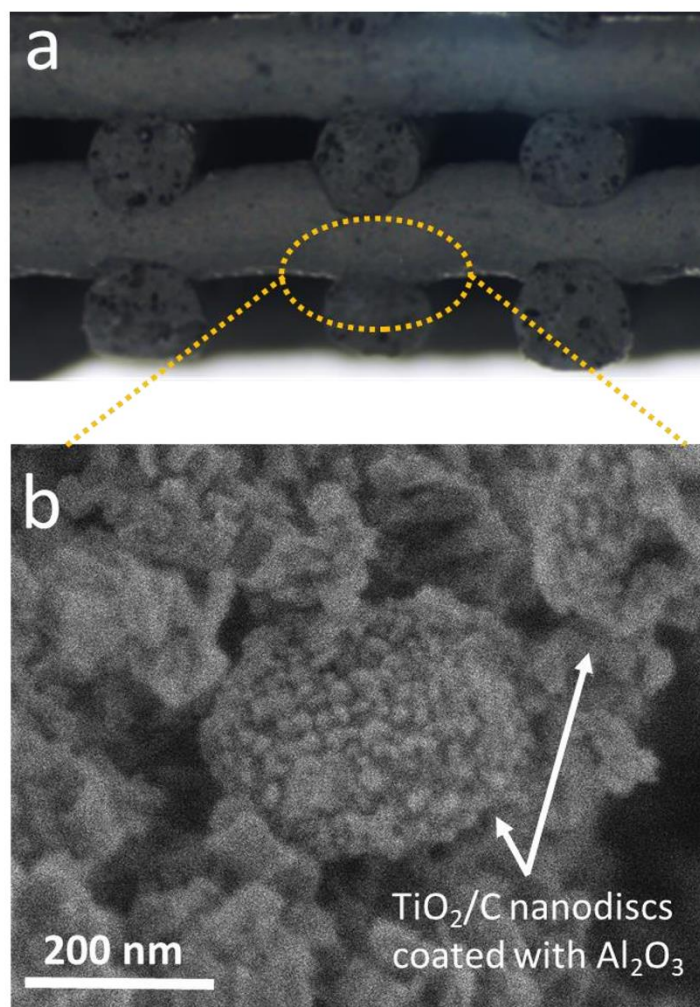


**Figure S11** (a) Optical and (b) SEM images of 3D printed pyrolyzed monolith  $\text{Al}_2\text{O}_3/\text{TiO}_2/\text{Pt}/\text{C}_{3\text{DP}}$  after the photocatalytic HER. The recorded images shows that the used samples exhibit no structural and morphological changes, confirming the good stability of the 3D printed MOF derived catalysts.

## **8.2 Additional information for Chapter 5 “Influence of internal and external surface area on impregnation and activity of 3D printed catalyst carriers”**

### **8.2.1 Reprint permission**

The contents for Chapter 5 and the corresponding supporting information in Chapter 8.2.2 for the manuscript titled “Influence of internal and external surface area on impregnation and activity of 3D printed catalyst carriers” have been published as Open Access in Catalysis Communications (Elsevier B. V.) under the terms and conditions of the Creative Commons Attribution CC BY-NC-ND 4.0. The authors possess the copyright of the reprinted material, manuscript and supporting information have been reprinted from ref. [296].

## 8.2.2 Supporting information

# Influence of internal and external surface area on impregnation and activity of 3D printed catalyst carriers

Paula F. Großmann<sup>a</sup>, Markus Tonigold<sup>b</sup>, Normen Szesni<sup>b</sup>, Richard W. Fischer<sup>b</sup>, Alexander Seidel<sup>c</sup>, Klaus Achterhold<sup>d</sup>, Franz Pfeiffer<sup>d,e</sup>, Bernhard Rieger<sup>a,\*</sup>

<sup>a</sup> WACKER-Chair of Macromolecular Chemistry, Catalysis Research Center, Department of Chemistry, School of Natural Sciences, Technical University of Munich, Lichtenbergstr. 4, 85748 Garching, Germany

<sup>b</sup> Clariant Produkte (Deutschland) GmbH, Waldheimer Str. 13, 83052 Bruckmühl, Germany

<sup>c</sup> HYDROGENIOUS LOHC TECHNOLOGIES GmbH, Weidenweg 13, 91058 Erlangen, Germany

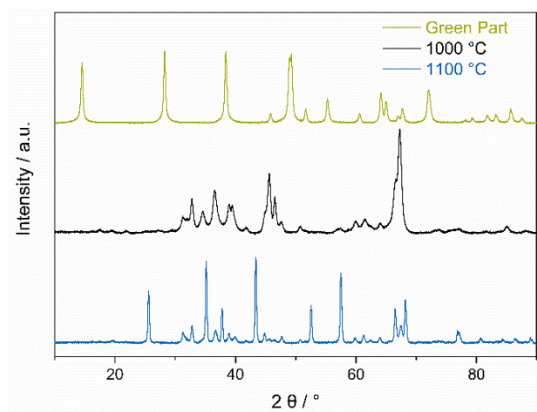
<sup>d</sup> Chair of Biomedical Physics, Department of Physics, School of Natural Sciences and Munich Institute of Biomedical Engineering, Technical University of Munich, James-Franck-Str. 1, 85748, Garching, Germany

<sup>e</sup> Department of Diagnostic and Interventional Radiology, School of Medicine, Klinikum rechts der Isar, Technical University of Munich, Ismaninger Str. 22, 81675 München, Germany

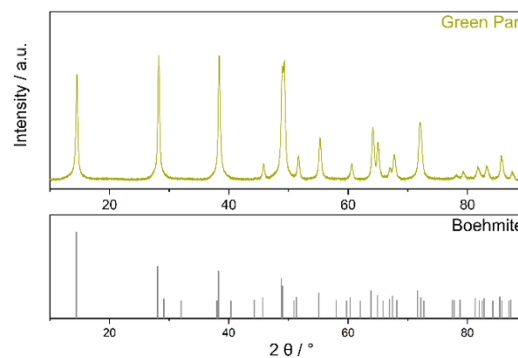
\* Corresponding author. *E-mail address:* rieger@tum.de

## Powder XRD analysis of the printed catalyst shapes

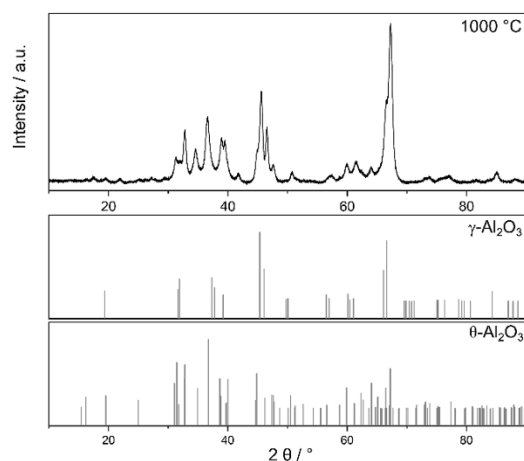
a) Green Part, calc. 1000 °C and calc. 1100 °C



b) Green Part and reference pattern



c) Calc. 1000 °C and reference pattern



d) Calc. 1100 °C and reference pattern

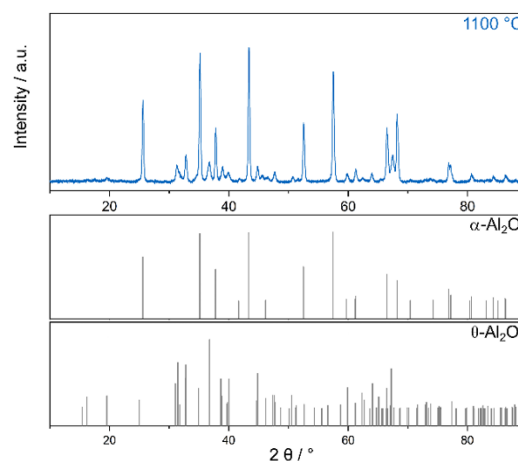


Figure S1: Comparison (a) of powder XRD analysis of uncalcined green part (b), after calcination at 1000 °C (c) and 1100 °C (d) with the respective reference pattern (boehmite: 98-008-2504;  $\gamma\text{-Al}_2\text{O}_3$ : boehmite derived: 98-009-9836;  $\theta\text{-Al}_2\text{O}_3$ : 98-008-2504;  $\alpha\text{-Al}_2\text{O}_3$ : 98-016-0903).

**Dimensions and densities of carriers**Table S1: Dimensions and densities of cylindrical and monolithic carrier in dependence on their calcination temperature (height  $h$ , diameter  $d$ , hole diameter  $d_{\text{hole}}$ , strand diameter  $d_{\text{strand}}$ , bulk density  $\rho_{\text{bulk}}$  and apparent solid density  $\rho_{\text{app}}$ ).

Shape	$T_{\text{calc}}$ / °C	$h$ /mm	$d$ / mm	$d_{\text{hole}}$ / mm	$d_{\text{strand}}$ / mm	$\rho_{\text{bulk}}$ / g·mL <sup>-1</sup>	$\rho_{\text{app}}$ / g·mL <sup>-1</sup>
Cyl.	1000	3.9 ± 0.1	3.6 ± 0.1	n.a.	n.a.	1.16 ± 0.01	3.42 ± 0.33
	1100	3.7 ± 0.1	3.4 ± 0.1	n.a.	n.a.	1.33 ± 0.02	3.21 ± 0.11
Monol.	1000	4.0 ± 0.1	21.1 ± 0.3	3.6 ± 0.5	0.41 ± 0.01	0.69 ± 0.02	3.12 ± 0.02
	1100	3.8 ± 0.2	19.8 ± 0.4	3.4 ± 0.2	0.40 ± 0.01	0.83 ± 0.02	3.47 ± 0.07

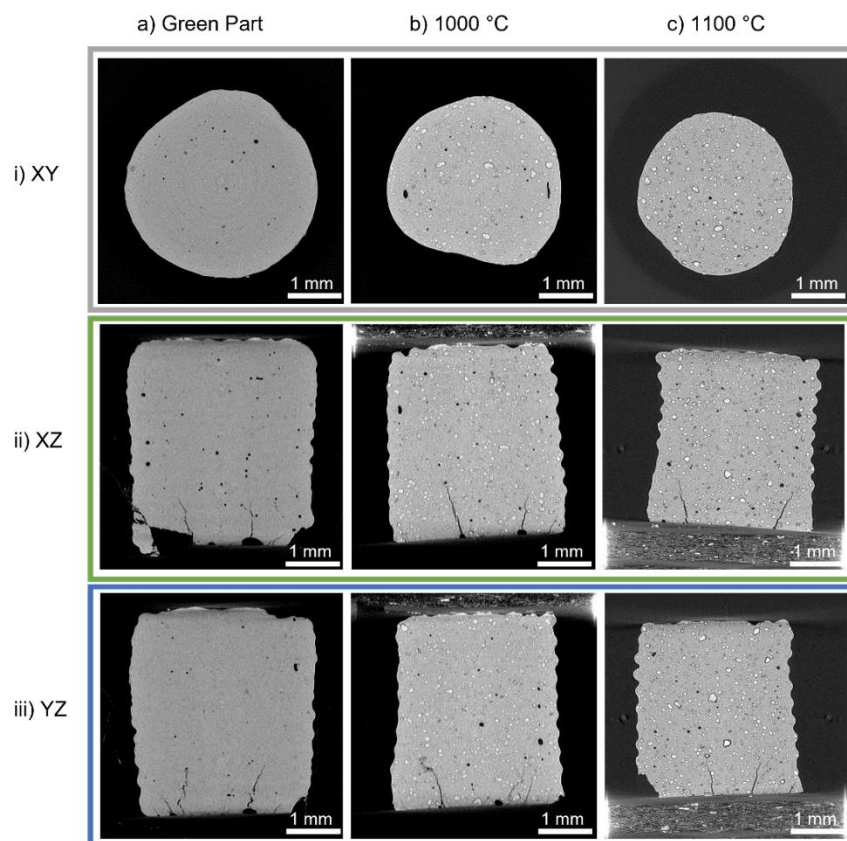
**$\mu$ CT Measurements of catalyst carriers prior to impregnation**

Figure S2:  $\mu$ CT scans of a) uncalcined (left), b) 1000 °C (center) and c) 1100 °C (right) cylindrical samples showing i) the XY slice (grey), ii) the XZ slice (green) and iii) the YZ slice (blue). The colors correspond to the cross-sections depicted in the experimental section of the manuscript.



**Physisorption of impregnated cylinders**Table S2: Specific surface area  $S_{\text{BET}}$  and total pore volume  $V_p$  of calcined catalyst, impregnated and recalcined as well as of reduced cylinders in dependence on the Pt loading and the calcination temperature determined by  $\text{N}_2$  physisorption.

$T_{\text{calc}}$ / °C	$\omega_{\text{target}}$ / wt.%	$S_{\text{BET}}$ / $\text{m}^2 \cdot \text{g}^{-1}$			$V_p$ / $\text{mL} \cdot \text{g}^{-1}$		
		Support	Impr. and calc.	Reduced	Support	Impr. and calc.	Reduced
1000	0.3	55	54	55	0.27	0.23	0.25
	0.9	55	52	51	0.27	0.23	0.20
1100	0.3	22	22	22	0.14	0.11	0.10
	0.9	22	31	23	0.14	0.17	0.13

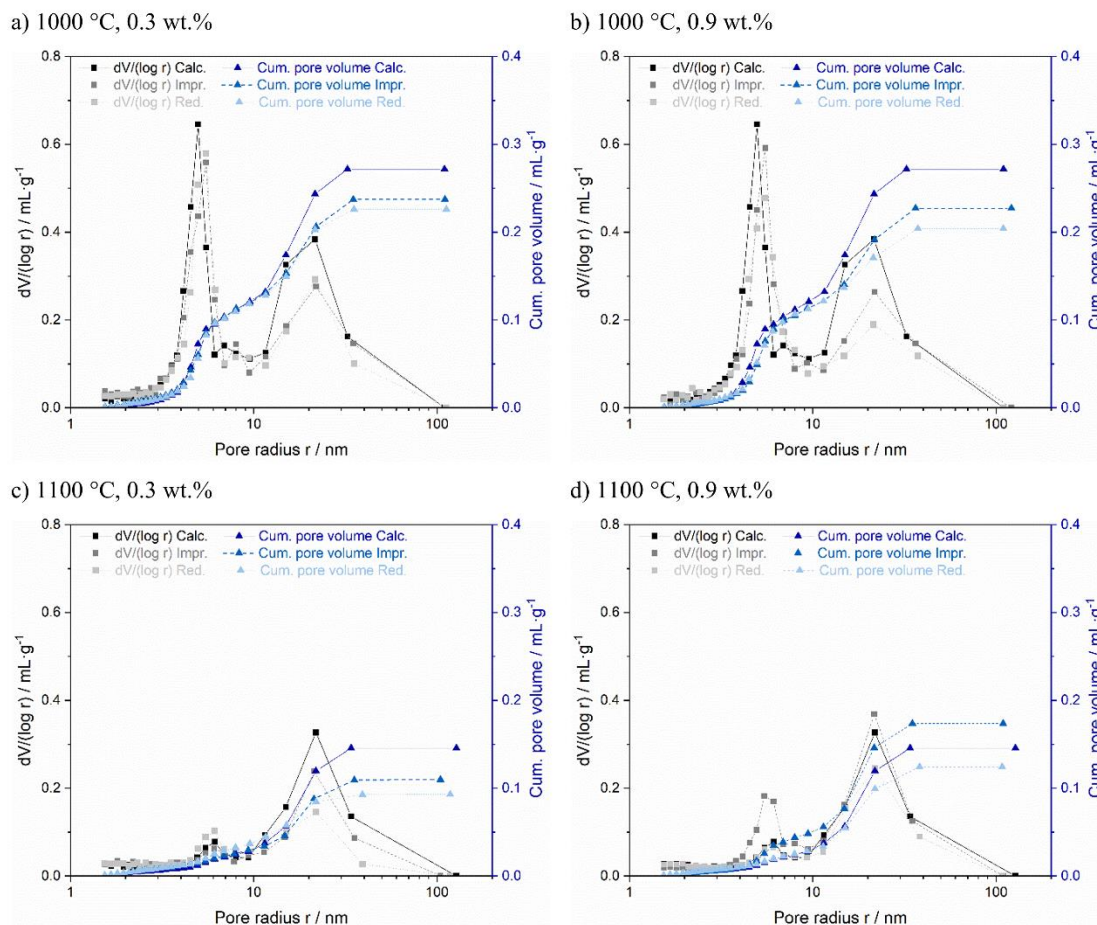


Figure S3: Pore size distributions and cumulative pore volume of calcined cylindrical carriers, impregnated and recalcined shapes and reduced ones at different calcination temperatures and target loadings determined by  $N_2$  physisorption. a) 1000 °C 0.3 wt.%; b) 1000 °C 0.9 wt.%; c) 1100 °C 0.3 wt.%; d) 1100 °C 0.9 wt.%.

**TEM images and metal particle distributions**

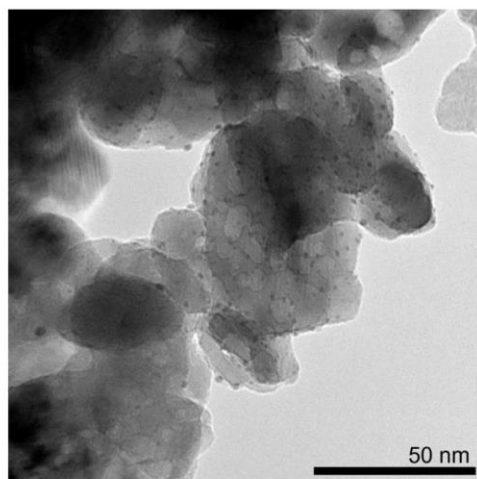
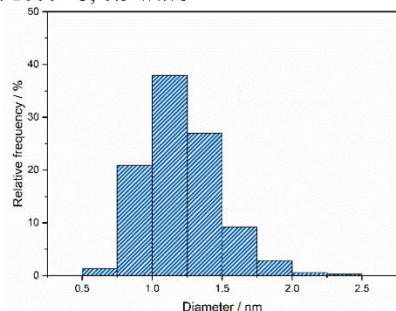
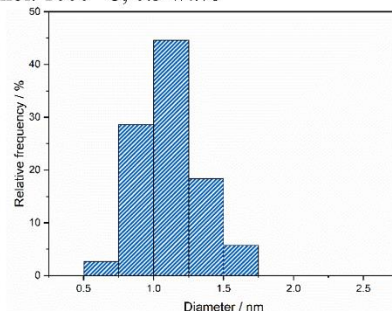


Figure S4: Exemplary TEM image of a cylinder calcined at 1000 °C with a target loading of 0.3 wt.%.

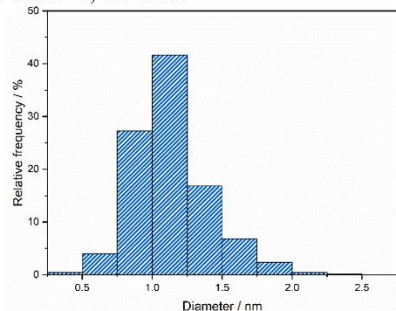
a) Cyl. 1000 °C, 0.3 wt.%



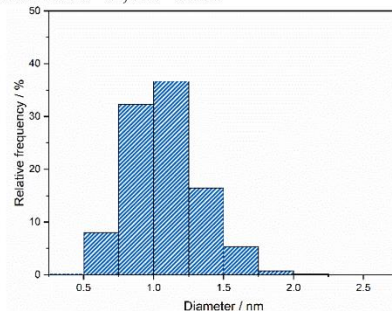
b) Monol. 1000 °C, 0.3 wt.%



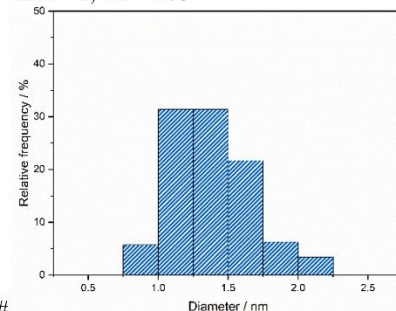
c) Cyl. 1000 °C, 0.9 wt.%



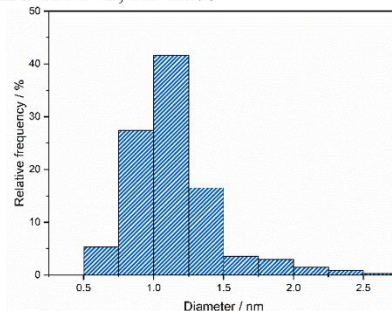
d) Monol. 1000 °C, 0.9 wt.%



e) Cyl. 1100 °C, 0.3 wt.%

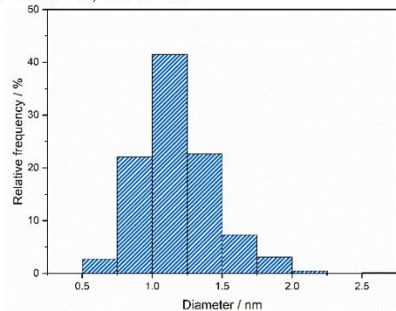


f) Monol. 1100 °C, 0.3 wt.%



#

g) Cyl. 1100 °C, 0.9 wt.%



h) Monol. 1100 °C, 0.9 wt.%

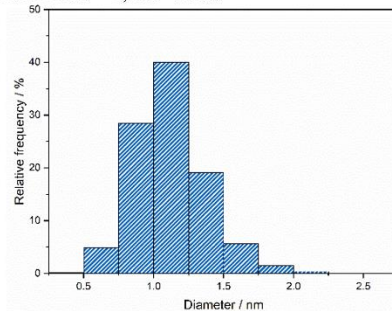


Figure S5: Metal particle size distributions as determined via TEM analysis.

a) Cyl. 1000 °C, 0.3wt.%; b) Monol. 1000 °C, 0.3wt.%; c) Cyl. 1000 °C, 0.9wt.%; d) Monol. 1000 °C, 0.9wt.%;  
 e) Cyl. 1100 °C, 0.3wt.%; f) Monol. 1100 °C, 0.3wt.%; g) Cyl. 1100 °C, 0.9wt.%; h) Monol. 1100 °C, 0.9wt.%;

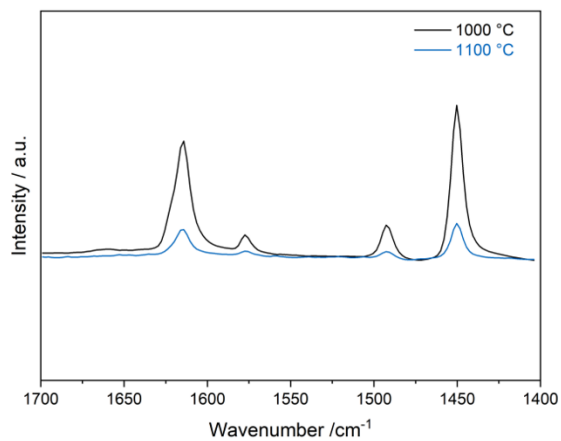
**IR spectra of pyridine adsorbed on catalyst carriers**

Figure S6: IR spectra of pyridine adsorbed on mortared cylindrical catalyst carriers calcined at either 1000 °C (black) or 1100 °C (blue). The band at 1451 cm<sup>-1</sup> and 1610 cm<sup>-1</sup> can be attributed to pyridine adsorbed on LAS whereas the band at around 1490 cm<sup>-1</sup> is commonly due to vibrations of PyH<sup>+</sup> and coordinately bound pyridine. [1–3]

Images of impregnated cylinders

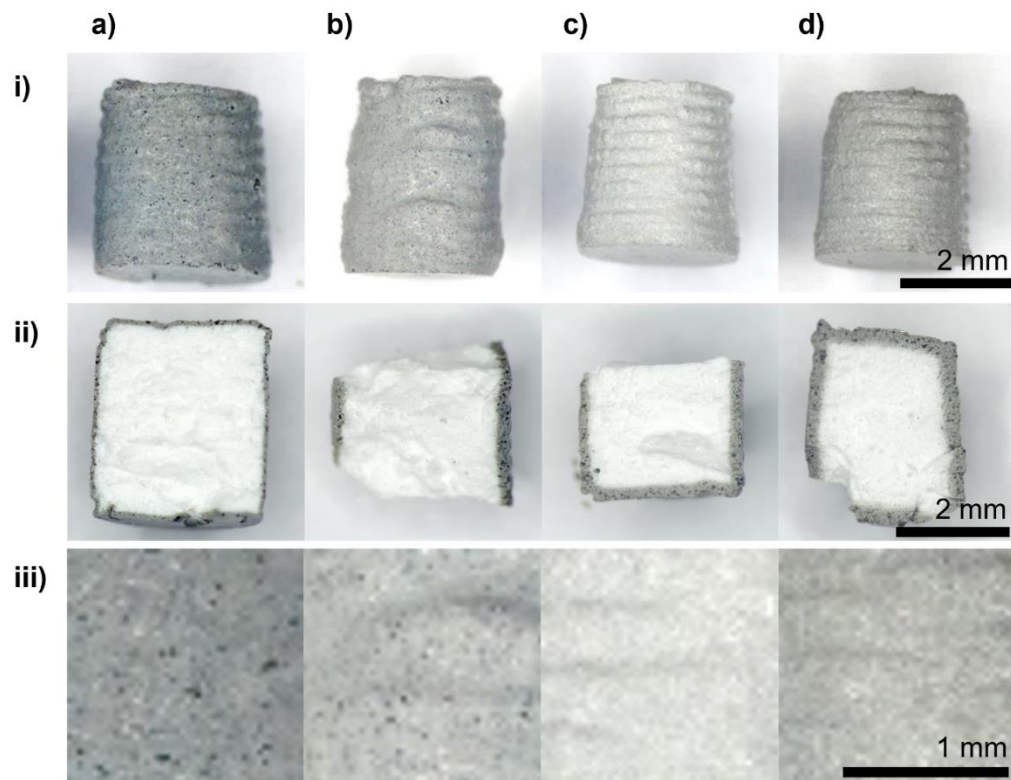


Figure S7: Light microscopy images of impregnated and reduced cylinders at different calcination temperatures and target loadings.

a) 1000 °C, 0.3 wt.%, b) 1000 °C, 0.9 wt.%, c) 1100 °C, 0.3 wt.%, d) 1100 °C, 0.9 wt.%;

i) side view, ii) cross section area, iii) detailed outer surface.

$\mu$ CT analysis of impregnated cylinders

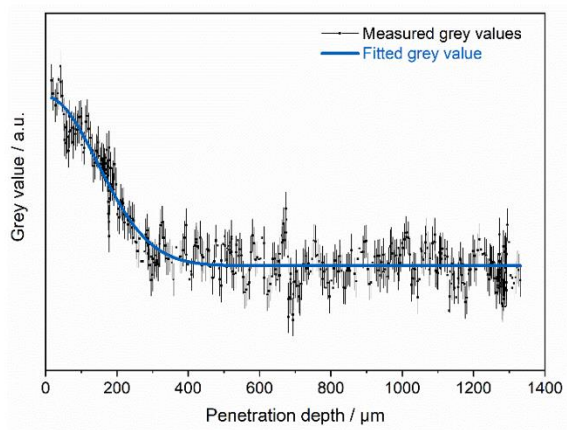


Figure S8: Exemplary single grey values (black) and the corresponding fit (blue) for the cylinder 1100 °C 0.9 wt.% as derived from  $\mu$ CT analysis.

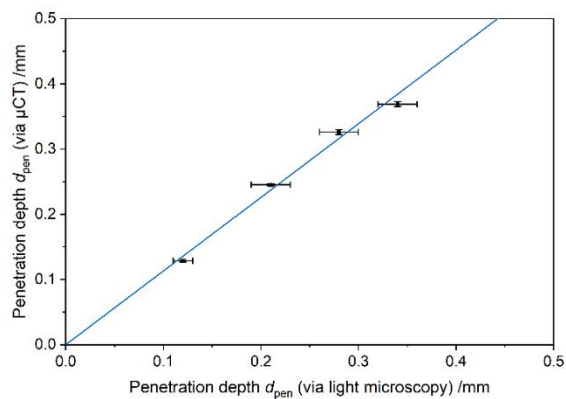


Figure S9: Penetration depth  $d_{pen}$  as calculated via  $\mu$ CT where the platinum density is at one tenth of the value at the surface of the cylinder over  $d_{pen}$  as determined via light microscopy and the respective linear fit.

**References**

- [1] M. Tamura, K.-i. Shimizu, A. Satsuma, Comprehensive IR study on acid/base properties of metal oxides, *Appl. Cat. A. Gen.* 433-434 (2012) 135–145. <https://doi.org/10.1016/j.apcata.2012.05.008>.
- [2] J.N. Kondo, R. Nishitani, E. Yoda, T. Yokoi, T. Tatsumi, K. Domen, A comparative IR characterization of acidic sites on HY zeolite by pyridine and CO probes with silica-alumina and  $\gamma$ -alumina references, *Phys. Chem. Chem. Phys.* 12 (2010) 11576–11586. <https://doi.org/10.1039/c0cp00203h>.
- [3] M.H. Healy, L.F. Wieserman, E.M. Arnett, K. Wefers, Infrared spectroscopy and microcalorimetric investigations of .delta.-.theta. and .kappa. aluminas using basic probe molecules: acetonitrile, pyridine, 2,6-lutidine, and n-butylamine, *Langmuir* 5 (1989) 114–123. <https://doi.org/10.1021/la00085a021>.



### **8.3 Additional information for Chapter 6 “Comparison of Direct Ink Writing and Binder Jetting for additive manufacturing of Pt/Al<sub>2</sub>O<sub>3</sub> catalysts for the dehydrogenation of perhydro-dibenzyltoluene”**

#### **8.3.1 Reprint permission**

The contents for Chapter 6 and the corresponding supporting information in Chapter 8.3.2 for the manuscript titled “Comparison of Direct Ink Writing and Binder Jetting for additive manufacturing of Pt/Al<sub>2</sub>O<sub>3</sub> catalysts for the dehydrogenation of perhydro-dibenzyltoluene” have been published in Chemical Engineering Journal (Elsevier B. V.). The authors possess the copyright of the reprinted material, manuscript and supporting information have been reprinted from ref. [297].

### 8.3.2 Supporting information

#### Supporting Information

#### Comparison of Direct Ink Writing and Binder Jetting for Additive Manufacturing of Pt/Al<sub>2</sub>O<sub>3</sub> Catalysts for the Dehydrogenation of Perhydro-dibenzyltoluene

Hanh My Bui<sup>a,b,1</sup>, Paula F. Großmann<sup>a,b,c,1</sup>, Anne Berger<sup>a,b,d</sup>, Alexander Seidel<sup>e</sup>, Markus Tonigold<sup>f</sup>, Normen Szesni<sup>f</sup>, Richard Fischer<sup>a,f</sup>, Bernhard Rieger<sup>a,b,c</sup>, Olaf Hinrichsen<sup>a,b,2</sup>

<sup>a</sup>Department of Chemistry, Technical University of Munich, Lichtenbergstraße 4, 85748, Garching, Germany

<sup>b</sup>Catalysis Research Center, Technical University of Munich, Ernst-Otto-Fischer-Straße 1, 85748, Garching, Germany

<sup>c</sup>WACKER-Chair of Macromolecular Chemistry, Technical University of Munich, Lichtenbergstraße 4, 85748, Garching, Germany

<sup>d</sup>Chair of Technical Electrochemistry, Technical University of Munich, Lichtenbergstraße 4, 85748, Garching, Germany

<sup>e</sup>HYDROGENIOUS LOHC TECHNOLOGIES GmbH, Weidenweg 13, 91058, Erlangen, Germany

<sup>f</sup>Clariant Produkte (Deutschland) GmbH, Waldheimer Straße 13, 83052, Bruckmühl, Germany

#### 1. Alumina phase determination

Phase determination of the 3D printed alumina supports was obtained via XRD analysis (Empyrean, Malvern Panalytical, UK). Cu-K<sub>α</sub> radiation ( $\lambda = 1.54056 \text{ \AA}$ ) and a monochromator were employed to scan the samples applying a step size of  $0.007^\circ$  and 70 steps/min from  $2\theta = 5^\circ - 90^\circ$ . Fig. [S1](#) compares the diffraction pattern of DIW and BJ printed supports calcined at  $1100^\circ\text{C}$ , as used for the LOHC dehydrogenation test. The reflex patterns reveal that the BJ printed support contains only  $\alpha\text{-Al}_2\text{O}_3$  whereas the DIW support consist of mainly  $\alpha\text{-Al}_2\text{O}_3$  with weak reflexes of  $\Theta\text{-Al}_2\text{O}_3$  phase. The two applied additive manufacturing techniques do not result in an alteration of the alumina structure, since the preparation of the raw materials only involve powder mixing.

<sup>1</sup>These authors equally contributed to this work.

<sup>2</sup>Corresponding author at: Technical University of Munich, Department of Chemistry, Lichtenbergstr. 4, 85748 Garching, Germany. E-mail: [olaf.hinrichsen@ch.tum.de](mailto:olaf.hinrichsen@ch.tum.de)

Moreover, thermal treatment in form of calcination and reduction was equal to conventional catalyst preparation, meaning that the alumina lattice structure is unaffected by processing by 3D printing which is also visible by no shifts in diffraction angle.

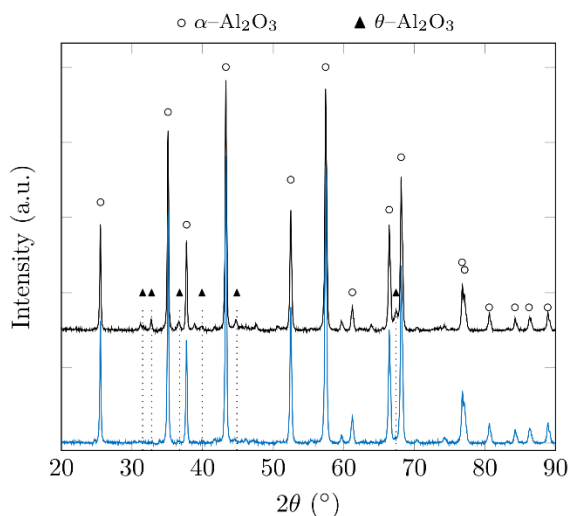


Figure S1: XRD diffraction pattern of alumina supports, printed by BJ (blue) and DIW (black). (Reference patterns:  $\alpha$ - $\text{Al}_2\text{O}_3$ : ICSD 01-075-1862,  $\theta$ - $\text{Al}_2\text{O}_3$ : PDF 00-023-1009).

15

## 2. Particle size of catalyst powder for LOHC dehydrogenation

Fig. S2 shows the particle size distribution of the used powder material. The particle size distribution of the ground monoliths used for the LOHC dehydrogenation test was determined by a laser diffraction particle size analyzer (LS 13 320 Particle Size Analyzer, Beckman Coulter, USA). The sample was measured after dispersion in distilled water as this represents the reaction conditions best (solid catalyst particles in liquid reactant).  $d_{10}$ ,  $d_{50}$ ,  $d_{90}$  values of the powder are 11.82  $\mu\text{m}$ , 81.51  $\mu\text{m}$  and 167.50  $\mu\text{m}$ , respectively. The mean diameter is 89.20  $\mu\text{m}$ .

2

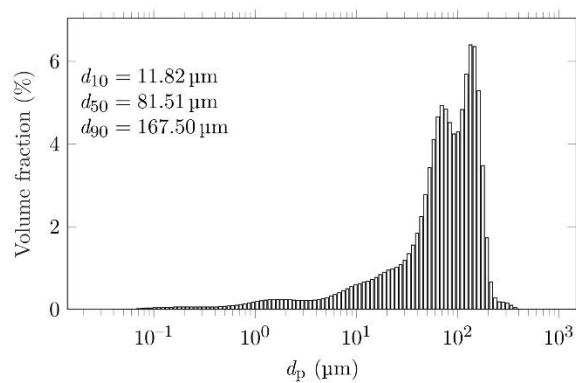


Figure S2: Particle size distribution of powder used for LOHC dehydrogenation, prepared by grinding of whole monoliths.

### 25 3. Pt Particle Size distribution TEM

Figs. S3 and S4 show the particle size distribution of the Pt nanoparticles on the 3D printed Pt/ $\text{Al}_2\text{O}_3$  catalysts. The target loading was 0.3 wt.%. For each sample, a minimum of 460 particles was counted on several micrographs taken on different zones of the TEM grid. The average particle diameters were  
30 used to calculate the metal dispersion.

## 3.1. Binder Jetting

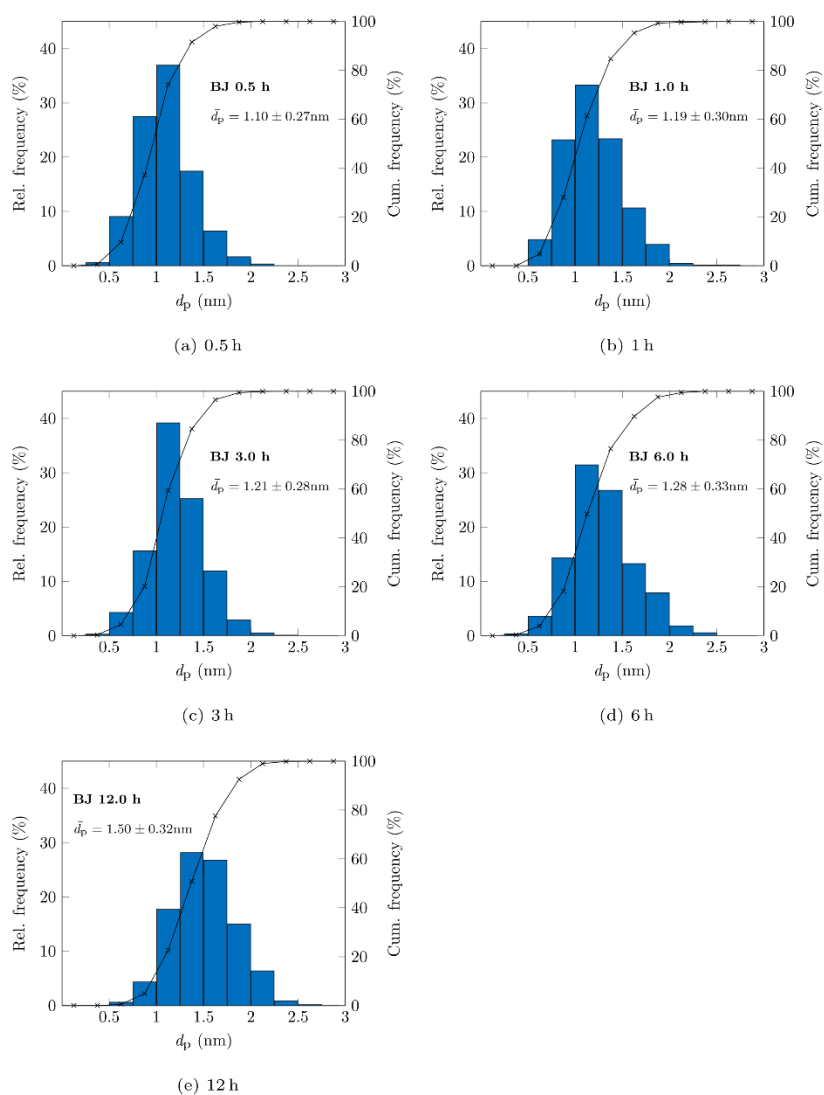


Figure S3: Pt particle size distribution by TEM of BJ printed Pt/Al<sub>2</sub>O<sub>3</sub> catalysts which were wet impregnated with a target Pt loading of 0.3 wt.% for varying durations.

## 3.2. Direct Ink Writing

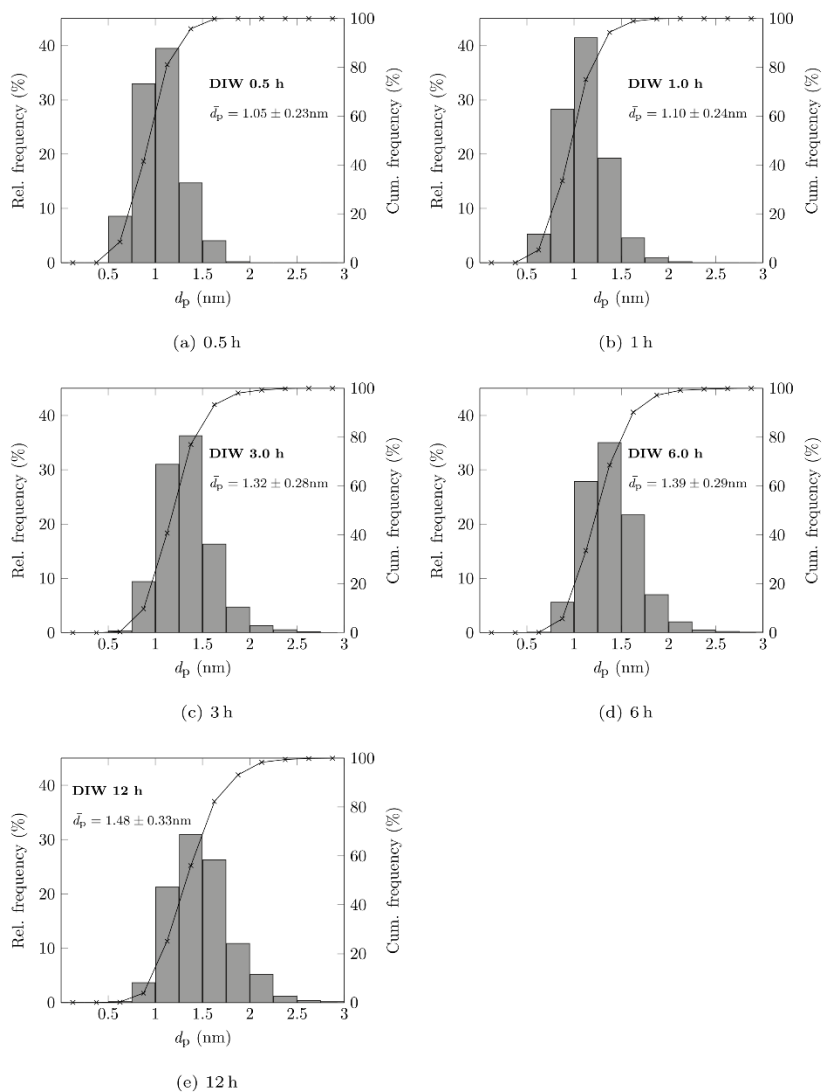


Figure S4: Pt particle size distribution by TEM of DIW printed Pt/Al<sub>2</sub>O<sub>3</sub> catalysts which were wet impregnated with a target Pt loading of 0.3 wt.% for varying durations.

## 8.4 Reprint permissions for figures

### Copyright permissions for **Figure 9** (ref. [151]):

RightsLink Printable License		https://s100.copyright.com/App/PrintableLicenseFrame.jsp?publis		RightsLink Printable License		https://s100.copyright.com/App/PrintableLicenseFrame.jsp?publis	
<p>ELSEVIER LICENSE TERMS AND CONDITIONS</p> <p>Feb 28, 2023</p> <hr/> <p>This Agreement between Technical University of Munich – Paula Großmann ("You") and Elsevier ("Elsevier") consists of your license details and the terms and conditions provided by Elsevier and Copyright Clearance Center.</p> <p>License Number 5497821344532</p> <p>License date Feb 28, 2023</p> <p>Licensed Content Publisher Elsevier</p> <p>Licensed Content Publication Catalysis Today</p> <p>Licensed Content Title Adsorption/catalytic properties of MIL-125 and NH2-MIL-125</p> <p>Licensed Content Author Se-Na Kim,Jun Kim,Hee-Young Kim,Hye-Young Cho,Wha-Seung Ahn</p> <p>Licensed Content Date Apr 15, 2013</p> <p>Licensed Content Volume 204</p> <p>Licensed Content Issue n/a</p> <p>Licensed Content Pages 9</p> <p>Start Page 85</p> <p>End Page 93</p>				<p>Type of Use reuse in a thesis/dissertation</p> <p>Portion figures/tables/illustrations</p> <p>Number of figures/tables/illustrations 1</p> <p>Format both print and electronic</p> <p>Are you the author of this Elsevier article? No</p> <p>Will you be translating? No</p> <p>Title Advanced Shaping of Catalysts via Additive Manufacturing – Direct Ink Writing in the Context of Heterogeneous Catalysis</p> <p>Institution name Technical University of Munich</p> <p>Expected presentation date May 2023</p> <p>Portions Scheme 1</p> <p>Requestor Location Technical University of Munich Lichtenbergstr. 4 Garching near Munich, 85747 Germany Attn: Technical University of Munich</p> <p>Publisher Tax ID GB 494 6272 12</p> <p>Total 0.00 EUR</p> <p>Terms and Conditions</p>			
1 von 8	28.02.2023,	2 von 8	28.02.2023,				

RightsLink Printable License		https://s100.copyright.com/App/PrintableLicenseFrame.jsp?publis		RightsLink Printable License		https://s100.copyright.com/App/PrintableLicenseFrame.jsp?publis	
<p><b>INTRODUCTION</b></p> <p>1. The publisher for this copyrighted material is Elsevier. By clicking "accept" in connection with completing this licensing transaction, you agree that the following terms and conditions apply to this transaction (along with the Billing and Payment terms and conditions established by Copyright Clearance Center, Inc. ("CCC"), at the time that you opened your Rightslink account and that are available at any time at <a href="http://myaccount.copyright.com">http://myaccount.copyright.com</a>).</p> <p><b>GENERAL TERMS</b></p> <p>2. Elsevier hereby grants you permission to reproduce the aforementioned material subject to the terms and conditions indicated.</p> <p>3. Acknowledgement: If any part of the material to be used (for example, figures) has appeared in our publication with credit or acknowledgement to another source, permission must also be sought from that source. If such permission is not obtained then that material may not be included in your publication/copies. Suitable acknowledgement to the source must be made, either as a footnote or in a reference list at the end of your publication, as follows:</p> <p>"Reprinted from Publication title, Vol /edition number, Author(s), Title of article / title of chapter, Pages No., Copyright (Year), with permission from Elsevier [OR APPLICABLE SOCIETY COPYRIGHT OWNER]." Also Lancet special credit - "Reprinted from The Lancet, Vol. number, Author(s), Title of article, Pages No., Copyright (Year), with permission from Elsevier."</p> <p>4. Reproduction of this material is confined to the purpose and/or media for which permission is hereby given.</p> <p>5. Altering/Modifying Material: Not Permitted. However figures and illustrations may be altered/adapted minimally to serve your work. Any other abbreviations, additions, deletions and/or any other alterations shall be made only with prior written authorization of Elsevier Ltd. (Please contact Elsevier's permissions helpdesk here). No modifications can be made to any Lancet figures/tables and they must be reproduced in full.</p> <p>6. If the permission fee for the requested use of our material is waived in this instance, please be advised that your future requests for Elsevier materials may attract a fee.</p> <p>7. Reservation of Rights: Publisher reserves all rights not specifically granted in the combination of (i) the license details provided by you and accepted in the course of this licensing transaction, (ii) these terms and conditions and (iii) CCC's Billing and Payment terms and conditions.</p> <p>8. License Contingent Upon Payment: While you may exercise the rights licensed immediately upon issuance of the license at the end of the licensing process for the transaction, provided that you have disclosed complete and accurate details of your proposed use, no license is finally effective unless and until full payment is received from you (either by publisher or by CCC) as provided in CCC's Billing and Payment terms and conditions. If full payment is not received on a timely basis, then any license preliminarily granted shall be deemed automatically revoked and shall be void as if never granted. Further, in the event</p>				<p>that you breach any of these terms and conditions or any of CCC's Billing and Payment terms and conditions, the license is automatically revoked and shall be void as if never granted. Use of materials as described in a revoked license, as well as any use of the materials beyond the scope of an unrevoked license, may constitute copyright infringement and publisher reserves the right to take any and all action to protect its copyright in the materials.</p> <p>9. Warranties: Publisher makes no representations or warranties with respect to the licensed material.</p> <p>10. Indemnity: You hereby indemnify and agree to hold harmless publisher and CCC, and their respective officers, directors, employees and agents, from and against any and all claims arising out of your use of the licensed material other than as specifically authorized pursuant to this license.</p> <p>11. No Transfer of License: This license is personal to you and may not be sublicensed, assigned, or transferred by you to any other person without publisher's written permission.</p> <p>12. No Amendment Except in Writing: This license may not be amended except in a writing signed by both parties (or, in the case of publisher, by CCC on publisher's behalf).</p> <p>13. Objection to Contrary Terms: Publisher hereby objects to any terms contained in any purchase order, acknowledgment, check endorsement or other writing prepared by you, which terms are inconsistent with these terms and conditions or CCC's Billing and Payment terms and conditions. These terms and conditions, together with CCC's Billing and Payment terms and conditions (which are incorporated herein), comprise the entire agreement between you and publisher (and CCC) concerning this licensing transaction. In the event of any conflict between your obligations established by these terms and conditions and those established by CCC's Billing and Payment terms and conditions, these terms and conditions shall control.</p> <p>14. Revocation: Elsevier or Copyright Clearance Center may deny the permissions described in this License at their sole discretion, for any reason or no reason, with a full refund payable to you. Notice of such denial will be made using the contact information provided by you. Failure to receive such notice will not alter or invalidate the denial. In no event will Elsevier or Copyright Clearance Center be responsible or liable for any costs, expenses or damage incurred by you as a result of a denial of your permission request, other than a refund of the amount(s) paid by you to Elsevier and/or Copyright Clearance Center for denied permissions.</p> <p><b>LIMITED LICENSE</b></p> <p>The following terms and conditions apply only to specific license types:</p> <p>15. <b>Translation:</b> This permission is granted for non-exclusive world <b>English</b> rights only unless your license was granted for translation rights. If you licensed translation rights you may only translate this content into the languages you requested. A professional translator must perform all translations and reproduce the content word for word preserving the integrity of the article.</p> <p>16. <b>Posting licensed content on any Website:</b> The following terms and conditions apply as follows: Licensing material from an Elsevier journal: All content posted to the web site must</p>			
1 von 8	28.02.2023,	4 von 8	28.02.2023,				

maintain the copyright information line on the bottom of each image; A hyper-text must be included to the Homepage of the journal from which you are licensing at <http://www.sciencedirect.com/science/journal/xxxxx> or the Elsevier homepage for books at <http://www.elsevier.com>; Central Storage: This license does not include permission for a scanned version of the material to be stored in a central repository such as that provided by Heron/XanEdu.

Licensing material from an Elsevier book: A hyper-text link must be included to the Elsevier homepage at <http://www.elsevier.com>. All content posted to the web site must maintain the copyright information line on the bottom of each image.

**Posting licensed content on Electronic reserve:** In addition to the above the following clauses are applicable: The web site must be password-protected and made available only to bona fide students registered on a relevant course. This permission is granted for 1 year only. You may obtain a new license for future website posting.

**17. For journal authors:** the following clauses are applicable in addition to the above:

**Preprints:**

A preprint is an author's own write-up of research results and analysis, it has not been peer-reviewed, nor has it had any other value added to it by a publisher (such as formatting, copyright, technical enhancement etc.).

Authors can share their preprints anywhere at any time. Preprints should not be added to or enhanced in any way in order to appear more like, or to substitute for, the final versions of articles however authors can update their preprints on arXiv or RePEc with their Accepted Author Manuscript (see below).

If accepted for publication, we encourage authors to link from the preprint to their formal publication via its DOI. Millions of researchers have access to the formal publications on ScienceDirect, and so links will help users to find, access, cite and use the best available version. Please note that Cell Press, The Lancet and some society-owned have different preprint policies. Information on these policies is available on the journal homepage.

**Accepted Author Manuscripts:** An accepted author manuscript is the manuscript of an article that has been accepted for publication and which typically includes author-incorporated changes suggested during submission, peer review and editor-author communications.

Authors can share their accepted author manuscript:

- immediately
  - via their non-commercial person homepage or blog
  - by updating a preprint in arXiv or RePEc with the accepted manuscript
  - via their research institute or institutional repository for internal institutional uses or as part of an invitation-only research collaboration work-group
  - directly by providing copies to their students or to research collaborators for their personal use
  - for private scholarly sharing as part of an invitation-only work group on commercial sites with which Elsevier has an agreement

- After the embargo period
  - via non-commercial hosting platforms such as their institutional repository
  - via commercial sites with which Elsevier has an agreement

In all cases accepted manuscripts should:

- link to the formal publication via its DOI
- bear a CC-BY-NC-ND license - this is easy to do
- if aggregated with other manuscripts, for example in a repository or other site, be shared in alignment with our hosting policy not be added to or enhanced in any way to appear more like, or to substitute for, the published journal article.

**Published journal article (JPA):** A published journal article (JPA) is the definitive final record of published research that appears or will appear in the journal and embodies all value-adding publishing activities including peer review co-ordination, copy-editing, formatting, (if relevant) pagination and online enrichment.

Policies for sharing publishing journal articles differ for subscription and gold open access articles:

**Subscription Articles:** If you are an author, please share a link to your article rather than the full-text. Millions of researchers have access to the formal publications on ScienceDirect, and so links will help your users to find, access, cite, and use the best available version.

Theses and dissertations which contain embedded JPAs as part of the formal submission can be posted publicly by the awarding institution with DOI links back to the formal publications on ScienceDirect.

If you are affiliated with a library that subscribes to ScienceDirect you have additional private sharing rights for others' research accessed under that agreement. This includes use for classroom teaching and internal training at the institution (including use in course packs and courseware programs), and inclusion of the article for grant funding purposes.

**Gold Open Access Articles:** May be shared according to the author-selected end-user license and should contain a [CrossMark logo](#), the end user license, and a DOI link to the formal publication on ScienceDirect.

Please refer to Elsevier's [posting policy](#) for further information.

**18. For book authors** the following clauses are applicable in addition to the above: Authors are permitted to place a brief summary of their work online only. You are not allowed to download and post the published electronic version of your chapter, nor may you scan the printed edition to create an electronic version. **Posting to a repository:** Authors are permitted to post a summary of their chapter only in their institution's repository.

**19. Thesis/Dissertation:** If your license is for use in a thesis/dissertation your thesis may be submitted to your institution in either print or electronic form. Should your thesis be published commercially, please reapply for permission. These requirements include permission for the Library and Archives of Canada to supply single copies, on demand, of the complete thesis and include permission for Proquest/UMI to supply single copies, on demand, of the complete thesis. Should your thesis be published commercially, please reapply for permission. Theses and dissertations which contain embedded JPAs as part of

the formal submission can be posted publicly by the awarding institution with DOI links back to the formal publications on ScienceDirect.

**Elsevier Open Access Terms and Conditions**

You can publish open access with Elsevier in hundreds of open access journals or in nearly 2000 established subscription journals that support open access publishing. Permitted third party re-use of these open access articles is defined by the author's choice of Creative Commons user license. See our [open access license policy](#) for more information.

**Terms & Conditions applicable to all Open Access articles published with Elsevier:**

Any reuse of the article must not represent the author as endorsing the adaptation of the article nor should the article be modified in such a way as to damage the author's honour or reputation. If any changes have been made, such changes must be clearly indicated.

The author(s) must be appropriately credited and we ask that you include the end user license and a DOI link to the formal publication on ScienceDirect.

If any part of the material to be used (for example, figures) has appeared in our publication with credit or acknowledgement to another source it is the responsibility of the user to ensure their reuse complies with the terms and conditions determined by the rights holder.

**Additional Terms & Conditions applicable to each Creative Commons user license:**

**CC BY:** The CC-BY license allows users to copy, to create extracts, abstracts and new works from the Article, to alter and revise the Article and to make commercial use of the Article (including reuse and/or resale of the Article by commercial entities), provided the user gives appropriate credit (with a link to the formal publication through the relevant DOI), provides a link to the license, indicates if changes were made and the licensor is not represented as endorsing the use made of the work. The full details of the license are available at <http://creativecommons.org/licenses/by/4.0>.

**CC BY NC SA:** The CC BY-NC-SA license allows users to copy, to create extracts, abstracts and new works from the Article, to alter and revise the Article, provided this is not done for commercial purposes, and that the user gives appropriate credit (with a link to the formal publication through the relevant DOI), provides a link to the license, indicates if changes were made and the licensor is not represented as endorsing the use made of the work. Further, any new works must be made available on the same conditions. The full details of the license are available at <http://creativecommons.org/licenses/by-nc-sa/4.0>.

**CC BY NC ND:** The CC BY-NC-ND license allows users to copy and distribute the Article, provided this is not done for commercial purposes and further does not permit distribution of the Article if it is changed or edited in any way, and provided the user gives appropriate credit (with a link to the formal publication through the relevant DOI), provides a link to the license, and that the licensor is not represented as endorsing the use made of the work. The full details of the license are available at <http://creativecommons.org/licenses/by-nc-nd/4.0>. Any commercial reuse of Open Access articles published with a CC BY NC SA or CC BY NC ND license requires permission from Elsevier and will be subject to a fee.

Commercial reuse includes:

- Associating advertising with the full text of the Article
- Charging fees for document delivery or access
- Article aggregation
- Systematic distribution via e-mail lists or share buttons

Posting or linking by commercial companies for use by customers of those companies.

**20. Other Conditions:**

v1.10

Questions? [customercare@copyright.com](mailto:customercare@copyright.com).



Copyright permissions for **Figure 15** (ref. [274]):

RightsLink Printable License	https://s100.copyright.com/App/PrintableLicenseFrame.jsp/publi	RightsLink Printable License	https://s100.copyright.com/App/PrintableLicenseFrame.jsp/publi
SPRINGER NATURE LICENSE TERMS AND CONDITIONS		High-res required	no
Feb 28, 2023		Will you be translating?	no
		Circulation/distribution	30 - 99
This Agreement between Technical University of Munich – Paula Grofmann ("You") and Springer Nature ("Springer Nature") consists of your license details and the terms and conditions provided by Springer Nature and Copyright Clearance Center.		Author of this Springer Nature content	no
License Number	5497820978092	Title	Advanced Shaping of Catalysts via Additive Manufacturing – Direct Ink Writing in the Context of Heterogeneous Catalysis
License date	Feb 28, 2023	Institution name	Technical University of Munich
Licensed Content Publisher	Springer Nature	Expected presentation date	May 2023
Licensed Content Publication	Nature Protocols	Portions	Figure 6
Licensed Content Title	3D printing of versatile reactionware for chemical synthesis	Requestor Location	Technical University of Munich Lichtenbergstr. 4 Garching near Munich, 85747 Germany Attn: Technical University of Munich
Licensed Content Author	Philip J Kitson et al	Total	0.00 USD
Licensed Content Date	Apr 14, 2016	Terms and Conditions	<b>Springer Nature Customer Service Centre GmbH Terms and Conditions</b> The following terms and conditions ("Terms and Conditions") together with the terms specified in your [RightsLink] constitute the License ("License") between you as Licensee and Springer Nature Customer Service Centre GmbH as Licensor. By clicking "accept" and completing the transaction for your use of the material ("Licensed Material"), you confirm your acceptance of and obligation to be bound by these Terms and Conditions.
Type of Use	Thesis/Dissertation		
Requestor type	academic/university or research institute		
Format	print and electronic		
Portion	figures/tables/illustrations		
Number of figures/tables/illustrations	1		
1 von 7	28.02.2023, 2 von 7		28.02.2023, 1

RightsLink Printable License	https://s100.copyright.com/App/PrintableLicenseFrame.jsp/publi	RightsLink Printable License	https://s100.copyright.com/App/PrintableLicenseFrame.jsp/publi														
<b>1. Grant and Scope of License</b>		formatting purposes provided such alterations do not alter the original meaning or intention of the Licensed Material and the new figure(s) are still accurate and representative of the Licensed Material. Any other changes including but not limited to, cropping, adapting, and/or omitting material that affect the meaning, intention or moral rights of the author(s) are strictly prohibited.															
1. 1. The Licensor grants you a personal, non-exclusive, non-transferable, non-sublicensable, revocable, world-wide License to reproduce, distribute, communicate to the public, make available, broadcast, electronically transmit or create derivative works using the Licensed Material for the purpose(s) specified in your RightsLink License Details only. Licenses are granted for the specific use requested in the order and for no other use, subject to these Terms and Conditions. You acknowledge and agree that the rights granted to you under this License do not include the right to modify, edit, translate, include in collective works, or create derivative works of the Licensed Material in whole or in part unless expressly stated in your RightsLink License Details. You may use the Licensed Material only as permitted under this Agreement and will not reproduce, distribute, display, perform, or otherwise use or exploit any Licensed Material in any way, in whole or in part, except as expressly permitted by this License.		3. 2. You must not use any Licensed Material as part of any design or trademark.															
1. 2. You may only use the Licensed Content in the manner and to the extent permitted by these Terms and Conditions, by your RightsLink License Details and by any applicable laws.		3. 3. Licensed Material may be used in Open Access Publications (OAP), but any such reuse must include a clear acknowledgment of this permission visible at the same time as the figures/tables/illustration or abstract and which must indicate that the Licensed Material is not part of the governing OA license but has been reproduced with permission. This may be indicated according to any standard referencing system but must include at a minimum 'Book/Journal title, Author, Journal Name (if applicable), Volume (if applicable), Publisher, Year, reproduced with permission from SNCSC'.															
1. 3. A separate license may be required for any additional use of the Licensed Material, e.g. where a license has been purchased for print use only, separate permission must be obtained for electronic re-use. Similarly, a License is only valid in the language selected and does not apply for editions in other languages unless additional translation rights have been granted separately in the License.		<b>4. STM Permission Guidelines</b>															
1. 4. Any content within the Licensed Material that is owned by third parties is expressly excluded from the License.		4. 1. An alternative scope of license may apply to signatories of the STM Permissions Guidelines ("STM PG") as amended from time to time and made available at <a href="https://www.stm-assoc.org/intellectual-property/permissions/permissions-guidelines/">https://www.stm-assoc.org/intellectual-property/permissions/permissions-guidelines/</a> .															
1. 5. Rights for additional reuses such as custom editions, computer/mobile applications, film or TV reuses and/or any other derivative rights requests require additional permission and may be subject to an additional fee. Please apply to <a href="mailto:journalpermissions@springernature.com">journalpermissions@springernature.com</a> or <a href="mailto:bookpermissions@springernature.com">bookpermissions@springernature.com</a> for these rights.		4. 2. For content reuse requests that qualify for permission under the STM PG, and which may be updated from time to time, the STM PG supersede the terms and conditions contained in this License.															
<b>2. Reservation of Rights</b>		4. 3. If a License has been granted under the STM PG, but the STM PG no longer apply at the time of publication, further permission must be sought from the Rightsholder. Contact <a href="mailto:journalpermissions@springernature.com">journalpermissions@springernature.com</a> or <a href="mailto:bookpermissions@springernature.com">bookpermissions@springernature.com</a> for these rights.															
Licensor reserves all rights not expressly granted to you under this License. You acknowledge and agree that nothing in this License limits or restricts Licensor's rights in or use of the Licensed Material in any way. Neither this License, nor any act, omission, or statement by Licensor or you, conveys any ownership right to you in any Licensed Material, or to any element or portion thereof. As between Licensor and you, Licensor owns and retains all right, title, and interest in and to the Licensed Material subject to the license granted in Section 1.1. Your permission to use the Licensed Material is expressly conditioned on you not impairing Licensor's or the applicable copyright owner's rights in the Licensed Material in any way.		<b>5. Duration of License</b>															
<b>3. Restrictions on use</b>		5. 1. Unless otherwise indicated on your License, a License is valid from the date of purchase ("License Date") until the end of the relevant period in the below table:															
3. 1. Minor editing privileges are allowed for adaptations for stylistic purposes or			<table border="1"> <tr> <td>Reuse in a medical communications project</td> <td>Reuse up to distribution or time period indicated in License</td> </tr> <tr> <td>Reuse in a dissertation/thesis</td> <td>Lifetime of thesis</td> </tr> <tr> <td>Reuse in a journal/magazine</td> <td>Lifetime of journal/magazine</td> </tr> <tr> <td>Reuse in a book/textbook</td> <td>Lifetime of edition</td> </tr> <tr> <td>Reuse on a website</td> <td>1 year unless otherwise specified in the License</td> </tr> <tr> <td>Reuse in a presentation/slide kit/poster</td> <td>Lifetime of presentation/slide kit/poster. Note: publication whether electronic or in print of presentation/slide kit/poster may require further permission.</td> </tr> <tr> <td>Reuse in conference proceedings</td> <td>Lifetime of conference proceedings</td> </tr> </table>	Reuse in a medical communications project	Reuse up to distribution or time period indicated in License	Reuse in a dissertation/thesis	Lifetime of thesis	Reuse in a journal/magazine	Lifetime of journal/magazine	Reuse in a book/textbook	Lifetime of edition	Reuse on a website	1 year unless otherwise specified in the License	Reuse in a presentation/slide kit/poster	Lifetime of presentation/slide kit/poster. Note: publication whether electronic or in print of presentation/slide kit/poster may require further permission.	Reuse in conference proceedings	Lifetime of conference proceedings
Reuse in a medical communications project	Reuse up to distribution or time period indicated in License																
Reuse in a dissertation/thesis	Lifetime of thesis																
Reuse in a journal/magazine	Lifetime of journal/magazine																
Reuse in a book/textbook	Lifetime of edition																
Reuse on a website	1 year unless otherwise specified in the License																
Reuse in a presentation/slide kit/poster	Lifetime of presentation/slide kit/poster. Note: publication whether electronic or in print of presentation/slide kit/poster may require further permission.																
Reuse in conference proceedings	Lifetime of conference proceedings																
3 von 7	28.02.2023, 4 von 7		28.02.2023, 1														

Reuse in an annual report	Lifetime of annual report
Reuse in training/CME materials	Reuse up to distribution or time period indicated in License
Reuse in newsmidia	Lifetime of newsmidia
Reuse in coursepack/classroom materials	Reuse up to distribution and/or time period indicated in license

**6. Acknowledgement**

6.1. The Licensor's permission must be acknowledged next to the Licensed Material in print. In electronic form, this acknowledgement must be visible at the same time as the figures/tables/illustrations or abstract and must be hyperlinked to the journal/book's homepage.

6.2. Acknowledgement may be provided according to any standard referencing system and at a minimum should include "Author, Article/Book Title, Journal name/Book imprint, volume, page number, year, Springer Nature".

**7. Reuse in a dissertation or thesis**

7.1. Where 'reuse in a dissertation/thesis' has been selected, the following terms apply: Print rights of the Version of Record are provided for; electronic rights for use only on institutional repository as defined by the Sherpa guideline ([www.sherpa.ac.uk/roneso](http://www.sherpa.ac.uk/roneso)) and only up to what is required by the awarding institution.

7.2. For theses published under an ISBN or ISSN, separate permission is required. Please contact [journalpermissions@springernature.com](mailto:journalpermissions@springernature.com) or [bookpermissions@springernature.com](mailto:bookpermissions@springernature.com) for these rights.

7.3. Authors must properly cite the published manuscript in their thesis according to current citation standards and include the following acknowledgement: *Reproduced with permission from Springer Nature*.

**8. License Fee**

You must pay the fee set forth in the License Agreement (the "License Fees"). All amounts payable by you under this License are exclusive of any sales, use, withholding, value added or similar taxes, government fees or levies or other assessments. Collection and/or remittance of such taxes to the relevant tax authority shall be the responsibility of the party who has the legal obligation to do so.

**9. Warranty**

9.1. The Licensor warrants that it has, to the best of its knowledge, the rights to license reuse of the Licensed Material. **You are solely responsible for ensuring that the material you wish to license is original to the Licensor and does not carry the copyright of another entity or third party (as credited in the published version).** If the credit line on any part of the Licensed Material indicates that it was reprinted or

adapted with permission from another source, then you should seek additional permission from that source to reuse the material.

9.2. EXCEPT FOR THE EXPRESS WARRANTY STATED HEREIN AND TO THE EXTENT PERMITTED BY APPLICABLE LAW, LICENSOR PROVIDES THE LICENSED MATERIAL "AS IS" AND MAKES NO OTHER REPRESENTATION OR WARRANTY. LICENSOR EXPRESSLY DISCLAIMS ANY LIABILITY FOR ANY CLAIM ARISING FROM OR OUT OF THE CONTENT, INCLUDING BUT NOT LIMITED TO ANY ERRORS, INACCURACIES, OMISSIONS, OR DEFECTS CONTAINED THEREIN, AND ANY IMPLIED OR EXPRESS WARRANTY AS TO MERCHANTABILITY OR FITNESS FOR A PARTICULAR PURPOSE. IN NO EVENT SHALL LICENSOR BE LIABLE TO YOU OR ANY OTHER PARTY OR ANY OTHER PERSON OR FOR ANY SPECIAL, CONSEQUENTIAL, INCIDENTAL, INDIRECT, PUNITIVE, OR EXEMPLARY DAMAGES, HOWEVER CAUSED, ARISING OUT OF OR IN CONNECTION WITH THE DOWNLOADING, VIEWING OR USE OF THE LICENSED MATERIAL REGARDLESS OF THE FORM OF ACTION, WHETHER FOR BREACH OF CONTRACT, BREACH OF WARRANTY, TORT, NEGLIGENCE, INFRINGEMENT OR OTHERWISE (INCLUDING, WITHOUT LIMITATION, DAMAGES BASED ON LOSS OF PROFITS, DATA, FILES, USE, BUSINESS OPPORTUNITY OR CLAIMS OF THIRD PARTIES), AND WHETHER OR NOT THE PARTY HAS BEEN ADVISED OF THE POSSIBILITY OF SUCH DAMAGES. THIS LIMITATION APPLIES NOTWITHSTANDING ANY FAILURE OF ESSENTIAL PURPOSE OF ANY LIMITED REMEDY PROVIDED HEREIN.

**10. Termination and Cancellation**

10.1. The License and all rights granted hereunder will continue until the end of the applicable period shown in Clause 5.1 above. Thereafter, this license will be terminated and all rights granted hereunder will cease.

10.2. Licensor reserves the right to terminate the License in the event that payment is not received in full or if you breach the terms of this License.

**11. General**

11.1. The License and the rights and obligations of the parties hereto shall be construed, interpreted and determined in accordance with the laws of the Federal Republic of Germany without reference to the stipulations of the CISG (United Nations Convention on Contracts for the International Sale of Goods) or to Germany's choice-of-law principle.

11.2. The parties acknowledge and agree that any controversies and disputes arising out of this License shall be decided exclusively by the courts of or having jurisdiction for Heidelberg, Germany, as far as legally permissible.

11.3. This License is solely for Licensor's and Licensee's benefit. It is not for the benefit of any other person or entity.

**Questions?** For questions on Copyright Clearance Center accounts or website issues

please contact [springernaturesupport@copyright.com](mailto:springernaturesupport@copyright.com) or +1-855-239-3415 (toll free in the US) or +1-978-646-2777. For questions on Springer Nature licensing please visit <https://www.springernature.com/gp/partners/rights-permissions-third-party-distribution>

**Other Conditions:**

Version 1.4 - Dec 2022

**Questions?** [customer-care@copyright.com](mailto:customer-care@copyright.com).

## 9 List of figures

<b>Figure 1:</b> Selection of typical catalytic shapes applied in industry, namely cylinders, hollow cylinders, tablets, spheres and multi-lobe structures. <sup>9,13</sup> .....	4
<b>Figure 2:</b> Schematic overview of important process characteristics influenced by the shape of the heterogeneous catalyst used. <sup>18,29</sup> .....	6
<b>Figure 3:</b> Schematic illustration of a uniform and the different egg-type catalyst. <sup>32,34</sup> .....	8
<b>Figure 4:</b> Lewis and Brønsted acid sites in zeolite catalysts. <sup>16,20,39</sup> .....	8
<b>Figure 5:</b> Schematic overview of the transport processes taking place in heterogeneous catalysis on catalyst carriers. <sup>12,42</sup> .....	9
<b>Figure 6:</b> Schematic overview of the LOHC concept. <sup>70</sup> .....	12
<b>Figure 7:</b> Catalytic perhydro-dibenzyl toluene/dibenzyl toluene cycle. <sup>80,95</sup> .....	13
<b>Figure 8:</b> Schematic illustration of the band structure of a photocatalyst during reaction. <sup>137,138</sup> .....	16
<b>Figure 9:</b> Synthesis and structure of NH <sub>2</sub> -MIL-125. Adapted with reprint permission from <sup>151</sup> .....	17
<b>Figure 10:</b> Schematic overview of the general process of additive manufacturing. <sup>178,181</sup> ...	20
<b>Figure 11:</b> Schematic illustration of the Direct Ink Writing process using a syringe-piston system. <sup>183,211</sup> .....	22
<b>Figure 12:</b> Schematic illustration of stabilization mechanisms of ceramic particles (top) and ink types typically employed in Direct Ink Writing. <sup>208,211,217</sup> .....	23
<b>Figure 13:</b> Number of publications including the terms “3D printing”, “3D printing and chemistry” and “3D printing and catalysis” per year from 2000 to 2022 based on literature research using Scopus. <sup>183</sup> .....	25
<b>Figure 14:</b> Fabrication of monolithic catalysts using polymeric templates. <sup>264</sup> .....	26
<b>Figure 15:</b> Design and function of catalytic active reaction ware presented by Kitson et al.. Adapted with reprint permission from <sup>274</sup> .....	27
<b>Figure 16:</b> Different woodpile patterns accessible by varying a) stacking angle, b) stacking orientation and c) size and spacing of the strands. <sup>10,224,276</sup> .....	28

## 10 List of tables

<b>Table 1:</b> Physico-chemical properties of dibenzyltoluene und perhydro-dibenzyltoluene. <sup>84,93-95,105,107</sup> .....	14
<b>Table 2:</b> Overview over commonly known 3D printing techniques based on their process categories according to ISO/ASTM DIS 52900:2018 alongside their technology and materials typically used. <sup>178,182,193-197</sup> .....	21
<b>Table 3:</b> Overview of DIW printed catalyst support structures, the respective loading of the active component, the shapes investigated and the test reaction in literature. ....	29
<b>Table 4:</b> Overview of DIW printed catalyst material, the shapes investigated and the test reaction in literature. ....	31

## 11 References

- (1) Donev, A.; Cisse, I.; Sachs, D.; Variano, E. A.; Stillinger, F. H.; Connelly, R.; Torquato, S.; Chaikin, P. M. Improving the density of jammed disordered packings using ellipsoids. *Science (New York, N.Y.)* **2004**, *303* (5660), 990–993. DOI: 10.1126/science.1093010.
- (2) van Hecke, M. Materials Science: Shape matters. *Science (New York, N.Y.)* **2007**, *317* (5834), 49–50. DOI: 10.1126/science.1145113.
- (3) Yunker, P. J.; Still, T.; Lohr, M. A.; Yodh, A. G. Suppression of the coffee-ring effect by shape-dependent capillary interactions. *Nature* **2011**, *476* (7360), 308–311. DOI: 10.1038/nature10344.
- (4) Vermant, J. Fluid mechanics: When shape matters. *Nature* **2011**, *476* (7360), 286–287. DOI: 10.1038/476286a.
- (5) Westrate, L. M.; Lee, J. E.; Prinz, W. A.; Voeltz, G. K. Form follows function: the importance of endoplasmic reticulum shape. *Annu. Rev. Biochem.* **2015**, *84*, 791–811. DOI: 10.1146/annurev-biochem-072711-163501.
- (6) Filippone, A. Comprehensive analysis of transport aircraft flight performance. *Progress in Aerospace Sciences* **2008**, *44* (3), 192–236. DOI: 10.1016/j.paerosci.2007.10.005.
- (7) John, V. B., Ed. *Introduction to Engineering Materials*; Palgrave Macmillan UK, **1983**. DOI: 10.1007/978-1-349-17190-3.
- (8) Chen, H.; Pang, J.; Koo, M.; Patrick, V. M. Shape Matters: Package Shape Informs Brand Status Categorization and Brand Choice. *J. of Retail.* **2020**, *96* (2), 266–281. DOI: 10.1016/j.jretai.2019.08.003.
- (9) Ludwig, T. Material- und Prozessentwicklung der Extrusionsbasierten Additiven Fertigung von Heterogenen Katalysatorformkörpern. Dissertation, Technische Universität München, München, **2019**.
- (10) Laguna, O. H.; Lietor, P. F.; Godino, F. I.; Corpas-Iglesias, F. A. A review on additive manufacturing and materials for catalytic applications: Milestones, key concepts, advances and perspectives. *Mater. Des.* **2021**, *208*, 109927. DOI: 10.1016/j.matdes.2021.109927.
- (11) Hurt, C.; Brandt, M.; Priya, S. S.; Bhatelia, T.; Patel, J.; Selvakannan, P.; Bhargava, S. Combining additive manufacturing and catalysis: a review. *Catal. Sci. Technol.* **2017**, *7* (16), 3421–3439. DOI: 10.1039/C7CY00615B.
- (12) G. Ertl; H. Knozinger; F. Schuth; J. Weitkamp. *Handbook of heterogeneous catalysis*, 2., completely rev. and enl. ed.; WILEY-VCH, **2008**.
- (13) Reschetilowski, W. *Einführung in die Heterogene Katalyse*; Springer Berlin Heidelberg, **2015**. DOI: 10.1007/978-3-662-46984-2.
- (14) de Jong, K. P. *Synthesis of Solid Catalysts*, 1st ed.; John Wiley & Sons Incorporated, **2009**.
- (15) Fecheté, I.; Wang, Y.; Védrine, J. C. The past, present and future of heterogeneous catalysis. *Catal. Today* **2012**, *189* (1), 2–27. DOI: 10.1016/j.cattod.2012.04.003.

- (16) Chorkendorff, I.; Niemantsverdriet, J. W. *Concepts of Modern Catalysis and Kinetics*; WILEY-VCH, **2003**.
- (17) Baerns, M., Ed. *Basic principles in applied catalysis*; Springer Series in Chemical Physics, Vol. 75; Springer, **2004**.
- (18) Mitchell, S.; Michels, N.-L.; Pérez-Ramírez, J. From powder to technical body: the undervalued science of catalyst scale up. *Chem. Soc. Rev.* **2013**, *42* (14), 6094–6112. DOI: 10.1039/c3cs60076a.
- (19) Perego, C.; Villa, P. Catalyst preparation methods. *Catal. Today* **1997**, *34* (3-4), 281–305. DOI: 10.1016/S0920-5861(96)00055-7.
- (20) Hagen, J. *Industrial catalysis: A practical approach*, Third completely revised and enlarged edition; WILEY-VCH, **2015**. DOI: 10.1002/9783527684625.
- (21) Jury, S. H. Diffusion in tabletted catalysts. *Can. J. Chem. Eng.* **1977**, *55* (5), 538–543. DOI: 10.1002/cjce.5450550510.
- (22) Rotaru, P.; Blejoiu, Ș. I. Influence of tableting pressure upon internal morphology of a Fe<sub>2</sub>O<sub>3</sub>-Cr<sub>2</sub>O<sub>3</sub> catalyst. *EPJ Appl. Phys.* **2001**, *16* (3), 167–173. DOI: 10.1051/epjap:2001206.
- (23) Rotaru, P.; Blejoiu, S. I.; Stanciu, M.; Stoenescu, G.; Mateescu, M.; Voiculescu, V. The influence of the tableting pressure upon the textural and diffusional properties of a Fe<sub>2</sub>O<sub>3</sub>-Cr<sub>2</sub>O<sub>3</sub> catalyst. *Microporous Mesoporous Mater.* **2005**, *83* (1-3), 159–164. DOI: 10.1016/j.micromeso.2005.04.010.
- (24) Avila, P.; Montes, M.; Miró, E. E. Monolithic reactors for environmental applications. *Chem. Eng. J.* **2005**, *109* (1-3), 11–36. DOI: 10.1016/j.cej.2005.02.025.
- (25) Cybulski, A.; Moulijn, J. A. Monoliths in Heterogeneous Catalysis. *Catal. Rev.* **1994**, *36* (2), 179–270. DOI: 10.1080/01614949408013925.
- (26) Schüth, F., Ed. *Handbook of porous solids*; WILEY-VCH, **2002**.
- (27) Boger, T.; Heibel, A. K.; Sorensen, C. M. Monolithic Catalysts for the Chemical Industry. *Ind. Eng. Chem. Res.* **2004**, *43* (16), 4602–4611. DOI: 10.1021/ie030730q.
- (28) Behr, A.; Agar, D. W.; Jörissen, J.; Vorholt, A. J. *Einführung in die Technische Chemie*, 2. Aufl. 2016; Springer Berlin Heidelberg, **2016**.
- (29) Akhtar, F.; Andersson, L.; Ogunwumi, S.; Hedin, N.; Bergström, L. Structuring adsorbents and catalysts by processing of porous powders. *J. Eur. Ceram. Soc.* **2014**, *34* (7), 1643–1666. DOI: 10.1016/j.jeurceramsoc.2014.01.008.
- (30) Bracconi, M. Intensification of catalytic reactors: A synergic effort of Multiscale Modeling, Machine Learning and Additive Manufacturing. *Chem. Eng. Process.* **2022**, *181* (5), 109148. DOI: 10.1016/j.cep.2022.109148.
- (31) Jungreuthmayer, C.; Steppert, P.; Sekot, G.; Zankel, A.; Reingruber, H.; Zanghellini, J.; Jungbauer, A. The 3D pore structure and fluid dynamics simulation of macroporous monoliths: High permeability due to alternating channel width. *J. Chromatogr. A* **2015**, *1425*, 141–149. DOI: 10.1016/j.chroma.2015.11.026.

- (32) Munnik, P.; Jongh, P. E. de; de Jong, K. P. Recent developments in the synthesis of supported catalysts. *Chem. Rev.* **2015**, *115* (14), 6687–6718. DOI: 10.1021/cr500486u.
- (33) Spieker, W. A.; Regalbuto, JR. A fundamental model of platinum impregnation onto alumina. *Chem. Eng. Sci.* **2001**, *56* (11), 3491–3504.
- (34) Chu, P.; Petersen, E. E.; Radke, C. J. Modeling wet impregnation of nickel on  $\gamma$ -alumina. *J. Catal.* **1989**, *117* (1), 52–70.
- (35) Villegas, L.; Masset, F.; Guilhaume, N. Wet impregnation of alumina-washcoated monoliths: Effect of the drying procedure on Ni distribution and on autothermal reforming activity. *Appl. Catal. A: Gen.* **2007**, *320*, 43–55. DOI: 10.1016/j.apcata.2006.12.011.
- (36) Morterra, C.; Magnacca, G. A case study: surface chemistry and surface structure of catalytic aluminas, as studied by vibrational spectroscopy of adsorbed species. *Catal. Today* **1996**, *27* (3-4), 497–532.
- (37) Shen, Y. F.; Suib, S. L.; Deeba, M.; Koermer, G. S. Luminescence and IR Characterization of Acid Sites on Alumina. *J. Catal.* **1994**, *146* (2), 483–490. DOI: 10.1006/jcat.1994.1086.
- (38) Healy, M. H.; Wieserman, L. F.; Arnett, E. M.; Wefers, K. Infrared spectroscopy and microcalorimetric investigations of  $\delta$ - $\theta$  and  $\kappa$  aluminas using basic probe molecules: acetonitrile, pyridine, 2,6-lutidine, and n-butylamine. *Langmuir* **1989**, *5* (1), 114–123. DOI: 10.1021/la00085a021.
- (39) Orazbayev, B.; Kozhakhmetova, D.; Wójtowicz, R.; Krawczyk, J. Modeling of a Catalytic Cracking in the Gasoline Production Installation with a Fuzzy Environment. *Energies* **2020**, *13* (18), 4736. DOI: 10.3390/en13184736.
- (40) Luyten, J.; Mullens, S.; Thijs, I. Designing with Pores - Synthesis and Applications. *KONA Powder Part. J.* **2010**, *28* (0), 131–142. DOI: 10.14356/kona.2010012.
- (41) Trimm, D. L.; Stanislaus, A. The control of pore size in alumina catalyst supports: A review. *Appl. Catal.* **1986**, *21* (2), 215–238.
- (42) Emig, G.; Klemm, E. *Chemische Reaktionstechnik*; Springer Berlin Heidelberg, **2017**. DOI: 10.1007/978-3-662-49268-0.
- (43) Steinborn, D. *Grundlagen der metallorganischen Komplexkatalyse*; Springer eBook Collection; Vieweg+Teubner, **2007**. DOI: 10.1007/978-3-8351-9085-6.
- (44) Thomas, J. M.; Thomas, W. J. *Principles and practice of heterogeneous catalysis*; VCH, **1997**.
- (45) Ostwald, W. Definition der Katalyse. *Z. Phys. Chem.* **1894** (15), 705–706.
- (46) NobelPrize.org. *The Nobel Prize in Chemistry 1909*. <https://www.nobelprize.org/prizes/chemistry/1909/summary/> (accessed 2022-09-04.).
- (47) Deacon, H. Improvement in the manufacture of chlorine (U. S. Patent No. US85370A) United States, **1868**.

- (48) Deacon, H. XXIX.—On Deacon's method of obtaining chlorine, as illustrating some principles of chemical dynamics. *J. Chem. Soc.* **1872**, 25 (0), 725–767. DOI: 10.1039/js8722500725.
- (49) Hasenclever, R. Ueber Chlorbereitung nach Deacon. *Ber. Dtsch. Chem. Ges.* **1876**, 9 (2), 1070–1073. DOI: 10.1002/cber.18760090211.
- (50) Knietsch, R. Ueber die Schwefelsäure und ihre Fabrication nach dem Contactverfahren. *Ber. Dtsch. Chem. Ges.* **1901**, 34 (3), 4069–4115.
- (51) Lapina, O.B.; Bal'zhinimaev, B.S.; Boghosian, S.; Eriksen, K.M.; Fehrmann, R. Progress on the mechanistic understanding of SO<sub>2</sub> oxidation catalysts. *Catal. Today* **1999**, 51 (3-4), 469–479. DOI: 10.1016/S0920-5861(99)00034-6.
- (52) Appl, M. Ammonia. In *Ullmann's Encyclopedia of Industrial Chemistry*; Wiley-VCH Verlag GmbH & Co. KGaA, **2000**; p 184. DOI: 10.1002/14356007.a02\_143.pub2.
- (53) Mittasch, A. Bemerkungen zur Katalyse. *Ber. dtsh. Chem. Ges. A/B* **1926**, 59 (1), 13–36. DOI: 10.1002/cber.19260590103.
- (54) NobelPrize.org. *The Nobel Prize in Chemistry 2007*. <https://www.nobelprize.org/prizes/chemistry/2007/summary/> (accessed 2022-09-05.).
- (55) Ertl, G. Elementarschritte bei der heterogenen Katalyse. *Angew. Chem.* **1990**, 102 (11), 1258–1266. DOI: 10.1002/ange.19901021108.
- (56) Ertl, G.; Lee, S. B.; Weiss, M. Kinetics of nitrogen adsorption on Fe(111). *Surf. Sci.* **1982**, 114 (2-3), 515–526. DOI: 10.1016/0039-6028(82)90702-6.
- (57) Erisman, J. W.; Sutton, M. A.; Galloway, J.; Klimont, Z.; Winiwarter, W. How a century of ammonia synthesis changed the world. *Nat. Geosci.* **2008**, 1 (10), 636–639. DOI: 10.1038/ngeo325.
- (58) Humphreys, J.; Lan, R.; Tao, S. Development and Recent Progress on Ammonia Synthesis Catalysts for Haber–Bosch Process. *Adv. Energy Sustain. Res.* **2021**, 2 (1), 2000043. DOI: 10.1002/aesr.202000043.
- (59) Smith, C.; Hill, A. K.; Torrente-Murciano, L. Current and future role of Haber–Bosch ammonia in a carbon-free energy landscape. *Energy Environ. Sci.* **2020**, 13 (2), 331–344. DOI: 10.1039/C9EE02873K.
- (60) Giddey, S.; Badwal, S. P. S.; Munnings, C.; Dolan, M. Ammonia as a Renewable Energy Transportation Media. *ACS Sustain. Chem. Eng.* **2017**, 5 (11), 10231–10239. DOI: 10.1021/acssuschemeng.7b02219.
- (61) Morlanés, N.; Katikaneni, S. P.; Paglieri, S. N.; Harale, A.; Solami, B.; Sarathy, S. M.; Gascon, J. A technological roadmap to the ammonia energy economy: Current state and missing technologies. *Chem. Eng. J.* **2021**, 408 (1), 127310. DOI: 10.1016/j.cej.2020.127310.
- (62) Valera-Medina, A.; Xiao, H.; Owen-Jones, M.; David, W.I.F.; Bowen, P. J. Ammonia for power. *Prog. Energy Combust. Sci.* **2018**, 69 (2), 63–102. DOI: 10.1016/j.pecs.2018.07.001.



- (63) Lee, S.; Kim, T.; Han, G.; Kang, S.; Yoo, Y.-S.; Jeon, S.-Y.; Bae, J. Comparative energetic studies on liquid organic hydrogen carrier: A net energy analysis. *Renew. Sust. Energ. Rev.* **2021**, *150* (2), 111447. DOI: 10.1016/j.rser.2021.111447.
- (64) Tarhan, C.; Çil, M. A. A study on hydrogen, the clean energy of the future: Hydrogen storage methods. *J. Energy Storage* **2021**, *40*, 102676. DOI: 10.1016/j.est.2021.102676.
- (65) Oswin, H. G. Power system functioning alternately for producing or consuming electrical energy (U. S. Patent No. US3416966A) United States, **1968**.
- (66) Taube, M.; Rippin, D.; Knecht, W.; Hakimifard, D.; Milisavljevic, B.; Grünenfelder, N. A prototype truck powered by hydrogen from organic liquid hydrides. *Int. J. Hydrog. Energy* **1985**, *10* (9), 595–599. DOI: 10.1016/0360-3199(85)90035-7.
- (67) Grünenfelder, N.; Schucan, T. Seasonal storage of hydrogen in liquid organic hydrides: description of the second prototype vehicle. *Int. J. Hydrog. Energy* **1989**, *14* (8), 579–586. DOI: 10.1016/0360-3199(89)90117-1.
- (68) Geburtig, D.; Preuster, P.; Bösmann, A.; Müller, K.; Wasserscheid, P. Chemical utilization of hydrogen from fluctuating energy sources – Catalytic transfer hydrogenation from charged Liquid Organic Hydrogen Carrier systems. *Int. J. Hydrog. Energy* **2016**, *41* (2), 1010–1017. DOI: 10.1016/j.ijhydene.2015.10.013.
- (69) Teichmann, D.; Stark, K.; Müller, K.; Zöttl, G.; Wasserscheid, P.; Arlt, W. Energy storage in residential and commercial buildings via Liquid Organic Hydrogen Carriers (LOHC). *Energy Environ. Sci.* **2012**, *5* (10), 9044. DOI: 10.1039/c2ee22070a.
- (70) Teichmann, D.; Arlt, W.; Wasserscheid, P.; Freymann, R. A future energy supply based on Liquid Organic Hydrogen Carriers (LOHC). *Energy Environ. Sci.* **2011**, *4* (8), 2767. DOI: 10.1039/c1ee01454d.
- (71) Scherer, G.; Newson E. Analysis of the seasonal energy storage of hydrogen in liquid organic hydrides. *Int. J. Hydrog. Energy* **1998**, *23* (1), 19–25. DOI: 10.1016/S0360-3199(97)00018-9.
- (72) Moradi, R.; Groth, K. M. Hydrogen storage and delivery: Review of the state of the art technologies and risk and reliability analysis. *Int. J. Hydrog. Energy* **2019**, *44* (23), 12254–12269. DOI: 10.1016/j.ijhydene.2019.03.041.
- (73) Rivard, E.; Trudeau, M.; Zaghbi, K. Hydrogen Storage for Mobility: A Review. *Materials (Basel, Switzerland)* **2019**, *12* (12). DOI: 10.3390/ma12121973.
- (74) Kang, D.; Yun, S.; Kim, B.-k. Review of the Liquid Hydrogen Storage Tank and Insulation System for the High-Power Locomotive. *Energies* **2022**, *15* (12), 4357. DOI: 10.3390/en15124357.
- (75) Holleman, A. F.; Wiberg, E. *Lehrbuch der anorganischen Chemie*, 101., verb. und stark erw. Aufl.; de Gruyter, **1995**.

- (76) Langmi, H. W.; Engelbrecht, N.; Modisha, P. M.; Bessarabov, D. Hydrogen storage. In *Electrochemical Power Sources: Fundamentals, Systems, and Applications*; Elsevier, 2022; pp 455–486. DOI: 10.1016/B978-0-12-819424-9.00006-9.
- (77) Shet, S. P.; Shanmuga Priya, S.; Sudhakar, K.; Tahir, M. A review on current trends in potential use of metal-organic framework for hydrogen storage. *Int. J. Hydrog. Energy* **2021**, *46* (21), 11782–11803. DOI: 10.1016/j.ijhydene.2021.01.020.
- (78) Suh, M. P.; Park, H. J.; Prasad, T. K.; Lim, D.-W. Hydrogen storage in metal-organic frameworks. *Chem. Rev.* **2012**, *112* (2), 782–835. DOI: 10.1021/cr200274s.
- (79) Murray, L. J.; Dincă, M.; Long, J. R. Hydrogen storage in metal-organic frameworks. *Chem. Soc. Rev.* **2009**, *38* (5), 1294–1314. DOI: 10.1039/b802256a.
- (80) Niermann, M.; Beckendorff, A.; Kaltschmitt, M.; Bonhoff, K. Liquid Organic Hydrogen Carrier (LOHC) – Assessment based on chemical and economic properties. *Int. J. Hydrog. Energy* **2019**, *44* (13), 6631–6654. DOI: 10.1016/j.ijhydene.2019.01.199.
- (81) Oner, O.; Khalilpour, K. Evaluation of green hydrogen carriers: A multi-criteria decision analysis tool. *Renew. Sust. Energ. Rev.* **2022**, *168* (April), 112764. DOI: 10.1016/j.rser.2022.112764.
- (82) Molkov, V.; Dadashzadeh, M.; Makarov, D. Physical model of onboard hydrogen storage tank thermal behaviour during fuelling. *Int. J. Hydrog. Energy* **2019**, *44* (8), 4374–4384. DOI: 10.1016/j.ijhydene.2018.12.115.
- (83) Schlapbach, L.; Züttel, A. Hydrogen-storage materials for mobile applications. *Nature* **2001**, *414* (6861), 353–358. DOI: 10.1038/35104634.
- (84) Sekine, Y.; Higo, T. Recent Trends on the Dehydrogenation Catalysis of Liquid Organic Hydrogen Carrier (LOHC): A Review. *Top. Catal.* **2021**, *64* (7-8), 470–480. DOI: 10.1007/s11244-021-01452-x.
- (85) Rao, P. C.; Yoon, M. Potential Liquid-Organic Hydrogen Carrier (LOHC) Systems: A Review on Recent Progress. *Energies* **2020**, *13* (22), 6040. DOI: 10.3390/en13226040.
- (86) Wagner, C.; Cholewa, M.; Ulmer, U.; Poncette, D.; Patyk, A.; Fichtner, M.; Dittmeyer, R.; Pfeifer, P. Konzept zur chemischen Wärmespeicherung mit flüssigen organischen Hydriden. *Chem. Ing. Tech.* **2017**, *89* (3), 341–345. DOI: 10.1002/cite.201600025.
- (87) Peters, W.; Seidel, A.; Herzog, S.; Bösmann, A.; Schwieger, W.; Wasserscheid, P. Macrokinetic effects in perhydro-N-ethylcarbazole dehydrogenation and H<sub>2</sub> productivity optimization by using egg-shell catalysts. *Energy Environ. Sci.* **2015**, *8* (10), 3013–3021. DOI: 10.1039/C5EE02024G.
- (88) Zhao, H. Y.; Oyama, S. T.; Naeemi, E. D. Hydrogen storage using heterocyclic compounds: The hydrogenation of 2-methylthiophene. *Catal. Today* **2010**, *149* (1-2), 172–184. DOI: 10.1016/j.cattod.2009.02.039.
- (89) Crabtree, R. H. Hydrogen storage in liquid organic heterocycles. *Energy Environ. Sci.* **2008**, *1* (1), 134. DOI: 10.1039/b805644g.

- (90) Müller, K. *Zielführende Weiterentwicklung von Energietechnologien*; Springer Fachmedien Wiesbaden, **2018**. DOI: 10.1007/978-3-658-23599-4.
- (91) Zhu, T.; Yang, M.; Chen, X.; Dong, Y.; Zhang, Z.; Cheng, H. A highly active bifunctional Ru–Pd catalyst for hydrogenation and dehydrogenation of liquid organic hydrogen carriers. *J. Catal.* **2019**, *378*, 382–391. DOI: 10.1016/j.jcat.2019.08.032.
- (92) Brückner, N.; Obesser, K.; Bösmann, A.; Teichmann, D.; Arlt, W.; Dungs, J.; Wasserscheid, P. Evaluation of industrially applied heat-transfer fluids as liquid organic hydrogen carrier systems. *ChemSusChem* **2014**, *7* (1), 229–235. DOI: 10.1002/cssc.201300426.
- (93) Eurol GmbH. *Malotherm SH, Sicherheitsdatenblatt*. [https://eurol.com/product\\_img/SDS/DE\\_E124838\\_SDS.pdf](https://eurol.com/product_img/SDS/DE_E124838_SDS.pdf) (accessed 2022-10-20).
- (94) Leu Energie GmbH & Co. KG. *Jarytherm DBT, Wärmeträgerfluid*. [https://www.leu-schmierstoffe.de/media/pdf/a0/2f/4f/TDS\\_TOTAL\\_JARYTHERM-DBT\\_FPW\\_201904\\_DE\\_DEU.pdf](https://www.leu-schmierstoffe.de/media/pdf/a0/2f/4f/TDS_TOTAL_JARYTHERM-DBT_FPW_201904_DE_DEU.pdf) (accessed 2022-10-20).
- (95) Müller, K.; Stark, K.; Emel'yanenko, V. N.; Varfolomeev, M. A.; Zaitsau, D. H.; Shoifet, E.; Schick, C.; Verevkin, S. P.; Arlt, W. Liquid Organic Hydrogen Carriers: Thermophysical and Thermochemical Studies of Benzyl- and Dibenzyl-toluene Derivatives. *Ind. Eng. Chem. Res.* **2015**, *54* (32), 7967–7976. DOI: 10.1021/acs.iecr.5b01840.
- (96) Do, G.; Preuster, P.; Aslam, R.; Bösmann, A.; Müller, K.; Arlt, W.; Wasserscheid, P. Hydrogenation of the liquid organic hydrogen carrier compound dibenzyltoluene – reaction pathway determination by <sup>1</sup>H NMR spectroscopy. *React. Chem. Eng.* **2016**, *1* (3), 313–320. DOI: 10.1039/C5RE00080G.
- (97) Dürr, S.; Müller, M.; Jorschick, H.; Helmin, M.; Bösmann, A.; Palkovits, R.; Wasserscheid, P. Carbon Dioxide-Free Hydrogen Production with Integrated Hydrogen Separation and Storage. *ChemSusChem* **2017**, *10* (1), 42–47. DOI: 10.1002/cssc.201600435.
- (98) Lee, S.; Lee, J.; Kim, T.; Han, G.; Lee, J.; Lee, K.; Bae, J. Pt/CeO<sub>2</sub> catalyst synthesized by combustion method for dehydrogenation of perhydro-dibenzyltoluene as liquid organic hydrogen carrier: Effect of pore size and metal dispersion. *Int. J. Hydrog. Energy* **2021**, *46* (7), 5520–5529. DOI: 10.1016/j.ijhydene.2020.11.038.
- (99) Jorschick, H.; Bulgarin, A.; Alletsee, L.; Preuster, P.; Bösmann, A.; Wasserscheid, P. Charging a Liquid Organic Hydrogen Carrier with Wet Hydrogen from Electrolysis. *ACS Sustain. Chem. Eng.* **2019**, *7* (4), 4186–4194. DOI: 10.1021/acssuschemeng.8b05778.
- (100) Jorschick, H.; Preuster, P.; Dürr, S.; Seidel, A.; Müller, K.; Bösmann, A.; Wasserscheid, P. Hydrogen storage using a hot pressure swing reactor. *Energy Environ. Sci.* **2017**, *10* (7), 1652–1659. DOI: 10.1039/C7EE00476A.
- (101) Shi, L.; Qi, S.; Qu, J.; Che, T.; Yi, C.; Yang, B. Integration of hydrogenation and dehydrogenation based on dibenzyltoluene as liquid organic hydrogen energy carrier. *Int. J. Hydrog. Energy* **2019**, *44* (11), 5345–5354. DOI: 10.1016/j.ijhydene.2018.09.083.

- (102) Ali, A.; Rohini, A. K.; Noh, Y. S.; Moon, D. J.; Lee, H. J. Hydrogenation of dibenzyltoluene and the catalytic performance of Pt/Al<sub>2</sub>O<sub>3</sub> with various Pt loadings for hydrogen production from perhydro-dibenzyltoluene. *Int. J. Energy Res.* **2021**, *39* (1), 2. DOI: 10.1002/er.7604.
- (103) Auer, F.; Blaumeiser, D.; Bauer, T.; Bösmann, A.; Szesni, N.; Libuda, J.; Wasserscheid, P. Boosting the activity of hydrogen release from liquid organic hydrogen carrier systems by sulfur-additives to Pt on alumina catalysts. *Catal. Sci. Technol.* **2019**, *9* (13), 3537–3547. DOI: 10.1039/c9cy00817a.
- (104) Auer, F. Katalysatorentwicklung für die Dehydrierung von Perhydro-Dibenzyltoluol. Dissertation, Friedrich-Alexander-Universität, Erlangen-Nürnberg, **2020**.
- (105) Seidel, A. M. Entwicklung eines technischen Platin-Trägerkatalysators zur Dehydrierung von Perhydro-Dibenzyltoluol. Dissertation, Friedrich-Alexander-Universität, Erlangen-Nürnberg, **2019**.
- (106) Aakko-Saksa, P. T.; Vehkamäki, M.; Kemell, M.; Keskiäli, L.; Simell, P.; Reinikainen, M.; Tapper, U.; Repo, T. Hydrogen release from liquid organic hydrogen carriers catalysed by platinum on rutile-anatase structured titania. *ChemComm* **2020**, *56* (11), 1657–1660. DOI: 10.1039/c9cc09715e.
- (107) Rude, T.; Dürr, S.; Preuster, P.; Wolf, M.; Wasserscheid, P. Benzyltoluene/perhydro benzyltoluene – pushing the performance limits of pure hydrocarbon liquid organic hydrogen carrier (LOHC) systems. *Sustain. Energy Fuels* **2022**, *6* (6), 1541–1553. DOI: 10.1039/D1SE01767E.
- (108) Jo, Y.; Wan Kim, T.; Oh, J.; Kim, D.; Suh, Y.-W. Mesoporous sulfur-decorated Pt–Al<sub>2</sub>O<sub>3</sub> for dehydrogenation of perhydro benzyltoluenes: Activity-favorable adsorption of reaction species onto electron-deficient Pt atoms. *J. Catal.* **2022**, *413*, 127–137. DOI: 10.1016/j.jcat.2022.06.025.
- (109) Dürr, S.; Zilm, S.; Geißelbrecht, M.; Müller, K.; Preuster, P.; Bösmann, A.; Wasserscheid, P. Experimental determination of the hydrogenation/dehydrogenation - Equilibrium of the LOHC system H0/H18-dibenzyltoluene. *Int. J. Hydrog. Energy* **2021**, *46* (64), 32583–32594. DOI: 10.1016/j.ijhydene.2021.07.119.
- (110) Müller, K.; Aslam, R.; Fischer, A.; Stark, K.; Wasserscheid, P.; Arlt, W. Experimental assessment of the degree of hydrogen loading for the dibenzyl toluene based LOHC system. *Int. J. Hydrog. Energy* **2016**, *41* (47), 22097–22103. DOI: 10.1016/j.ijhydene.2016.09.196.
- (111) Huynh, N.-D.; Hur, S. H.; Kang, S. G. Tuning the dehydrogenation performance of dibenzyl toluene as liquid organic hydrogen carriers. *Int. J. Hydrog. Energy* **2021**, *46* (70), 34788–34796. DOI: 10.1016/j.ijhydene.2021.08.039.
- (112) Jorschick, H.; Geißelbrecht, M.; Ebl, M.; Preuster, P.; Bösmann, A.; Wasserscheid, P. Benzyltoluene/dibenzyltoluene-based mixtures as suitable liquid organic hydrogen carrier systems for low temperature applications. *Int. J. Hydrog. Energy* **2020**, *45* (29), 14897–14906. DOI: 10.1016/j.ijhydene.2020.03.210.

- (113) Bulgarin, A.; Jorschick, H.; Preuster, P.; Bösmann, A.; Wasserscheid, P. Purity of hydrogen released from the Liquid Organic Hydrogen Carrier compound perhydro dibenzyltoluene by catalytic dehydrogenation. *Int. J. Hydrog. Energy* **2020**, *45* (1), 712–720. DOI: 10.1016/j.ijhydene.2019.10.067.
- (114) Hoskins, B. F.; Robson, R. Design and construction of a new class of scaffolding-like materials comprising infinite polymeric frameworks of 3D-linked molecular rods. A reappraisal of the zinc cyanide and cadmium cyanide structures and the synthesis and structure of the diamond-related frameworks  $[N(CH_3)_4][Cu^I Zn^{II}(CN)_4]$  and  $Cu^I[4,4',4'',4''']$ -tetracyanotetraphenylmethane $BF_4 \cdot xC_6H_5NO_2$ . *J. Am. Chem. Soc.* **1990**, *112* (4), 1546–1554. DOI: 10.1021/ja00160a038.
- (115) Hussain, M. Z. Metal-organic Framework (MOFs) Derived Nanocomposites: Synthesis and Applications in Photocatalysis. Dissertation, University of Exeter, **2020**.
- (116) Dhakshinamoorthy, A.; Asiri, A. M.; García, H. Metal-Organic Framework (MOF) Compounds: Photocatalysts for Redox Reactions and Solar Fuel Production. *Angew. Chem. Int. Ed.* **2016**, *55* (18), 5414–5445. DOI: 10.1002/anie.201505581.
- (117) Caro, J. Quo Vadis, MOF? *Chem. Ing. Tech.* **2018**, *90* (11), 1759–1768. DOI: 10.1002/cite.201800034.
- (118) Caro, J. Are MOF membranes better in gas separation than those made of zeolites? *Curr. Opin. Chem. Eng.* **2011**, *1* (1), 77–83. DOI: 10.1016/j.coche.2011.08.007.
- (119) Zhang, Y.; Feng, X.; Yuan, S.; Zhou, J.; Wang, B. Challenges and recent advances in MOF–polymer composite membranes for gas separation. *Inorg. Chem. Front.* **2016**, *3* (7), 896–909. DOI: 10.1039/C6QI00042H.
- (120) Kang, Z.; Fan, L.; Sun, D. Recent advances and challenges of metal–organic framework membranes for gas separation. *J. Mater. Chem. A* **2017**, *5* (21), 10073–10091. DOI: 10.1039/C7TA01142C.
- (121) Panda, S. K.; Mishra, S.; Singh, A. K. Recent progress in the development of MOF-based optical sensors for  $Fe^{3+}$ . *Dalton Trans.* **2021**, *50* (21), 7139–7155. DOI: 10.1039/d1dt00353d.
- (122) Gonçalves, J. M.; Martins, P. R.; Rocha, D. P.; Matias, T. A.; Julião, M. S. S.; Munoz, R. A. A.; Angnes, L. Recent trends and perspectives in electrochemical sensors based on MOF-derived materials. *J. Mater. Chem. C* **2021**, *9* (28), 8718–8745. DOI: 10.1039/D1TC02025K.
- (123) Lawson, H. D.; Walton, S. P.; Chan, C. Metal-Organic Frameworks for Drug Delivery: A Design Perspective. *ACS Appl. Mater. Interfaces.* **2021**, *13* (6), 7004–7020. DOI: 10.1021/acsami.1c01089.
- (124) Mallakpour, S.; Nikkhoo, E.; Hussain, C. M. Application of MOF materials as drug delivery systems for cancer therapy and dermal treatment. *Coord. Chem. Rev.* **2022**, *451*, 214262. DOI: 10.1016/j.ccr.2021.214262.
- (125) Fathieh, F.; Kalmutzki, M. J.; Kapustin, E. A.; Waller, P. J.; Yang, J.; Yaghi, O. M. Practical water production from desert air. *Sci. Adv.* **2018**, *4* (6), eaat3198. DOI: 10.1126/sciadv.aat3198.

- (126) Service, R. F. Crystalline nets snare water and make fuel from thin air. *Science (New York, N.Y.)* **2019**, *365* (6457), 964–965. DOI: 10.1126/science.365.6457.964.
- (127) Hussain, M. Z.; Yang, Z.; Huang, Z.; Jia, Q.; Zhu, Y.; Xia, Y. Recent Advances in Metal-Organic Frameworks Derived Nanocomposites for Photocatalytic Applications in Energy and Environment. *Adv. Sci. (Weinh.)* **2021**, *8* (14), e2100625. DOI: 10.1002/advs.202100625.
- (128) Wang, Z.; Tao, H.; Yue, Y. Metal-Organic-Framework-Based Cathodes for Enhancing the Electrochemical Performances of Batteries: A Review. *ChemElectroChem* **2019**, *6* (21), 5358–5374. DOI: 10.1002/celec.201900843.
- (129) Wang, L.; Han, Y.; Feng, X.; Zhou, J.; Qi, P.; Wang, B. Metal–organic frameworks for energy storage: Batteries and supercapacitors. *Coord. Chem. Rev.* **2016**, *307*, 361–381. DOI: 10.1016/j.ccr.2015.09.002.
- (130) Lee, J.; Farha, O. K.; Roberts, J.; Scheidt, K. A.; Nguyen, S. T.; Hupp, J. T. Metal-organic framework materials as catalysts. *Chem. Soc. Rev.* **2009**, *38* (5), 1450–1459. DOI: 10.1039/b807080f.
- (131) Konnerth, H.; Matsagar, B. M.; Chen, S. S.; Precht, M. H.G.; Shieh, F.-K.; Wu, K. C.-W. Metal-organic framework (MOF)-derived catalysts for fine chemical production. *Coord. Chem. Rev.* **2020**, *416* (2017), 213319. DOI: 10.1016/j.ccr.2020.213319.
- (132) Goetjen, T. A.; Liu, J.; Wu, Y.; Sui, J.; Zhang, X.; Hupp, J. T.; Farha, O. K. Metal-organic framework (MOF) materials as polymerization catalysts: a review and recent advances. *ChemComm* **2020**, *56* (72), 10409–10418. DOI: 10.1039/d0cc03790g.
- (133) Downes, C. A.; Marinescu, S. C. Electrocatalytic Metal-Organic Frameworks for Energy Applications. *ChemSusChem* **2017**, *10* (22), 4374–4392. DOI: 10.1002/cssc.201701420.
- (134) Wang, Q.; Gao, Q.; Al-Enizi, A. M.; Nafady, A.; Ma, S. Recent advances in MOF-based photocatalysis: environmental remediation under visible light. *Inorg. Chem. Front.* **2020**, *7* (2), 300–339. DOI: 10.1039/C9QI01120J.
- (135) Fujita, M.; Kwon, Y. J.; Washizu, S.; Ogura, K. Preparation, Clathration Ability, and Catalysis of a Two-Dimensional Square Network Material Composed of Cadmium(II) and 4,4'-Bipyridine. *J. Am. Chem. Soc.* **1994**, *116* (3), 1151–1152. DOI: 10.1021/ja00082a055.
- (136) Ochedi, F. O.; Liu, D.; Yu, J.; Hussain, A.; Liu, Y. Photocatalytic, electrocatalytic and photoelectrocatalytic conversion of carbon dioxide: a review. *Environ. Chem. Lett.* **2021**, *19* (2), 941–967. DOI: 10.1007/s10311-020-01131-5.
- (137) Li, X.; Wang, Z.; Wang, L. Metal–Organic Framework-Based Materials for Solar Water Splitting. *Small Science* **2021**, *1* (5), 2000074. DOI: 10.1002/smssc.202000074.
- (138) Zhang, K.; Hu, H.; Shi, L.; Jia, B.; Huang, H.; Han, X.; Sun, X.; Ma, T. Strategies for Optimizing the Photocatalytic Water-Splitting Performance of Metal–Organic Framework-Based Materials. *Small Science* **2021**, *1* (12), 2100060. DOI: 10.1002/smssc.202100060.

- (139) Wang, C.-C.; Zhang, Y.-Q.; Li, J.; Wang, P. Photocatalytic CO<sub>2</sub> reduction in metal–organic frameworks: A mini review. *J. Mol. Struct.* **2015**, *1083* (97), 127–136. DOI: 10.1016/j.molstruc.2014.11.036.
- (140) García, H.; Navalón, S. *Metal-Organic Frameworks: Applications in Separations and Catalysis*; John Wiley & Sons, Incorporated, **2018**.
- (141) Bedia, J.; Muelas-Ramos, V.; Peñas-Garzón, M.; Gómez-Avilés, A.; Rodríguez, J.; Belver, C. A Review on the Synthesis and Characterization of Metal Organic Frameworks for Photocatalytic Water Purification. *Catalysts* **2019**, *9* (1), 52. DOI: 10.3390/catal9010052.
- (142) Wang, W.; Xu, X.; Zhou, W.; Shao, Z. Recent Progress in Metal-Organic Frameworks for Applications in Electrocatalytic and Photocatalytic Water Splitting. *Adv. Sci. (Weinh.)* **2017**, *4* (4), 1600371. DOI: 10.1002/advs.201600371.
- (143) Song, F.; Li, W.; Sun, Y. Metal–Organic Frameworks and Their Derivatives for Photocatalytic Water Splitting. *Inorganics* **2017**, *5* (3), 40. DOI: 10.3390/inorganics5030040.
- (144) Nasalevich, M. A.; Becker, R.; Ramos-Fernandez, E. V.; Castellanos, S.; Veber, S. L.; Fedin, M. V.; Kapteijn, F.; Reek, J. N. H.; van der Vlugt, J. I.; Gascon, J. Co@NH<sub>2</sub>-MIL-125(Ti): cobaloxime-derived metal–organic framework-based composite for light-driven H<sub>2</sub> production. *Energy Environ. Sci.* **2015**, *8* (1), 364–375. DOI: 10.1039/C4EE02853H.
- (145) An, Y.; Xu, B.; Liu, Y.; Wang, Z.; Wang, P.; Dai, Y.; Qin, X.; Zhang, X.; Huang, B. Photocatalytic Overall Water Splitting over MIL-125(Ti) upon CoPi and Pt Co-catalyst Deposition. *ChemistryOpen* **2017**, *6* (6), 701–705. DOI: 10.1002/open.201700100.
- (146) Remiro-Buenamañana, S.; Cabrero-Antonino, M.; Martínez-Guanter, M.; Álvaro, M.; Navalón, S.; García, H. Influence of co-catalysts on the photocatalytic activity of MIL-125(Ti)-NH<sub>2</sub> in the overall water splitting. *Appl. Catal. B: Environ.* **2019**, *254* (12), 677–684. DOI: 10.1016/j.apcatb.2019.05.027.
- (147) Qiu, J.; Yang, L.; Li, M.; Yao, J. Metal nanoparticles decorated MIL-125-NH<sub>2</sub> and MIL-125 for efficient photocatalysis. *Mater. Res. Bull.* **2019**, *112*, 297–306. DOI: 10.1016/j.materresbull.2018.12.038.
- (148) Dan-Hardi, M.; Serre, C.; Frot, T.; Rozes, L.; Maurin, G.; Sanchez, C.; Férey, G. A new photoactive crystalline highly porous titanium(IV) dicarboxylate. *J. Am. Chem. Soc.* **2009**, *131* (31), 10857–10859. DOI: 10.1021/ja903726m.
- (149) Horiuchi, Y.; Toyao, T.; Saito, M.; Mochizuki, K.; Iwata, M.; Higashimura, H.; Anpo, M.; Matsuoka, M. Visible-Light-Promoted Photocatalytic Hydrogen Production by Using an Amino-Functionalized Ti(IV) Metal–Organic Framework. *J. Phys. Chem. C* **2012**, *116* (39), 20848–20853. DOI: 10.1021/jp3046005.
- (150) Abdul Mubarak, N. S.; Foo, K. Y.; Schneider, R.; Abdelhameed, R. M.; Sabar, S. The chemistry of MIL-125 based materials: Structure, synthesis, modification strategies and photocatalytic applications. *J. Environ. Chem. Eng.* **2022**, *10* (1), 106883. DOI: 10.1016/j.jece.2021.106883.

- (151) Kim, S.-N.; Kim, J.; Kim, H.-Y.; Cho, H.-Y.; Ahn, W.-S. Adsorption/catalytic properties of MIL-125 and NH<sub>2</sub>-MIL-125. *Catal. Today* **2013**, *204*, 85–93. DOI: 10.1016/j.cattod.2012.08.014.
- (152) Hendon, C. H.; Tiana, D.; Fontecave, M.; Sanchez, C.; D'arras, L.; Sassoie, C.; Rozes, L.; Mellot-Draznieks, C.; Walsh, A. Engineering the optical response of the titanium-MIL-125 metal-organic framework through ligand functionalization. *J. Am. Chem. Soc.* **2013**, *135* (30), 10942–10945. DOI: 10.1021/ja405350u.
- (153) Sohail, M.; Yun, Y.-N.; Lee, E.; Kim, S. K.; Cho, K.; Kim, J.-N.; Kim, T. W.; Moon, J.-H.; Kim, H. Synthesis of Highly Crystalline NH<sub>2</sub>-MIL-125 (Ti) with S-Shaped Water Isotherms for Adsorption Heat Transformation. *Cryst. Growth Des.* **2017**, *17* (3), 1208–1213. DOI: 10.1021/acs.cgd.6b01597.
- (154) Gomes Silva, C.; Luz, I.; Llabrés i Xamena, F. X.; Corma, A.; García, H. Water stable Zr-benzenedicarboxylate metal-organic frameworks as photocatalysts for hydrogen generation. *Chemistry* **2010**, *16* (36), 11133–11138. DOI: 10.1002/chem.200903526.
- (155) Yue, K.; Zhang, X.; Jiang, S.; Chen, J.; Yang, Y.; Bi, F.; Wang, Y. Recent advances in strategies to modify MIL-125 (Ti) and its environmental applications. *J. Mol. Liq.* **2021**, *335*, 116108. DOI: 10.1016/j.molliq.2021.116108.
- (156) Fujishima, A.; Honda, K. Electrochemical photolysis of water at a semiconductor electrode. *Nature* **1972**, *238* (5358), 37–38. DOI: 10.1038/238037a0.
- (157) Yoon, J. W.; Kim, D. H.; Kim, J.-H.; Jang, H. W.; Lee, J.-H. NH<sub>2</sub>-MIL-125(Ti)/TiO<sub>2</sub> nanorod heterojunction photoanodes for efficient photoelectrochemical water splitting. *Appl. Catal. B: Environ.* **2019**, *244*, 511–518. DOI: 10.1016/j.apcatb.2018.11.057.
- (158) Ali, M.; Pervaiz, E.; Noor, T.; Rabi, O.; Zahra, R.; Yang, M. Recent advancements in MOF- based catalysts for applications in electrochemical and photoelectrochemical water splitting: A review. *Int. J. Energy Res.* **2021**, *45* (2), 1190–1226. DOI: 10.1002/er.5807.
- (159) Lee, K. J.; Lee, J. H.; Jeoung, S.; Moon, H. R. Transformation of Metal-Organic Frameworks/Coordination Polymers into Functional Nanostructured Materials: Experimental Approaches Based on Mechanistic Insights. *Acc. Chem. Res.* **2017**, *50* (11), 2684–2692. DOI: 10.1021/acs.accounts.7b00259.
- (160) Rahmani, A.; Emrooz, H. B. M.; Abedi, S.; Morsali, A. Synthesis and characterization of CdS/MIL-125 (Ti) as a photocatalyst for water splitting. *Mater. Sci. Semicond.* **2018**, *80* (2), 44–51. DOI: 10.1016/j.mssp.2018.02.013.
- (161) Cui, W.; Shang, J.; Bai, H.; Hu, J.; Xu, D.; Ding, J.; Fan, W.; Shi, W. In-situ implantation of plasmonic Ag into metal-organic frameworks for constructing efficient Ag/NH<sub>2</sub>-MIL-125/TiO<sub>2</sub> photoanode. *Chem. Eng. J.* **2020**, *388*, 124206. DOI: 10.1016/j.cej.2020.124206.
- (162) Zhang, B.; Zhang, J.; Tan, X.; Shao, D.; Shi, J.; Zheng, L.; Zhang, J.; Yang, G.; Han, B. MIL-125-NH<sub>2</sub>@TiO<sub>2</sub> Core-Shell Particles Produced by a Post-Solvothermal Route for High-Performance Photocatalytic H<sub>2</sub> Production. *ACS Appl. Mater. Interfaces.* **2018**, *10* (19), 16418–16423. DOI: 10.1021/acsami.8b01462.



- (163) Hussain, M. Z.; Bahri, M.; Heinz, W. R.; Jia, Q.; Ersen, O.; Kratky, T.; Fischer, R. A.; Zhu, Y.; Xia, Y. An in situ investigation of the thermal decomposition of metal-organic framework NH<sub>2</sub>-MIL-125 (Ti). *Microporous Mesoporous Mater.* **2021**, *316*, 110957. DOI: 10.1016/j.micromeso.2021.110957.
- (164) Xia, W.; Mahmood, A.; Zou, R.; Xu, Q. Metal-organic frameworks and their derived nanostructures for electrochemical energy storage and conversion. *Energy Environ. Sci.* **2015**, *8* (7), 1837–1866. DOI: 10.1039/C5EE00762C.
- (165) Hussain, M. Z.; van der Linden, B.; Yang, Z.; Jia, Q.; Chang, H.; Fischer, R. A.; Kapteijn, F.; Zhu, Y.; Xia, Y. Bimetal-organic framework derived multi-heterostructured TiO<sub>2</sub>/Cu<sub>x</sub>O/C nanocomposites with superior photocatalytic H<sub>2</sub> generation performance. *J. Mater. Chem. A* **2021**, *9* (7), 4103–4116. DOI: 10.1039/D0TA10853G.
- (166) Zhang, X.; Yang, Y.; Lv, X.; Wang, Y.; Cui, L. Effects of Preparation Method on the Structure and Catalytic Activity of Ag-Fe<sub>2</sub>O<sub>3</sub> Catalysts Derived from MOFs. *Catalysts* **2017**, *7* (12), 382. DOI: 10.3390/catal7120382.
- (167) Wang, Z.; Li, M.; Ye, Y.; Yang, Y.; Lu, Y.; Ma, X.; Zhang, Z.; Xiang, S. MOF-derived binary mixed carbon/metal oxide porous materials for constructing simultaneous determination of hydroquinone and catechol sensor. *J. Solid State Electrochem.* **2019**, *23* (1), 81–89. DOI: 10.1007/s10008-018-4111-z.
- (168) Zhang, X.; Lv, X.; Bi, F.; Lu, G.; Wang, Y. Highly efficient Mn<sub>2</sub>O<sub>3</sub> catalysts derived from Mn-MOFs for toluene oxidation: The influence of MOFs precursors. *Mol. Catal.* **2020**, *482*, 110701. DOI: 10.1016/j.mcat.2019.110701.
- (169) Voskanyan, A. A.; Li, C.-Y. V.; Chan, K.-Y.; Gao, L. Combustion synthesis of Cr<sub>2</sub>O<sub>3</sub> octahedra with a chromium-containing metal-organic framework as a sacrificial template. *CrystEngComm* **2015**, *17* (13), 2620–2623. DOI: 10.1039/C4CE02529F.
- (170) Xiang, D.; Wang, J.; Zhang, X. Synthesis of Highly Efficient CuCeZr Catalyst Derived from UiO-66 Precursor for CO Oxidation. *Catal. Lett.* **2020**, *150* (9), 2630–2639. DOI: 10.1007/s10562-020-03164-5.
- (171) deKrafft, K. E.; Wang, C.; Lin, W. Metal-organic framework templated synthesis of Fe<sub>2</sub>O<sub>3</sub>/TiO<sub>2</sub> nanocomposite for hydrogen production. *Adv. Mater.* **2012**, *24* (15), 2014–2018. DOI: 10.1002/adma.201200330.
- (172) Li, J.-S.; Li, S.-L.; Tang, Y.-J.; Han, M.; Dai, Z.-H.; Bao, J.-C.; Lan, Y.-Q. Nitrogen-doped Fe/Fe<sub>3</sub>C@graphitic layer/carbon nanotube hybrids derived from MOFs: efficient bifunctional electrocatalysts for ORR and OER. *ChemComm* **2015**, *51* (13), 2710–2713. DOI: 10.1039/c4cc09062d.
- (173) Yang, S.; Li, X.; Zeng, G.; Cheng, M.; Huang, D.; Liu, Y.; Zhou, C.; Xiong, W.; Yang, Y.; Wang, W.; Zhang, G. Materials Institute Lavoisier (MIL) based materials for photocatalytic applications. *Coord. Chem. Rev.* **2021**, *438* (2017), 213874. DOI: 10.1016/j.ccr.2021.213874.

- (174) Liu, Z.; Wu, Y.; Chen, J.; Li, Y.; Zhao, J.; Gao, K.; Na, P. Effective elimination of As(III) via simultaneous photocatalytic oxidation and adsorption by a bifunctional cake-like TiO<sub>2</sub> derived from MIL-125(Ti). *Catal. Sci. Technol.* **2018**, *8* (7), 1936–1944. DOI: 10.1039/C8CY00125A.
- (175) Li, L.; Wang, X.-S.; Liu, T.-F.; Ye, J. Titanium-Based MOF Materials: From Crystal Engineering to Photocatalysis. *Small Methods* **2020**, *4* (12), 2000486. DOI: 10.1002/smt.202000486.
- (176) Scaife, D. E. Oxide semiconductors in photoelectrochemical conversion of solar energy. *Solar Energy* **1980**, *25* (1), 41–54. DOI: 10.1016/0038-092X(80)90405-3.
- (177) Hussain, M. Z.; Yang, Z.; van der Linden, B.; Heinz, W. R.; Bahri, M.; Ersen, O.; Jia, Q.; Fischer, R. A.; Zhu, Y.; Xia, Y. MOF-Derived Multi-heterostructured Composites for Enhanced Photocatalytic Hydrogen Evolution: Deciphering the Roles of Different Components. *Energy Fuels* **2022**, *36* (19), 12212–12225. DOI: 10.1021/acs.energyfuels.2c02319.
- (178) Gibson, I.; Rosen, D.; Stucker, B. *Additive manufacturing technologies: 3D printing, rapid prototyping and direct digital manufacturing*, Second Edition; Springer, **2015**.
- (179) Kodama, H. Automatic method for fabricating a three-dimensional plastic model with photo-hardening polymer. *Rev. Sci. Instrum.* **1981**, *52* (11), 1770–1773. DOI: 10.1063/1.1136492.
- (180) Hull, C. W. Apparatus for production of three-dimensional objects by stereolithography. (U. S. Patent No. US4575330A), United States, **1986**.
- (181) Lachmayer, R.; Lippert, R. b.; Fahlbusch, T. *3D-Druck beleuchtet*; Springer Berlin Heidelberg, **2016**. DOI: 10.1007/978-3-662-49056-3.
- (182) Klocke, F. *Fertigungsverfahren 5*; Springer Berlin Heidelberg, **2015**. DOI: 10.1007/978-3-540-69512-7.
- (183) Saggiomo, V. 3D Printed Devices for Catalytic Systems. In *Catalyst Immobilization*; Benaglia, M., Puglisi, A., Eds.; Wiley, **2020**; pp 369–408. DOI: 10.1002/9783527817290.ch11.
- (184) Kessler, A.; Hickel, R.; Reymus, M. 3D Printing in Dentistry-State of the Art. *Operative dentistry* **2020**, *45* (1), 30–40. DOI: 10.2341/18-229-L.
- (185) Dawood, A.; Marti Marti, B.; Sauret-Jackson, V.; Darwood, A. 3D printing in dentistry. *British dental journal* **2015**, *219* (11), 521–529. DOI: 10.1038/sj.bdj.2015.914.
- (186) Kumar, L. J.; Krishnadas Nair, C. G. Current Trends of Additive Manufacturing in the Aerospace Industry. In *Advances in 3D Printing & Additive Manufacturing Technologies*; Wimpenny, D. I., Pandey, P. M., Kumar, L. J., Eds.; Springer Singapore, **2017**; pp 39–54. DOI: 10.1007/978-981-10-0812-2\_4.
- (187) Lim, C. W. J.; Le, K. Q.; Lu, Q.; Wong, C. H. An Overview of 3-D Printing in Manufacturing, Aerospace, and Automotive Industries. *IEEE Potentials* **2016**, *35* (4), 18–22. DOI: 10.1109/MPOT.2016.2540098.

- (188) Wu, P.; Wang, J.; Wang, X. A critical review of the use of 3-D printing in the construction industry. *Autom.* **2016**, *68* (4), 21–31. DOI: 10.1016/j.autcon.2016.04.005.
- (189) Tay, Y. W. D.; Panda, B.; Paul, S. C.; Noor Mohamed, N. A.; Tan, M. J.; Leong, K. F. 3D printing trends in building and construction industry: a review. *Virtual Phys. Prototyp.* **2017**, *12* (3), 261–276. DOI: 10.1080/17452759.2017.1326724.
- (190) Liu, Z.; Zhang, M.; Bhandari, B.; Wang, Y. 3D printing: Printing precision and application in food sector. *Trends Food Sci.* **2017**, *69*, 83–94. DOI: 10.1016/j.tifs.2017.08.018.
- (191) Sun, J.; Peng, Z.; Zhou, W.; Fuh, J. Y.H.; Hong, G. S.; Chiu, A. A Review on 3D Printing for Customized Food Fabrication. *Procedia Manuf.* **2015**, *1* (4), 308–319. DOI: 10.1016/j.promfg.2015.09.057.
- (192) Ho, C. M. B.; Ng, S. H.; Yoon, Y.-J. A review on 3D printed bioimplants. *Int. J. Precis. Eng. Manuf.* **2015**, *16* (5), 1035–1046. DOI: 10.1007/s12541-015-0134-x.
- (193) Guo, N.; Leu, M. C. Additive manufacturing: technology, applications and research needs. *Front. Mech. Eng.* **2013**, *8* (3), 215–243. DOI: 10.1007/s11465-013-0248-8.
- (194) Deutsches Institut für Normung e.V. *Additive Fertigung - Grundlagen:Terminologie*, **2018**.
- (195) Gebhardt, A. *3D-Drucken:Grundlagen und Anwendungen des Additive Manufacturing (AM)*; Hanser, **2014**.
- (196) Fastermann, P. *3D-Drucken*; Springer Berlin Heidelberg, **2014**. DOI: 10.1007/978-3-642-40964-6.
- (197) Dilberoglu, U. M.; Gharehpapagh, B.; Yaman, U.; Dolen, M. The Role of Additive Manufacturing in the Era of Industry 4.0. *Procedia Manuf.* **2017**, *11*, 545–554. DOI: 10.1016/j.promfg.2017.07.148.
- (198) Pelz, J. S.; Ku, N.; Meyers, M. A.; Vargas-Gonzalez, L. R. Additive manufacturing of structural ceramics: a historical perspective. *J. Mater. Res. Technol.* **2021**, *15* (10), 670–695. DOI: 10.1016/j.jmrt.2021.07.155.
- (199) Chen, Z.; Li, Z.; Li, J.; Liu, C.; Lao, C.; Fu, Y.; Liu, C.; Li, Y.; Wang, P.; He, Y. 3D printing of ceramics: A review. *J. Eur. Ceram. Soc.* **2019**, *39* (4), 661–687. DOI: 10.1016/j.jeurceramsoc.2018.11.013.
- (200) Moritz, T.; Maleksaeedi, S. Additive manufacturing of ceramic components. *Addit. Manuf.*, **2018**, 105–161.
- (201) Lakhdar, Y.; Tuck, C.; Binner, J.; Terry, A.; Goodridge, R. Additive manufacturing of advanced ceramic materials. *Prog. Mater. Sci.* **2021**, *116* (2–3), 100736. DOI: 10.1016/j.pmatsci.2020.100736.
- (202) Cesarano, J., III; Calvert, P. D. Freeforming objects with low binder slurry. (U. S. Patent No. US6027326A) United States, **2000**.
- (203) Cesarano, J. A Review of Robocasting Technology. *Mater. Res. Soc. Symp. Proc.* **1998**, 542. DOI: 10.1557/PROC-542-133.

- (204) Lewis, J. A.; Smay, J. E.; Stuecker, J.; Cesarano, J. Direct Ink Writing of Three-Dimensional Ceramic Structures. *J. Am. Ceram. Soc.* **2006**, *89* (12), 3599–3609. DOI: 10.1111/j.1551-2916.2006.01382.x.
- (205) Lewis, J. A. Direct Ink Writing of 3D Functional Materials. *Adv. Funct. Mater.* **2006**, *16* (17), 2193–2204. DOI: 10.1002/adfm.200600434.
- (206) Smay, J. E.; Cesarano, J.; Lewis, J. A. Colloidal Inks for Directed Assembly of 3-D Periodic Structures. *Langmuir* **2002**, *18* (14), 5429–5437. DOI: 10.1021/la0257135.
- (207) Lewis, J. A. Direct-write assembly of ceramics from colloidal inks. *Curr. Opin. Solid State Mater. Sci.* **2002**, *6* (3), 245–250. DOI: 10.1016/S1359-0286(02)00031-1.
- (208) del-Mazo-Barbara, L.; Ginebra, M.-P. Rheological characterisation of ceramic inks for 3D direct ink writing: A review. *J. Eur. Ceram. Soc.* **2021**, *41* (16), 18–33. DOI: 10.1016/j.jeurceramsoc.2021.08.031.
- (209) Shahzad, A.; Lazoglu, I. Direct ink writing (DIW) of structural and functional ceramics: Recent achievements and future challenges. *Compos. B. Eng.* **2021**, *225*, 109249. DOI: 10.1016/j.compositesb.2021.109249.
- (210) Feilden, E. Additive Manufacturing of Ceramics and Ceramic Composites via Robocasting. Dissertation, Imperial College London, London, **2017**.
- (211) Lamnini, S.; Elsayed, H.; Lakhdar, Y.; Baino, F.; Smeacetto, F.; Bernardo, E. Robocasting of advanced ceramics: ink optimization and protocol to predict the printing parameters - A review. *Heliyon* **2022**, *8* (9), e10651. DOI: 10.1016/j.heliyon.2022.e10651.
- (212) Schlordt, T.; Keppner, F.; Travitzky, N.; Greil, P. Robocasting of alumina lattice truss structures. *J. Ceram. Sci. Technol.* **2012**, *3* (2), 81–87.
- (213) Xu, Q.; Lv, Y.; Dong, C.; Sreepred, T. S.; Tian, A.; Zhang, H.; Tang, Y.; Yu, Z.; Li, N. Three-dimensional micro/nanoscale architectures: fabrication and applications. *Nanoscale* **2015**, *7* (25), 10883–10895. DOI: 10.1039/c5nr02048d.
- (214) Chan, S. S. L.; Sesso, M. L.; Franks, G. V. Direct ink writing of hierarchical porous alumina-stabilized emulsions: Rheology and printability. *J. Am. Ceram. Soc.* **2020**, *103* (10), 5554–5566. DOI: 10.1111/jace.17305.
- (215) Stuecker, J. N.; Cesarano, J.; Hirschfeld, D. A. Control of the viscous behavior of highly concentrated mullite suspensions for robocasting. *J. Mater. Process. Technol.* **2003**, *142* (2), 318–325. DOI: 10.1016/S0924-0136(03)00586-7.
- (216) Feilden, E.; Blanca, E. G.-T.; Giuliani, F.; Saiz, E.; Vandeperre, L. Robocasting of structural ceramic parts with hydrogel inks. *J. Eur. Ceram. Soc.* **2016**, *36* (10), 2525–2533. DOI: 10.1016/j.jeurceramsoc.2016.03.001.
- (217) Peng, E.; Zhang, D.; Ding, J. Ceramic Robocasting: Recent Achievements, Potential, and Future Developments. *Adv. Mater.* **2018**, *30* (47), e1802404. DOI: 10.1002/adma.201802404.

- (218) Lefevre, J.; Gysen, M.; Mullens, S.; Meynen, V.; van Noyen, J. The benefit of design of support architectures for zeolite coated structured catalysts for methanol-to-olefin conversion. *Catal. Today* **2013**, *216*, 18–23. DOI: 10.1016/j.cattod.2013.05.020.
- (219) Tubío, C. R.; Azuaje, J.; Escalante, L.; Coelho, A.; Guitián, F.; Sotelo, E.; Gil, A. 3D printing of a heterogeneous copper-based catalyst. *J. Catal.* **2016**, *334*, 110–115. DOI: 10.1016/j.jcat.2015.11.019.
- (220) Thakkar, H.; Eastman, S.; Hajari, A.; Rownaghi, A. A.; Knox, J. C.; Rezaei, F. 3D-Printed Zeolite Monoliths for CO<sub>2</sub> Removal from Enclosed Environments. *ACS Appl. Mater. Interfaces.* **2016**, *8* (41), 27753–27761. DOI: 10.1021/acsami.6b09647.
- (221) Thakkar, H.; Eastman, S.; Al-Naddaf, Q.; Rownaghi, A. A.; Rezaei, F. 3D-Printed Metal-Organic Framework Monoliths for Gas Adsorption Processes. *ACS Appl. Mater. Interfaces.* **2017**, *9* (41), 35908–35916. DOI: 10.1021/acsami.7b11626.
- (222) Azuaje, J.; Tubío, C. R.; Escalante, L.; Gómez, M.; Guitián, F.; Coelho, A.; Caamaño, O.; Gil, A.; Sotelo, E. An efficient and recyclable 3D printed  $\alpha$ -Al<sub>2</sub>O<sub>3</sub> catalyst for the multicomponent assembly of bioactive heterocycles. *Appl. Catal. A: Gen.* **2017**, *530*, 203–210. DOI: 10.1016/j.apcata.2016.11.031.
- (223) Díaz-Marta, A. S.; Tubío, C. R.; Carbajales, C.; Fernández, C.; Escalante, L.; Sotelo, E.; Guitián, F.; Barrio, V. L.; Gil, A.; Coelho, A. Three-Dimensional Printing in Catalysis: Combining 3D Heterogeneous Copper and Palladium Catalysts for Multicatalytic Multicomponent Reactions. *ACS Catal.* **2018**, *8* (1), 392–404. DOI: 10.1021/acscatal.7b02592.
- (224) Hajimirzaee, S.; Doyle, A. M. 3D printed catalytic converters with enhanced activity for low-temperature methane oxidation in dual-fuel engines. *Fuel* **2020**, *274* (1), 117848. DOI: 10.1016/j.fuel.2020.117848.
- (225) Vadnere, M.; Amidon, G.; Lindenbaum, S.; Haslam, J. Thermodynamic studies on the gel-sol transition of some pluronic polyols. *Int. J. Pharm.* **1984**, *22* (2-3), 207–218. DOI: 10.1016/0378-5173(84)90022-X.
- (226) Thakkar, H.; Eastman, S.; Al-Mamoori, A.; Hajari, A.; Rownaghi, A. A.; Rezaei, F. Formulation of Aminosilica Adsorbents into 3D-Printed Monoliths and Evaluation of Their CO<sub>2</sub> Capture Performance. *ACS Appl. Mater. Interfaces.* **2017**, *9* (8), 7489–7498. DOI: 10.1021/acsami.6b16732.
- (227) Lefevre, J.; Mullens, S.; Meynen, V. The impact of formulation and 3D-printing on the catalytic properties of ZSM-5 zeolite. *Chem. Eng. J.* **2018**, *349*, 260–268. DOI: 10.1016/j.cej.2018.05.058.
- (228) Middelkoop, V.; Vamvakeros, A.; Wit, D. de; Jacques, S. D.M.; Danaci, S.; Jacquot, C.; Vos, Y. de; Matras, D.; Price, S. W.T.; Beale, A. M. 3D printed Ni/Al<sub>2</sub>O<sub>3</sub> based catalysts for CO<sub>2</sub> methanation - a comparative and operando XRD-CT study. *J. CO<sub>2</sub> Util.* **2019**, *33* (2016), 478–487. DOI: 10.1016/j.jcou.2019.07.013.

- (229) Kotobuki, M. Properties of Al<sub>2</sub>O<sub>3</sub> Pastes Using Inorganic Na<sub>2</sub>SiO<sub>3</sub> Binder and Organic Binder for Direct Ink Writing. *Phys. Status Solidi B* **2022**, 259 (9), 2100520. DOI: 10.1002/pssb.202100520.
- (230) Baltazar, J.; Torres, P.M.C.; Dias-de-Oliveira, J.; Pinho-da-Cruz, J.; Gouveia, S.; Olhero, S. Influence of filament patterning in structural properties of dense alumina ceramics printed by robocasting. *J. Manuf. Process.* **2021**, 68, 569–582. DOI: 10.1016/j.jmapro.2021.05.043.
- (231) Gloria, A.; Russo, T.; De Santis, R.; Ambrosio, L. 3D Fiber Deposition Technique to Make Multifunctional and Tailor-Made Scaffolds for Tissue Engineering Applications. *J. Appl. Biomater. Biomech.* **2009**, 7 (3), 141–152.
- (232) Stanciuc, A.-M.; Sprecher, C. M.; Adrien, J.; Roiban, L. I.; Alini, M.; Gremillard, L.; Peroglio, M. Robocast zirconia-toughened alumina scaffolds: Processing, structural characterisation and interaction with human primary osteoblasts. *J. Eur. Ceram. Soc.* **2018**, 38 (3), 845–853. DOI: 10.1016/j.jeurceramsoc.2017.08.031.
- (233) Daguano, J. K. M. B.; Santos, C.; Alves, M. F. R. P.; Lopes da Silva, J. V.; Souza, M. T.; Fernandes, M. H. F. V. State of the art in the use of bioceramics to elaborate 3D structures using robocasting. *Int. J. Adv. Med. Sci.* **2019**, 2 (1), 55. DOI: 10.25061/2595-3931/IJAMB/2019.v2i1.28.
- (234) Monfared, M. H.; Nemati, A.; Loghman, F.; Ghasemian, M.; Farzin, A.; Beheshtizadeh, N.; Azami, M. A deep insight into the preparation of ceramic bone scaffolds utilizing robocasting technique. *Ceram. Int.* **2022**, 48 (5), 5939–5954. DOI: 10.1016/j.ceramint.2021.11.268.
- (235) Hao, L.; Tang, D.; Sun, T.; Xiong, W.; Feng, Z.; Evans, K. E.; Li, Y. Direct Ink Writing of Mineral Materials: A review. *Int. J. of Precis. Eng. and Manuf.-Green Tech.* **2021**, 8 (2), 665–685. DOI: 10.1007/s40684-020-00222-6.
- (236) Peng, E.; Wei, X.; Garbe, U.; Yu, D.; Edouard, B.; Liu, A.; Ding, J. Robocasting of dense yttria-stabilized zirconia structures. *J Mater Sci* **2018**, 53 (1), 247–273. DOI: 10.1007/s10853-017-1491-x.
- (237) M'Barki, A.; Bocquet, L.; Stevenson, A. Linking Rheology and Printability for Dense and Strong Ceramics by Direct Ink Writing. *Sci. Rep.* **2017**, 7 (1), 6017. DOI: 10.1038/s41598-017-06115-0.
- (238) Zhu, C.; Han, T. Y.-J.; Duoss, E. B.; Golobic, A. M.; Kuntz, J. D.; Spadaccini, C. M.; Worsley, M. A. Highly compressible 3D periodic graphene aerogel microlattices. *Nat. Commun.* **2015**, 6, 6962. DOI: 10.1038/ncomms7962.
- (239) Chen, B.; Jiang, Y.; Tang, X.; Pan, Y.; Hu, S. Fully Packaged Carbon Nanotube Supercapacitors by Direct Ink Writing on Flexible Substrates. *ACS applied materials & interfaces* **2017**, 9 (34), 28433–28440. DOI: 10.1021/acsami.7b06804.
- (240) Jiang, P.; Ji, Z.; Zhang, X.; Liu, Z.; Wang, X. Recent advances in direct ink writing of electronic components and functional devices. *Prog. Addit. Manuf.* **2018**, 3 (1-2), 65–86. DOI: 10.1007/s40964-017-0035-x.

- (241) Larson, C. M.; Choi, J. J.; Gallardo, P. A.; Henderson, S. W.; Niemack, M. D.; Rajagopalan, G.; Shepherd, R. F. Direct Ink Writing of Silicon Carbide for Microwave Optics. *Adv. Eng. Mater.* **2016**, *18* (1), 39–45. DOI: 10.1002/adem.201500298.
- (242) Jones, I. K.; Seeley, Z. M.; Cherepy, N. J.; Duoss, E. B.; Payne, S. A. Direct ink write fabrication of transparent ceramic gain media. *Opt. Mater.* **2018**, *75* (4), 19–25. DOI: 10.1016/j.optmat.2017.10.005.
- (243) Nan, B.; Galindo-Rosales, F. J.; Ferreira, J. M.F. 3D printing vertically: Direct ink writing free-standing pillar arrays. *Mater. Today* **2020**, *35* (8), 16–24. DOI: 10.1016/j.mattod.2020.01.003.
- (244) Chen, T.; Sun, A.; Chu, C.; Wu, H.; Wang, J.; Wang, J.; Li, Z.; Guo, J.; Xu, G. Rheological behavior of titania ink and mechanical properties of titania ceramic structures by 3D direct ink writing using high solid loading titania ceramic ink. *J. Alloys Compd.* **2019**, *783*, 321–328. DOI: 10.1016/j.jallcom.2018.12.334.
- (245) Diloksumpan, P.; Ruijter, M. de; Castilho, M.; Gbureck, U.; Vermonden, T.; van Weeren, P. R.; Malda, J.; Levato, R. Combining multi-scale 3D printing technologies to engineer reinforced hydrogel-ceramic interfaces. *Biofabrication* **2020**, *12* (2), 25014. DOI: 10.1088/1758-5090/ab69d9.
- (246) Rueschhoff, L.; Costakis, W.; Michie, M.; Youngblood, J.; Trice, R. Additive Manufacturing of Dense Ceramic Parts via Direct Ink Writing of Aqueous Alumina Suspensions. *Int. J. Appl. Ceram. Technol.* **2016**, *13* (5), 821–830. DOI: 10.1111/ijac.12557.
- (247) Fu, Z.; Freihart, M.; Wahl, L.; Fey, T.; Greil, P.; Travitzky, N. Micro- and macroscopic design of alumina ceramics by robocasting. *J. Eur. Ceram. Soc.* **2017**, *37* (9), 3115–3124. DOI: 10.1016/j.jeurceramsoc.2017.03.052.
- (248) Yang, L.; Zeng, X.; Ditta, A.; Feng, B.; Su, L.; Zhang, Y. Preliminary 3D printing of large inclined-shaped alumina ceramic parts by direct ink writing. *J. Adv. Ceram.* **2020**, *9* (3), 312–319. DOI: 10.1007/s40145-020-0369-6.
- (249) Faes, M.; Vleugels, J.; Vogeler, F.; Ferraris, E. Extrusion-based additive manufacturing of ZrO<sub>2</sub> using photoinitiated polymerization. *CIRP J. Manuf. Sci. Technol.* **2016**, *14*, 28–34. DOI: 10.1016/j.cirpj.2016.05.002.
- (250) Han, D.; Lee, H. Recent advances in multi-material additive manufacturing: methods and applications. *Curr. Opin. Chem. Eng.* **2020**, *28*, 158–166. DOI: 10.1016/j.coche.2020.03.004.
- (251) Xu, C.; Quinn, B.; Lebel, L. L.; Therriault, D.; L'Espérance, G. Multi-Material Direct Ink Writing (DIW) for Complex 3D Metallic Structures with Removable Supports. *ACS Appl. Mater. Interfaces* **2019**, *11* (8), 8499–8506. DOI: 10.1021/acsami.8b19986.
- (252) Hartings, M. R.; Ahmed, Z. Chemistry from 3D printed objects. *Nat. Rev. Chem.* **2019**, *3* (5), 305–314. DOI: 10.1038/s41570-019-0097-z.
- (253) Zhou, X.; Liu, C.-j. Three-dimensional Printing for Catalytic Applications: Current Status and Perspectives. *Adv. Funct. Mater.* **2017**, *27* (30), 1701134. DOI: 10.1002/adfm.201701134.

- (254) Ludwig, T.; Seckendorff, J.; Troll, C.; Fischer, R.; Tonigold, M.; Rieger, B.; Hinrichsen, O. Additive Manufacturing of Al<sub>2</sub>O<sub>3</sub> -Based Carriers for Heterogeneous Catalysis. *Chem. Ing. Tech.* **2018**, *90* (5), 703–707. DOI: 10.1002/cite.201700151.
- (255) Bogdan, E.; Michorczyk, P. 3D Printing in Heterogeneous Catalysis-The State of the Art. *Materials (Basel, Switzerland)* **2020**, *13* (20). DOI: 10.3390/ma13204534.
- (256) Li, T.; Gonzalez-Gutierrez, J.; Raguž, I.; Holzer, C.; Li, M.; Cheng, P.; Kitzmantel, M.; Shi, L.; Huang, L. Material extrusion additively manufactured alumina monolithic structures to improve the efficiency of plasma-catalytic oxidation of toluene. *Addit. Manuf.* **2021**, *37*, 101700. DOI: 10.1016/j.addma.2020.101700.
- (257) Sangiorgi, A.; Gonzalez, Z.; Ferrandez-Montero, A.; Yus, J.; Sanchez-Herencia, A. J.; Galassi, C.; Sanson, A.; Ferrari, B. 3D Printing of Photocatalytic Filters Using a Biopolymer to Immobilize TiO<sub>2</sub> Nanoparticles. *J. Electrochem. Soc.* **2019**, *166* (5), H3239-H3248. DOI: 10.1149/2.0341905jes.
- (258) Car, F.; Brnadić, G.; Tomašić, V.; Vrsaljko, D. Advanced preparation method of monolithic catalyst carriers using 3D-printing technology. *Prog. Addit. Manuf.* **2022**, *7* (4), 797–808. DOI: 10.1007/s40964-022-00266-x.
- (259) Bui, H. M.; Fischer, R.; Szesni, N.; Tonigold, M.; Achterhold, K.; Pfeiffer, F.; Hinrichsen, O. Development of a manufacturing process for Binder Jet 3D printed porous Al<sub>2</sub>O<sub>3</sub> supports used in heterogeneous catalysis. *Addit. Manuf.* **2022**, *50*, 102498. DOI: 10.1016/j.addma.2021.102498.
- (260) Bui, H. M.; Großmann, P. F.; Gros, T.; Blum, M.; Berger, A.; Fischer, R.; Szesni, N.; Tonigold, M.; Hinrichsen, O. 3D printed co-precipitated Ni-Al CO<sub>2</sub> methanation catalysts by Binder Jetting: Fabrication, characterization and test in a single pellet string reactor. *Appl. Catal. A: Gen.* **2022**, *643*, 118760. DOI: 10.1016/j.apcata.2022.118760.
- (261) Huo, C.; Tian, X.; Nan, Y.; Qiu, Z.; Zhong, Q.; Huang, X.; Yu, S.; Li, D. Regulation mechanism of the specific surface area of alumina ceramic carriers with hierarchical porosity fabricated by powder bed fusion. *Ceram. Int.* **2021**, *47* (21), 30954–30962. DOI: 10.1016/j.ceramint.2021.08.198.
- (262) Agueniou, F.; Vidal, H.; Yeste, M. P.; Hernández-Garrido, J. C.; Cauqui, M. A.; Rodríguez-Izquierdo, J. M.; Calvino, J. J.; Gatica, J. M. Ultrathin Washcoat and Very Low Loading Monolithic Catalyst with Outstanding Activity and Stability in Dry Reforming of Methane. *Nanomaterials* **2020**, *10* (3). DOI: 10.3390/nano10030445.
- (263) Agueniou, F.; Vidal, H.; Dios López, J. de; Hernández-Garrido, J. C.; Cauqui, M. A.; Botana, F. J.; Calvino, J. J.; Galvita, V. V.; Gatica, J. M. 3D-printing of metallic honeycomb monoliths as a doorway to a new generation of catalytic devices: the Ni-based catalysts in methane dry reforming showcase. *Catal. Commun.* **2021**, *148* (1), 106181. DOI: 10.1016/j.catcom.2020.106181.



- (264) Michorczyk, P.; Hędrzak, E.; Węgrzyniak, A. Preparation of monolithic catalysts using 3D printed templates for oxidative coupling of methane. *J. Mater. Chem. A* **2016**, *4* (48), 18753–18756. DOI: 10.1039/C6TA08629B.
- (265) Alimi, O. A.; Akinnawo, C. A.; Meijboom, R. Monolith catalyst design via 3D printing: a reusable support for modern palladium-catalyzed cross-coupling reactions. *New J. Chem.* **2020**, *44* (43), 18867–18878. DOI: 10.1039/D0NJ03651J.
- (266) Alimi, O. A.; Ncongwane, T. B.; Meijboom, R. Design and fabrication of a monolith catalyst for continuous flow epoxidation of styrene in polypropylene printed flow reactor. *Chem. Eng. Res. Des.* **2020**, *159*, 395–409. DOI: 10.1016/j.cherd.2020.04.025.
- (267) Rokicińska, A.; Drozdek, M.; Bogdan, E.; Węgrzynowicz, A.; Michorczyk, P.; Kuśtrowski, P. Combustion of toluene over cobalt-modified MFI zeolite dispersed on monolith produced using 3D printing technique. *Catal. Today* **2021**, *375*, 369–376. DOI: 10.1016/j.cattod.2020.04.005.
- (268) Li, Y.; Chen, S.; Cai, X.; Hong, J.; Wu, X.; Xu, Y.; Zou, J.; Chen, B. H. Rational design and preparation of hierarchical monoliths through 3D printing for syngas methanation. *J. Mater. Chem. A* **2018**, *6* (14), 5695–5702. DOI: 10.1039/C8TA01597J.
- (269) Davó-Quñonero, A.; Sorolla-Rosario, D.; Bailón-García, E.; Lozano-Castelló, D.; Bueno-López, A. Improved asymmetrical honeycomb monolith catalyst prepared using a 3D printed template. *J. Hazard. Mater.* **2019**, *368*, 638–643. DOI: 10.1016/j.jhazmat.2019.01.092.
- (270) Xu, X.; Zhang, M.; Jiang, P.; Liu, D.; Wang, Y.; Xu, X.; Ji, Z.; Jia, X.; Wang, H.; Wang, X. Direct ink writing of Pd-Decorated Al<sub>2</sub>O<sub>3</sub> ceramic based catalytic reduction continuous flow reactor. *Ceram. Int.* **2022**, *48* (8), 10843–10851. DOI: 10.1016/j.ceramint.2021.12.301.
- (271) Alimi, O. A.; Akinnawo, C. A.; Onisuru, O. R.; Meijboom, R. 3-D printed microreactor for continuous flow oxidation of a flavonoid. *J. Flow Chem.* **2020**, *10* (3), 517–531. DOI: 10.1007/s41981-020-00089-3.
- (272) Parra-Cabrera, C.; Achille, C.; Kuhn, S.; Ameloot, R. 3D printing in chemical engineering and catalytic technology: structured catalysts, mixers and reactors. *Chem. Soc. Rev.* **2018**, *47* (1), 209–230. DOI: 10.1039/c7cs00631d.
- (273) Wei, Q.; Li, H.; Liu, G.; He, Y.; Wang, Y.; Tan, Y. E.; Wang, D.; Peng, X.; Yang, G.; Tsubaki, N. Metal 3D printing technology for functional integration of catalytic system. *Nat. Commun.* **2020**, *11* (1), 4098. DOI: 10.1038/s41467-020-17941-8.
- (274) Kitson, P. J.; Glatzel, S.; Chen, W.; Lin, C.-G.; Song, Y.-F.; Cronin, L. 3D printing of versatile reactionware for chemical synthesis. *Nat. Protoc.* **2016**, *11* (5), 920–936. DOI: 10.1038/nprot.2016.041.
- (275) Kovacev, N.; Li, S.; Zeraati-Rezaei, S.; Hemida, H.; Tsolakis, A.; Essa, K. Effects of the internal structures of monolith ceramic substrates on thermal and hydraulic properties: additive manufacturing, numerical modelling and experimental testing. *Int. J. Adv. Manuf. Technol.* **2021**, *112* (3-4), 1115–1132. DOI: 10.1007/s00170-020-06493-2.

- (276) Ferrizz, R. M.; Stuecker, J. N.; Cesarano, J.; Miller, J. E. Monolithic Supports with Unique Geometries and Enhanced Mass Transfer. *Ind. Eng. Chem. Res.* **2005**, *44* (2), 302–308. DOI: 10.1021/ie049468r.
- (277) Stuecker, J. N.; Miller, J. E.; Ferrizz, R. E.; Mudd, J. E.; Cesarano, J. Advanced Support Structures for Enhanced Catalytic Activity. *Ind. Eng. Chem. Res.* **2004**, *43* (1), 51–55. DOI: 10.1021/ie030291v.
- (278) Noyen, J.; Wilde, A.; Schroeven, M.; Mullens, S.; Luyten, J. Ceramic Processing Techniques for Catalyst Design: Formation, Properties, and Catalytic Example of ZSM-5 on 3-Dimensional Fiber Deposition Support Structures. *Int. J. Appl. Ceram. Technol.* **2012**, *9* (5), 902–910. DOI: 10.1111/j.1744-7402.2012.02781.x.
- (279) Danaci, S.; Protasova, L.; Snijkers, F.; Bouwen, W.; Bengaouer, A.; Marty, P. Innovative 3D-manufacture of structured copper supports post-coated with catalytic material for CO<sub>2</sub> methanation. *Chem. Eng. Process.* **2018**, *127*, 168–177. DOI: 10.1016/j.cep.2018.03.023.
- (280) Lucentini, I.; García Colli, G.; Luzi, C.; Serrano, I.; Soler, L.; Divins, N. J.; Martínez, O. M.; Llorca, J. Modelling and simulation of catalytic ammonia decomposition over Ni-Ru deposited on 3D-printed CeO<sub>2</sub>. *Chem. Eng. J.* **2022**, *427*, 131756. DOI: 10.1016/j.cej.2021.131756.
- (281) Konarova, M.; Aslam, W.; Ge, L.; Ma, Q.; Tang, F.; Rudolph, V.; Beltramini, J. N. Enabling Process Intensification by 3 D Printing of Catalytic Structures. *ChemCatChem* **2017**, *9* (21), 4132–4138. DOI: 10.1002/cctc.201700829.
- (282) Quintanilla, A.; Casas, J. A.; Miranzo, P.; Osendi, M. I.; Belmonte, M. 3D-Printed Fe-doped silicon carbide monolithic catalysts for wet peroxide oxidation processes. *Appl. Catal. B: Environ.* **2018**, *235*, 246–255. DOI: 10.1016/j.apcatb.2018.04.066.
- (283) Li, X.; Rezaei, F.; Rownaghi, A. A. Methanol-to-olefin conversion on 3D-printed ZSM-5 monolith catalysts: Effects of metal doping, mesoporosity and acid strength. *Microporous Mesoporous Mater.* **2018**, *276*, 1–12. DOI: 10.1016/j.micromeso.2018.09.016.
- (284) Mendez-Arriaga, F.; La Calleja, E. d.; Ruiz-Huerta, L.; Caballero-Ruiz, A.; Almanza, R. TiO<sub>2</sub> 3D structures for environmental purposes by additive manufacturing: Photoactivity test and reuse. *Mater. Sci. Semicond. Process.* **2019**, *100* (2015), 35–41. DOI: 10.1016/j.mssp.2019.04.034.
- (285) Magzoub, F.; Li, X.; Al-Darwish, J.; Rezaei, F.; Rownaghi, A. A. 3D-printed ZSM-5 monoliths with metal dopants for methanol conversion in the presence and absence of carbon dioxide. *Appl. Catal. B* **2019**, *245*, 486–495. DOI: 10.1016/j.apcatb.2019.01.008.
- (286) Zhou, X.; Liu, C.-j. Three-dimensional printing of porous carbon structures with tailorable pore sizes. *Catal. Today* **2020**, *347*, 2–9. DOI: 10.1016/j.cattod.2018.05.044.
- (287) Vega, G.; Quintanilla, A.; Menendez, N.; Belmonte, M.; Casas, J. A. 3D honeycomb monoliths with interconnected channels for the sustainable production of dihydroxybenzenes: towards the intensification of selective oxidation processes. *Chem. Eng. Process.* **2021**, *165*, 108437. DOI: 10.1016/j.cep.2021.108437.

- (288) Salazar-Aguilar, A. D.; Quintanilla, A.; Vega-Díaz, S. M.; Casas, J. A.; Miranzo, P.; Osendi, M. I.; Belmonte, M. Iron-based metal-organic frameworks integrated into 3D printed ceramic architectures. *Open Ceramics* **2021**, *5*, 100047. DOI: 10.1016/j.oceram.2020.100047.
- (289) Quintanilla, A.; Vega, G.; López, P.; García, F.; Madurga, E.; Belmonte, M.; Casas, J. A. Enhanced Fluid Dynamics in 3D Monolithic Reactors to Improve the Chemical Performance: Experimental and Numerical Investigation. *Ind. Eng. Chem. Res.* **2021**, *60* (41), 14701–14712. DOI: 10.1021/acs.iecr.1c03098.
- (290) Lawson, S.; Farsad, A.; Rezaei, F.; Ludlow, D.; Rownaghi, A. A. Direct Ink Writing of Metal Oxide/H-ZSM-5 Catalysts for n-Hexane Cracking: A New Method of Additive Manufacturing with High Metal Oxide Loading. *ACS Appl. Mater. Interfaces* **2021**, *13* (1), 781–794. DOI: 10.1021/acsami.0c20752.
- (291) Karsten, T.; Middelkoop, V.; Matras, D.; Vamvakeros, A.; Poulston, S.; Grosjean, N.; Rollins, B.; Gallucci, F.; Godini, H. R.; Jacques, S. D. M.; Beale, A. M.; Repke, J.-U. Multi-Scale Studies of 3D Printed Mn–Na–W/SiO<sub>2</sub> Catalyst for Oxidative Coupling of Methane. *Catalysts* **2021**, *11* (3), 290. DOI: 10.3390/catal11030290.
- (292) Jacquot, C.; Middelkoop, V.; Köckritz, A.; Pohar, A.; Bienert, R.; Kellici, S.; Bărăgău, I.-A.; Venezia, B.; Gavriilidis, A.; Likozar, B.; Beale, A. M. 3D printed catalytic reactors for aerobic selective oxidation of benzyl alcohol into benzaldehyde in continuous multiphase flow. *SM&T* **2021**, *30* (1), e00329. DOI: 10.1016/j.susmat.2021.e00329.
- (293) Álvarez, F.; Cifuentes, A.; Serrano, I.; Franco, L.; Fargas, G.; Fenollosa, F.; Uceda, R.; Llanes, L.; Tardivat, C.; Llorca, J.; Roa, J. J. Optimization of the sintering thermal treatment and the ceramic ink used in direct ink writing of  $\alpha$ -Al<sub>2</sub>O<sub>3</sub>: Characterization and catalytic application. *J. Eur. Ceram. Soc.* **2022**, *42* (6), 2921–2930. DOI: 10.1016/j.jeurceramsoc.2022.01.032.
- (294) Symes, M. D.; Kitson, P. J.; Yan, J.; Richmond, C. J.; Cooper, G. J. T.; Bowman, R. W.; Vilbrandt, T.; Cronin, L. Integrated 3D-printed reactionware for chemical synthesis and analysis. *Nat. Chem.* **2012**, *4* (5), 349–354. DOI: 10.1038/nchem.1313.
- (295) Hussain, M. Z.; Großmann, P. F.; Kohler, F.; Kratky, T.; Kronthaler, L.; van der Linden, B.; Rodewald, K.; Rieger, B.; Fischer, R. A.; Xia, Y. 3D Printed MOF-Derived Composites for Enhanced Photocatalytic Hydrogen Generation. *Sol. RRL* **2022**, 2200552. DOI: 10.1002/solr.202200552.
- (296) Großmann, P. F.; Tonigold, M.; Szesni, N.; Fischer, R. W.; Seidel, A.; Achterhold, K.; Pfeiffer, F.; Rieger, B. Influence of internal and external surface area on impregnation and activity of 3D printed catalyst carriers. *Catal. Commun.* **2023**, *175*, 106610. DOI: 10.1016/j.catcom.2023.106610.
- (297) Bui, H. M.; Großmann, P. F.; Berger, A.; Seidel, A.; Tonigold, M.; Szesni, N.; Fischer, R.; Rieger, B.; Hinrichsen, O. Comparison of Direct Ink Writing and Binder Jetting for additive manufacturing of Pt/Al<sub>2</sub>O<sub>3</sub> catalysts for the dehydrogenation of perhydro-dibenzyltoluene. *Chem. Eng. J.* **2023**, *12* (4), 141361. DOI: 10.1016/j.cej.2023.141361.